NAS 1.60:1766

ORIGINAL

NASA Technical Paper 1766

COMPLETED

Investigation of Convergent-Divergent Nozzles Applicable to Reduced-Power Supersonic Cruise Aircraft

Bobby L. Berrier and Richard J. Re

DECEMBER 1980

NASA

NASA Technical Paper 1766

Investigation of Convergent-Divergent Nozzles Applicable to Reduced-Power Supersonic Cruise Aircraft

Bobby L. Berrier and Richard J. Re
Langley Research Center
Hampton, Virginia

NASA
National Aeronautics
and Space Administration

Scientific and Technical
Information Branch

1980

SUMMARY

An investigation has been conducted of isolated convergent-divergent nozzles to determine the effect of several design parameters on nozzle performance. Tests were conducted using high-pressure air for propulsion simulation at Mach numbers from 0.60 to 2.86 at an angle of attack of 0^{o} at nozzle pressure ratios from jet off to 46.0. Three power settings (dry, partial afterburning, and maximum afterburning), three nozzle lengths, and nozzle expansion ratios from 1.22 to 2.24 were investigated. In addition, the effects of nozzle throat radius and a cusp in the external boattail geometry were studied.

The results of this study indicate that, for nozzles operating near design conditions, increasing nozzle length increases nozzle thrust-minus-drag performance. Nozzle throat radius and an external boattail cusp had negligible effects on nozzle drag or internal performance.

INTRODUCTION

Research on aircraft design relative to the installation of the propulsive exhaust system into the airframe has received increasing attention in recent years. Summaries of some of this effort are contained in references 1 to 4. In reference 1, Nichols indicated that from the viewpoint of performance, exhaust-nozzle/airframe integration is the most critical design feature of an aircraft.

Most current operational military aircraft have been designed for efficient subsonic cruise and subsonic-transonic maneuverability; supersonic performance has been considered a "fallout" or off-design condition. As a result, past and current propulsion integration studies have emphasized the subsonic-transonic speed regime with little data being obtained at supersonic conditions (ref. 5). However, after analysis of the air operations during recent conflicts, much discussion has taken place concerning aircraft vulnerability over enemy territory; one method proposed to reduce aircraft vulnerability is to provide efficient supersonic cruise capability to future combat aircraft. The design guidelines for military supersonic cruise fighter-type aircraft ("supercruiser") would be substantially different from those of current combat aircraft which have fallout or off-design supersonic performance and even from those of supersonic transport type aircraft which have fallout or off-design subsonic performance. Indeed, the supercruiser mission may include both subsonic and supersonic cruise segments. In this case, neither the subsonic nor the supersonic speed regimes can be considered an off-design condition. The fact that many design guidelines tend to be contradictory for the subsonic and supersonic speed regimes (ref. 5) greatly aggravates the exhaust-nozzle/airframe integration problem. Supersonic cruise with reduced power (nonafterburning or partial afterburning) has been suggested as one method of improving supersonic cruise efficiency. Since current fighter aircraft generally require afterburning power to fly at supersonic speeds, wind-tunnel data on closed-down, dry-power nozzles at Mach numbers above 1.3 are almost nonexistent. Although reduced-power operation could reduce spe-

cific fuel consumption and also infrared signature, with current engines it could also accentuate nozzle/airframe integration problems at supersonic speeds because of increased boattail angle and closure area.

This paper presents the results of a parametric wind-tunnel investigation of isolated convergent-divergent nozzles which could be applicable to supersonic cruise military aircraft. The effects of nozzle divergent-flap length (boattail angle) on the internal and external performance of dry, partial afterburning and maximum afterburning convergent-divergent nozzles are presented with expansion ratios representative of both subsonic and supersonic operation. In addition, the effects of nozzle divergence angle, throat radius, and external nozzle contour are discussed.

This investigation was conducted in the Langley 16-Foot Transonic Tunnel (16FTT) at Mach numbers from 0.60 to 1.20 and in the Langley Unitary Plan Wind Tunnel (UPWT) at Mach numbers from 2.16 to 2.86. Jet total-pressure ratio was varied from approximately 1.0 (jet off) to 15 (depending on nozzle power setting and Mach number) in the transonic facility and to approximately 46.0 (10.0 for two configurations) in the unitary plan tunnel. All configurations were tested without tails and at 0° angle of attack.

SYMBOLS

All forces and angles are referred to the model centerline (body axis). Wind axes are equivalent to body axes since angle of attack was 0° for the current investigation.

A_b area of nozzle base at exit (includes flow area and physical nozzle base area), cm^2

A_e nozzle exit area, cm^2

A_g projected area of metric break gap in axial direction, $A_m - A_i$, cm^2

A_i internal-cavity cross-sectional area of model, cm^2

A_m maximum cross-sectional area of model, 182.415 cm^2

A_s sonic flow area, $(W_p/W_i)A_t$, cm^2

A_t nozzle geometric throat area, cm^2

b axial distance from nozzle connect station (Sta. 137.16) to center of radius leading to nozzle convergent section (see fig. 3), cm

$C_{D,n}$ nozzle total drag coefficient (External pressure + External friction), $D_n/q_{\infty}A_m$

$C_{D,nf}$ nozzle external-friction drag coefficient

$(C_p)_{crit}$ critical (locally sonic flow) pressure coefficient

$C_{p,b}$	nozzle base pressure coefficient
$C_{p,n}$	nozzle boattail static pressure coefficient, $(p_n - p_\infty)/q_\infty$
C_s	stream thrust-correction factor
$D_{f,cb}$	friction drag on model centerbody, N
D_n	nozzle drag (Pressure + Friction), N
d_b	diameter of nozzle base at exit, cm
d_e	nozzle exit diameter, cm
d_m	maximum model diameter, 15.24 cm
d_t	nozzle geometric throat diameter, cm
F	nozzle gross thrust, N
$F_{A,bal}$	axial force measured by balance, positive forward, N
$F_{A,mom}$	momentum tare axial force due to bellows, N
F_i	ideal isentropic gross thrust, N
F_V	vacuum thrust, N
l	nozzle length, cm
l_f	projected axial length of nozzle divergent flap (axial distance from nozzle throat to nozzle exit), cm
M	free-stream Mach number
M_e	jet-flow Mach number at nozzle exit
N_{Re}	Reynolds number based on total model length
p_e	static pressure at nozzle exit, Pa
p_g	local pressure in metric-break gap, Pa
p_i	internal static pressure, Pa
p_n	local nozzle static pressure, Pa
$p_{t,j}$	jet total pressure, Pa
$p_{t,\infty}$	free-stream total pressure, Pa
$(p_{t,j}/p_\infty)_{des}$	nozzle design pressure ratio for fully expanded isentropic flow

p_∞	free-stream static pressure, Pa
q_∞	free-stream dynamic pressure, Pa
R	gas constant for air, 287.3 J/kg-K
$T_{t,j}$	jet total temperature, K
$T_{t,\infty}$	free-stream total temperature, K
V_e	jet-flow velocity at nozzle exit, cm/sec
W_i	ideal mass-flow rate, kg/sec
W_p	actual mass-flow rate, kg/sec
x	axial distance measured from nozzle connect station, positive downstream, cm
$(x/l)_{sep}$	theoretical external flow separation point given as fraction of nozzle length
β	nozzle terminal boattail angle, deg
γ	ratio of specific heats, 1.3997 for air
δ	nozzle exhaust divergence angle (see fig. 3), deg
θ	nozzle internal convergent approach angle, deg
ϕ	meridian angle about model axis, positive for clockwise direction when facing upstream, 0° at top of model, deg

Abbreviations:

A/B	afterburning
Atm.	atmospheric
Max	maximum
R	radius
Sta.	station
Sub.	subsonic
Super.	supersonic
UPWT	Unitary Plan Wind Tunnel
16FTT	16-Foot Transonic Tunnel

Configuration designations:

D	dry-power nozzle
P	partial-afterburning-power nozzle
A	maximum-afterburning-power nozzle
S	short ($0.814 < l/d_m < 0.868$) nozzle length
M	medium ($0.928 < l/d_m < 0.978$) nozzle length
L	long ($1.114 < l/d_m < 1.161$) nozzle length

APPARATUS AND METHODS

Wind Tunnels

The experimental investigation was conducted in the Langley 16FTT and the Langley UPWT. The Langley 16FTT is a single-return, atmospheric tunnel with a slotted, octagonal test section and continuous air exchange. The tunnel has a speed range capability from $M = 0.20$ to $M = 1.30$. High-speed tests were performed in the low Mach number test section of the Langley UPWT, which is a variable-pressure, continuous-flow facility. The test section is approximately 1.219 meters square and 2.134 meters long, and the nozzle leading to the test section is of the asymmetric, sliding-block type which provides continuous variation in Mach number from about 1.50 to 2.90. A complete description of the wind tunnels and their operating characteristics can be found in references 6 and 7.

Model and Support System

Photographs of the model installed in the Langley 16FTT and UPWT are shown in figure 1, and a sketch of the sting-strut-supported single-engine model (16FTT installation) with a typical nozzle installed is presented in figure 2. The isolated (no empennage surfaces or afterbody boattail) nozzle model is composed of three major parts, located as follows:

	Model station, cm
Forebody:	
16FTT	0 to 67.31
UPWT	15.24 to 67.31
Centerbody	67.31 to 137.16
Nozzle	137.16 to exit

The axisymmetric forebody was nonmetric (not attached to balance). For tests in the 16FTT, an ogive forebody (see fig. 2) starting at station 0 was used to reduce the strength of the external flow expansion around the forebody shoulder.

In order to reduce model length and avoid wall-reflected shocks at supersonic speeds, a shorter conical forebody starting at station 15.24 (not shown) was utilized for tests in the UPWT. As shown in figure 2, a 0.15-cm gap in the external skin at the metric-break station (Sta. 67.31) prevented fouling between the nonmetric forebody and metric centerbody and nozzle.

An external high-pressure air system provided a continuous flow of clean, dry air in both facilities at a controlled temperature of about 300 K. Air was brought through the support-system strut by six tubes and collected in a high-pressure plenum located in the forebody (see fig. 2) and routed aft. The air was then discharged perpendicularly into the integral-model centerbody/low-pressure plenum/tailpipe through eight multiholed sonic nozzles equally spaced around the aft end of the high-pressure plenum. This design minimized any forces imposed by the transfer of axial momentum as the air passed from the nonmetric high-pressure plenum to the metric centerbody. Two opposing flexible metal bellows are used as seals and serve to compensate for axial forces caused by pressurization.

In the 16FTT, the model was located on the wind-tunnel center line. The center line of the sting, which supports the strut in the 16FTT (see figs. 1 and 2), was 55.88 cm below the wind-tunnel center line. The sting portion of the support system was 5.08 cm by 10.16 cm in cross section, with the top and bottom capped by half-cylinders of 2.54-cm radius. The strut was 5 percent thick with a constant 50.8-cm chord (see fig. 2) in the streamwise direction and was swept 45°. In the UPWT, only the strut support was used and the model was mounted from the tunnel sidewall (see fig. 1).

Nozzle geometry simulated a variable-geometry, balanced-beam, convergent-divergent conical nozzle typical of those currently in use on modern fighter aircraft but with a larger range of nozzle expansion ratio (A_e/A_t) and divergent flap length. Figure 3 presents sketches and a table giving nozzle internal and external geometry. The nozzles attached directly to the centerbody at station 137.16. Nozzle power settings representing dry, partial-afterburning and maximum-afterburning operation were investigated. Each nozzle power setting was investigated with expansion ratios representative of subsonic (A_e/A_t = 1.22 or 1.25) and supersonic (A_e/A_t = 1.69, 1.89, 1.97, or 2.24) operation. In addition, each combination of nozzle power setting and expansion ratio was generally investigated with either two or three different divergent flap lengths l_f. The short flap length represents a baseline nozzle which is typical of current fighter aircraft hardware. The two longer flap lengths (higher nozzle fineness ratio l/d_m) represent nozzle designs which would be expected for airplanes designed to cruise efficiently at supersonic speeds. Nozzle divergent flap length varies slightly with nozzle power setting and expansion ratio for each basic flap length (short, medium, or long), since axial distance (divergent flap length defined along body axis) varies as the flap rotates. In addition to these variables, two additional nozzles (see fig. 3(b)) were tested to investigate the effects of a cusp in the external nozzle geometry and of a sharp throat.

Nozzle configurations have been assigned a coded configuration number to facilitate discussion and data comparisons. The code has a format of letter-number-letter where

(1) The first letter denotes nozzle power setting as follows:

D - dry

P - partial

A - maximum afterburning

(2) The second character, a number, indicates the nozzle expansion ratio A_e/A_t.

(3) The last letter indicates nozzle fineness ratio or divergent flap length as follows:

S - short; $0.814 < l/d_m < 0.868$

M - medium; $0.928 < l/d_m < 0.978$

L - long; $1.114 < l/d_m < 1.161$

Instrumentation

A five-component balance was used to measure external (aerodynamic) and internal (thrust) forces and moments (excluding rolling moment) on the model downstream of station 67.31. (See fig. 2.) Jet total pressure was measured in the centerbody at the location shown in figure 2 by means of a five-probe rake. A thermocouple was used to measure jet total temperature. Air total pressure and total temperature were also measured in the high-pressure plenum before the airflow was discharged through the eight sonic nozzles into the centerbody. These measurements were used in calculating the nozzle mass-flow rate W_p as explained in the section "Data Reduction." In addition, an electronic turbine flowmeter was used as a backup measurement of air mass-flow rate to the nozzle.

External static-pressure orifices were located on all nozzles at constant values of x/l as shown in figure 4. Internal pressures were measured in the forebody cavity at six internal orifice locations. Pressure in the metric-break gap (Sta. 67.31) was measured at four aft-facing orifice locations in the forebody gap base.

Tests

Data were obtained in the Langley 16FTT at static conditions (M = 0) and Mach numbers from 0.60 to 1.20 and in the Langley UPWT at static conditions and Mach numbers from 2.16 to 2.86. The 16FTT is an atmospheric total-pressure facility and the UPWT is capable of varying total pressure. Nominal values of free-stream test conditions for each facility are presented in table 1. The nominal values given in table 1 vary slightly with atmospheric conditions (16FTT), addition of nozzle mass flow (UPWT), and nozzle length (N_{Re} based on total model length).

Angle of attack was held constant at 0^{o} during the investigation. The ratio of jet total pressure to free-stream static pressure was varied from approximately 1.0 (jet off) to about 46.0, depending on Mach number. Two configurations (P-2.24-S and P-2.24-L) were tested at nozzle pressure ratios up to approximately 110.0 at $M = 2.86$ to simulate large plumes which could occur for missile applications.

To insure a turbulent boundary layer over the nozzles, a 0.38-cm-wide transition strip of No. 100 carborundum grit was fixed 5.72 cm downstream of the model nose in the 16FTT. In the UPWT, a 0.32-cm-wide transition strip of No. 35 grit was fixed 3.05 cm downstream of the model nose.

Data Reduction

All data for both the model and the wind tunnel were recorded simultaneously on magnetic tape. Approximately 11 frames of data, taken at a rate of 2 frames per second in the 16FTT, and 60 frames of data, taken at a rate of 30 frames per second in the UPWT, were used for each data point; average values were used in computations. The average value of jet total pressure (average of five probes, see fig. 2) was also used in all computations. The recorded data were used to compute standard force and pressure coefficients. Drag coefficient is referenced to model maximum cross-sectional area.

At wind-on conditions, thrust minus nozzle drag was obtained from the five-component balance and computed from the equation

$$F - D_n = F_{A,bal} + \sum_{j=1}^{4} (p_{g,j} - p_\infty) A_{g,j} + \sum_{j=1}^{6} (p_{i,j} - p_\infty) A_{i,j} - F_{A,mom} + D_{f,cb} \qquad (1)$$

Included in the balance term $F_{A,bal}$ are external and internal axial forces on the metric centerbody and nozzle including thrust, nozzle drag (friction and pressure), centerbody friction drag (pressure drag equal to zero since centerbody has no projected area), axial force resulting from a pressure-area term acting at the metric break, and bellows momentum tares. The second and third terms of equation (1) correct the balance measurement for pressure-area forces acting at the metric break. These terms arise from the fact that the model is a partially metric, afterbody propulsion model. These terms would not exist for typical aerodynamic studies of completely metric (no metric break) models. The fourth term of equation (1) corrects the balance measurement for bellows momentum tares. Although the bellows arrangement was designed to minimize pressure and momentum interactions with the balance, small-bellows tares on axial force still exist. These tares result from a small pressure difference between the

ends of the bellows when internal velocities are high and also from small differences in the forward and aft bellows spring constants when the bellows are pressurized. Bellows tares were determined by running calibration nozzles with known performance; more detailed discussion of this procedure is contained in references 8 and 9. The last term of equation (1) removes the friction drag of the cylindrical centerbody (Sta. 67.31 to Sta. 137.16) from the balance measurement. Friction drag of the centerbody was removed from all performance parameters since this part of the model is not actually part of the nozzle design. Friction drag was calculated using the Frankl and Voishel equation for compressible, turbulent flow on a flat plate as given in reference 10.

Nozzle drag D_n was obtained for each configuration by adding nozzle pressure drag to a computed value of nozzle skin-friction drag (method of Frankl and Voishel). Nozzle pressure drag was obtained by a pressure-area integration using measured nozzle static pressures over the external nozzle boattail surface and base (Sta. 137.16 to end of nozzle). In the 16FTT, all nozzle static pressures were used in the pressure-area integration; because of indications of support-strut interference on the bottom row of nozzle pressure orifices (see fig. 4, $\phi = 180^{\circ}$) in the UPWT, only the top row ($\phi = 0^{\circ}$) of pressure orifices was used in the pressure-area integration at $M = 2.16$ to $M = 2.86$.

Nozzle internal performance (thrust) was obtained at static conditions directly from equation (1) since pressure and friction drag equal zero at $M = 0$. At wind-on conditions, nozzle internal performance was computed from the equation

$$F = (F - D_n) + D_n \tag{2}$$

The first term $(F - D_n)$ of equation (2) is obtained from equation (1), and the second term of equation (2) D_n is obtained from the pressure-area integration and friction drag calculation discussed previously. Internal nozzle performance F should be independent of Mach number unless the nozzle is not choked (subsonic internal flow) or the internal jet exhaust flow separates from the nozzle divergent flap.

The primary measurement of nozzle mass-flow rate W_p was obtained from total pressure and temperature measurements in the high-pressure plenum. The discharge coefficients W_p/W_i of the eight sonic nozzles in the high-pressure plenum were determined by testing calibration nozzles with known flow characteristics. The sonic nozzle discharge coefficient was combined with the total pressure and temperature measured in the high-pressure plenum to determine the mass-flow rate. A detailed discussion of this procedure can be found in reference 8. Using the mass-flow rate thus determined, ideal thrust of the nozzle can be computed from the equation

$$F_i = W_p \sqrt{(RT_{t,j}) \frac{2\gamma}{\gamma - 1} \left[1 - \left(\frac{p_\infty}{p_{t,j}} \right)^{\frac{\gamma - 1}{\gamma}} \right]} \tag{3}$$

Unfortunately, problems were experienced in the UPWT with measurements required for both the primary (high-pressure plenum) and backup (electronic turbine) methods of determining mass-flow rate. The following procedure was used to correct data obtained in the UPWT. As mentioned previously, thrust F and thrust ratio F/F_i are independent of free-stream Mach number when the nozzle is choked and no internal flow separation exists. Therefore, the static ($M = 0$) thrust ratio data obtained in the UPWT was curve fit to the static and wind-on thrust ratio data obtained in the 16FTT at all values of nozzle pressure ratio which did not obviously produce internal flow separation (nozzle pressure ratios near and above the design value given in fig. 3). Using these values of F/F_i and measured values of F, the values of mass-flow rate W_p were determined from equation (3), which gave the required values of ideal thrust F_i. The values of W_p determined in this manner were then combined with computed values of ideal mass-flow rate W_i to provide adjusted values of discharge coefficient W_p/W_i for the UPWT. These adjusted values of discharge coefficient result in the same values of wind-off thrust ratio in the UPWT as obtained in the 16FTT. These adjusted values are presented with the basic data in a later section of this paper. The static ($M = 0$) nozzle-pressure-ratio range did not cover the range tested at $M = 2.16$ to 2.86 in the UPWT. However, the adjusted values of discharge coefficient determined by this procedure were found to be independent of nozzle pressure ratio for most configurations and were a constant value for $p_{t,j}/p_\infty > 20.0$ for all configurations. Thus, at wind-on conditions in the UPWT, this constant value of adjusted discharge coefficient was assumed at all nozzle pressure ratios tested and was used to determine the value of W_p used in the ideal thrust (eq. (3)) and thrust ratio F/F_i. As is shown subsequently, this procedure produces consistent UPWT data which agree well with the 16FTT data and theoretical values of F/F_i. The adjusted values of discharge coefficient contain some of the suspect measurements in ideal mass-flow rate which caused the original problem. Thus, little or no attention should be paid to the absolute values of the adjusted discharge coefficients. However, since discharge coefficient is independent of nozzle pressure ratio at values above choke and the discharge coefficients obtained in the 16FTT were not adjusted but are presented as measured, these values can be used as the correct indication of discharge-coefficient magnitude.

Stream thrust-correction factor C_s is used in this paper as an indication of real nozzle flow losses excluding overexpansion and underexpansion losses. As shown in the following derivation, stream thrust-correction factor is a function of nozzle geometry and is independent of ambient pressure (and thus free-stream Mach number). Use of the momentum equation for one-dimensional, isentropic flow in a nozzle provides the following well-known expression for thrust (see ref. 11):

$$F = W_p V_e + A_e(p_e - p_\infty) \tag{4}$$

or in ratio form

$$\frac{F}{F_i} = \frac{W_p V_e + A_e(p_e - p_\infty)}{F_i} \tag{5}$$

From equation (4), vacuum thrust or stream thrust ($p_\infty = 0$) is seen as follows:

$$F_v = W_p V_e + A_e p_e \tag{6}$$

Substituting equation (6) into equation (5) gives

$$\frac{F}{F_i} = \frac{F_v - A_e p_\infty}{F_i} \tag{7}$$

Dividing the numerator and denominator of equation (7) by $p_{t,j}A_s$ results in

$$\frac{F}{F_i} = \frac{\dfrac{F_v}{p_{t,j}A_s} - \dfrac{A_e p_\infty}{p_{t,j}A_s}}{\dfrac{F_i}{p_{t,j}A_s}} \tag{8}$$

where A_s is the sonic flow area. Viscous effects reduce the amount of flow passing through the geometric throat due to momentum and vena contracta losses. The sonic flow area is proportionately less than the geometric throat area A_t by the ratio of actual to ideal mass-flow rate. Thus,

$$A_s = (W_p/W_i)A_t \tag{9}$$

The dimensionless term $F_v/p_{t,j}A_s$ in equation (8) is the vacuum thrust coefficient for isentropic, one-dimensional flow. However, real nozzle flows are not isentropic or one-dimensional. Thus, maximum values of vacuum thrust coefficient are unattainable. Typical real nozzle losses include nonuniform profiles at the throat, friction losses, shock losses, and divergence losses downstream of the throat. In general, such losses can be combined into a single term, stream thrust-correction factor, which is defined as

$$C_s = \frac{\left(\dfrac{F_v}{p_{t,j}A_s}\right)_{actual}}{\left(\dfrac{F_v}{p_{t,j}A_s}\right)_{ideal}} \tag{10}$$

The ideal or isentropic vacuum thrust coefficient in the denominator is sometimes called the impulse function and is defined in reference 11 as

$$\left(\frac{F_V}{p_{t,j}A_s}\right)_{ideal} = \frac{p_e}{p_{t,j}}\frac{A_e}{A_s}\left(1 + \gamma M_e^2\right) \tag{11}$$

where $p_e/p_{t,j}$ and M_e are functions of nozzle geometry A_e/A_t and flow conditions W_p/W_i (together yield A_e/A_s) and are independent of ambient pressure (no overexpansion or underexpansion losses) and free-stream Mach number. Substituting equations (10) and (11) into equation (8) yields

$$\frac{F}{F_i} = \frac{C_s\left[\frac{p_e}{p_{t,j}}\frac{A_e}{A_s}\left(1 + \gamma M_e^2\right)\right] - \frac{p_\infty}{p_{t,j}}\frac{A_e}{A_s}}{\frac{F_i}{p_{t,j}A_s}} \tag{12}$$

Solving for C_s and simplifying yields the following expression, used to compute the stream thrust-correction factors presented in this paper:

$$C_s = \frac{\frac{F}{p_{t,j}A_s} + \frac{A_e}{A_s}\frac{p_\infty}{p_{t,j}}}{\frac{p_e}{p_{t,j}}\frac{A_e}{A_s}\left(1 + \gamma M_e^2\right)} \tag{13}$$

where F is the measured nozzle thrust obtained as discussed previously in this section.

Internal thrust losses in nozzles with nonisentropic divergent flap contours result from nozzle exit momentum vectors (radial velocity components) which are not aligned with the thrust (or body-axial) axis because of nozzle wall divergence at the exit. The divergence loss for the nozzles of this investigation is estimated by using the following theoretical equation from reference 12:

$$\text{Divergence loss} = 1.0 - 0.5(1 + \cos\delta) \tag{14}$$

DISCUSSION

Basic Data

The basic force (drag and thrust) data are presented in figures 5 to 23 as a function of nozzle pressure ratio $p_{t,j}/p$ for all configurations at all Mach numbers investigated. Each figure presents basic data for one configuration and consists of four parts (with exception of fig. 22, configuration P-2.24(Sharp)-L, which was not tested at $M > 1.20$) organized as follows:

Part (a) - Presents nozzle drag coefficient $C_{D,n}$ for all Mach numbers.

Part (b) - Presents thrust ratio F/F_i and discharge coefficient W_p/W_i obtained in the 16FTT ($0.00 \leq M \leq 1.20$). Also shown, as solid symbols and dash-dot-dash line, are adjusted data (see section entitled "Data Reduction") at $M = 0.0$ from the UPWT. Theoretical estimates of thrust ratio are shown as a dashed line.

Part (c) - Presents thrust ratio and adjusted discharge coefficient (dash-dot-dash line) obtained in the UPWT ($M = 0.00$, 2.16, 2.50, and 2.86). Thrust ratio values were obtained by use of the adjusted values of discharge coefficient as explained in the data reduction section of this paper. The dashed line again represents theoretical estimates of thrust ratio.

Part (d) - Presents nozzle thrust-minus-drag ratio $(F - D_n)/F_i$ for all Mach numbers.

Nozzle drag coefficient.- Nozzle drag coefficient, shown in part (a) of figures 5 to 23, exhibits trends with increasing nozzle pressure ratio which are similar to previous studies of nozzle drag (refs. 13 and 14). As a result of a base-bleed effect, a significant drag reduction generally occurs with initial jet operation. Then, as nozzle pressure ratio is increased from very low values, jet entrainment effects tend to dominate the flow field, and nozzle drag increases as a result of the aspiration caused by the pumping action of the jet exhaust. At a nozzle pressure ratio generally between 2.0 and 4.0, a maximum value of jet-on drag is reached and any further increase in nozzle pressure ratio reduces nozzle drag as plume blockage effects become dominant and the compression region at the nozzle trailing edge is increased in strength.

It is interesting to note that negative nozzle drag (thrust) was obtained on several configurations. (See figs. 6, 7, 11, 12, 14, and 17.) Negative nozzle drag can be produced by substantial pressure recovery over the nozzle boattail at subsonic speeds and by jet exhaust pressurization of separated and/or base regions at supersonic speeds. Nozzle pressure distributions are discussed in a subsequent section of this paper. Unfortunately, negative nozzle drag occurs only for unrealistic test conditions, that is, at nozzle pressure ratios which are higher than typical airplane operating nozzle pressure ratios (fig. 6, for example) or at nozzle expansion ratios which are too low for the test Mach

number (fig. 17, for example). It should also be noted that nozzle drag for the high-expansion-ratio (A_e/A_t = 1.97 and 2.24) partial and maximum afterburning power nozzles (figs. 12 to 14, 20, and 21) approaches the computed value of nozzle friction drag at $M \geq 2.16$. Computed values of nozzle friction drag coefficient are given at the top of each nozzle drag coefficient plot. This trend indicates that pressure drag for these configurations and test conditions approaches zero. This trend might be expected since these configurations have little projected area in the axial direction.

Internal nozzle performance.- Nozzle thrust ratio F/F_i and discharge coefficient W_p/W_i are presented in parts (b) and (c) of figures 5 to 23 (part (b) only of fig. 22). Data from the UPWT were adjusted by the procedure outlined in the data reduction section. Also shown in these figure parts are one-dimensional, isentropic, theoretical estimates of nozzle thrust ratio corrected for nozzle divergence and internal friction losses. (See refs. 11 and 12.)

Nozzle internal performance (thrust ratio) should be independent of free-stream Mach number as long as the nozzle is choked ($p_{t,j}/p_\infty > 1.89$) and no internal flow separation exists on the nozzle divergent flaps. Examination of the thrust ratio data at low nozzle pressure ratios clearly indicates internal flow separation for most if not all configurations, particularly for nozzles with high expansion ratios (and thus high divergence angles δ, see fig. 3). The nozzle pressure ratio required to eliminate internal flow separation tends to increase with increasing nozzle expansion ratio. For example, internal flow separation appears to occur at

$p_{t,j}/p_\infty < 2.0$ to 3.0 for $A_e/A_t \leq 1.25$ (see fig. 11)

$p_{t,j}/p_\infty < 3.0$ to 4.0 for $A_e/A_t = 1.69$ (see fig. 15)

$p_{t,j}/p_\infty < 4.0$ to 5.0 for $1.69 < A_e/A_t \leq 1.97$ (see figs. 16 and 20)

$p_{t,j}/p_\infty < 5.0$ to 6.0 for $A_e/A_t = 2.24$ (see fig. 14)

At nozzle pressure ratios sufficiently high to eliminate internal flow separation, nozzle thrust ratio is shown to be relatively independent of free-stream Mach number. For example, at typical operating pressure ratios ($p_{t,j}/p_\infty = 4.0$ for $A_e/A_t \leq 1.25$ and $p_{t,j}/p_\infty = 26.0$ for $A_e/A_t \geq 1.69$), thrust ratio generally varied less than 1 percent of F/F_i for all Mach numbers and agreed with the theoretical estimate to within 1.5 percent of F/F_i. The variation of thrust ratio with nozzle pressure ratio is typical of convergent-divergent nozzles. Peak thrust ratio occurs at or near the design nozzle pressure ratio. (See fig. 3.) At nozzle pressure ratios lower than $(p_{t,j}/p_\infty)_{des}$, nozzle overexpansion losses occur; at nozzle pressure ratios higher than $(p_{t,j}/p_\infty)_{des}$, nozzle underexpansion losses occur.

Theoretically, nozzle discharge coefficient W_p/W_i is a function only of internal nozzle geometry and should be independent of both Mach number and nozzle pressure ratio when the nozzle is choked. These trends are indicated by the discharge coefficient data (16FTT) of the current investigation. In addition, discharge coefficients for configurations with similar internal geometry (for example, compare figs. 5, 6, and 7) agree to within 1/2 percent.

Nozzle thrust-minus-drag ratio.- Nozzle thrust-minus-drag ratio $(F - D_n)/F_i$ is presented in part (d) of figures 5 to 23 (part (c) of fig. 22) as a function of nozzle pressure ratio for all Mach numbers tested. Nozzle thrust-minus-drag ratio for a given nozzle pressure ratio generally decreases with increasing Mach number at subsonic speeds because of increasing drag on the nozzle boattail.

Pressure Distributions

Static-pressure-coefficient distributions on the nozzle boattail are presented in figures 24 to 42 for each configuration, in the same configuration order as the basic data, at selected free-stream Mach numbers and nozzle pressure ratios. Data are shown for the top ($\phi = 0^o$) orifice row only. (See fig. 4.) Theoretical pressure distributions were computed at $M = 0.90$ by using the computer algorithm DONBOL (ref. 15) and are presented in figures 24 to 42 as dashed lines. DONBOL is a Neumann solution for inviscid external flow coupled to a modified Reshotko-Tucker integral boundary-layer technique, the control volume method of Presz in separated regions, and an inviscid one-dimensional solution for jet exhaust flow. Theoretical pressure distributions were computed at $M \geq 2.16$ by an inviscid method of characteristics code for configurations D-1.22-S (fig. 24) and P-2.24-S (fig. 31) only.

Typical nozzle boattail pressure distributions on configurations with large boattail angles (for example, see figs. 24 to 26) are characterized at subsonic speeds by a strong expansion near the start of the nozzle boattail followed by pressure recovery on the remaining portion of the boattail to positive values of pressure coefficient near the nozzle exit. External flow expansion around the nozzle shoulder was so strong at $M = 0.80$ and 0.90 that regions of local supersonic flow are indicated by pressure coefficients below $(C_p)_{crit}$. However, pressure recovery is sufficient in some cases to produce negative values of nozzle drag (thrust) as mentioned previously. At $M = 0.90$, the pressure distributions show evidence of a standing shock at x/l of about 0.20 followed by external flow separation (predicted at $x/l = 0.25$ by DONBOL). Agreement of the theoretical and experimental pressure distributions is poor in the expansion region. This poor agreement is explained by the fact that the theoretical method of reference 15 is limited to subsonic free-stream Mach numbers below that for which local flow on the nozzle becomes sonic; it is obvious from the experimental data that a region of locally supersonic flow exists on the nozzles not only at $M = 0.90$, but also at $M = 0.80$.

At subsonic speeds, jet interference effects on boattail pressures are extensive. At $M = 0.60$ and 0.80, jet operation influences boattail pressures as far forward as the first pressure orifice located at $x/l = 0.025$. Close examination of pressure coefficient trends with increasing nozzle pressure ratio explains the trends of nozzle drag discussed previously.

At supersonic speeds, nozzle boattail pressure distributions on configurations with large boattail angles (for example, see figs. 24 to 26) are characterized by expansion of the external flow down the nozzle boattail until a standing shock is reached, after which the external flow is completely separated. Jet interference effects are limited at supersonic speeds and do not feed forward of the standing shock wave. However, jet operation has a large impact on the location of the standing shock wave and thus controls the size of the separated flow region; jet interference effects in this region are large. The method-of-characteristics theoretical estimate (see fig. 24(c)) generally indicates the correct data trend of the pressure distributions at supersonic speeds until the standing shock and attendant separated flow region on the nozzle boattail is reached, at which point the experimental data depart from the trend established by the theory. Thus, agreement between experiment and theory becomes worse with increasing nozzle pressure ratio. Also, the theoretical estimate of boattail static pressure coefficient was generally too low over the entire nozzle boattail length. This was probably caused by the inviscid assumption in the theoretical method. A check calculation using a boundary-layer displacement thickness indicated this to be the case.

Typical nozzle boattail pressure distributions on configurations with small boattail angles (for example, see figs. 39 and 40) are characterized at all Mach numbers by a weak expansion region at the nozzle shoulder and little or no downstream pressure recovery. The data also indicate little or no external flow separation for these configurations. Jet interference effects at subsonic speeds again feed all the way forward to $x/l = 0.025$ but, at supersonic speeds, are generally limited to the last two orifice locations near the nozzle exit ($x/l = 0.875$ and 0.950). Although the theoretical method of reference 15 generally provides better agreement with data at the nozzle shoulder for low boattail angle nozzles (no locally supersonic flow) than for high boattail angle nozzles, it underpredicts the negative magnitude of pressure coefficient at $M = 0.90$. This is because the inviscid, one-dimensional solution for the jet exhaust flow neglects the effects of jet plume entrainment.

Pressure distributions on configurations with nozzle boattail angles between the two extremes discussed previously can be found in figures 27 to 38. The method-of-characteristics estimate of the pressure distributions for configuration P-2.24-S (fig. 31) at $M \geq 2.16$ is in good agreement with the experimental data until a standing shock on the nozzle boattail is reached.

Stream Thrust-Correction Factors

Stream thrust-correction factors (see section entitled "Data Reduction") for each nozzle investigated are presented in figure 43 as a function of nozzle pressure ratio. Data are presented for three test Mach numbers for each configuration. As discussed previously, stream thrust-correction factor C_S is a function of nozzle geometry and is independent of ambient pressure and thus free-stream Mach number. In addition, C_S is independent of nozzle pressure ratio $p_{t,j}/p_\infty$ when the nozzle is flowing full. Internal jet-flow separation would obviously have a large effect on static pressure at the nozzle exit, and therefore on the ideal vacuum thrust coefficient (eqs. (10) and (11)). The data for the stream thrust-correction factor are shown in figure 43 and are essen-

tially independent of both Mach number and nozzle pressure ratio over a range of nozzle pressure ratios indicated in figure 43 by the solid-line fairing. This solid-line fairing represents a constant value of C_s obtained by averaging all data over the nozzle pressure ratio range indicated by the fairing. At nozzle pressure ratios lower than those faired, large variations in C_s occur with varying Mach number and especially with varying nozzle pressure ratio. This variation in C_s indicates internal jet-flow separation from the divergent nozzle walls over this range of nozzle pressure ratio. As noted in the discussion of the internal nozzle performance data (thrust ratio data in figs. 5 to 23), the nozzle pressure ratio required to eliminate internal flow separation increases with increasing nozzle expansion ratio. Similar results are indicated by the C_s data (nozzle pressure ratio at which C_s becomes a constant) in figure 43. However, the C_s data indicate higher values of $p_{t,j}/p_\infty$ required to eliminate internal separation than estimated from the thrust ratio data. For example, based on the C_s data, internal flow separation appears to occur at the following nozzle pressure ratios:

$$p_{t,j}/p_\infty < 3.0 \text{ to } 5.0 \quad \text{for} \quad A_e/A_t \leq 1.25$$

$$p_{t,j}/p_\infty < 5.0 \text{ to } 6.0 \quad \text{for} \quad A_e/A_t = 1.69$$

$$p_{t,j}/p_\infty < 5.0 \text{ to } 7.0 \quad \text{for} \quad 1.69 < A_e/A_t \leq 1.97$$

$$p_{t,j}/p_\infty < 6.0 \text{ to } 8.0 \quad \text{for} \quad A_e/A_t = 2.24$$

This result indicates that C_s is a more sensitive parameter than F/F_i for indication of nozzle internal flow separation. Comparison of the nozzle pressure ratios required to eliminate internal separation with the design nozzle pressure ratios (fig. 3) indicates that, even though the nozzle is operating overexpanded ($p_{t,j}/p_\infty < (p_{t,j}/p_\infty)_{des}$), the nozzle reaches a full flowing condition (no internal separation) at nozzle pressure ratios well below design, especially for the higher expansion ratio nozzles.

Performance Comparisons

In order to simplify data analysis, various performance parameters have been cross-plotted at selected nozzle pressure ratios. Figure 44 presents a typical variation of nozzle pressure ratio with Mach number for a turbofan engine, which was used for comparison purposes in this investigation. Although discussion for this particular schedule of nozzle pressure ratio as a function of M would generally be applicable for other schedules, the relative differences between comparisons may vary.

Effect of nozzle length on drag coefficient.- The effect of nozzle length on nozzle drag coefficient for each test Mach number at typical operating nozzle pressure ratios is presented in figure 45. As shown, the effect of nozzle

length on drag is dependent on nozzle power setting, expansion ratio A_e/A_t, and Mach number. In general, the effect of nozzle length becomes more significant as power setting and/or expansion ratio is reduced (boattail angle increased). Also, the most pronounced effects of nozzle length occur in the speed range from M = 0.90 to 1.20; nozzle length effects are small at high supersonic speeds.

In general, nozzle drag coefficient for configurations with low expansion ratios (circle symbols) decreases with increasing nozzle length at all power settings for $M \leq 1.2$. However, this beneficial effect is more pronounced at the dry power setting than at the Max A/B power setting. At $M \geq 2.16$, the medium length nozzle has the lowest drag at the dry power setting, and increasing nozzle length increases drag at the Max A/B power setting. For nozzles with high expansion ratios (square symbols), nozzle drag is generally decreased by increasing nozzle length at dry power setting, but the short or medium length nozzles have the lowest drag at partial A/B or Max A/B power setting.

Nozzle drag on configurations for which increasing length increases drag (generally high power setting and/or expansion ratio - small boattail angle) is dominated by viscous effects; that is, friction drag is increased more than pressure drag is reduced as nozzle length is increased. This effect might be expected since nozzle pressure drag approaches zero (see section entitled "Nozzle Drag Coefficient") for nozzles with small boattail angles (little projected area in axial direction), especially at high supersonic speeds. Nozzle drag on configurations for which increasing length decreases drag (generally low power setting and/or expansion ratio - large boattail angle) is dominated by pressure effects.

It should be noted that increasing nozzle length affects internal performance and nozzle weight in addition to external drag. Thus, relative ranking of nozzles should not be attempted based on nozzle drag alone. Nozzle length effects on internal performance are discussed in a subsequent section of this paper. Although increased nozzle length results in higher nozzle weight, the detailed study required to provide this trade information is beyond the scope of the current investigation.

Effect of nozzle length on internal (thrust) performance.- In addition to nozzle external geometry, varying nozzle length also causes a variation in nozzle internal geometry. For a constant power setting and expansion ratio, increasing nozzle length decreases nozzle divergence angle δ for the nozzles of this investigation. As discussed previously, stream thrust-correction factor C_s is a measure of nozzle internal flow (thrust) losses resulting from nozzle geometry effects. Figure 46 shows the effect of nozzle divergence angle (nozzle length) on stream thrust-correction factor. The values of C_s shown in figure 46 correspond to the average constant values represented by the solid-line fairings in figure 43 for each configuration. Also shown in figure 46, as dashed lines, are estimates of divergence losses obtained from equation (14) in the section entitled "Data Reduction."

As shown in figure 46, decreasing divergence angle (increasing nozzle length) decreases internal performance for nozzles having low expansion ratios A_e/A_t. At first, this appears to be a data anomaly since divergence losses are

shown to decrease with decreasing divergence angle. However, for nozzles with low expansion ratios, substantial increases in nozzle length are required for small decreases in divergence angle. Thus, only small reductions in divergence losses are possible by increasing nozzle length. For example, increasing divergent flap length l_f by 65 percent (from $l_f/d_m = 0.447$ to $l_f/d_m = 0.740$) on the dry power nozzles with $A_e/A_t = 1.22$ results in only a 1.55^o reduction in δ (from $\delta = 3.60^o$ to $\delta = 2.05^o$, see fig. 3). This divergence angle reduction results in a reduction of only 0.0003 in divergence losses (or increase in C_s). An increase in nozzle length of this magnitude, however, would result in a substantial increase in nozzle internal friction losses. Thus, for nozzles with low expansion ratios, it is possible that decreasing divergence angle by increasing nozzle length could result in small internal-nozzle performance (thrust) penalties. For nozzles with high expansion ratios, decreasing divergence angle (increasing nozzle length) reduces divergence losses and increases internal-nozzle performance at all power settings as expected.

Power-setting and expansion-ratio variations have only small effects on nozzle internal losses resulting from nozzle geometry (note that C_s does not account for nozzle underexpansion or overexpansion losses). For example, values of C_s for the nozzles with $A_e/A_t = 1.69$, 1.89, and 2.24 at the partial A/B power setting ($\delta \approx 11.7^o$ for all three nozzles) vary by only 0.005. At the Max A/B power setting, the values of C_s, which indicate internal losses less than predicted by divergence angle alone, are probably caused by test accuracy (approximately 0.005 in C_s).

Effect of cusp in external boattail.- Many operational nozzles have cusps in the external boattail contour when operating at expansion ratios greater than required for subsonic cruise ($A_e/A_t \approx 1.20$) or power settings greater than dry power (partial or Max A/B). This cusp is formed at the external flap hinge line as nozzle exit area is increased. The effect of a cusp on nozzle performance was investigated in the current study by testing the long, Max A/B nozzle with $A_e/A_t = 1.25$ (configuration A-1.25-L) with and without an external cusp in the external geometry at $x/l = 0.183$. All other nozzle design parameters were held constant. (See fig. 3.) The effects of an external cusp on selected nozzle boattail pressure distributions and on nozzle boattail drag are presented in figures 47 and 48, respectively.

As shown in figure 47, an external cusp tends to decrease nozzle static pressure coefficients immediately upstream of the cusp and increase nozzle static pressure coefficients downstream of the cusp. The pressure distributions at supersonic speeds, particularly at $M = 1.20$, indicate a standing shock wave at the cusp location ($x/l = 0.183$). Although the effect of the cusp on nozzle static pressure diminishes with increasing distance downstream of the cusp, it tends to persist all the way to the nozzle exit, particularly at $M = 1.20$.

As noted, an external cusp produces opposite effects on static pressure coefficients upstream and downstream of the cusp; these opposite effects tend to offset each other when the static pressures are integrated to obtain nozzle drag. Figure 48 shows that the effect of the external cusp on nozzle drag is negligible.

Effect of throat radius.- In order to determine the effect of throat radius on nozzle performance, the long, partial A/B (P-2.24-L) nozzle configuration with $A_e/A_t = 2.24$ was tested with both a radius and sharp corner (see fig. 3) at the throat. A comparison of the internal performance (thrust ratio) for these configurations is presented in figure 49. The sharp throat configuration was not tested at $M > 1.20$ since thrust ratio is independent of Mach number for fully developed nozzle flow. The results in figure 49 indicate that the effect of throat radius on thrust ratio is small at all Mach numbers except when nozzle pressure ratios are less than 2.5. At nozzle pressure ratios greater than 2.5, the configuration with a radius at the throat (P-2.24-L) generally has slightly higher performance than the configuration with a sharp corner at the throat (P-2.24(Sharp)-L). The effect of throat radius diminishes with increasing nozzle pressure ratio. At nozzle pressure ratios greater than 6.0, the values of C_s for these two configurations are nearly identical (see fig. 43(f)), which indicate that throat radius has little effect on nozzle internal performance when no internal flow separation exists.

Effect of Mach number.- Nozzle drag coefficient $C_{D,n}$, thrust ratio F/F_i, and thrust-minus-drag ratio $(F - D_n)/F_i$ are presented as a function of Mach number in figures 50, 51, and 52, respectively. These summary figures were obtained by cross-plotting the data from figures 5 to 23 at a typical operating pressure ratio (see fig. 44) for each Mach number tested. Data for low-expansion-ratio nozzles ($A_e/A_t \leq 1.25$) are presented at $M \leq 1.20$ on the left side of each figure and data for high-expansion-ratio nozzles ($A_e/A_t \geq 1.69$) are presented at $M \geq 1.20$ on the right side of each figure. Full-scale operational nozzles typically have variable-expansion ratios between minimum and maximum values which are set by nozzle hardware limitations. Thus, as operational airplanes accelerate through the Mach number range (and nozzle pressure-ratio range as shown in fig. 44), the nozzle expansion ratio is controlled such that the nozzle operates at the design pressure ratio for each flight Mach number. Obviously, this is not possible with subscale model hardware without a great deal of expense (remotely variable nozzle or many configurations). Thus, with fixed model hardware (fixed A_e/A_t), each model nozzle configuration operates on design at only one Mach number and nozzle-pressure-ratio condition (design nozzle pressure ratio from fig. 3 and Mach number from fig. 44). The on-design operating condition for each configuration tested is indicated in figures 50 to 52 by crossmarks on the data fairings.

As shown in figure 50, nozzle drag increases rapidly with increasing Mach number in the transonic speed regime ($0.8 < M < 1.2$). Above $M = 1.2$, nozzle drag coefficient decreases with increasing Mach number. Nozzle drag coefficient decreases with increasing nozzle power setting and, at a constant power setting, decreases with increasing expansion ratio. Maximum thrust ratio occurs near the on-design operating condition as shown in figure 51. Nozzle overexpansion losses occur at Mach numbers below the on-design value and nozzle underexpansion losses occur at Mach numbers above the on-design value. Thrust-minus-drag ratio (fig. 52), which combines both external and internal losses, indicates substantial losses (1.5 to 13.5 percent) in the transonic speed range due primarily to high nozzle drag.

On-design configuration comparison.- Performance comparisons for each nozzle configuration tested are presented in figure 53 at on-design operating con-

ditions (cross-plot of on-design data, crossmarks, from figs. 50 through 52). It should be noted that these data are for an isolated (no wings or tails) model and installation effects would have to be accounted for in an actual airplane configuration.

For all configurations tested, increasing nozzle length for constant nozzle power setting and expansion ratio increases overall nozzle performance $(F - D_n)/F_i$. However, it is interesting to note that although this same result was obtained for both subsonic and supersonic mission segments, it was caused by different and opposite effects in each speed regime. For subsonic mission segments shown in figure 53(a) for low expansion ratios, increasing nozzle length decreased nozzle drag coefficient $C_{D,n}$ (top part of figure), but also decreased nozzle thrust ratio F/F_i (total bar length on bottom part of figure) except for the long, dry-power nozzle configuration. These results and their causes were discussed previously. Although these effects tend to offset each other, the drag reduction with increasing nozzle length was greater than the internal thrust loss, such that overall nozzle performance (shaded portion of bar on bottom part of figure) increased with increasing nozzle length.

For supersonic mission segments with high expansion ratios (fig. 53(b)), increasing nozzle length increased nozzle thrust ratio but also generally increased nozzle drag coefficient (except for the dry-power nozzle). Similar to results at subsonic speeds, these effects also tend to offset each other. However, at supersonic speeds, the increase in thrust ratio with increasing nozzle length was greater than the performance loss associated with the increased nozzle drag. Thus overall nozzle performance again increased with increasing nozzle length.

CONCLUSIONS

An investigation has been conducted in the Langley 16-Foot Transonic Tunnel and the Langley Unitary Plan Wind Tunnel of convergent-divergent nozzles applicable to reduced-power supersonic-cruise aircraft. Tests were conducted using high-pressure air for propulsion simulation at Mach numbers from 0.60 to 2.86, at an angle of attack of 0°, and at nozzle pressure ratios from jet off to 46.0. Results from this study indicate the following conclusions for nozzles operating near design conditions:

1. For constant nozzle power setting and expansion ratio, increasing nozzle length increases overall (thrust-minus-drag) nozzle performance.

2. Increasing nozzle length for nozzles with low expansion ratios generally decreases nozzle drag (improved pressure recovery) but also decreases nozzle internal performance (increased internal friction losses).

3. Increasing nozzle length for nozzles with high expansion ratios increases internal-nozzle performance (reduced divergence losses) but generally also increases nozzle drag (increased external friction drag).

4. A cusp in the external nozzle boattail geometry caused offsetting trends in the boattail static pressure distributions and thus produced negligible effects on nozzle boattail drag.

5. Throat radius had a negligible effect on nozzle internal performance at nozzle pressure ratios above 2.5.

Langley Research Center
National Aeronautics and Space Administration
Hampton, VA 23665
November 4, 1980

REFERENCES

1. Nichols, Mark R.: Aerodynamics of Airframe-Engine Integration of Supersonic Aircraft. NASA TN D-3390, 1966.

2. Runckel, Jack F.: Jet-Exit and Airframe Interference Studies on Twin-Engine-Fuselage Aircraft Installations. NASA TM X-1274, 1966.

3. Corson, Blake W., Jr.; and Runckel, Jack F.: Exploratory Studies of Aircraft Afterbody and Exhaust-Nozzle Interaction. NASA TM X-1925, 1969.

4. Runckel, Jack F.: Interference Between Exhaust System and Afterbody of Twin-Engine Fuselage Configurations. NASA TN D-7525, 1974.

5. Berrier, Bobby L.; and Staff, Propulsion Integration Section: A Review of Several Propulsion Integration Features Applicable to Supersonic-Cruise Fighter Aircraft. NASA TM X-73991, 1976.

6. Schaefer, William T., Jr.: Characteristics of Major Active Wind Tunnels at the Langley Research Center. NASA TM X-1130, 1965.

7. Corson, Blake W., Jr.; Runckel, Jack F.; and Igoe, William B.: Calibration of the Langley 16-Foot Transonic Tunnel With Test Section Air Removal. NASA TR R-423, 1974.

8. Capone, Francis J.: The Effects on Propulsion-Induced Aerodynamic Forces of Vectoring a Partial-Span Rectangular Jet at Mach Numbers From 0.40 to 1.20. NASA TN D-8039, 1975.

9. Capone, Francis J.: Static Performance of Five Twin-Engine Nonaxisymmetric Nozzles With Vectoring and Reversing Capability. NASA TP-1224, 1978.

10. Shapiro, Ascher H: The Dynamics and Thermodynamics of Compressible Fluid Flow. Vol II. Ronald Press Co., c.1954.

11. Shapiro, Ascher H.: The Dynamics and Thermodynamics of Compressible Fluid Flow. Vol. I. Ronald Press Co., c.1953.

12. Sutton, George P.: Rocket Propulsion Elements. Second ed. John Wiley & Sons, Inc., c.1956.

13. Berrier, Bobby L.: Effect of Nonlifting Empennage Surfaces on Single-Engine Afterbody/Nozzle Drag at Mach Numbers From 0.5 to 2.2. NASA TN D-8326, 1977.

14. Compton, William B., III; and Runckel, Jack F.: Jet Effects on the Boattail Axial Force of Conical Afterbodies at Subsonic and Transonic Speeds. NASA TM X-1960, 1970.

15. Putman, Lawrence E.: DONBOL: A Computer Program for Predicting Axisymmetric Nozzle Afterbody Pressure Distributions and Drag at Subsonic Speeds. NASA TM-78779, 1979.

TABLE 1.- NOMINAL FREE-STREAM TEST CONDITIONS

M	Facility	$p_{t,\infty}$, kPa	p_∞, kPa	q_∞, kPa	$T_{t,\infty}$, K	N_{Re}
0.00	16FTT	101.4	101.4	----	Atm.	----------
.00	UPWT	20.7	20.7	----	Atm.	----------
.60	16FTT	101.4	79.6	20.1	319	15.9×10^6
.80	↓	↓	66.5	29.9	329	18.3
.85	↓	↓	63.2	32.1	331	18.6
.90	↓	↓	60.0	34.1	333	18.9
.95	↓	↓	56.5	35.9	336	19.1
1.20	↓	↓	41.7	42.1	339	19.7
2.16	UPWT	64.1	6.4	20.7	325	9.0
2.50	↓	76.5	4.5	19.3	↓	↓
2.86	↓	93.1	3.1	17.9	↓	↓

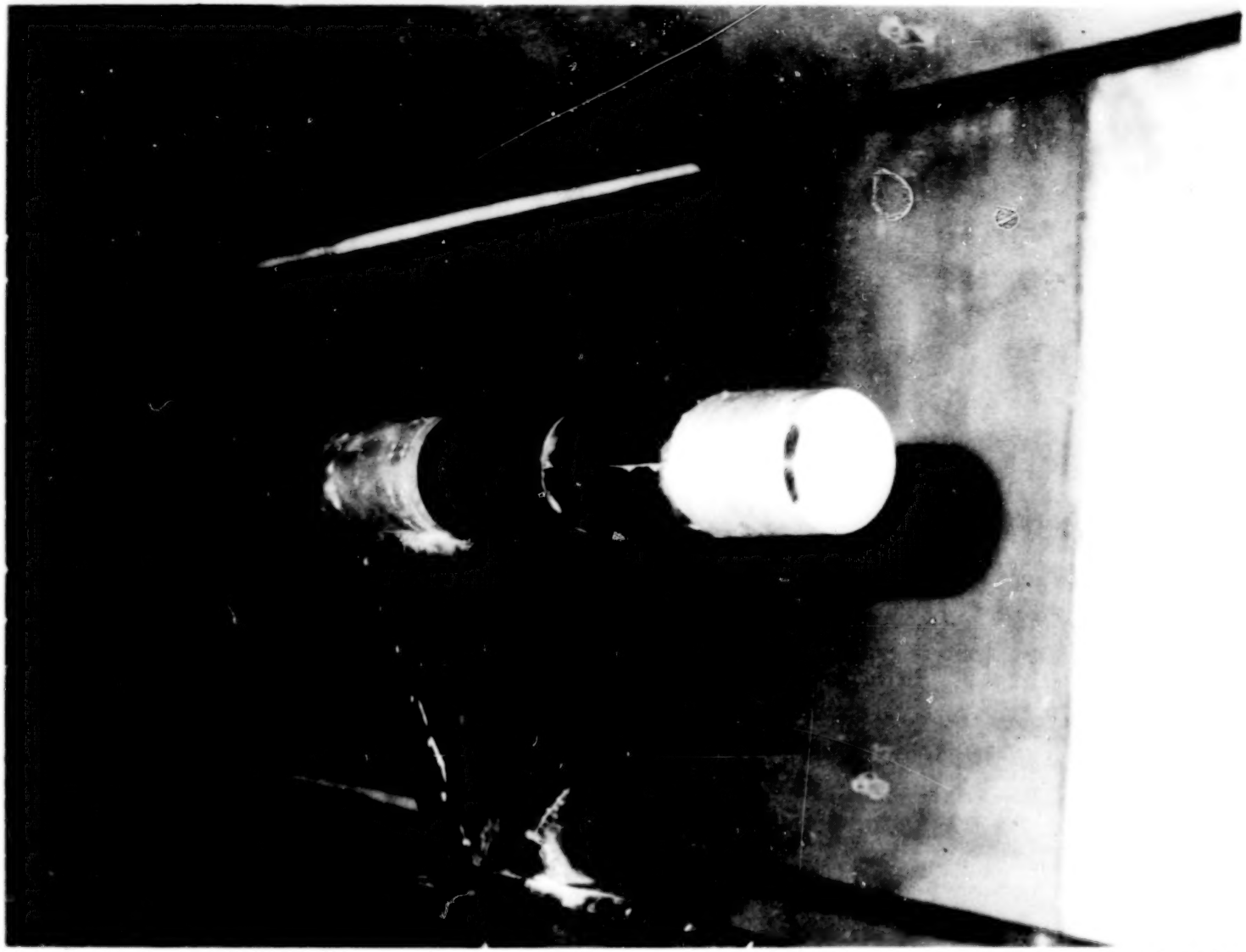

L-78-5575

(a) Langley 16-Foot Transonic Tunnel.

Figure 1.- Photographs of model installed in wind-tunnel facilities.

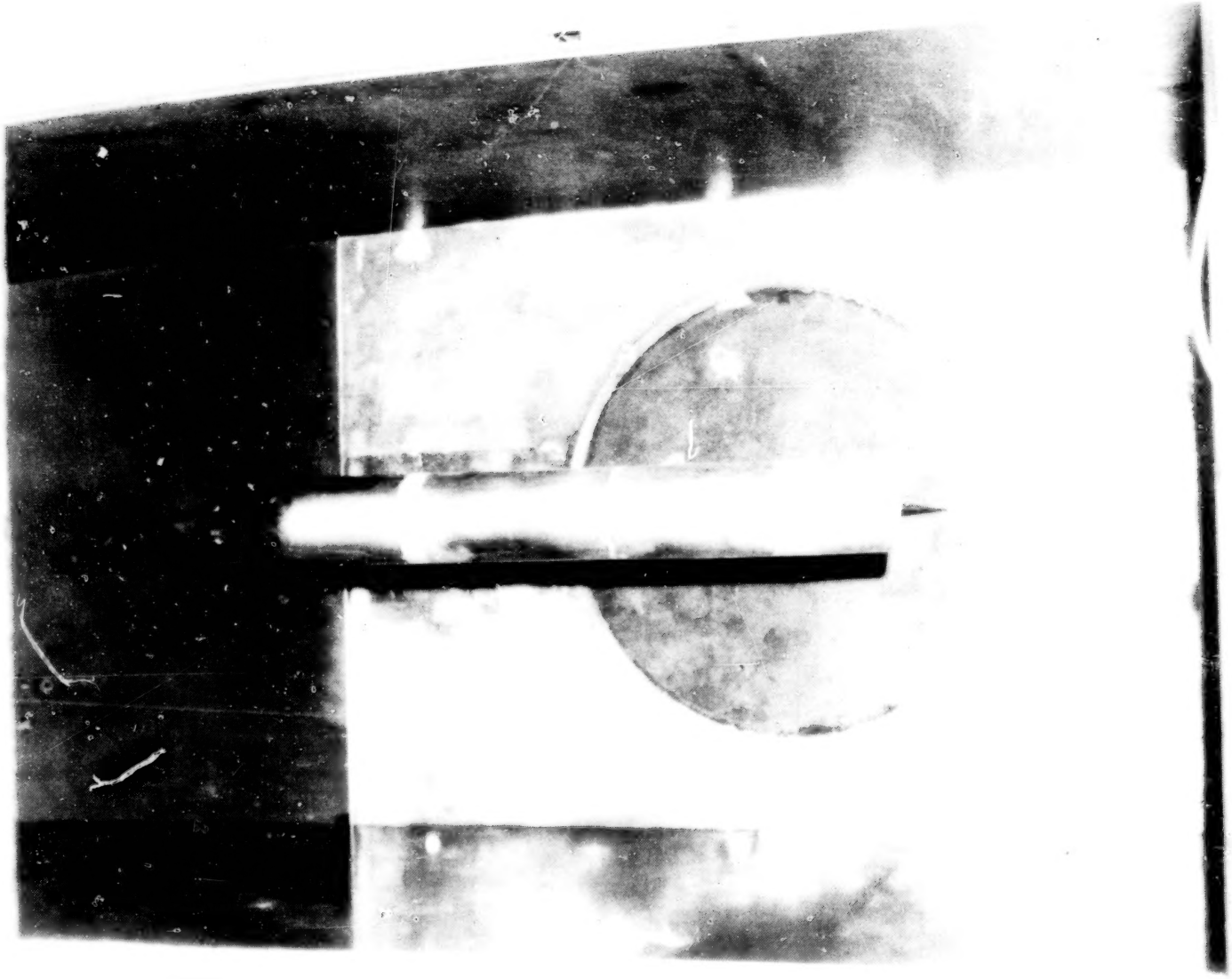

L-79-8211

(b) Langley Unitary Plan Wind Tunnel.

Figure 1.- Concluded.

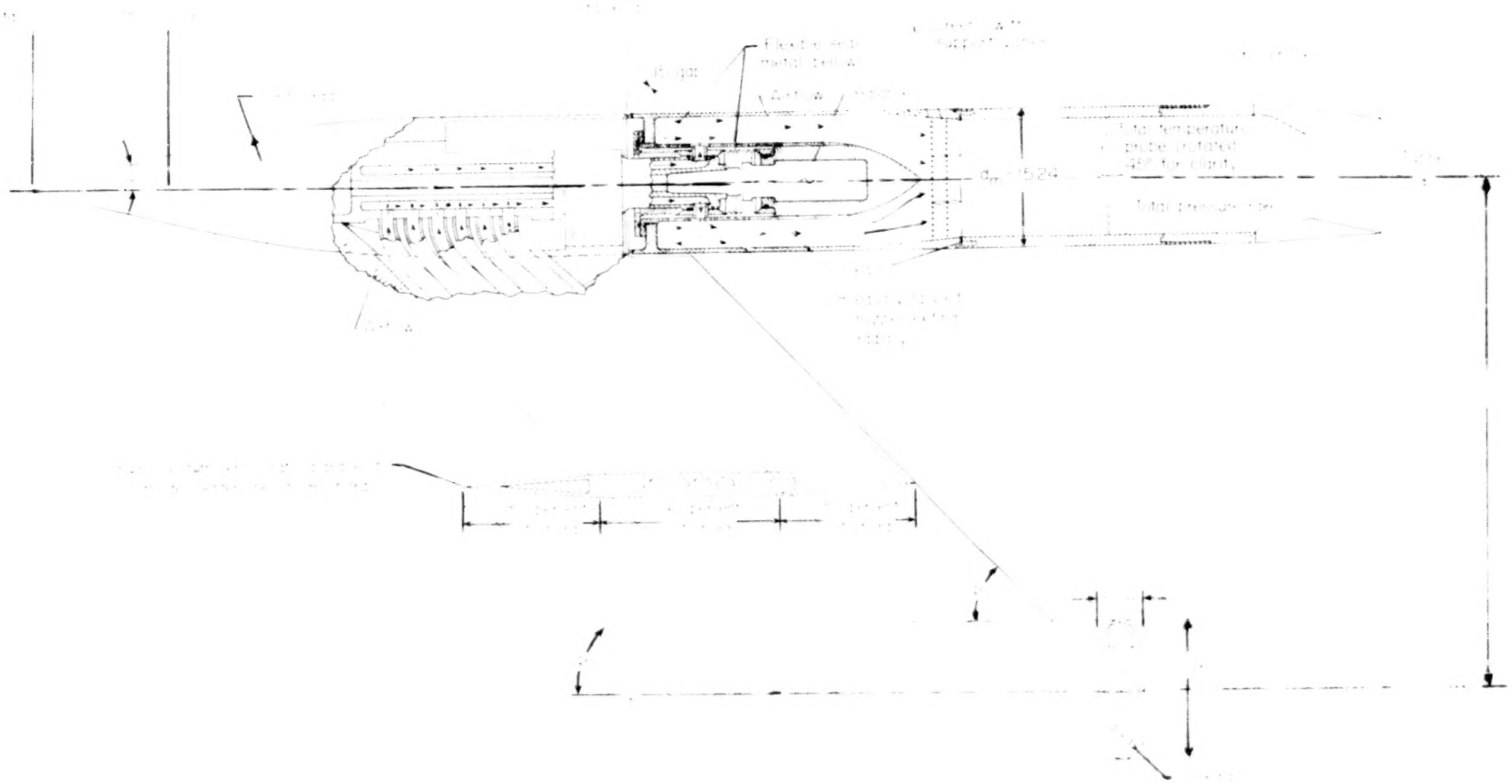

Figure 2.- Sketch showing general arrangement of model (16FTT installation).
(All dimensions are in centimeters unless otherwise noted.)

Sketch typical except for configurations P-2.24 (sharp)-L and A-1.25-L (cusp)

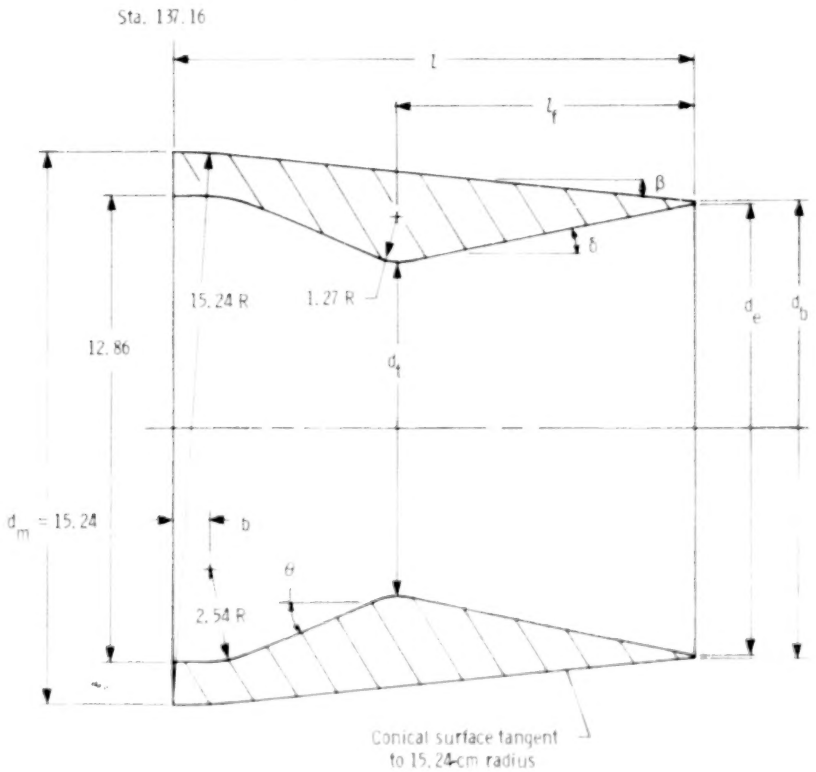

Note: Values for dimension b are 1.15 for dry power nozzles, 0.98 for partial A/B power nozzles, and 0.05 for Max A/B power nozzles.

Configuration	Flight segment	Power setting	$(p_{t,j}/p_{\infty})_{des}$	Design dimensions									
				d_f, cm	d_e, cm	A_e/A_t	l_f/d_m	l/d_m	A_b/A_m	A_e/A_b	ϕ, deg	δ, deg	β, deg
D-1.22-S	Sub. cruise	Dry	4.00	7.57	8.36	1.22	0.447	0.831	0.310	0.970	37.93	3.60	18.30
D-1.22-M	↓	↓	↓	↓	↓	↓	.557	.941	↓	↓	↓	2.70	15.40
D-1.22-L	↓	↓	↓	↓	↓	↓	.740	1.124	↓	↓	↓	2.05	12.30
D-2.24-S	Super. cruise	↓	12.90	↓	11.33	2.24	.430	.814	.565	.978	↓	16.50	9.70
D-2.24-M	↓	↓	↓	↓	↓	↓	.544	.929	↓	↓	↓	13.00	8.30
D-2.24-L	↓	↓	↓	↓	↓	↓	.730	1.114	↓	↓	↓	9.70	6.70
P-1.25-M	Sub. accel.	Partial A/B	4.25	9.08	10.15	1.25	.556	.966	.455	.975	22.73	4.00	10.50
P-2.24-S	Super. cruise	↓	12.90	↓	13.59	2.24	.422	.832	.811	.982	↓	20.00	3.55
P-2.24-M	↓	↓	↓	↓	↓	↓	.538	.948	↓	↓	↓	15.60	3.10
P-2.24-L	↓	↓	↓	↓	↓	↓	.725	1.135	↓	↓	↓	11.60	2.60
P-1.69-S	↓	↓	7.82	↓	11.81	1.69	.438	.848	.614	.979	↓	11.77	7.90
P-1.89-M	↓	↓	9.59	↓	12.48	1.89	.546	.956	.684	.980	↓	11.72	5.40
A-1.25-S	Sub. combat	Max A/B	4.25	10.36	11.58	1.25	.445	.868	.590	.978	11.77	5.30	8.30
A-1.25-M	↓	↓	↓	↓	↓	↓	.556	.978	↓	↓	↓	4.15	7.20
A-1.25-L	↓	↓	↓	↓	↓	↓	.739	1.161	↓	↓	↓	3.10	6.00
A-1.97-S	Super. dash	↓	10.36	↓	14.53	1.97	.426	.848	.925	.983	↓	18.60	1.30
A-1.97-L	↓	↓	↓	↓	↓	↓	.727	1.160	↓	↓	↓	11.00	.97
P-2.24-sharp-L	Super. cruise	Partial A/B	12.90	9.08	13.59	2.24	.725	1.135	.811	.982	21.27	11.54	2.60
A-1.25-L(cusp)	Sub. combat	Max A/B	4.25	10.36	11.58	1.25	.739	1.161	.590	.978	11.77	3.10	5.60

(a) Parametric nozzle set.

Figure 3.- Sketches and geometric parameters for test nozzles. (All dimensions in cm unless otherwise noted.)

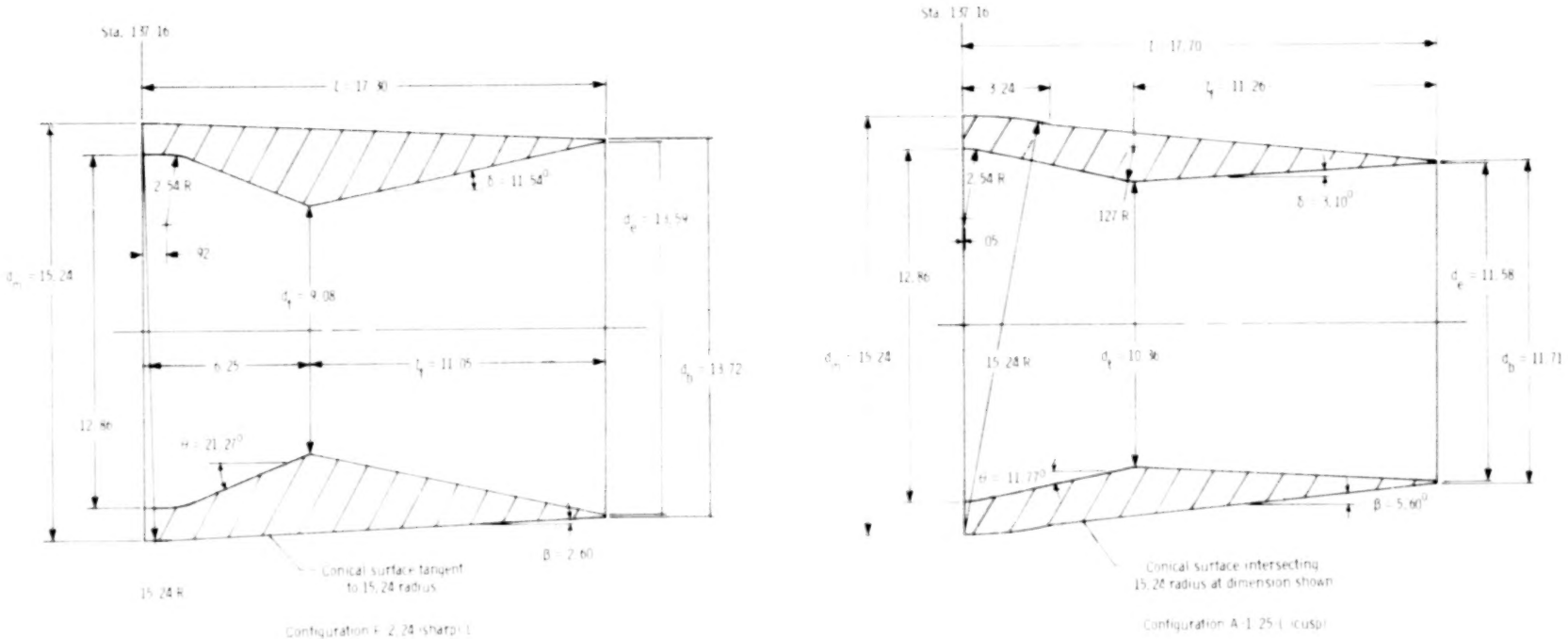

(b) Special purpose nozzles.

Figure 3.- Concluded.

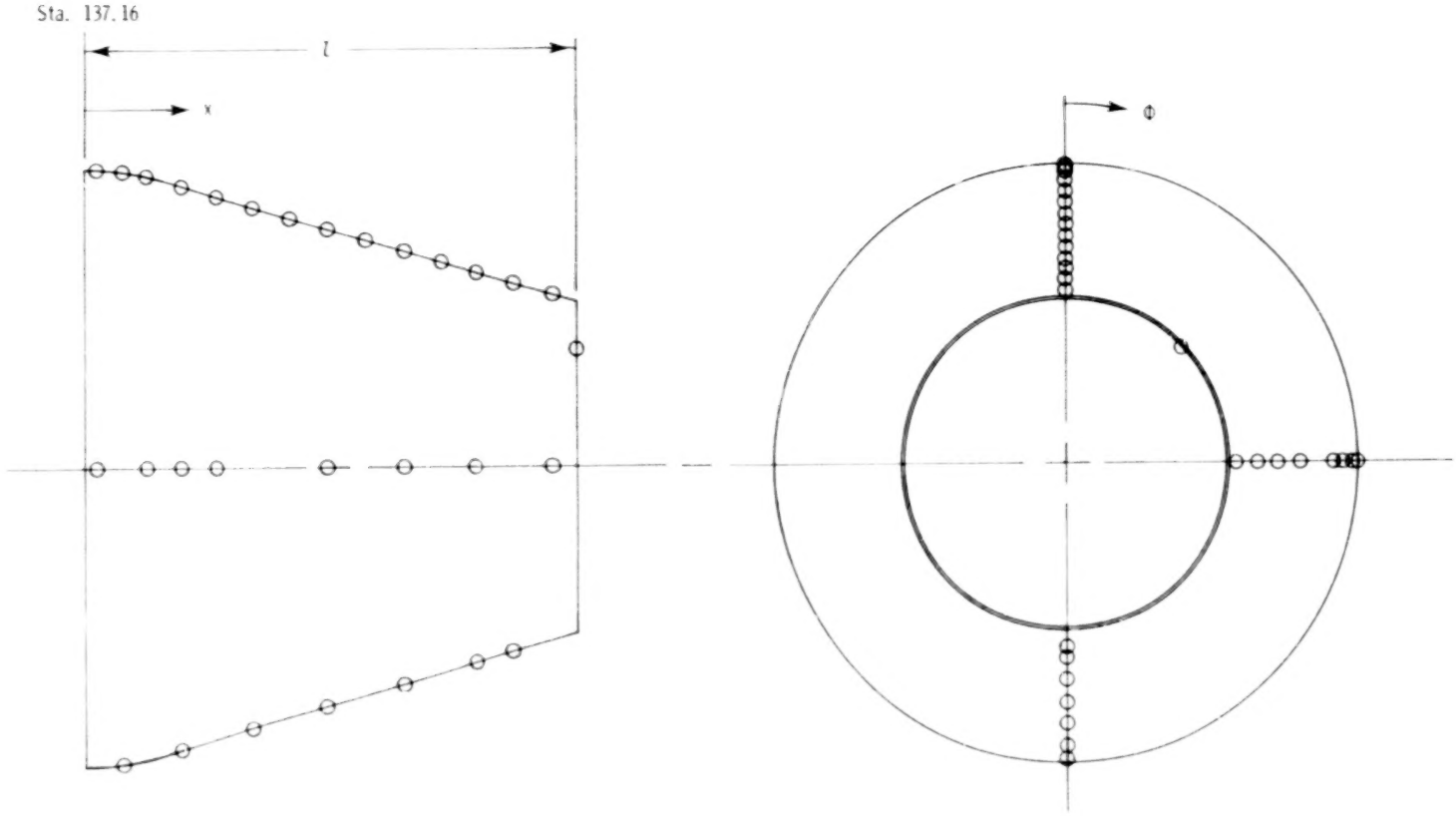

Φ, deg	x/l														
	.025	.075	.125	.200	.275	.350	.425	.500	.575	.650	.725	.800	.875	.950	Base
0	x	x	x	x	x	x	x	x	x	x	x	x	x	x	
45															x
90	x		x	x	x			x		x		x		x	
180		x		x		x		x		x		x	x		

Figure 4.- Sketch of nozzle showing external pressure orifice locations (typical for all nozzles). (All dimensions are in centimeters.)

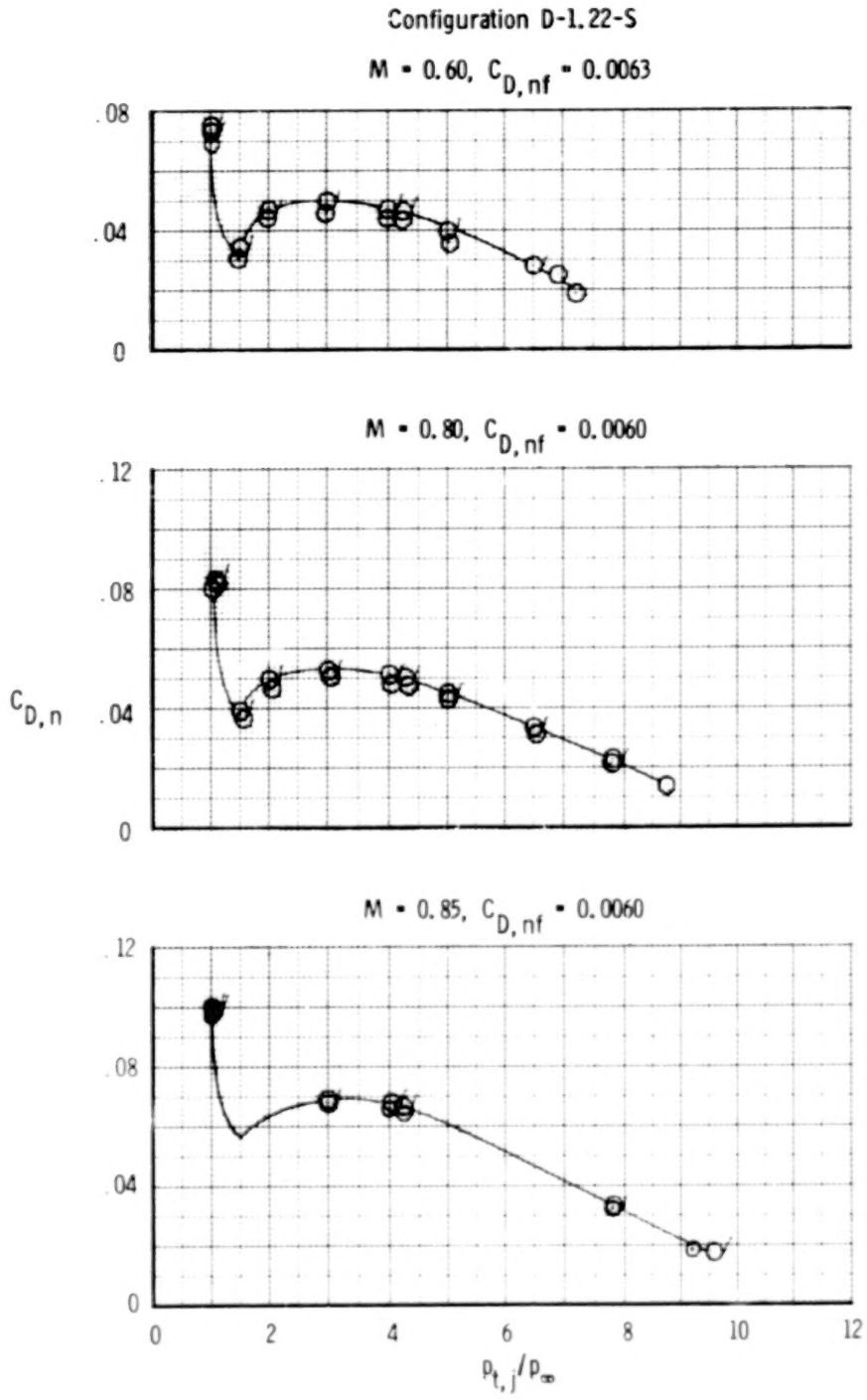

(a) Variation of nozzle drag coefficient.

Figure 5.- Variation of nozzle drag coefficient, thrust-minus-drag ratio, thrust ratio, and mass-flow ratio with nozzle pressure ratio for configuration D-1.22-S. Dashed line indicates theoretical values. Flagged symbols indicate data used to determine F/F_i.

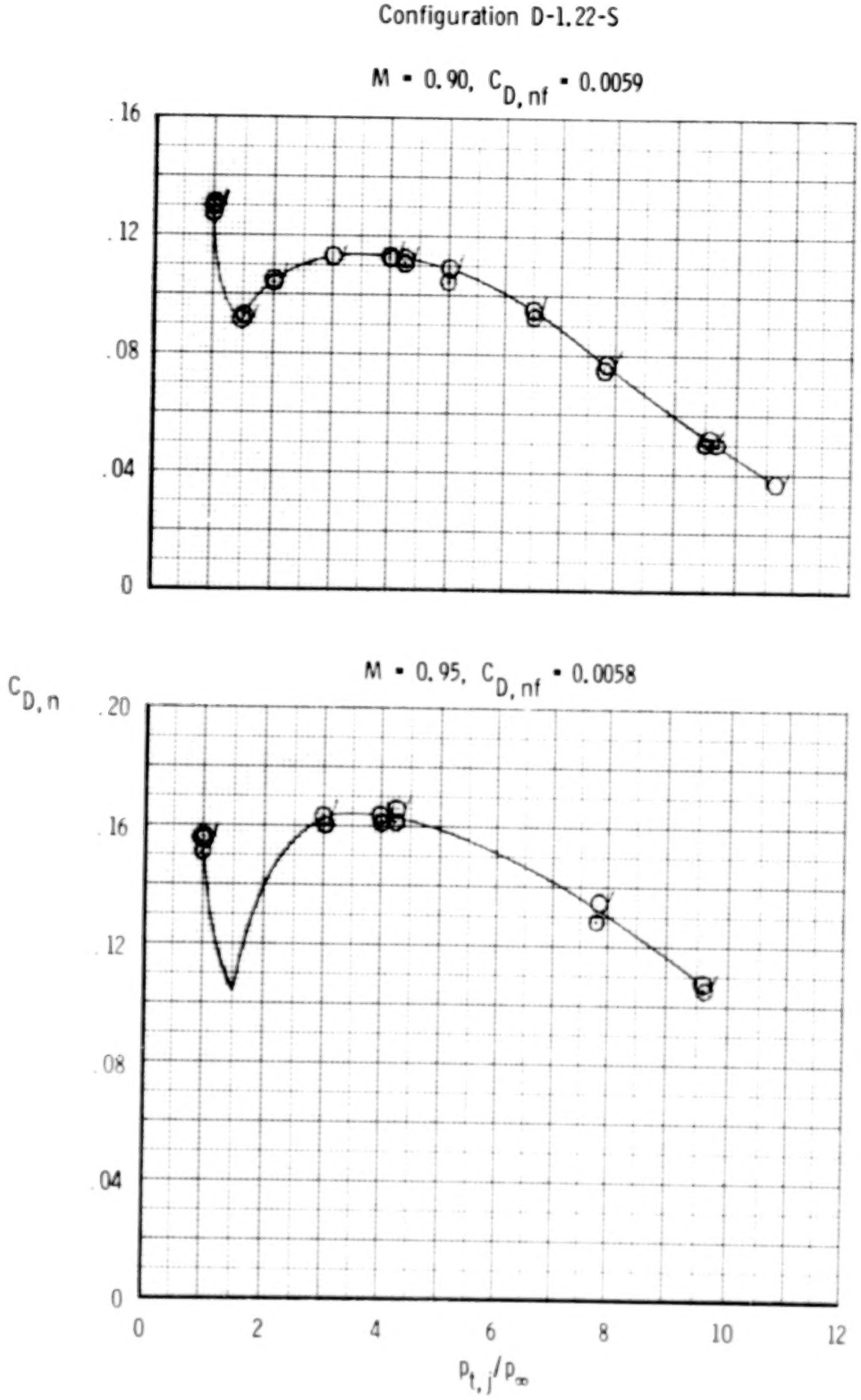

(a) Continued.

Figure 5.- Continued.

Configuration D-1.22-S

M = 1.20, $C_{D,nf}$ = 0.0056

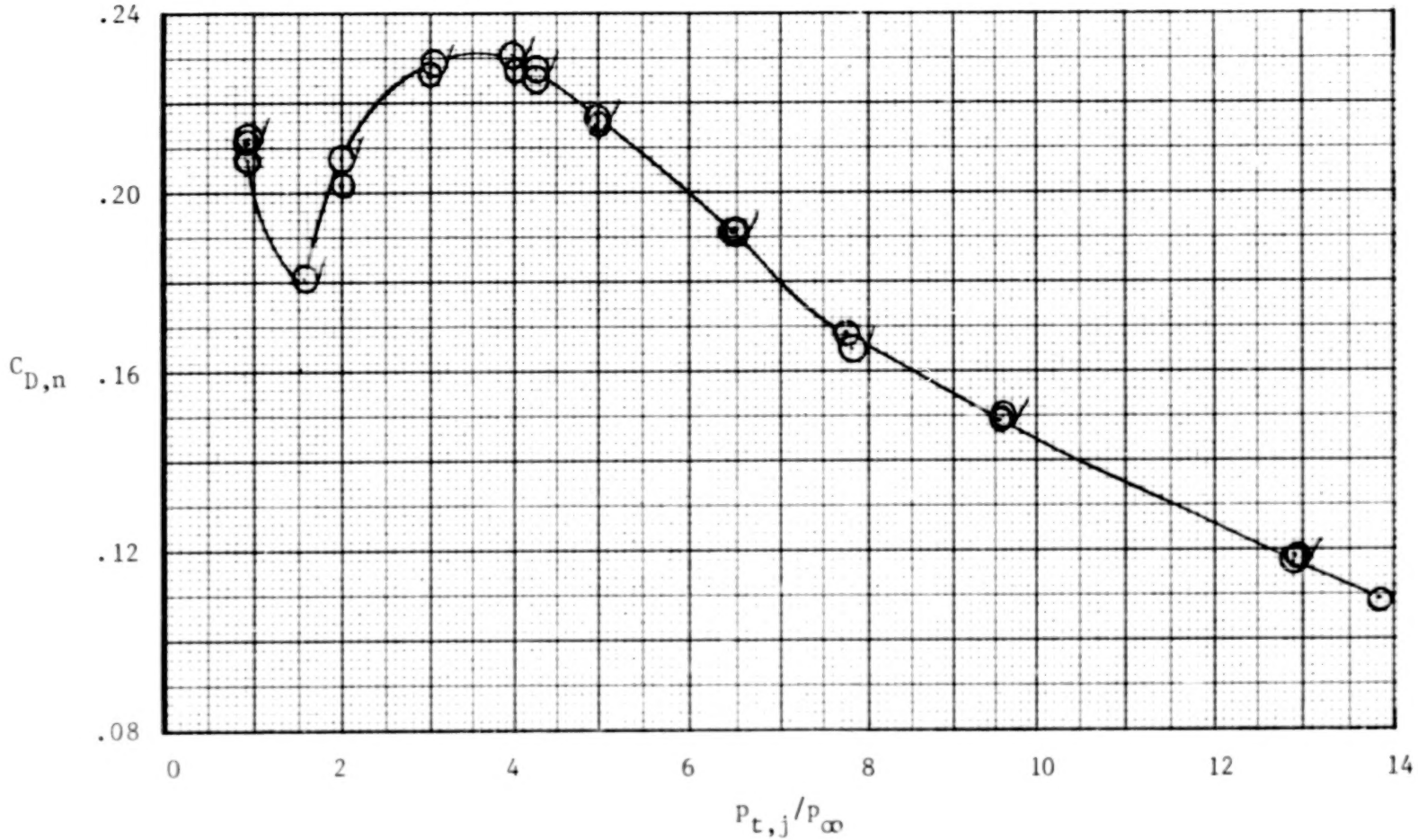

(a) Continued.

Figure 5.- Continued.

BLANK PAGE

BLANK PAGE

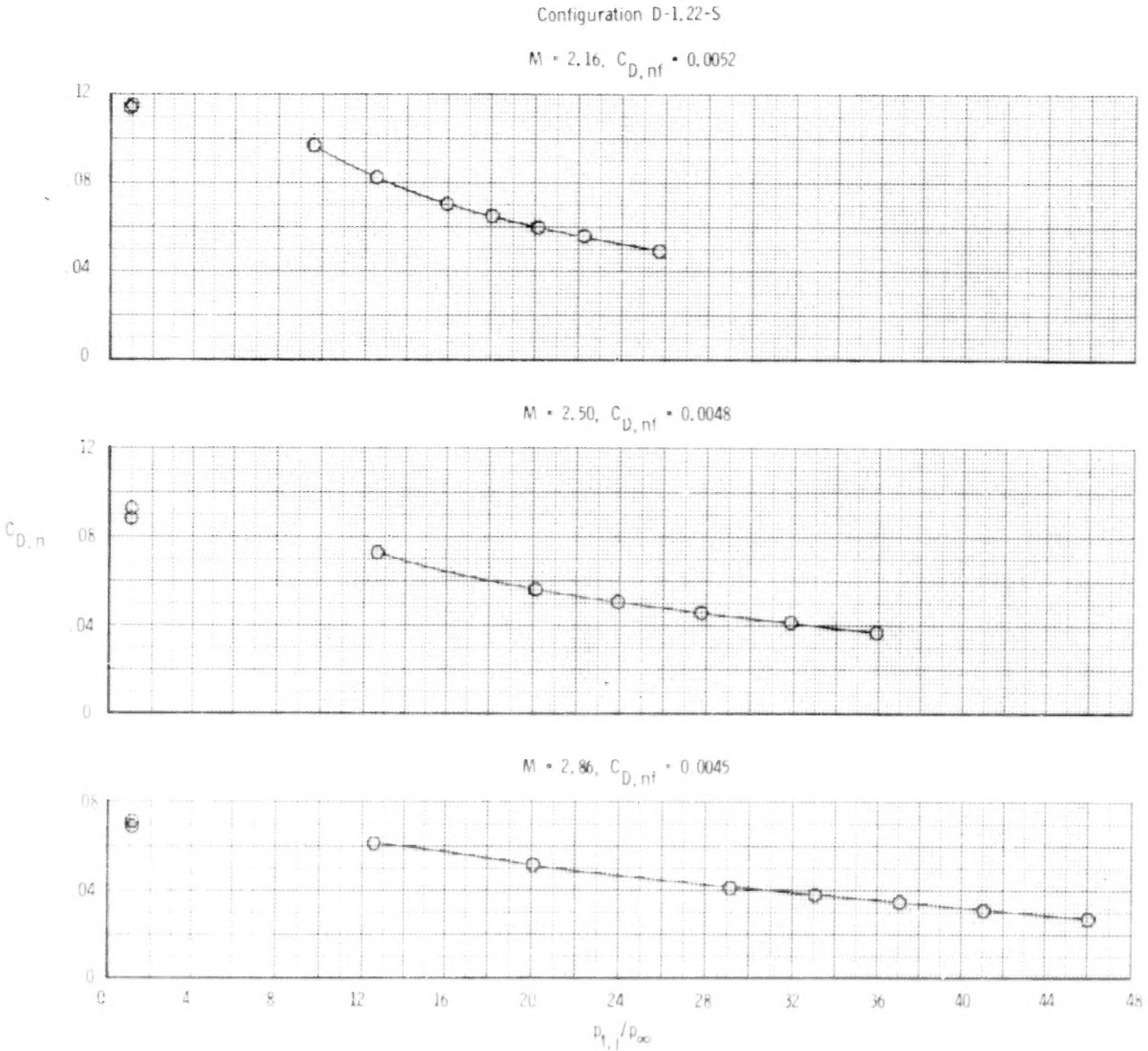

(a) Concluded.

Figure 5.- Continued.

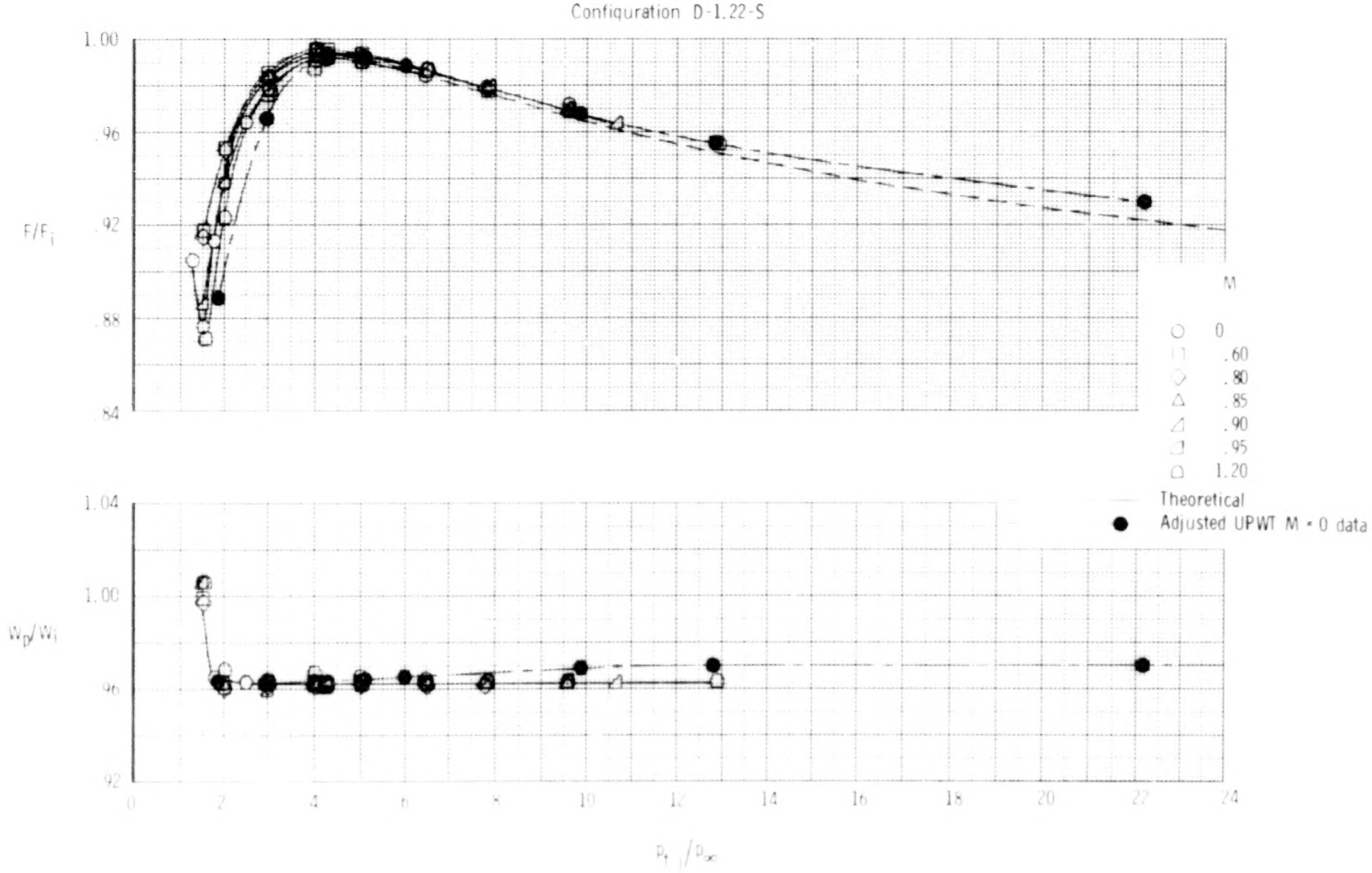

(b) Variation of thrust ratio and mass-flow ratio at subsonic and transonic speeds (16FTT).

Figure 5.- Continued.

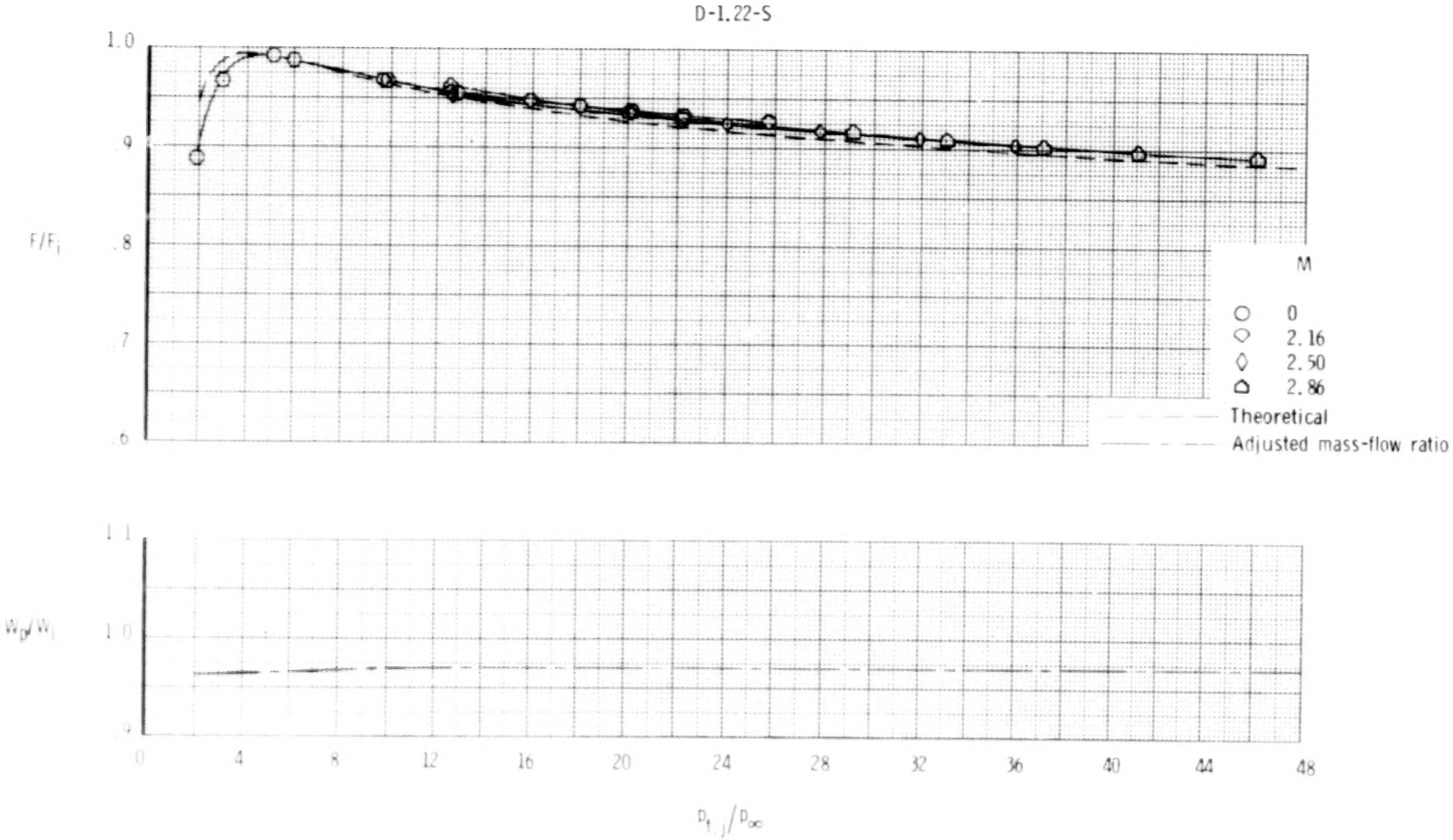

(c) Variation of thrust ratio and mass-flow ratio at supersonic speeds (UPWT).

Figure 5.- Continued.

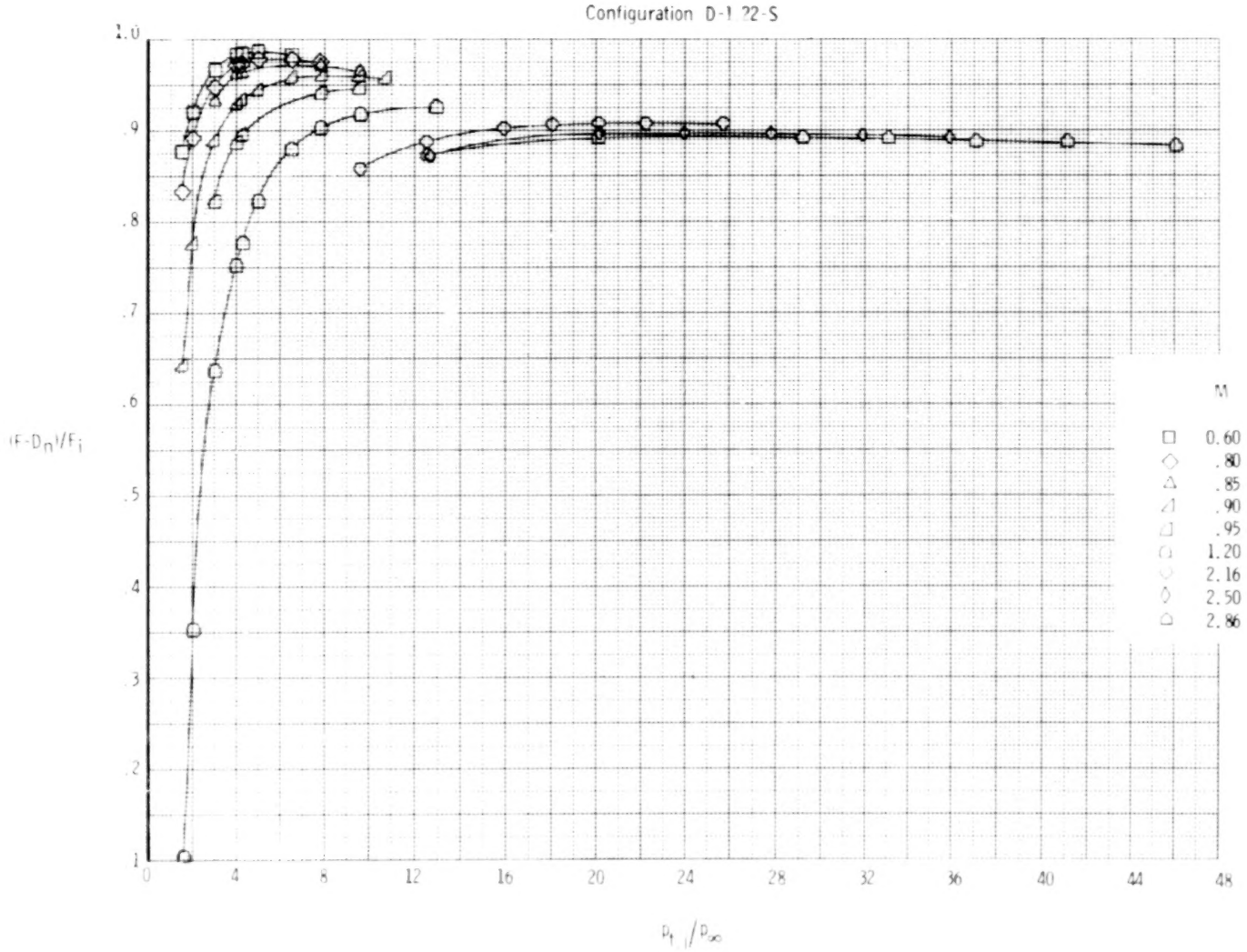

(d) Variation of thrust-minus-drag ratio.

Figure 5.- Concluded.

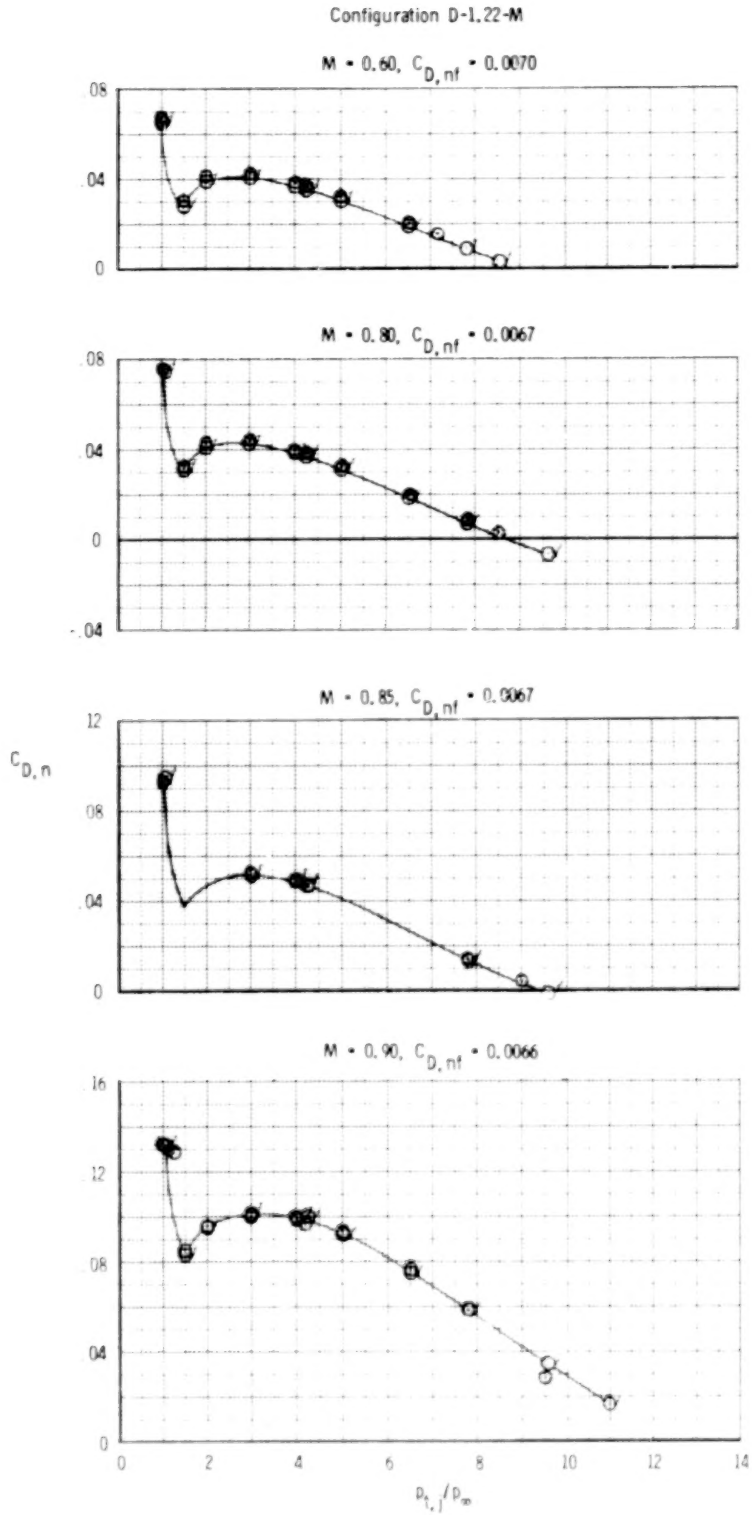

(a) Variation of nozzle drag coefficient.

Figure 6.- Variation of nozzle drag coefficient, thrust-minus-drag ratio, thrust ratio, and mass-flow ratio with nozzle pressure ratio for configuration D-1.22-M. Dashed line indicates theoretical values. Flagged symbols indicate data used to determine F/F_i.

Configuration D-1.22-M

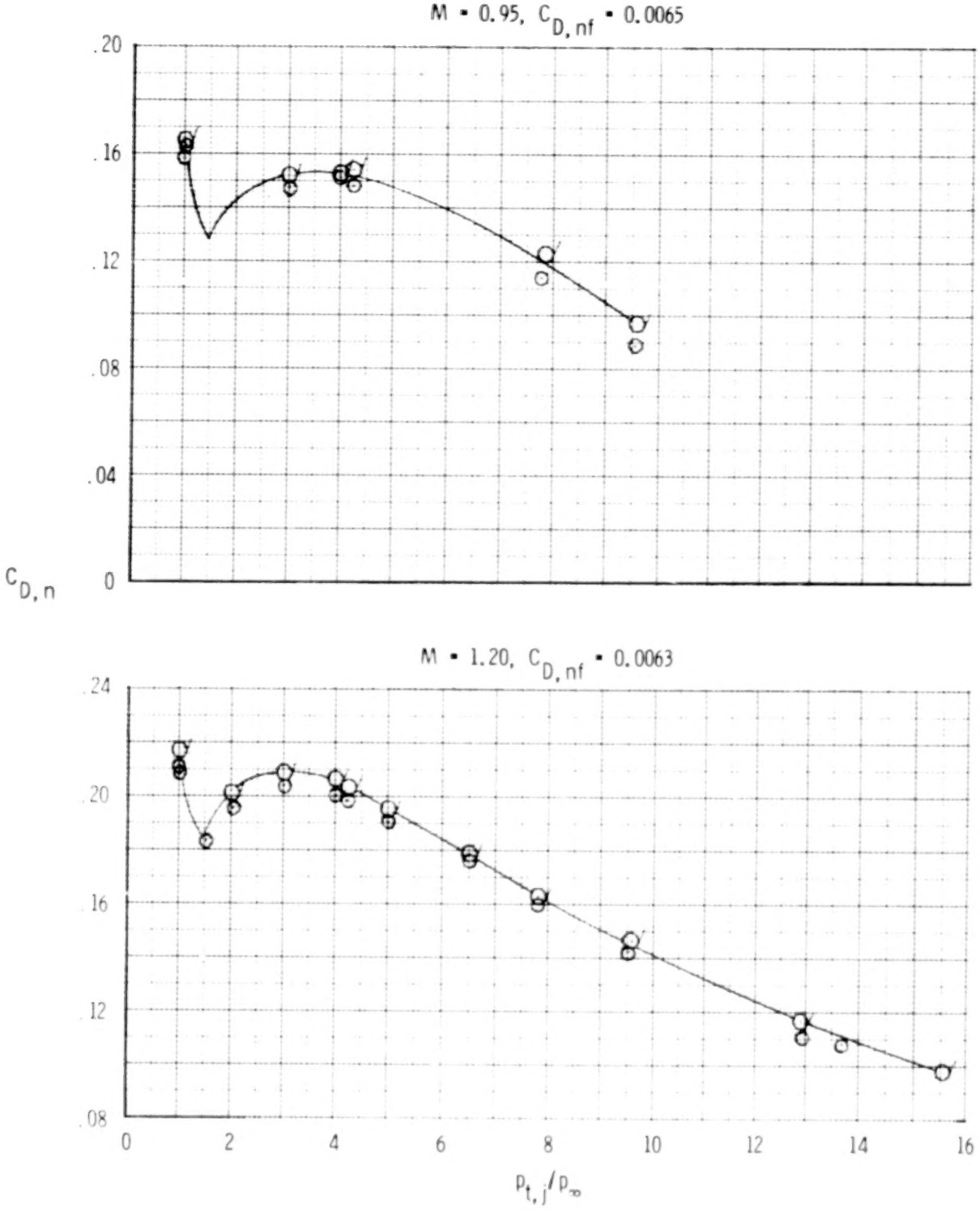

(a) Continued.

Figure 6.- Continued.

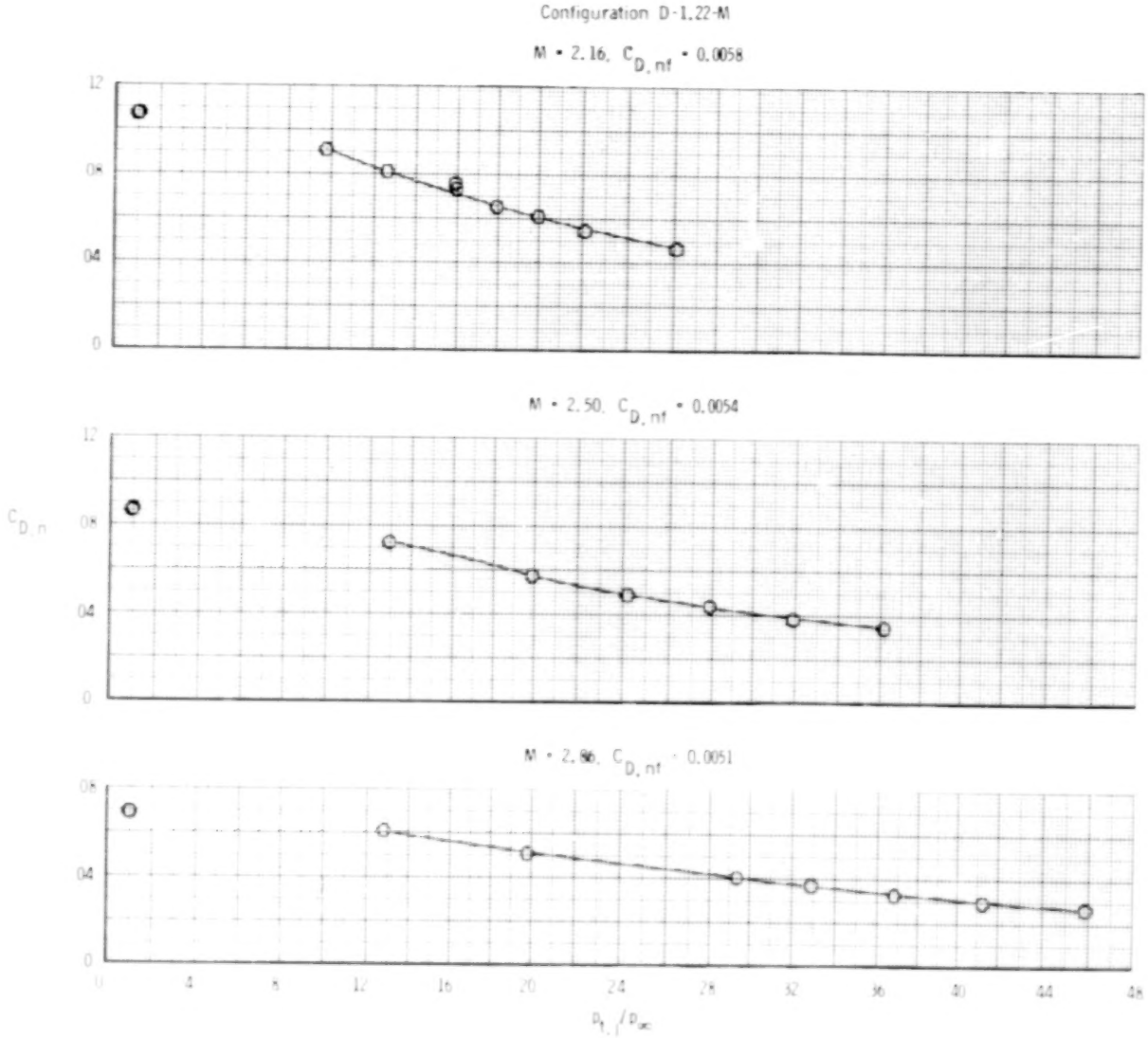

(a) Concluded.

Figure 6.- Continued.

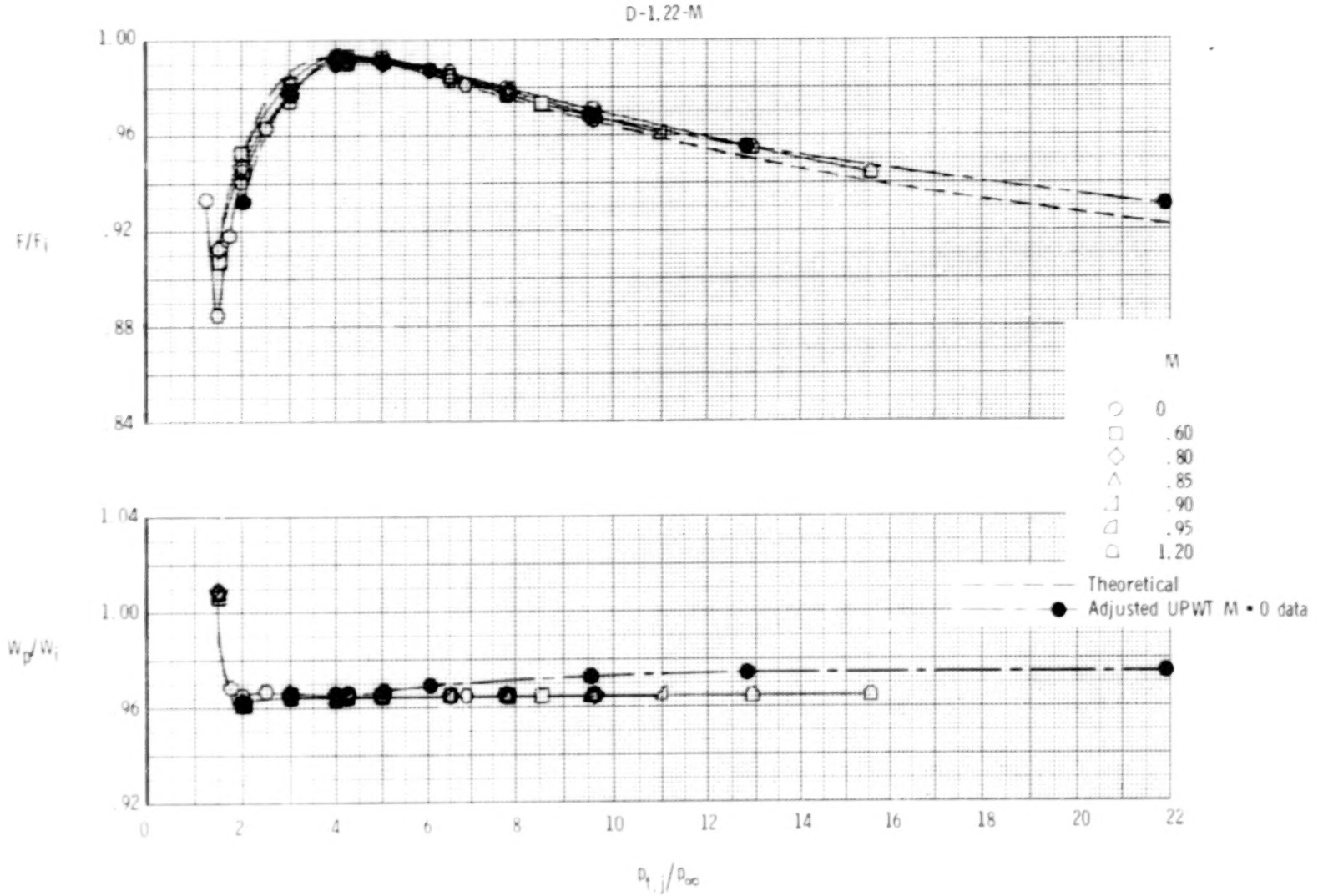

(b) Variation of thrust ratio and mass-flow ratio at subsonic and transonic speeds (16FTT).

Figure 6.- Continued.

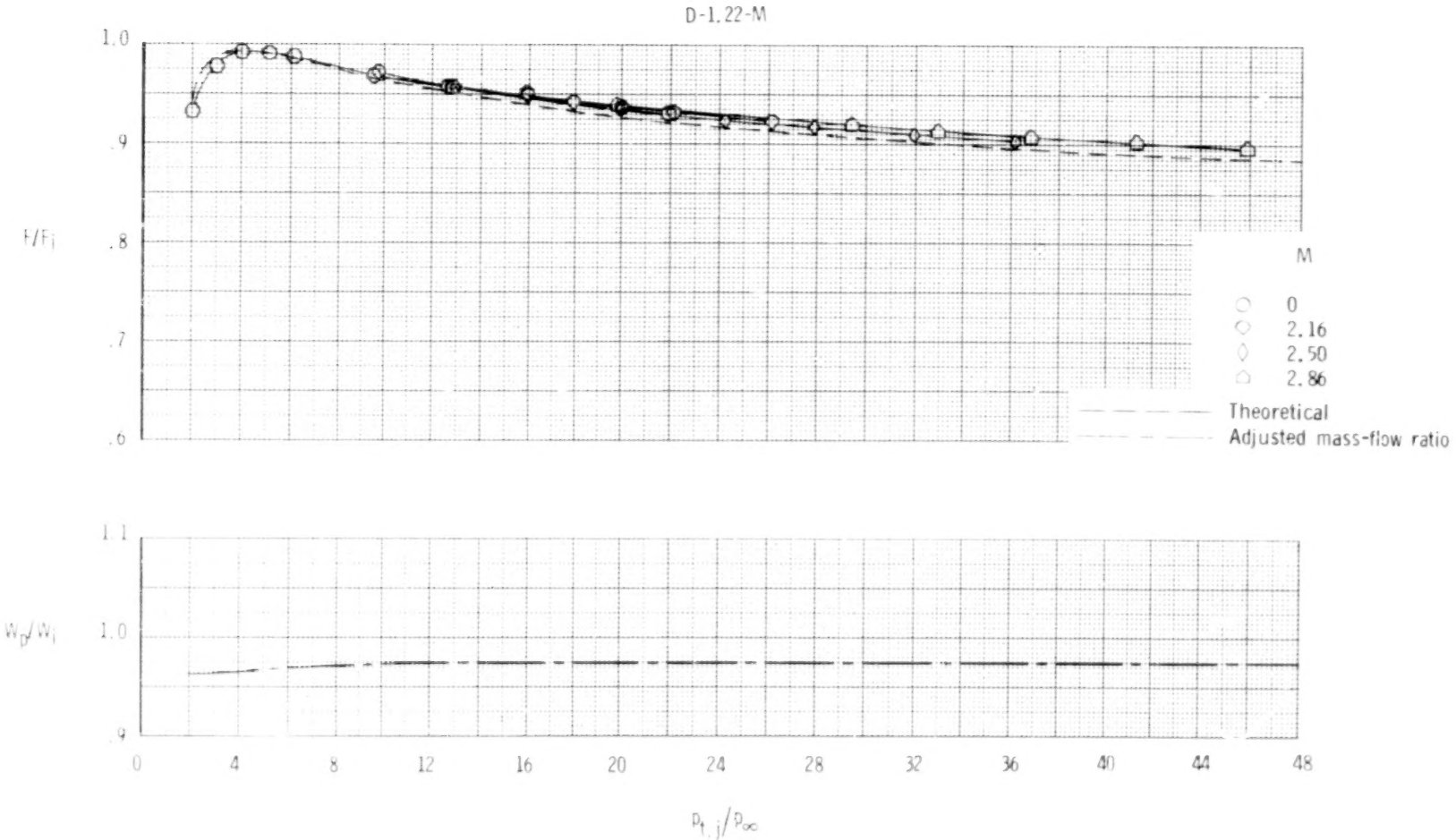

(c) Variation of thrust ratio and mass-flow ratio at supersonic speeds (UPWT).

Figure 6.- Continued.

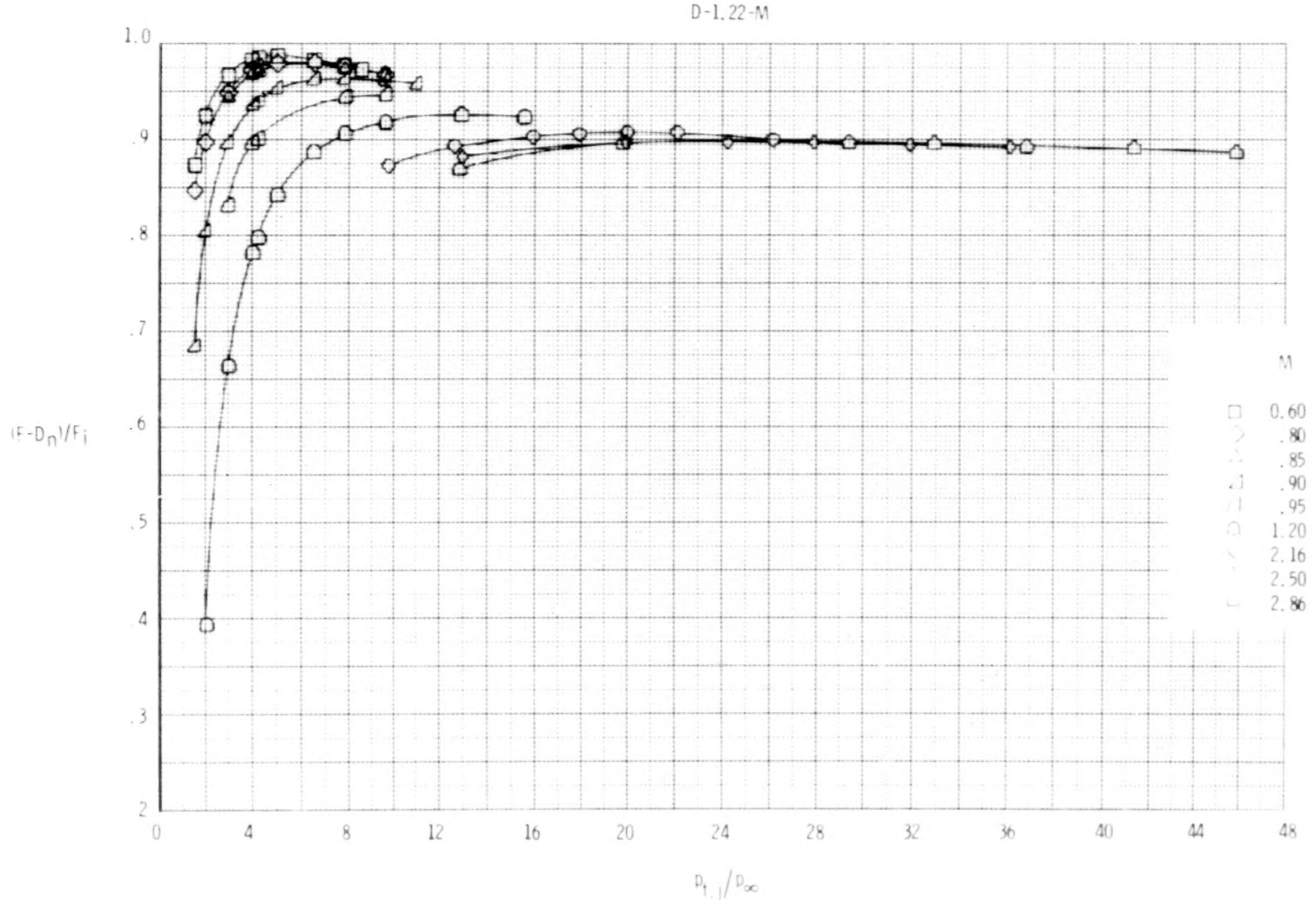

(d) Variation of thrust-minus-drag ratio.

Figure 6.- Concluded.

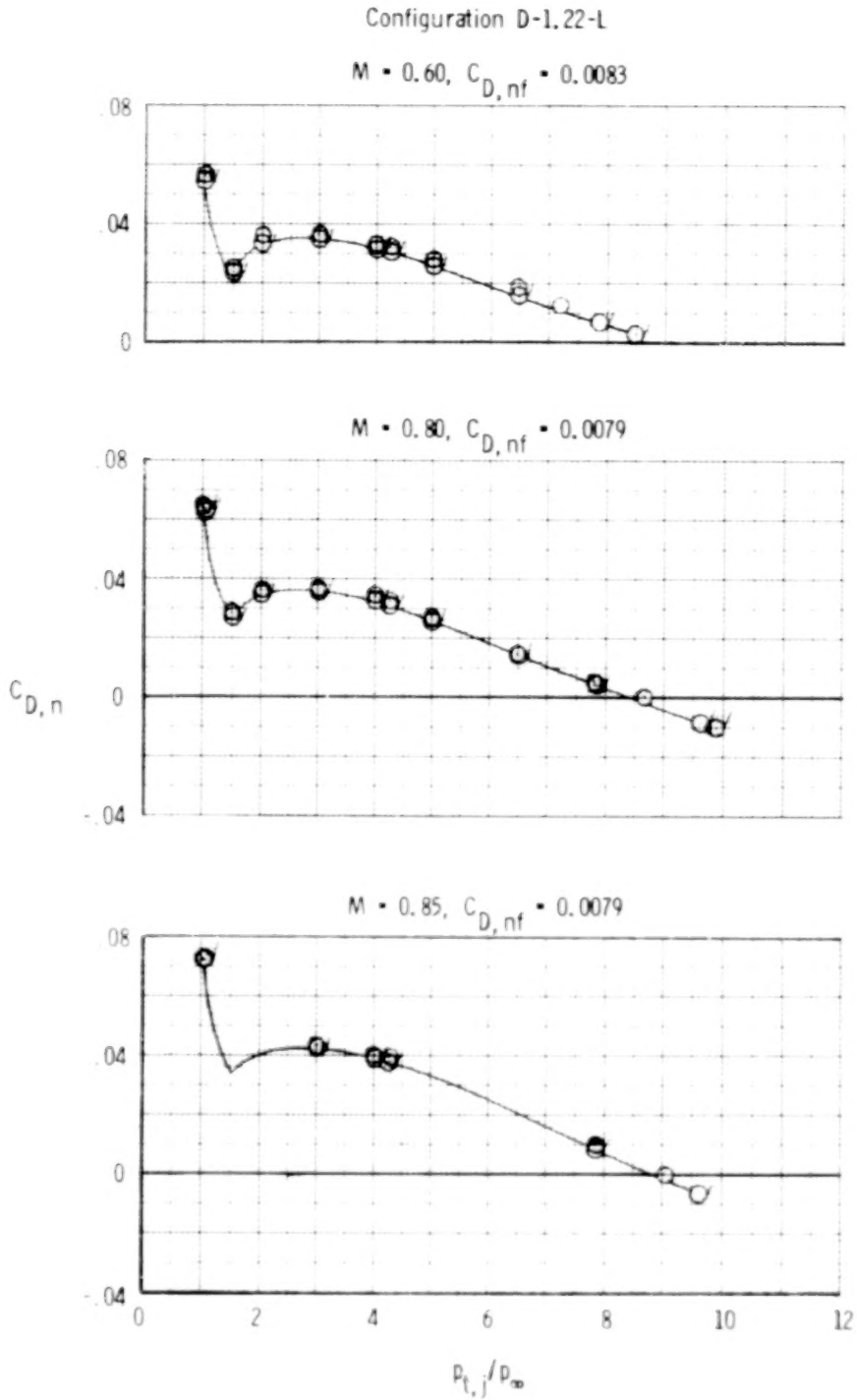

(a) Variation of nozzle drag coefficient.

Figure 7.- Variation of nozzle drag coefficient, thrust-minus-drag ratio, thrust ratio, and mass-flow ratio with nozzle pressure ratio for configuration D-1.22-L. Dashed line indicates theoretical values. Flagged symbols indicate data used to determine F/F_i.

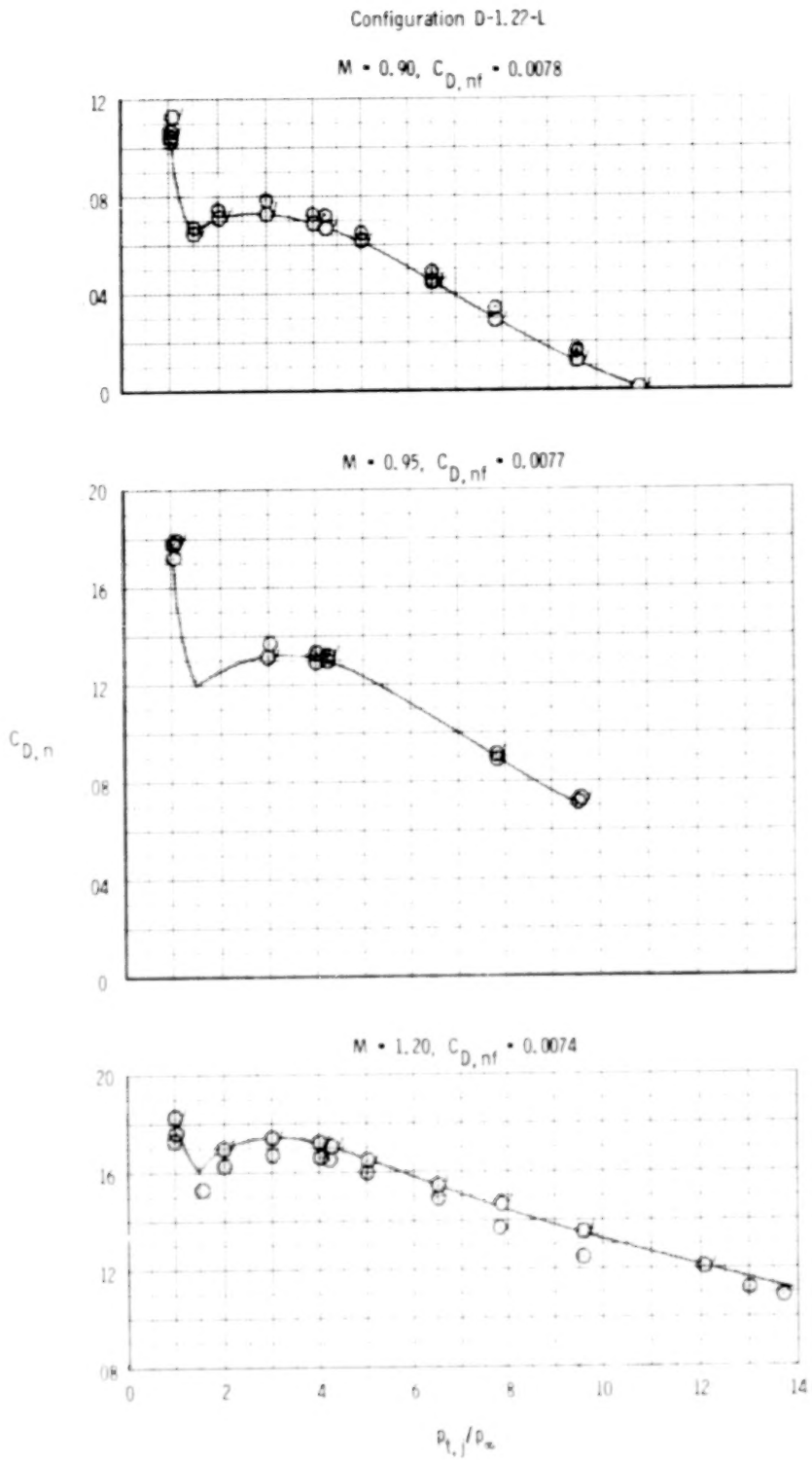

(a) Continued.

Figure 7.- Continued.

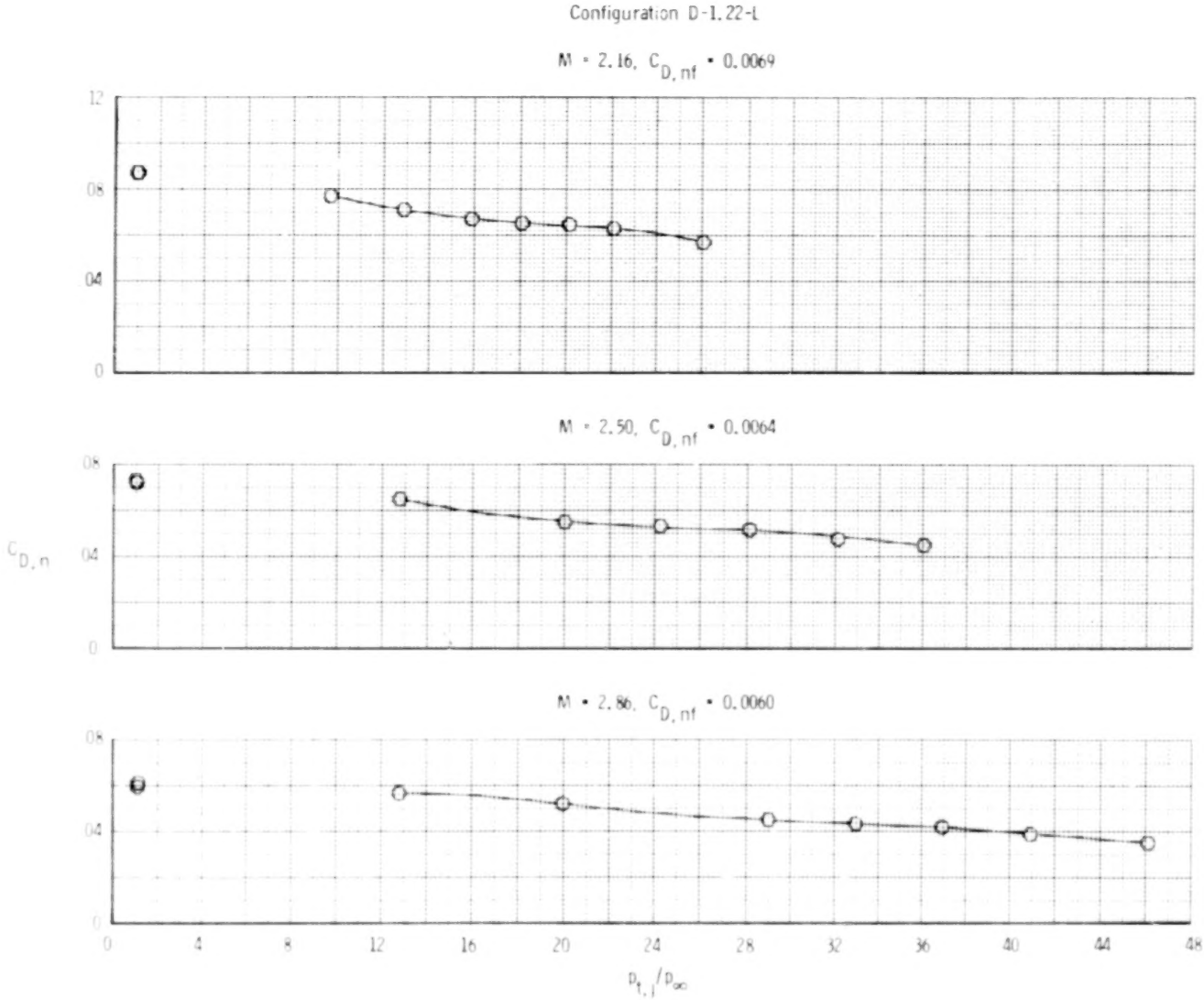

(a) Concluded.

Figure 7.- Continued.

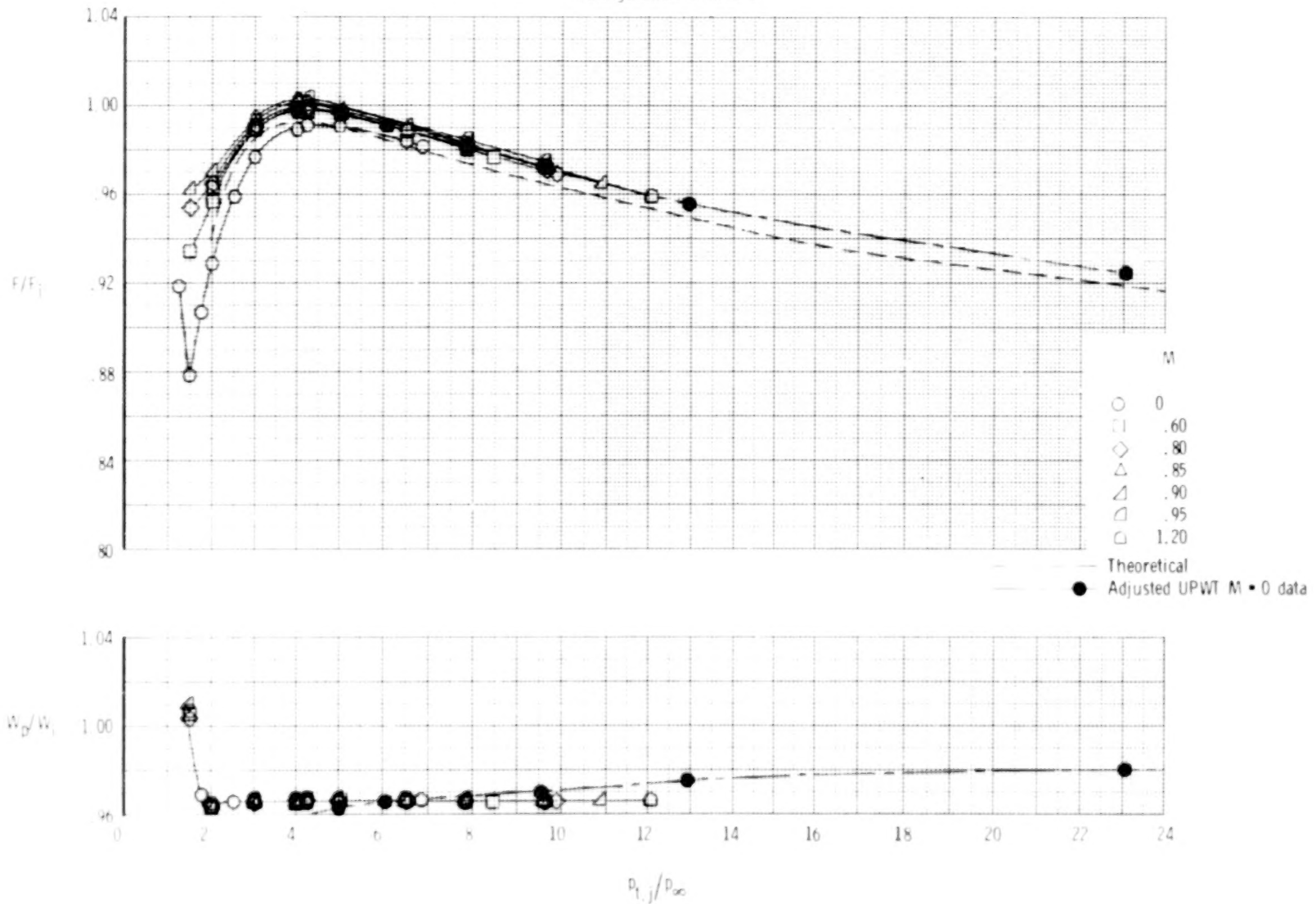

(b) Variation of thrust ratio and mass-flow ratio at subsonic and transonic speeds (16FTT).

Figure 7.- Continued.

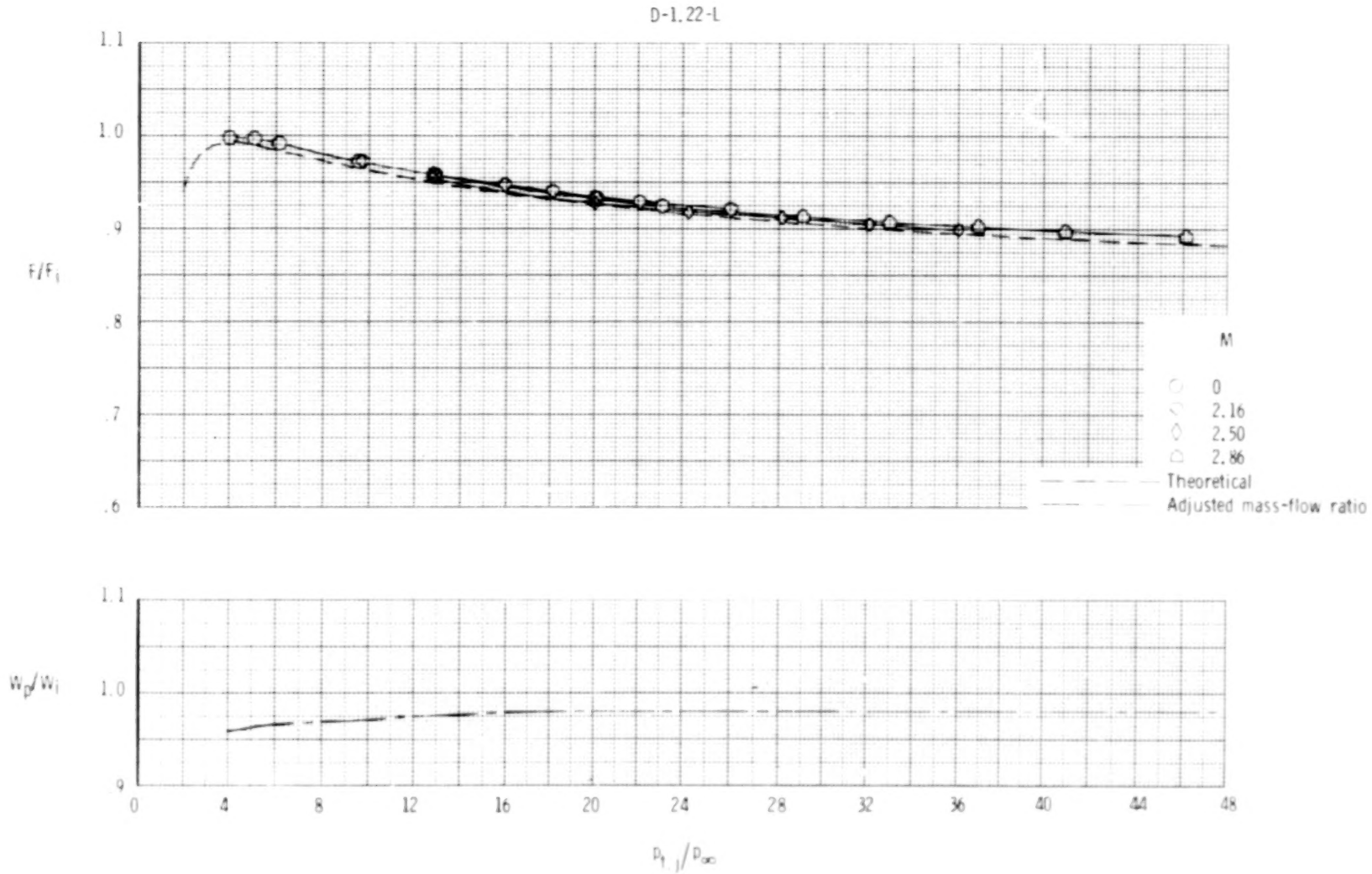

(c) Variation of thrust ratio and mass-flow ratio at supersonic speeds (UPWT).

Figure 7.- Continued.

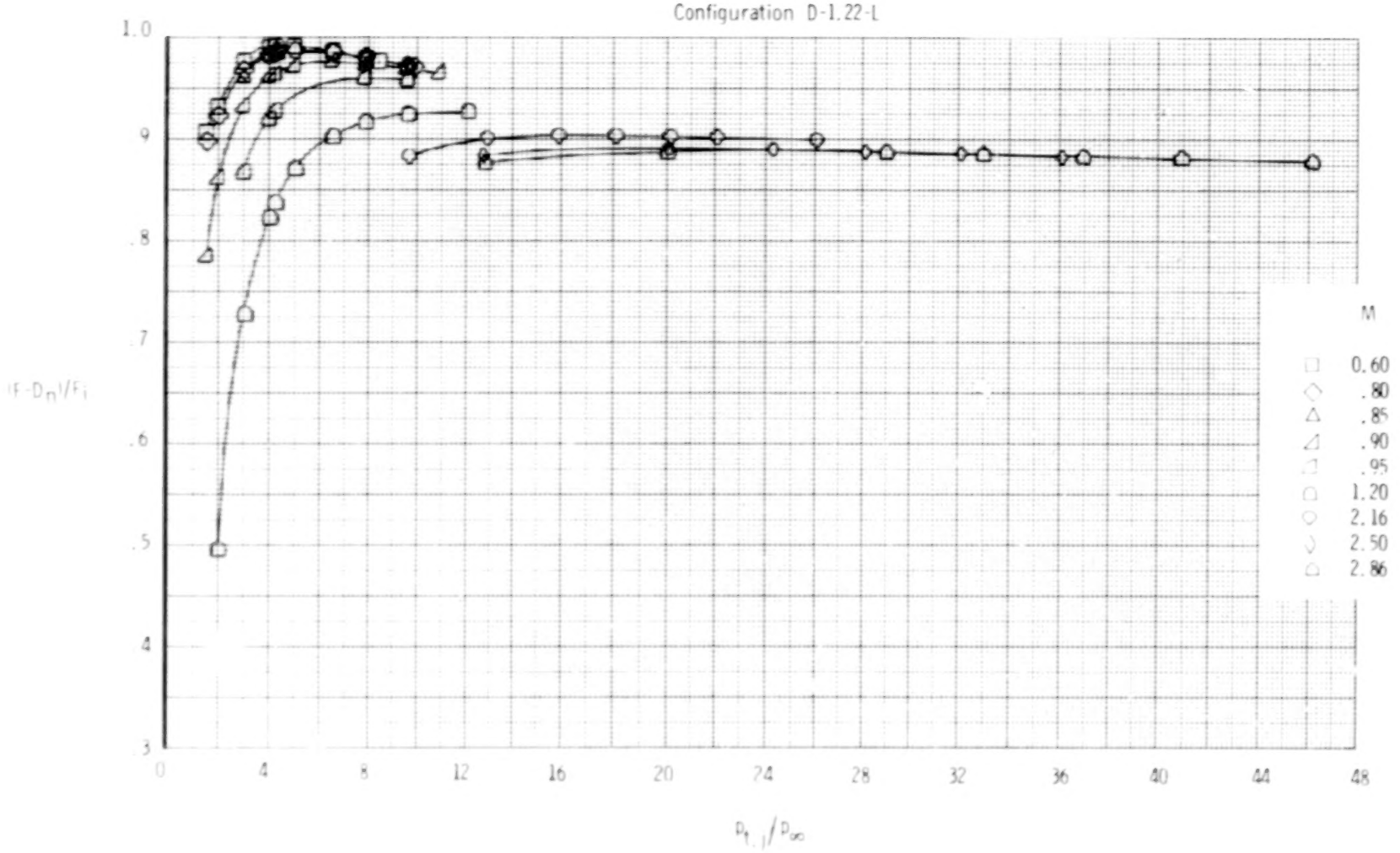

(d) Variation of thrust-minus-drag ratio.

Figure 7.- Concluded.

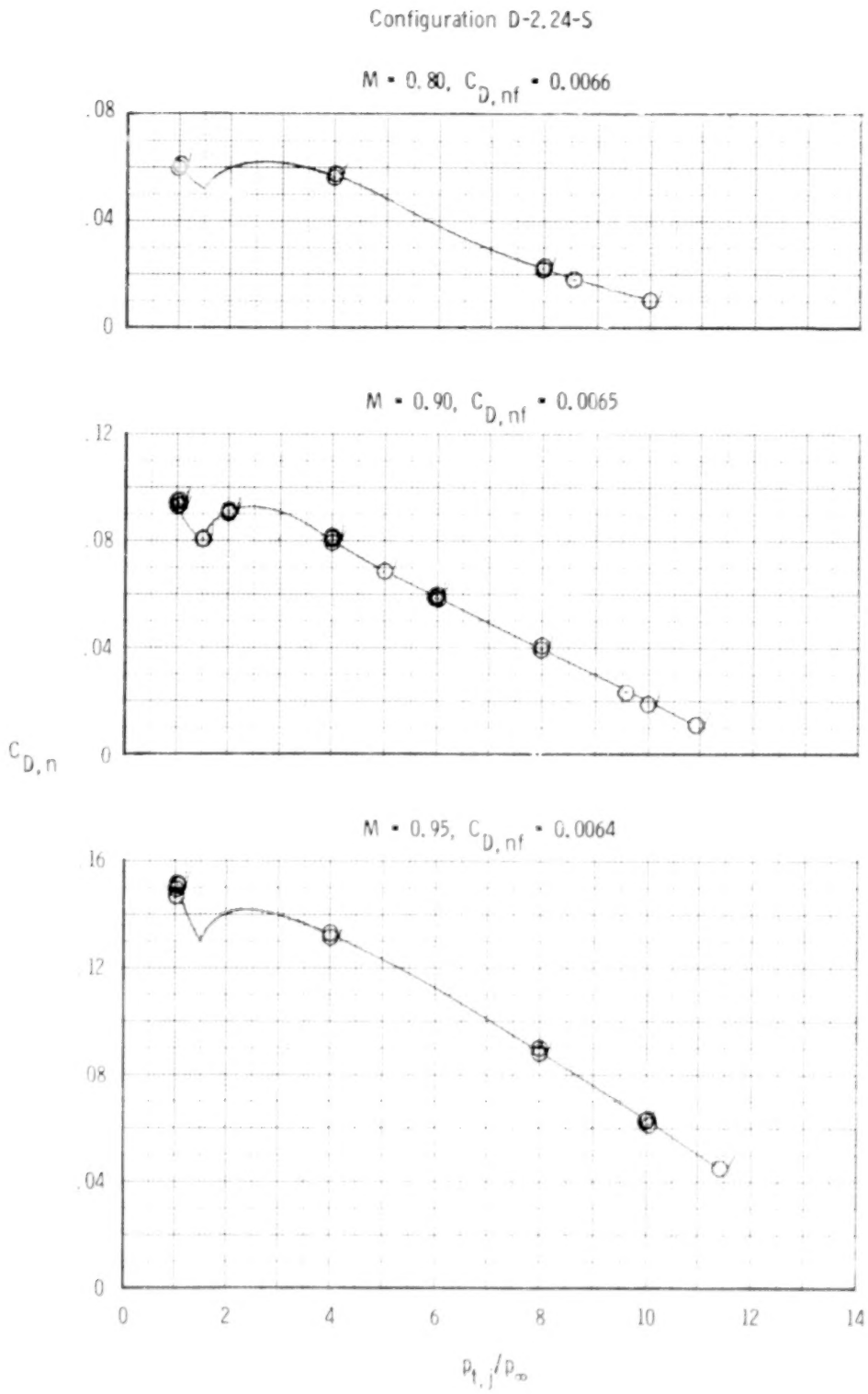

(a) Variation of nozzle drag coefficient.

Figure 8.- Variation of nozzle drag coefficient, thrust-minus-drag ratio, thrust ratio, and mass-flow ratio with nozzle pressure ratio for configuration D-2.24-S. Dashed line indicates theoretical values. Flagged symbols indicate data used to determine F/F_i.

Configuration D-2.24-S

M = 1.20, $C_{D,nf}$ = 0.0061

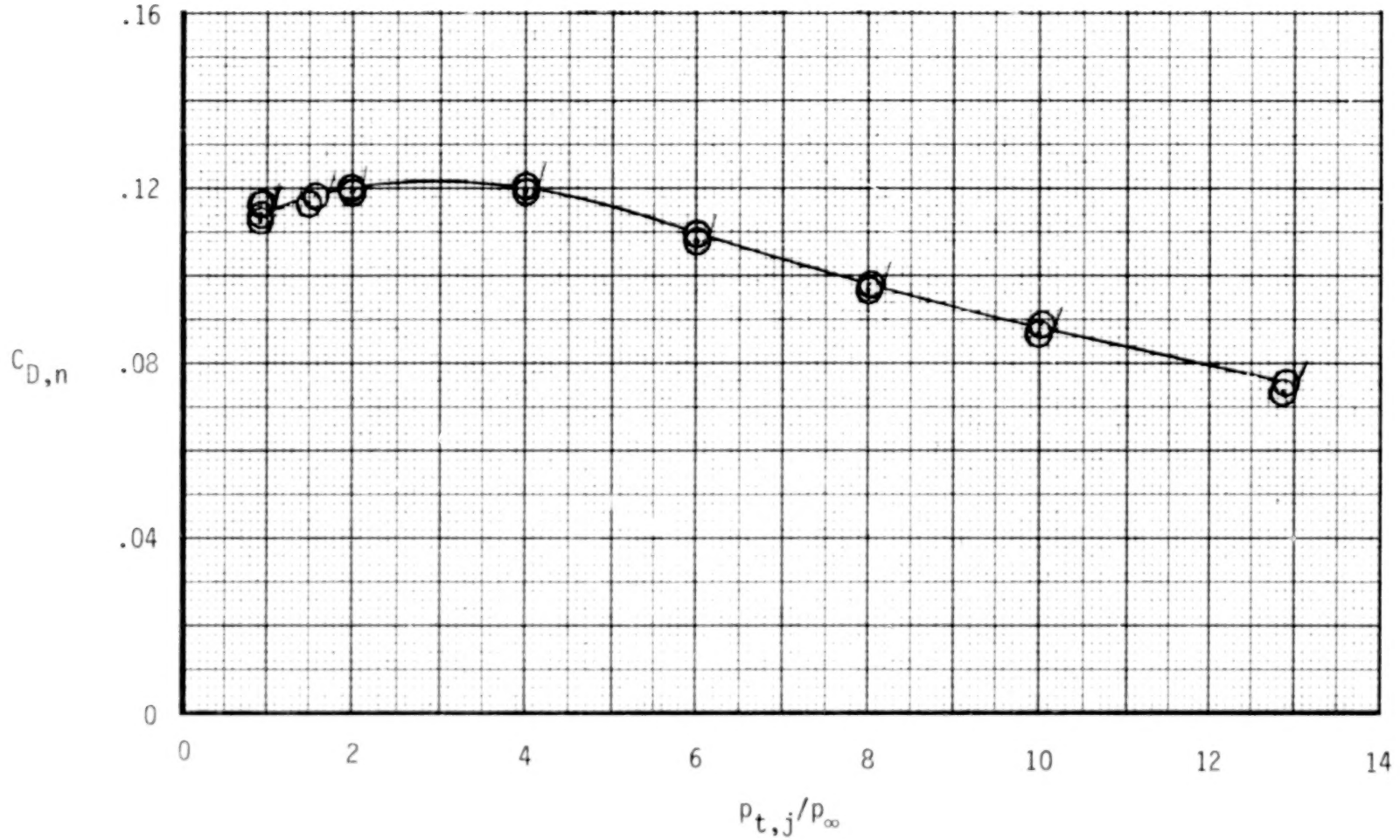

(a) Continued.

Figure 8.- Continued.

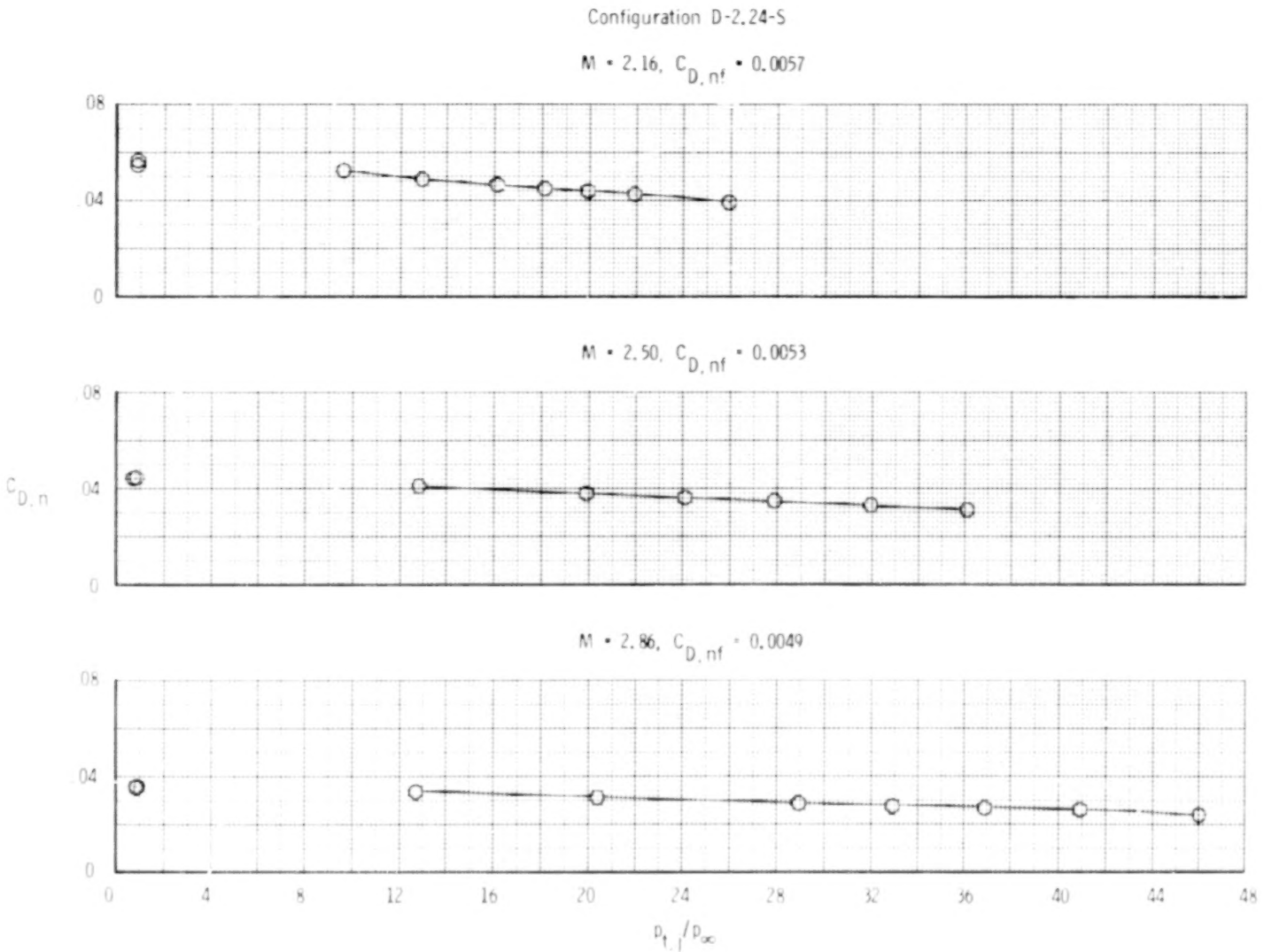

(a) Concluded.

Figure 8.- Continued.

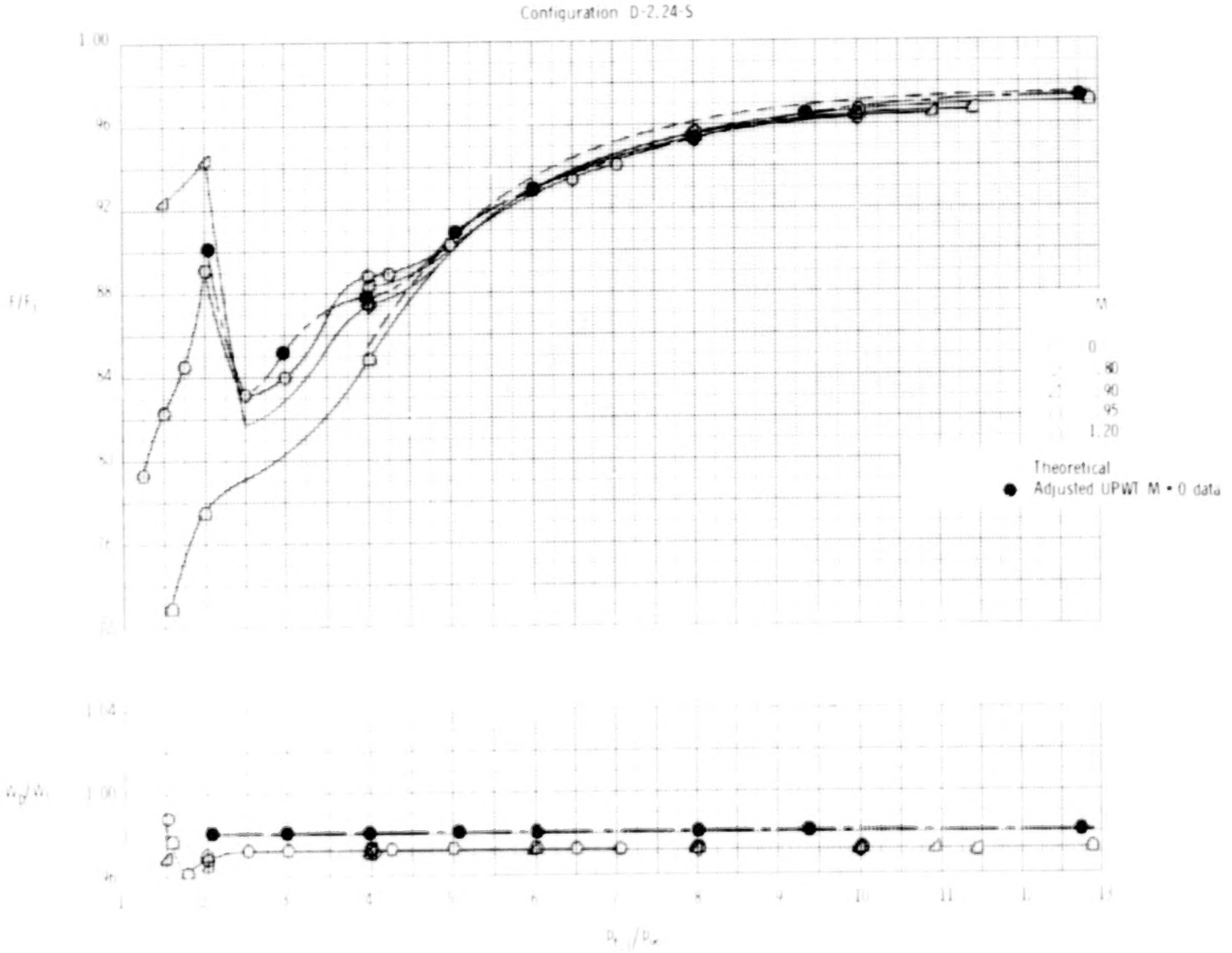

(b) Variation of thrust ratio and mass-flow ratio at subsonic and transonic speeds (16FTT).

Figure 8.- Continued.

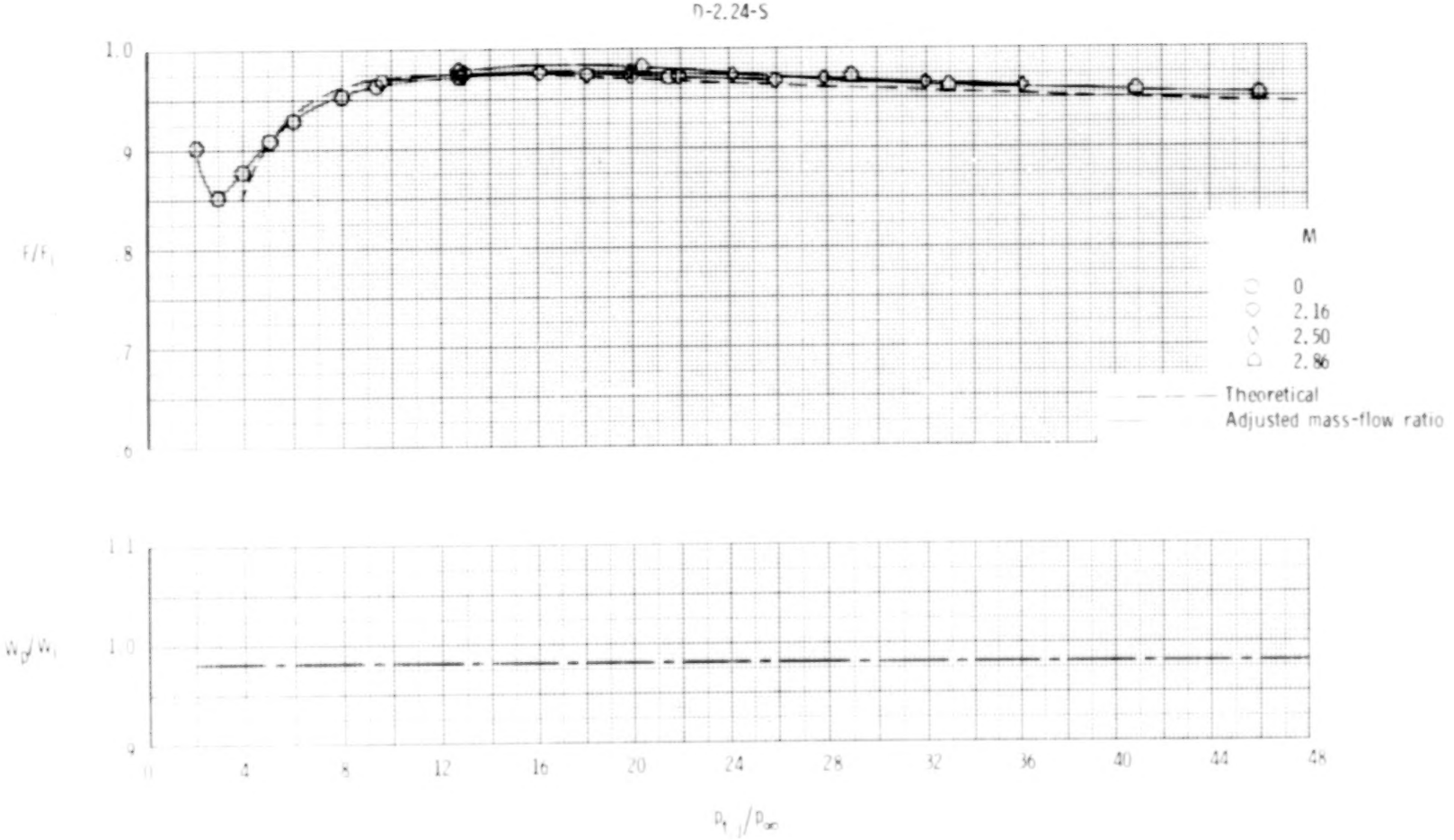

(c) Variation of thrust ratio and mass-flow ratio at supersonic speeds (UPWT).

Figure 8.- Continued.

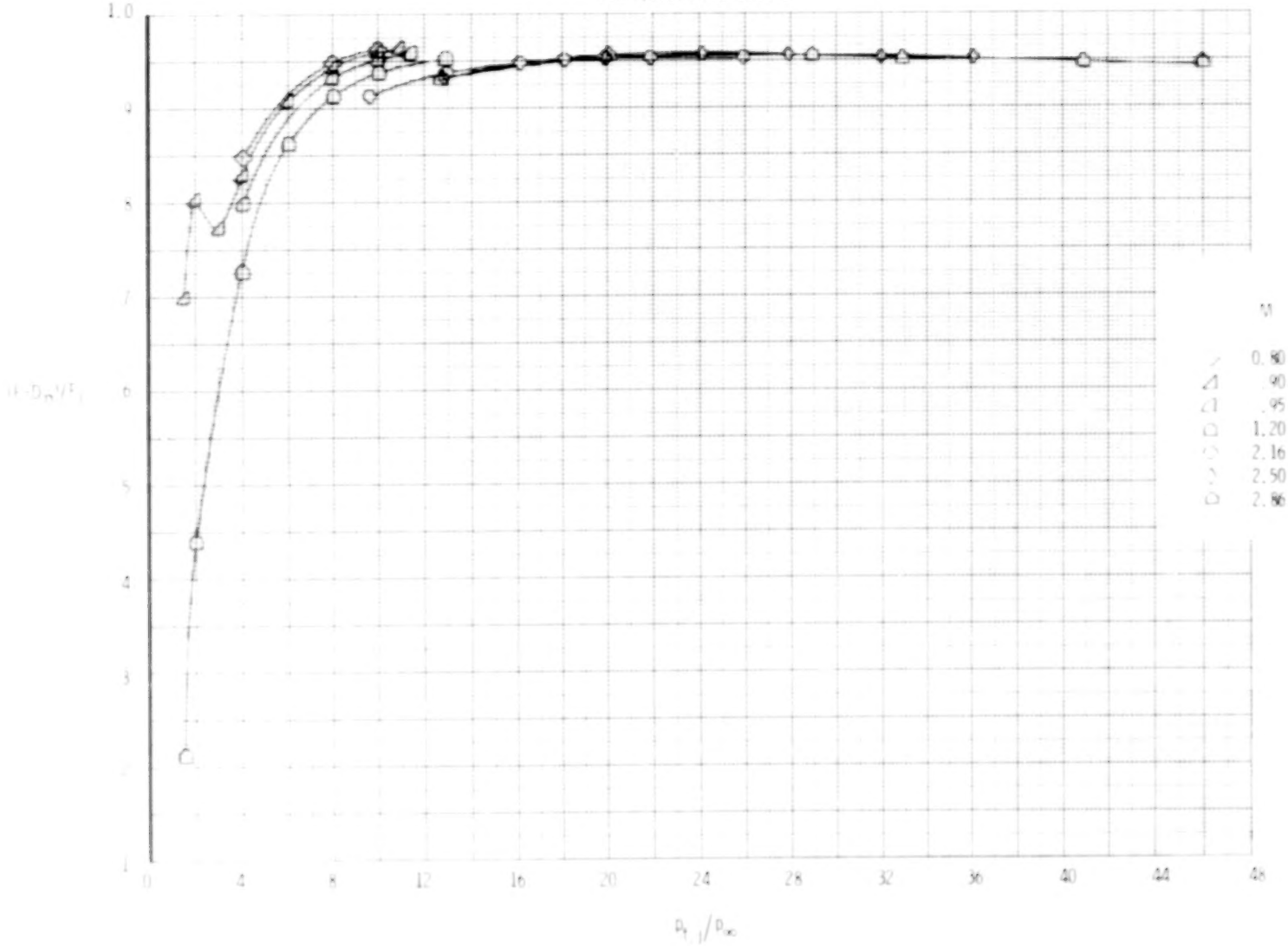

(d) Variation of thrust-minus-drag ratio.

Figure 8.- Concluded.

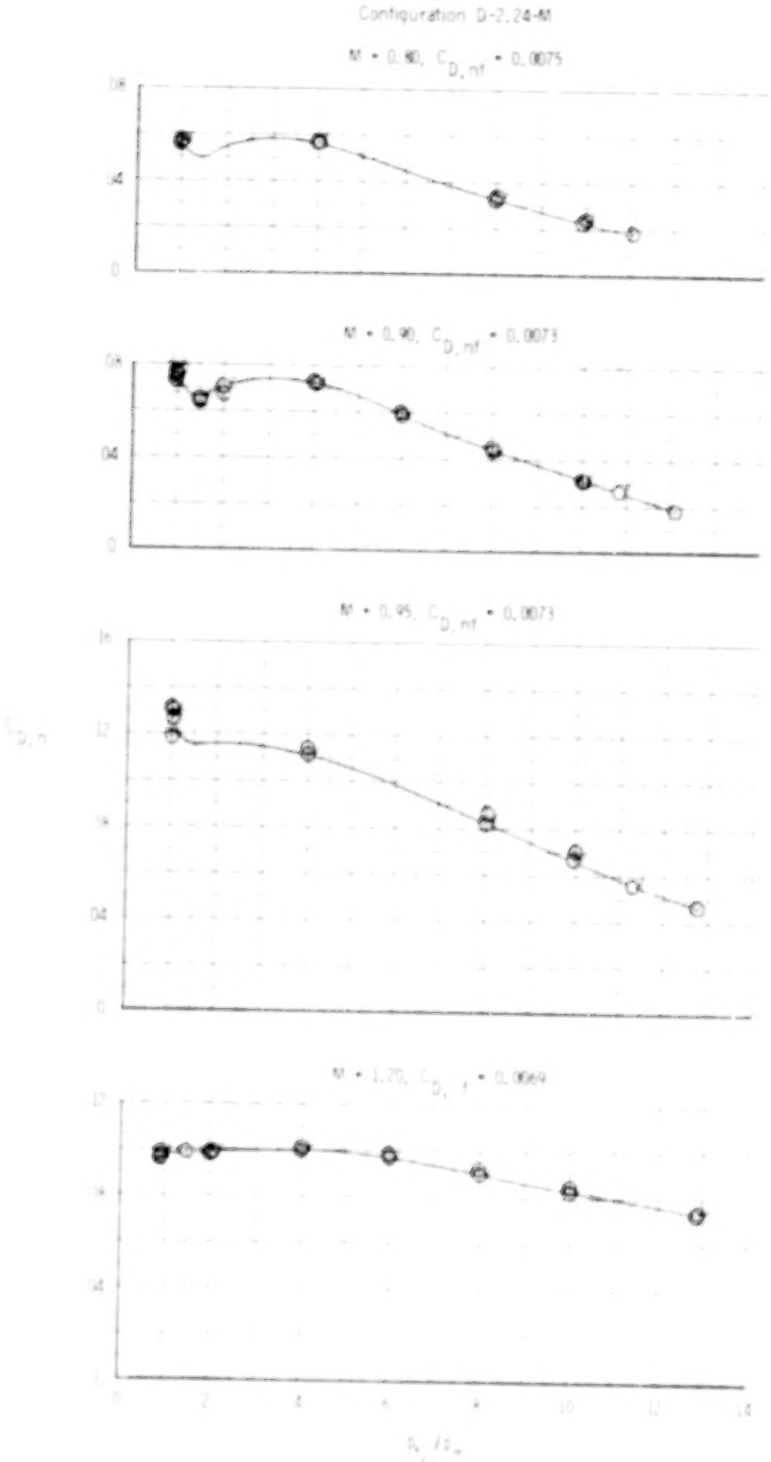

(a) Variation of nozzle drag coefficient.

Figure 9.- Variation of nozzle drag coefficient, thrust-minus-drag ratio, thrust ratio, and mass-flow ratio with nozzle pressure ratio for configuration D-2.24-M. Dashed line indicates theoretical values. Flagged symbols indicate data used to determine F/F_i.

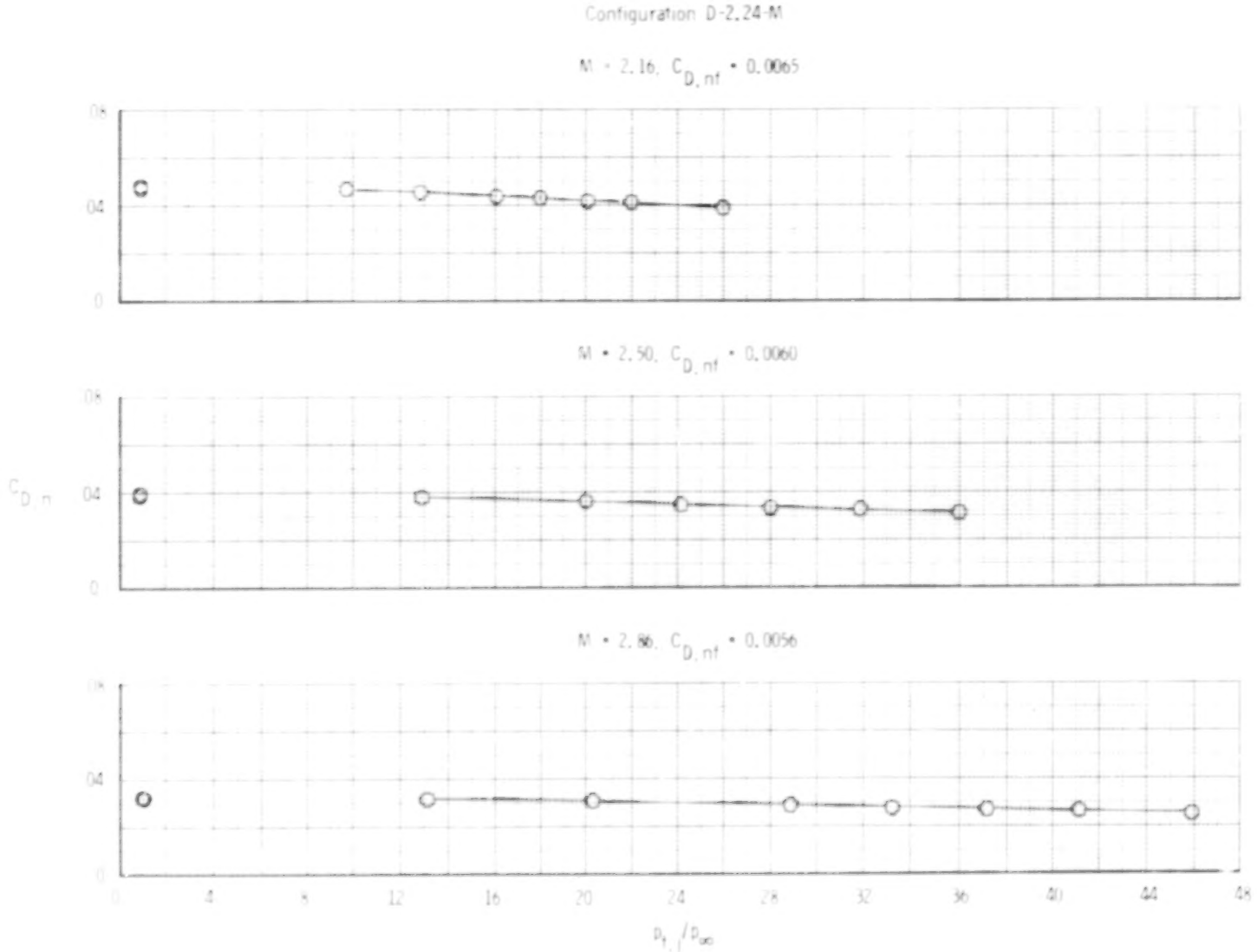

(a) Concluded.

Figure 9.- Continued.

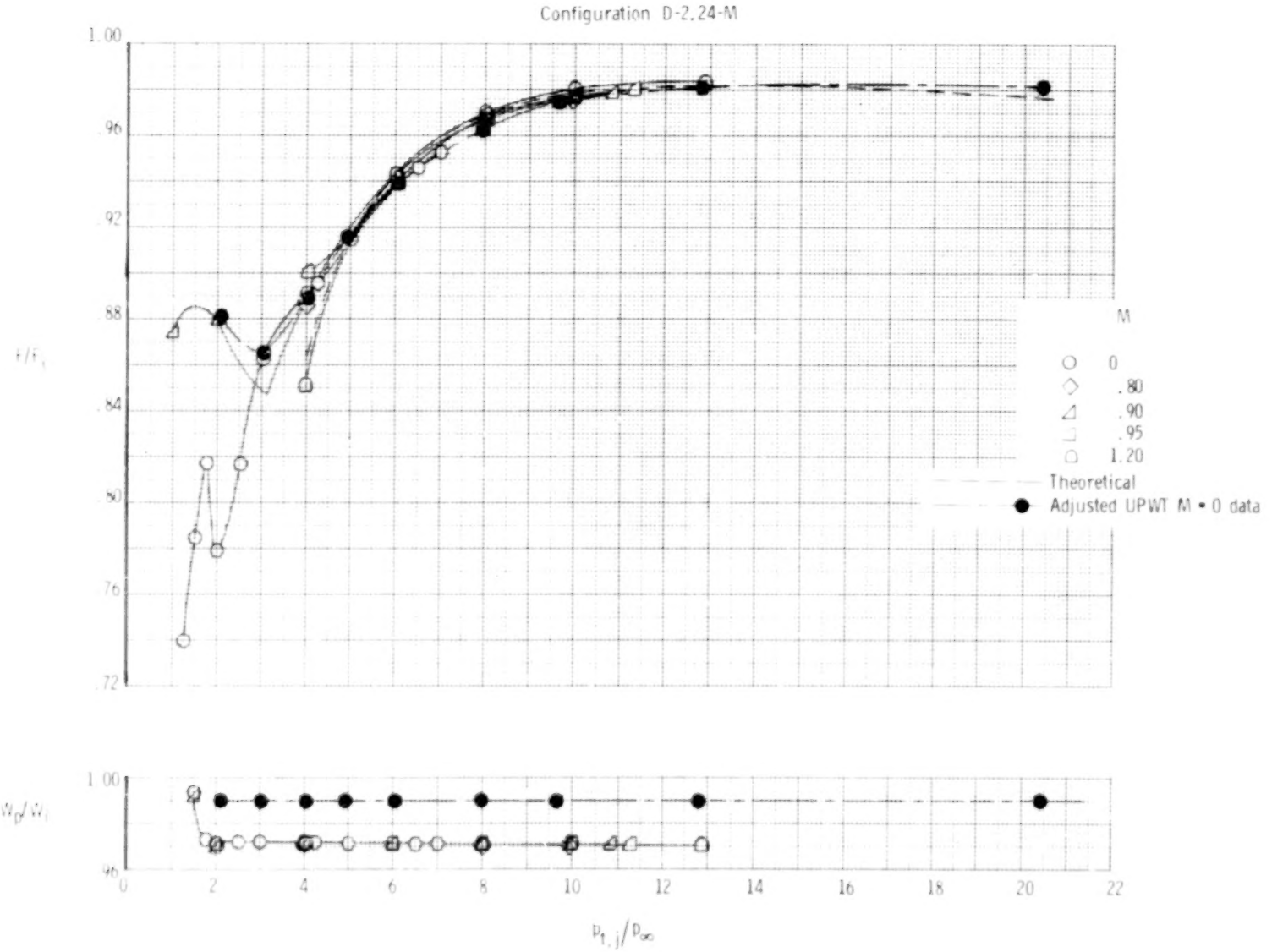

(b) Variation of thrust ratio and mass-flow ratio at subsonic and transonic speeds (16FTT).

Figure 9.- Continued.

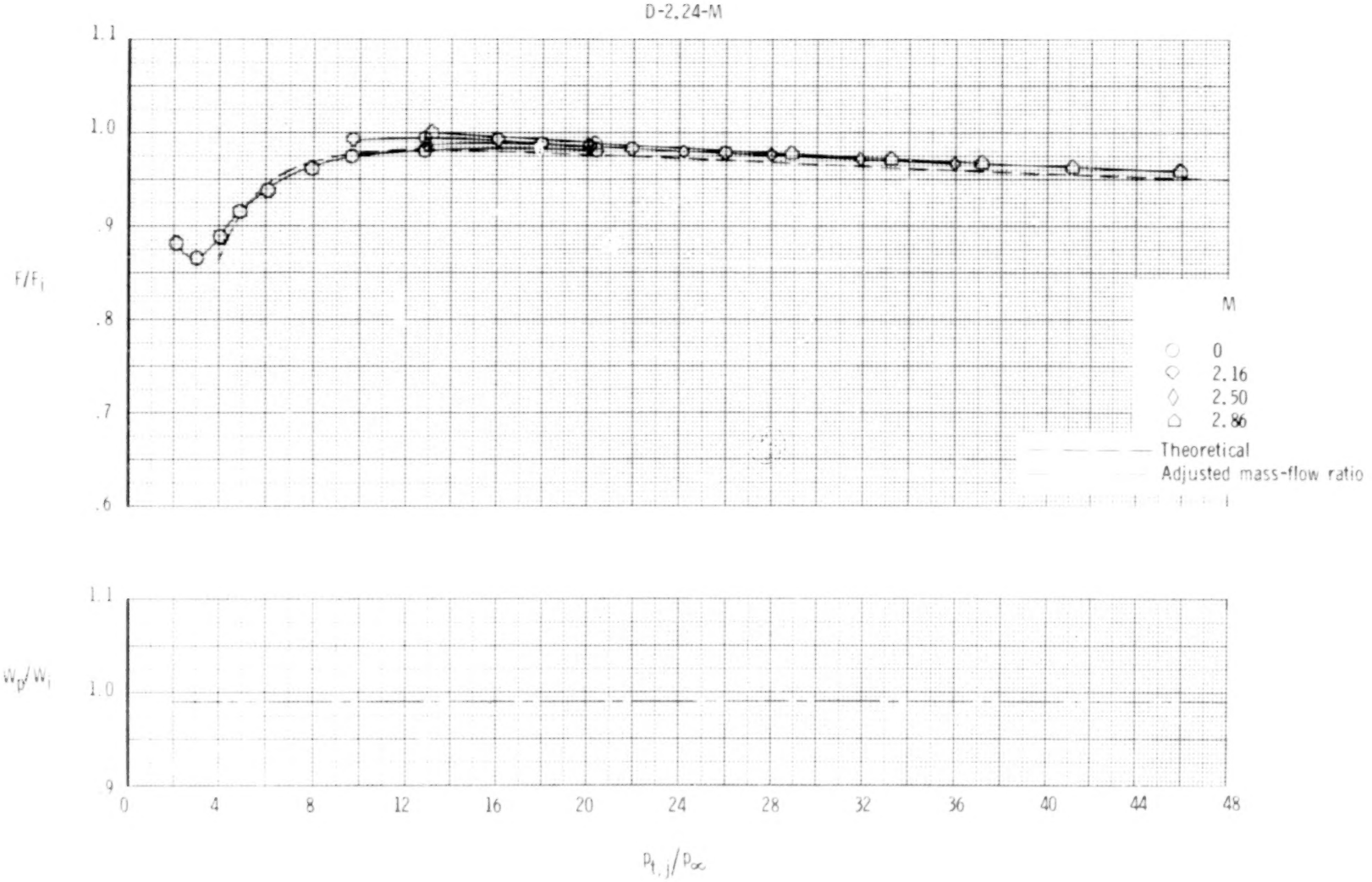

(c) Variation of thrust ratio and mass-flow ratio at supersonic speeds (UPWT).

Figure 9.- Continued.

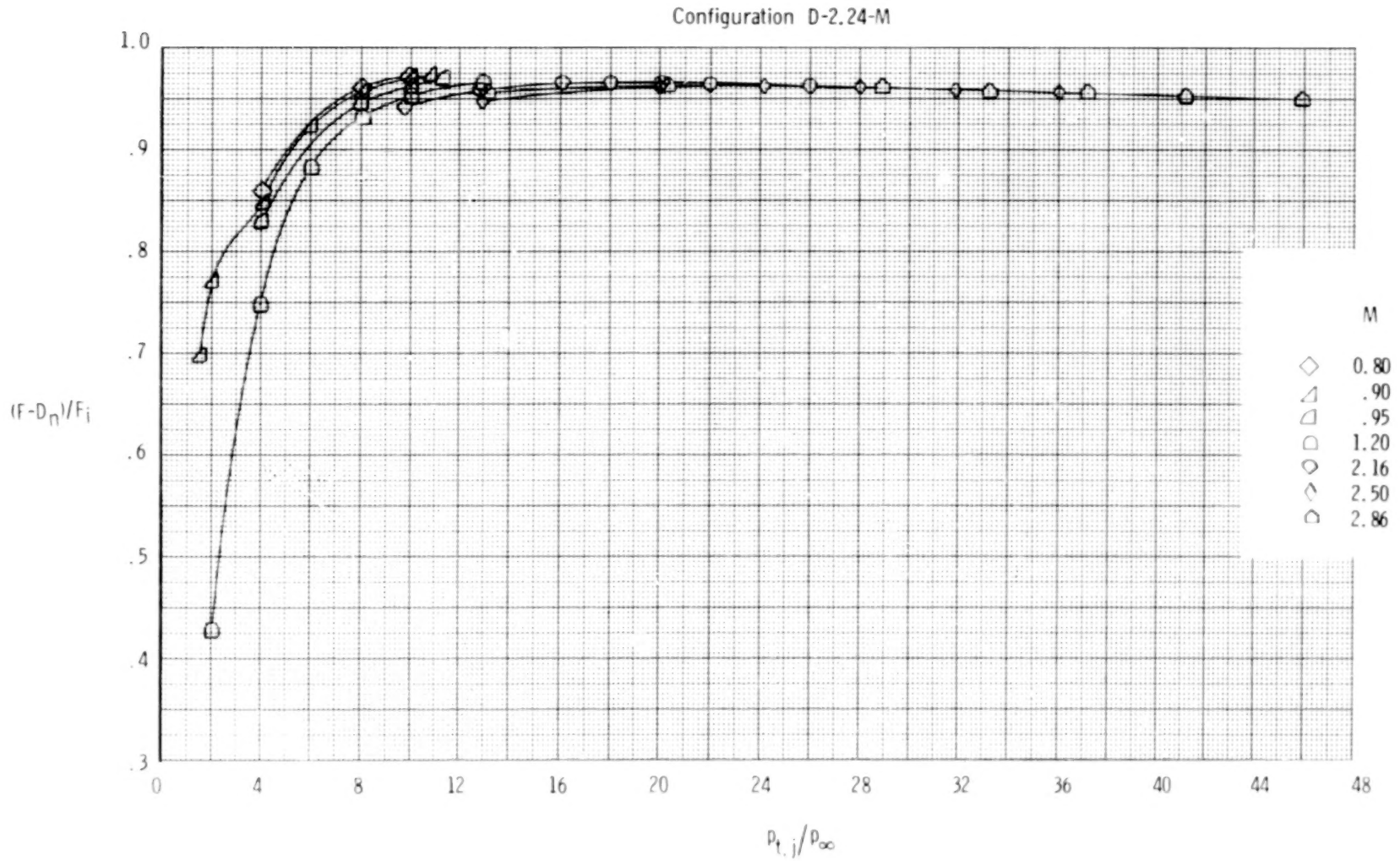

(d) Variation of thrust-minus-drag ratio.

Figure 9.- Concluded.

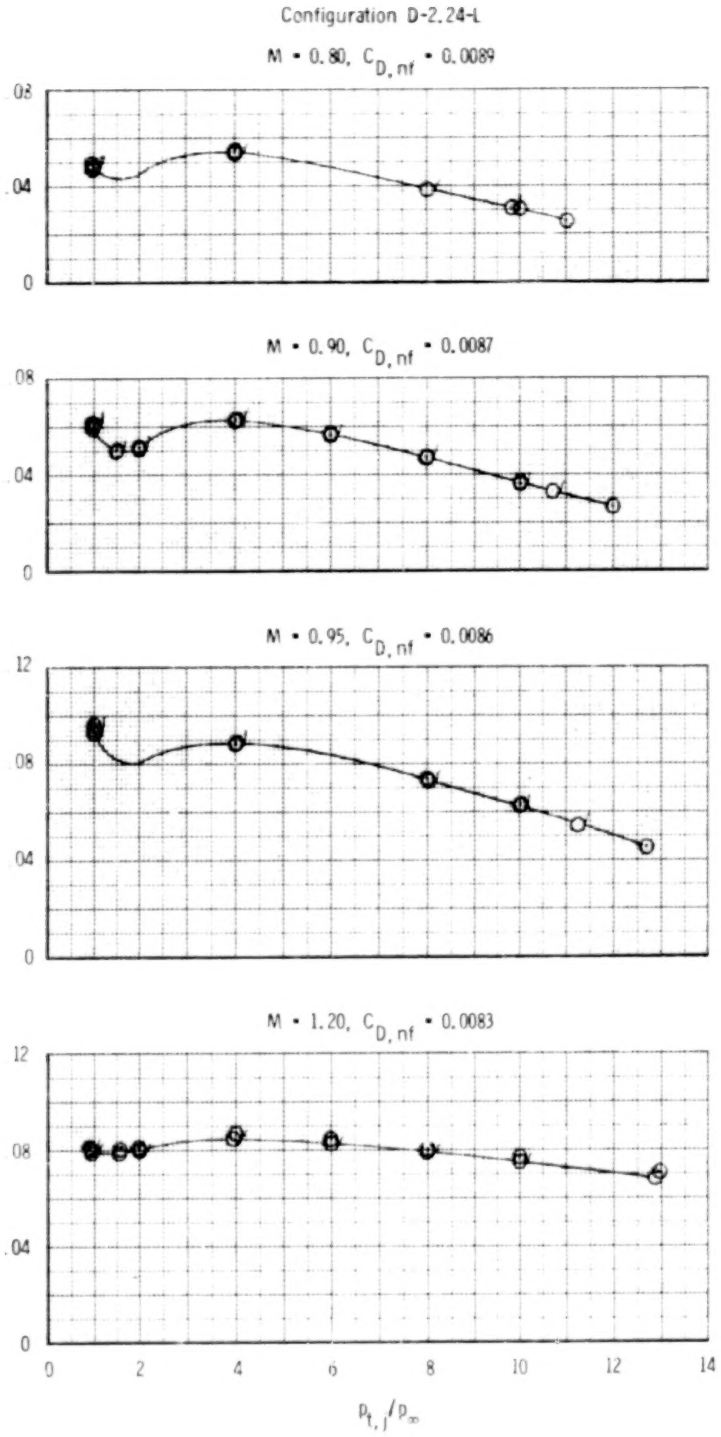

(a) Variation of nozzle drag coefficient.

Figure 10.- Variation of nozzle drag coefficient, thrust-minus-drag ratio, thrust ratio, and mass-flow ratio with nozzle pressure ratio for configuration D-2.24-L. Dashed line indicates theoretical values. Flagged symbols indicate data used to determine F/F_i.

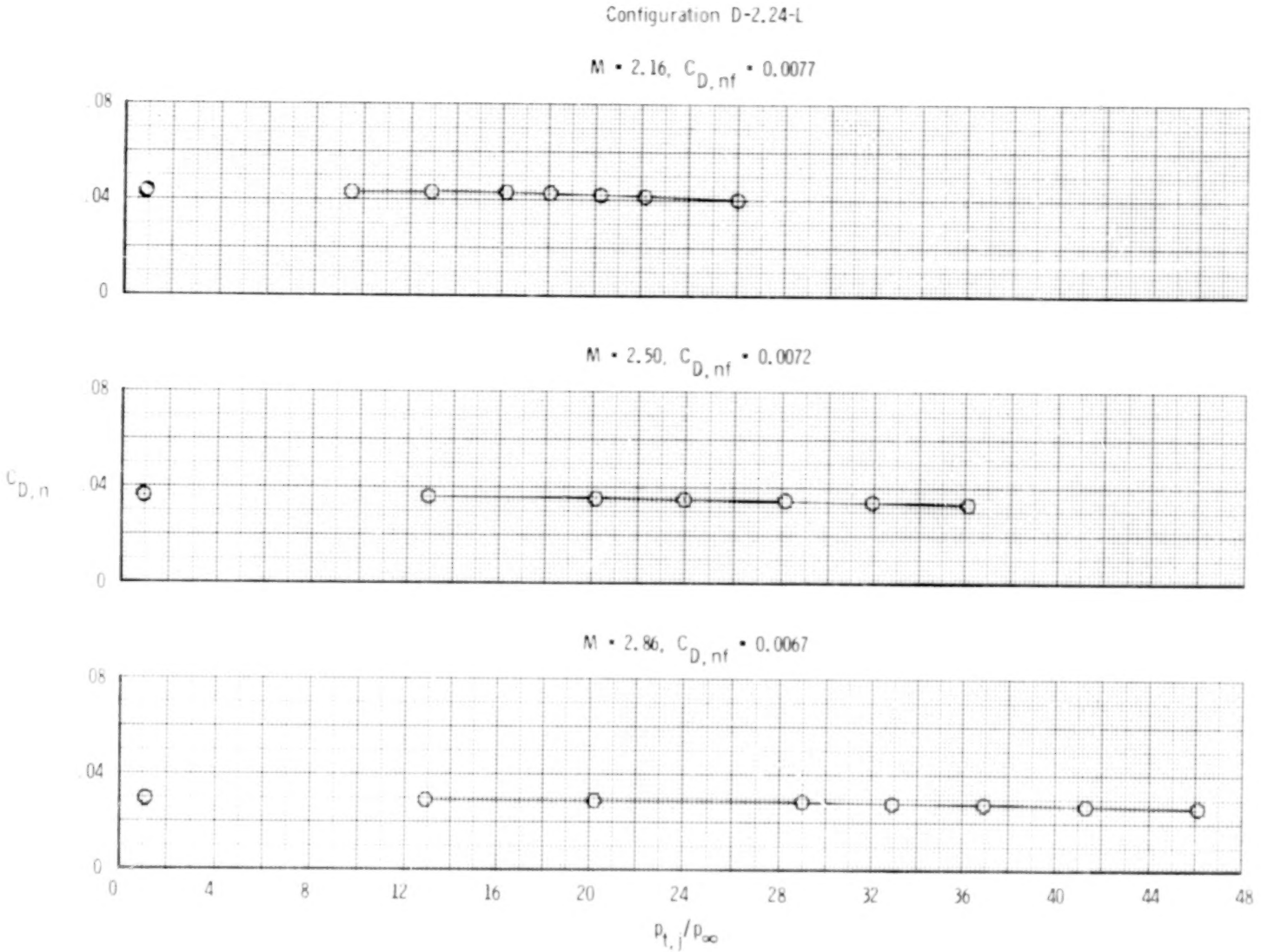

(a) Concluded.

Figure 10.- Continued.

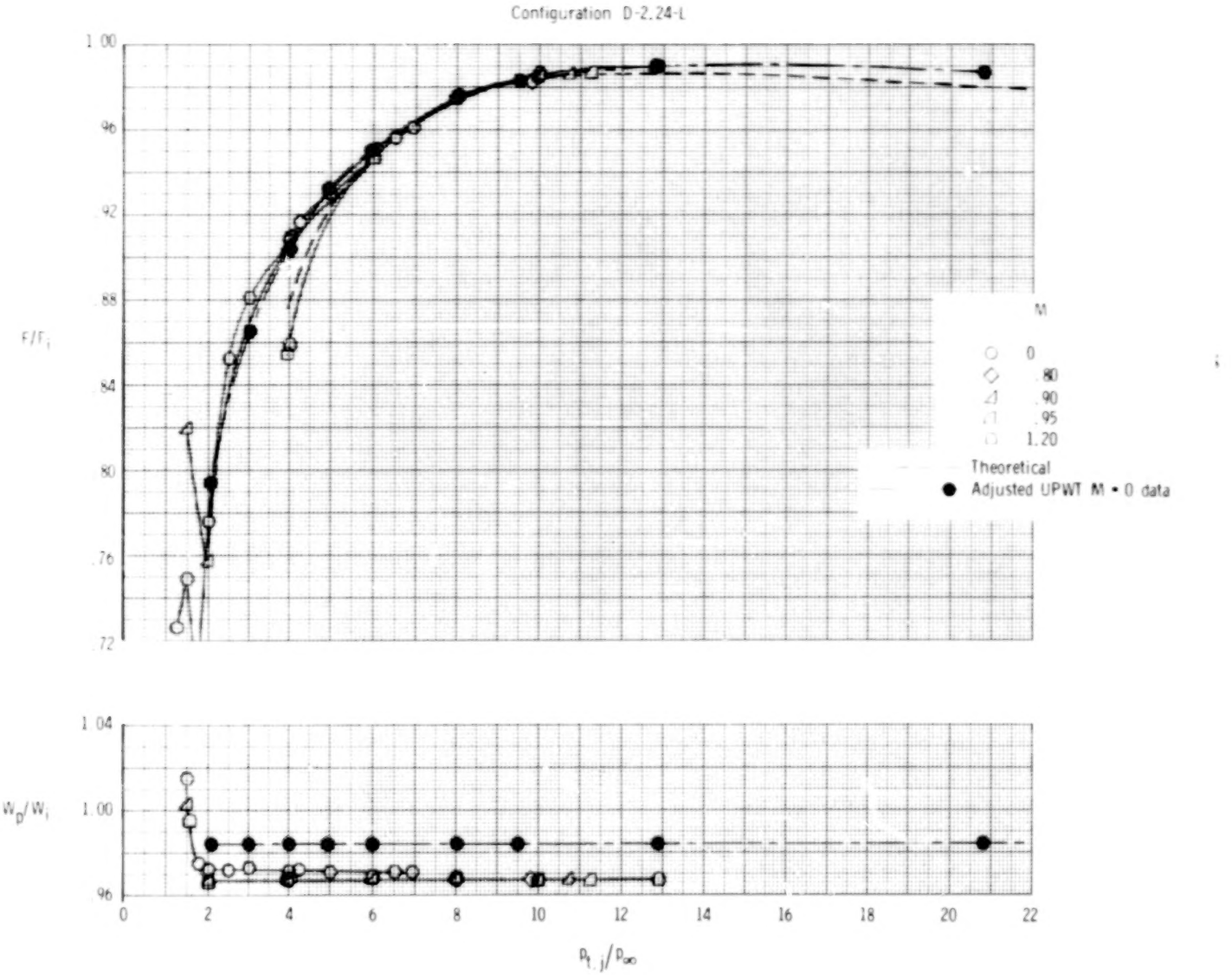

(b) Variation of thrust ratio and mass-flow ratio at subsonic and transonic speeds (16FTT).

Figure 10.- Continued.

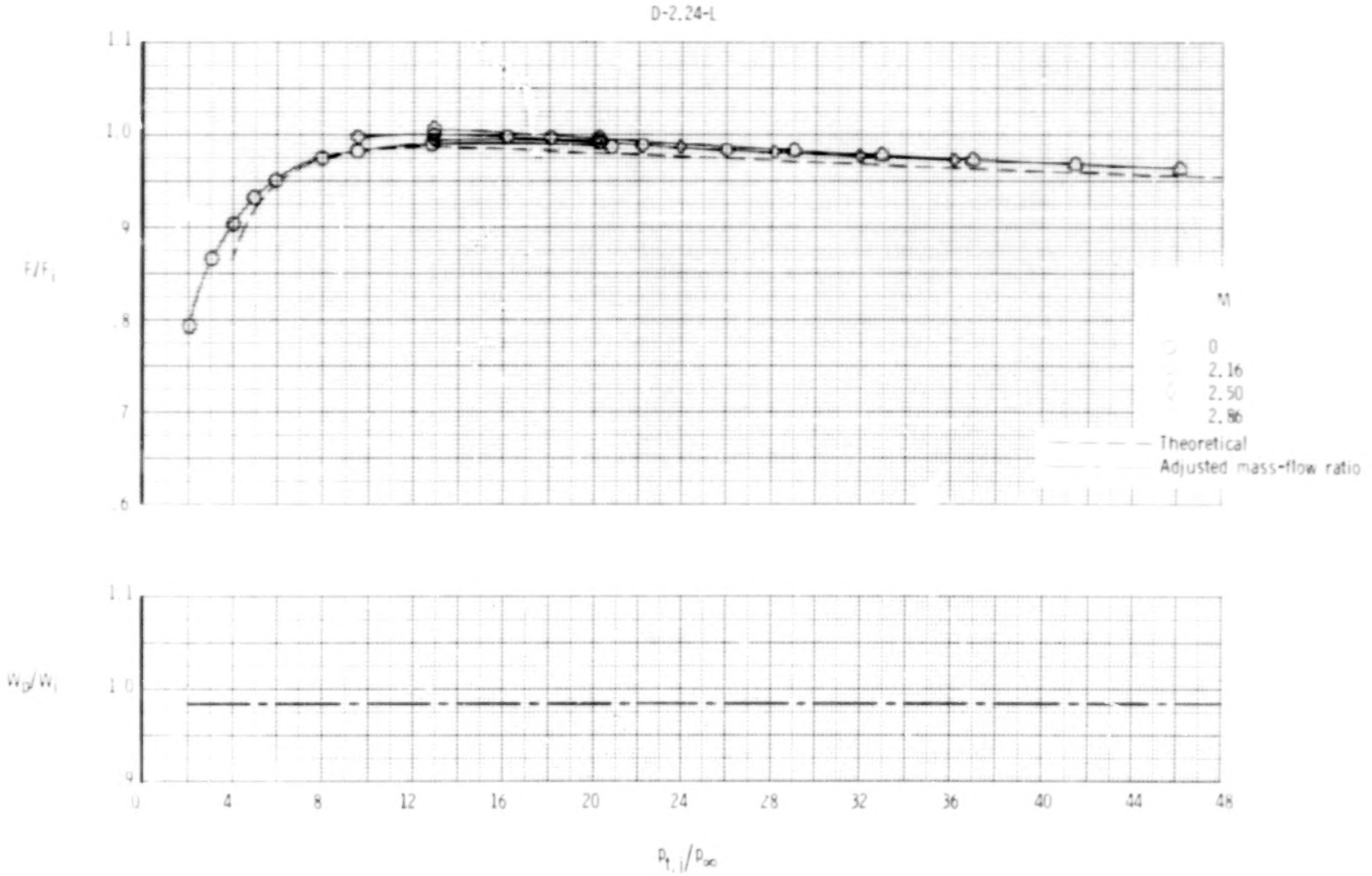

(c) Variation of thrust ratio and mass-flow ratio at supersonic speeds (UPWT).

Figure 10.- Continued.

BLANK PAGE

BLANK PAGE

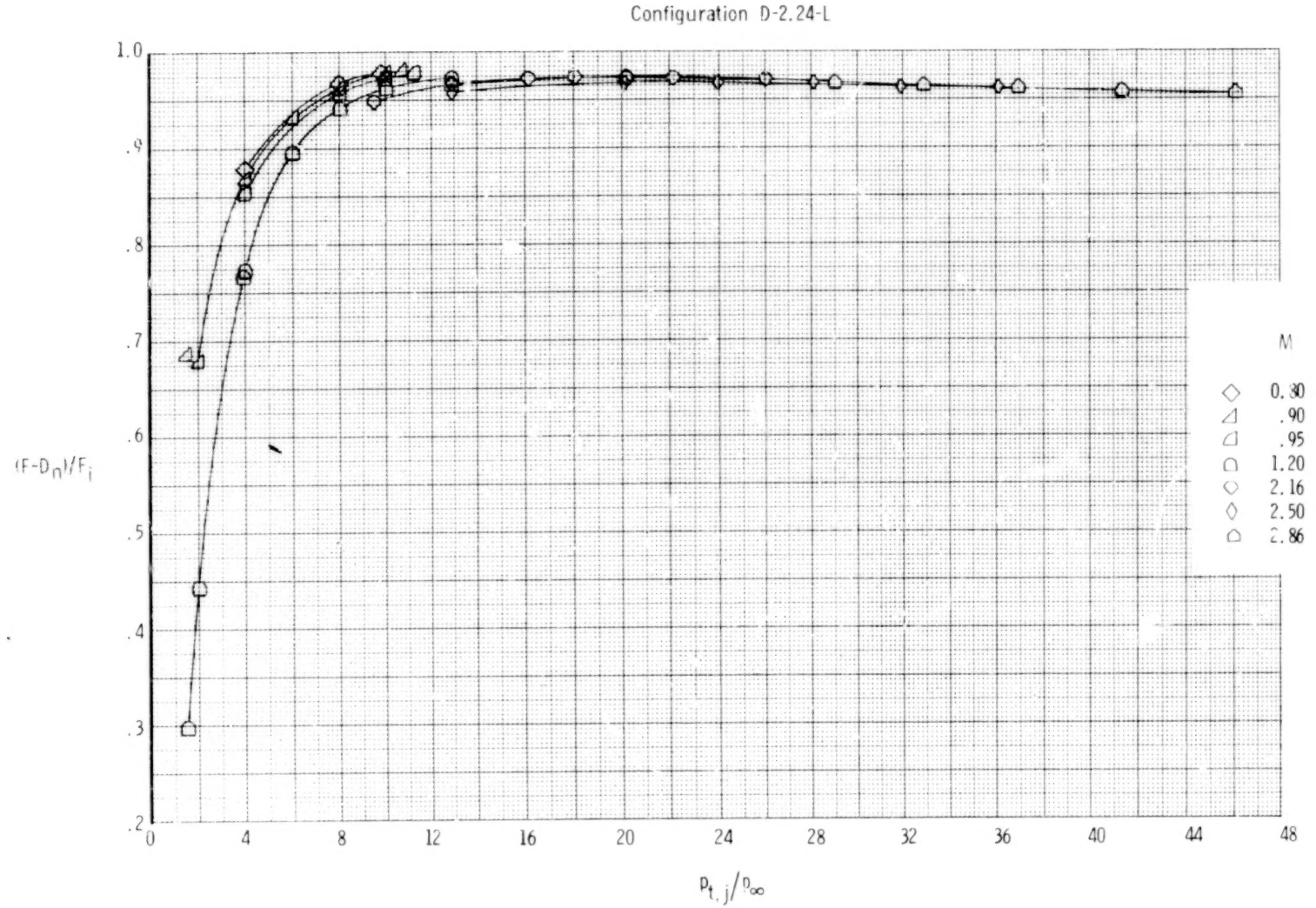

(d) Variation of thrust-minus-drag ratio.

Figure 10.- Concluded.

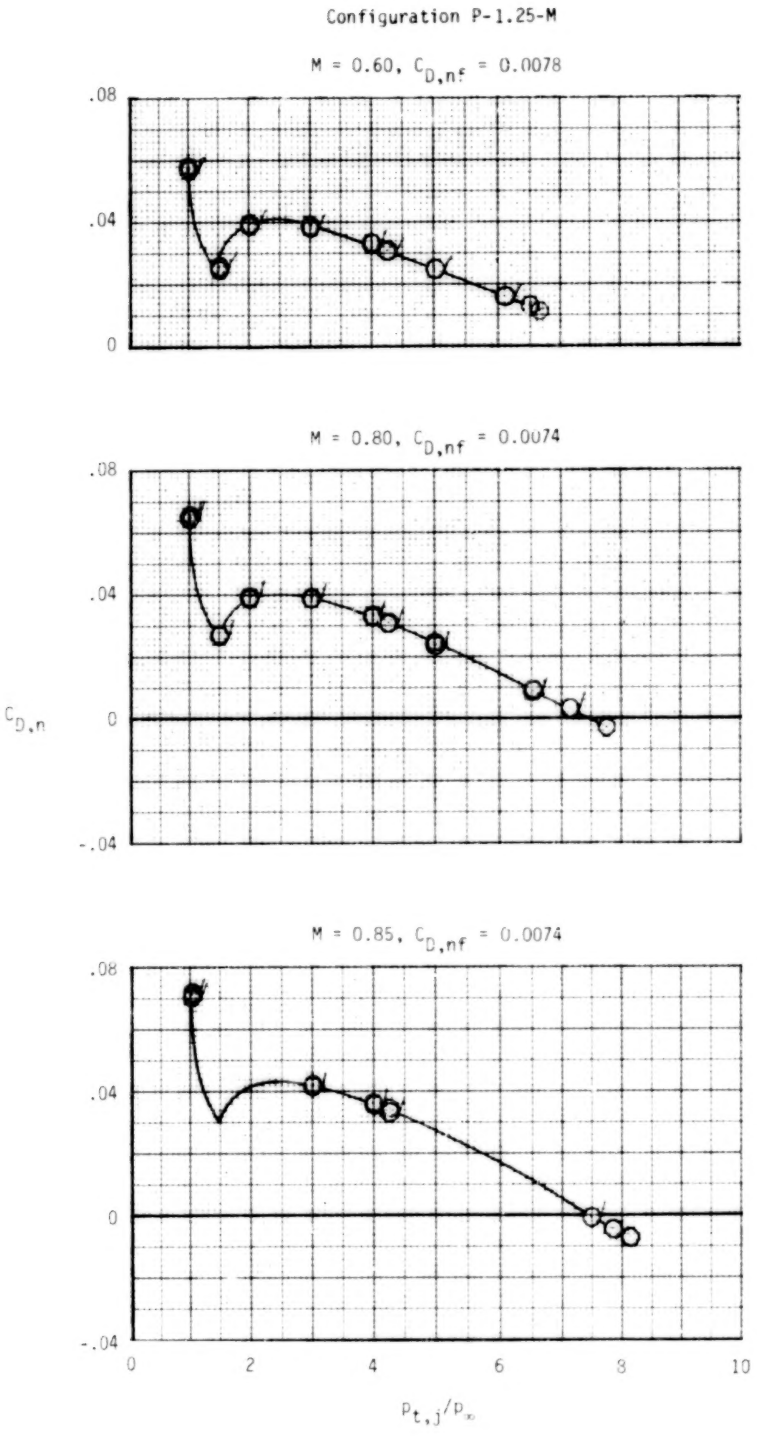

(a) Variation of nozzle drag coefficient.

Figure 11.- Variation of nozzle drag coefficient, thrust-minus-drag ratio, thrust ratio, and mass-flow ratio with nozzle pressure for configuration P-1.25-M. Dashed line indicates theoretical values. Flagged symbols indicate data used to determine F/F_i.

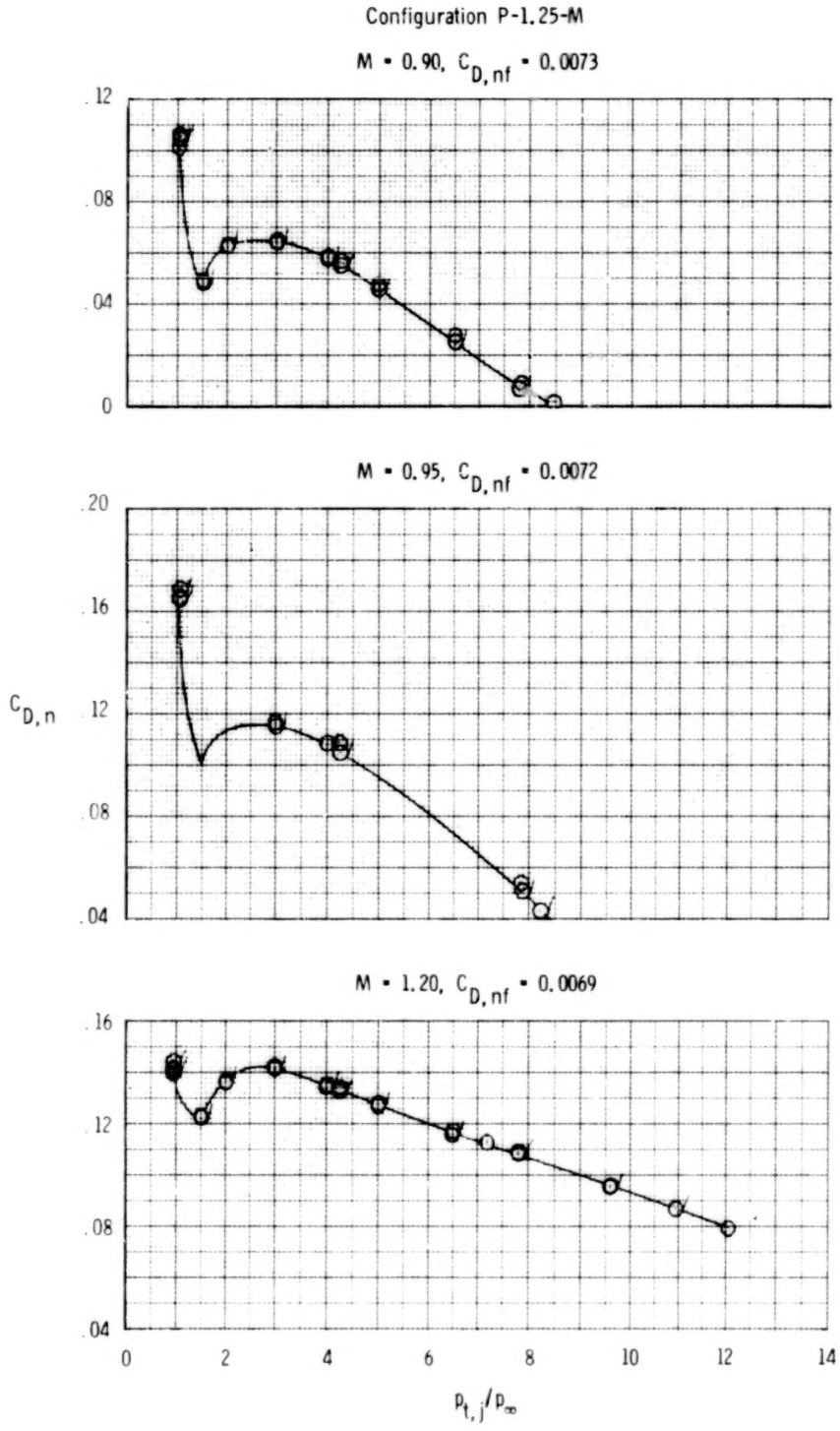

(a) Continued.

Figure 11.- Continued.

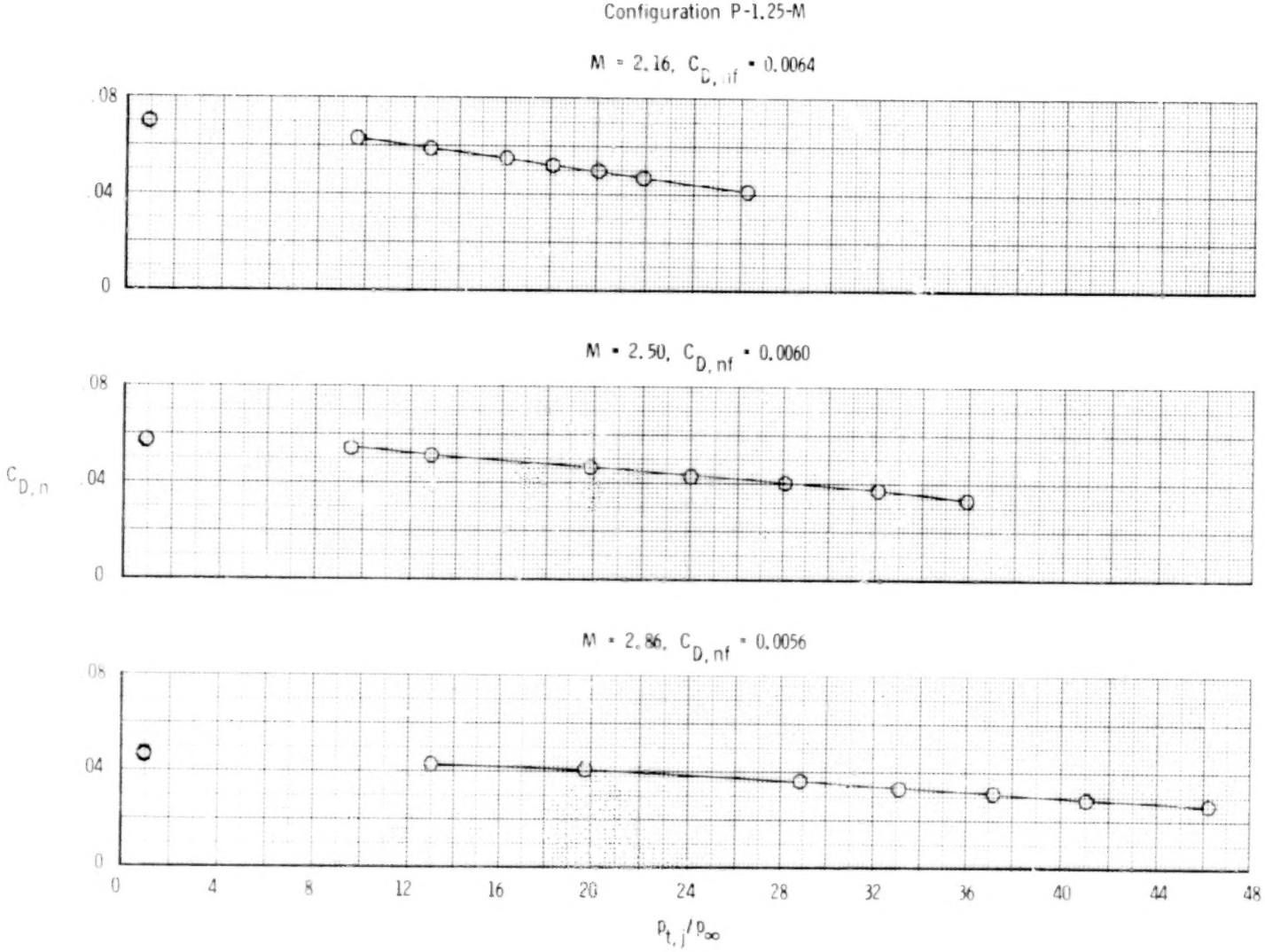

(a) Concluded.

Figure 11.- Continued.

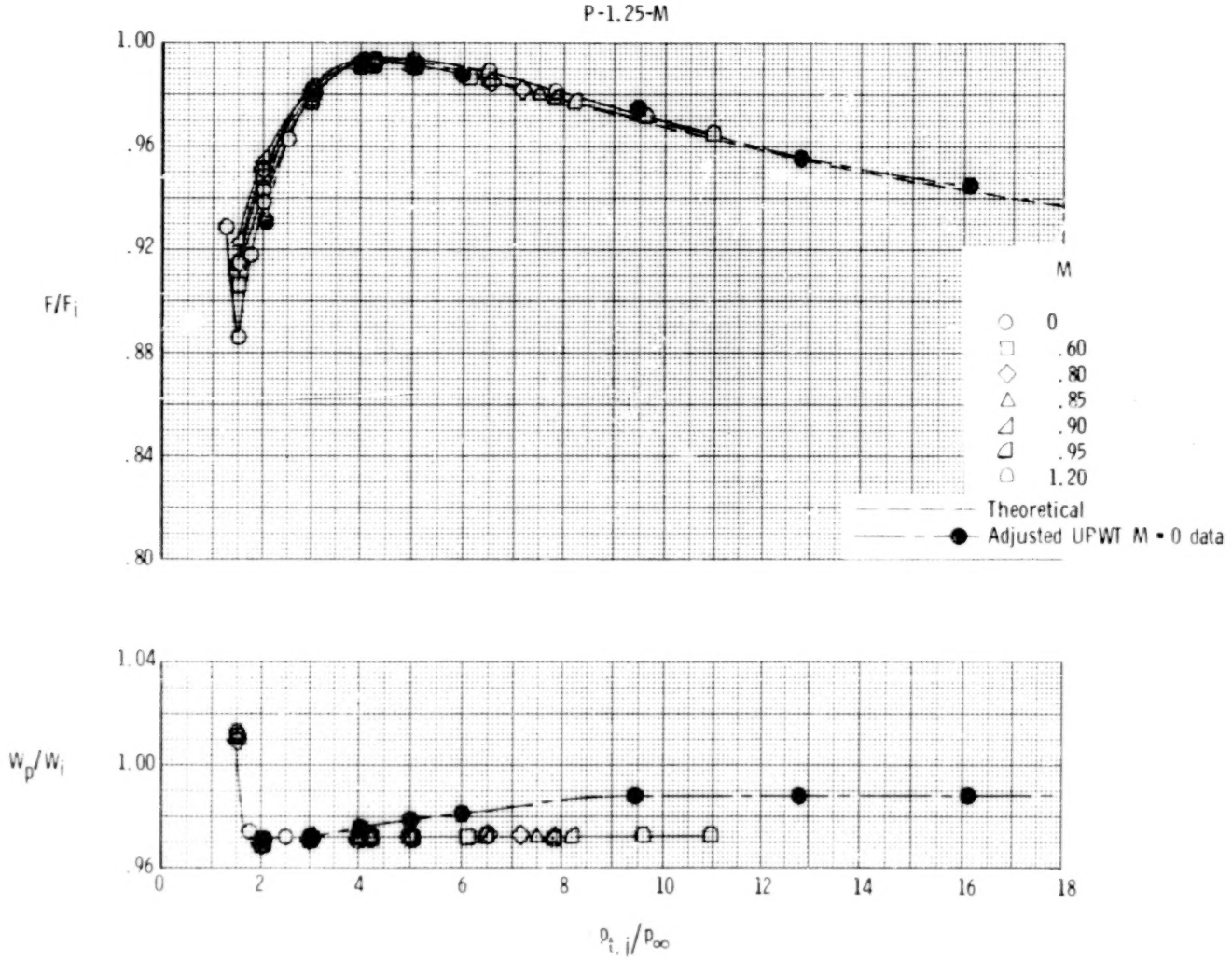

(b) Variation of thrust ratio and mass-flow ratio at subsonic and transonic speeds (16FTT).

Figure 11.- Continued.

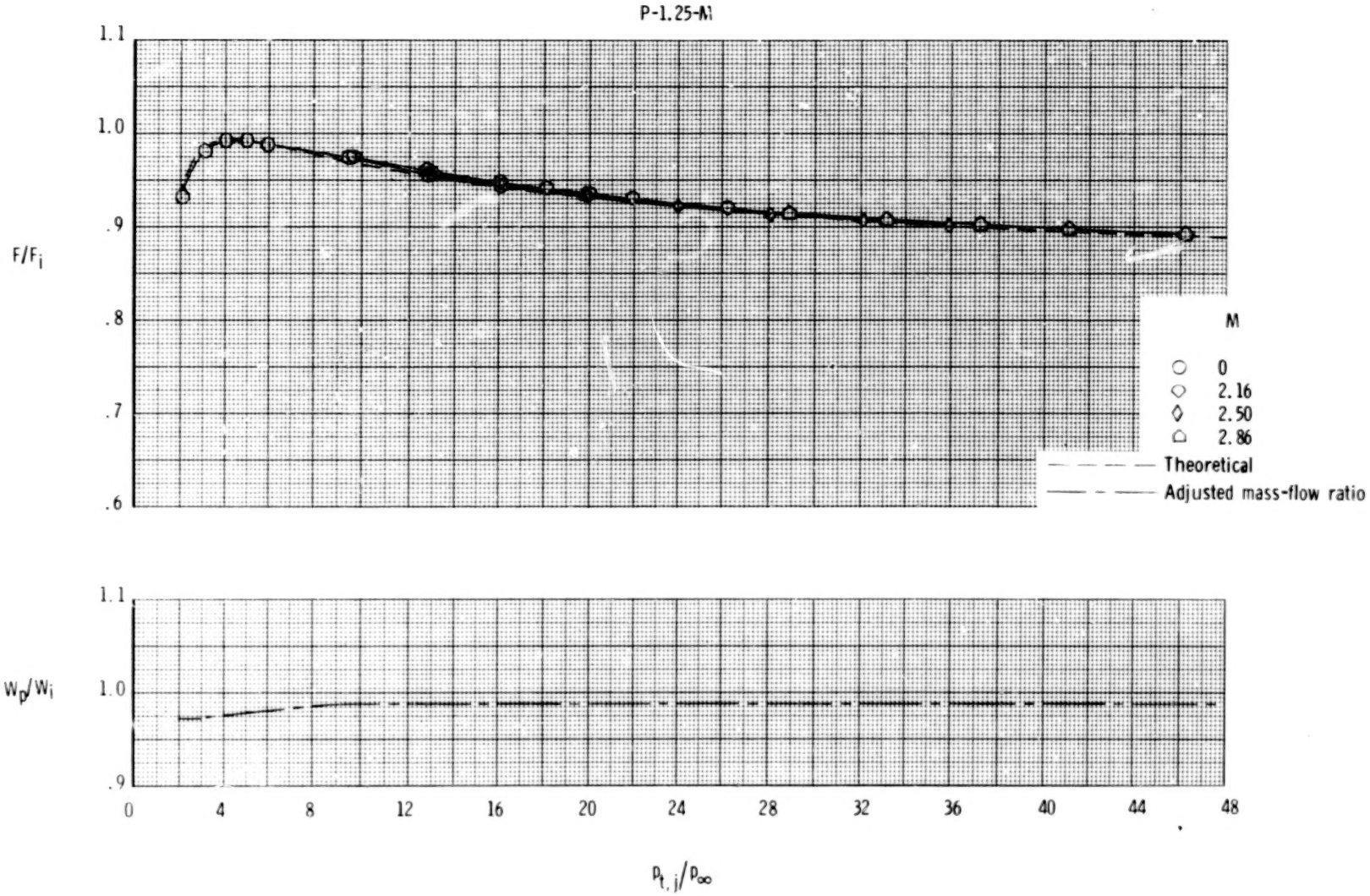

(c) Variation of thrust ratio and mass-flow ratio at supersonic speeds (UPWT).

Figure 11.- Continued.

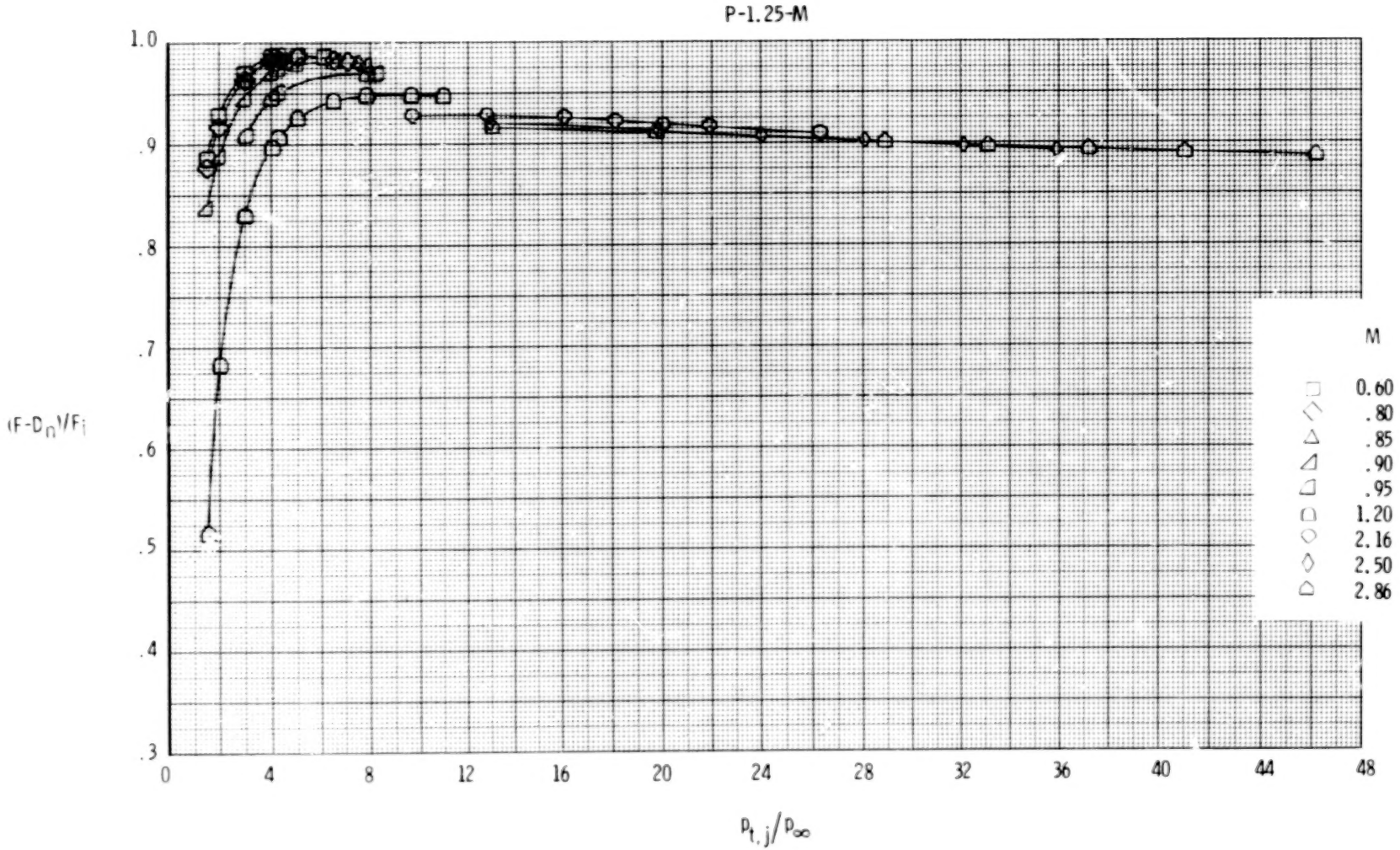

(d) Variation of thrust-minus-drag ratio.

Figure 11.- Concluded.

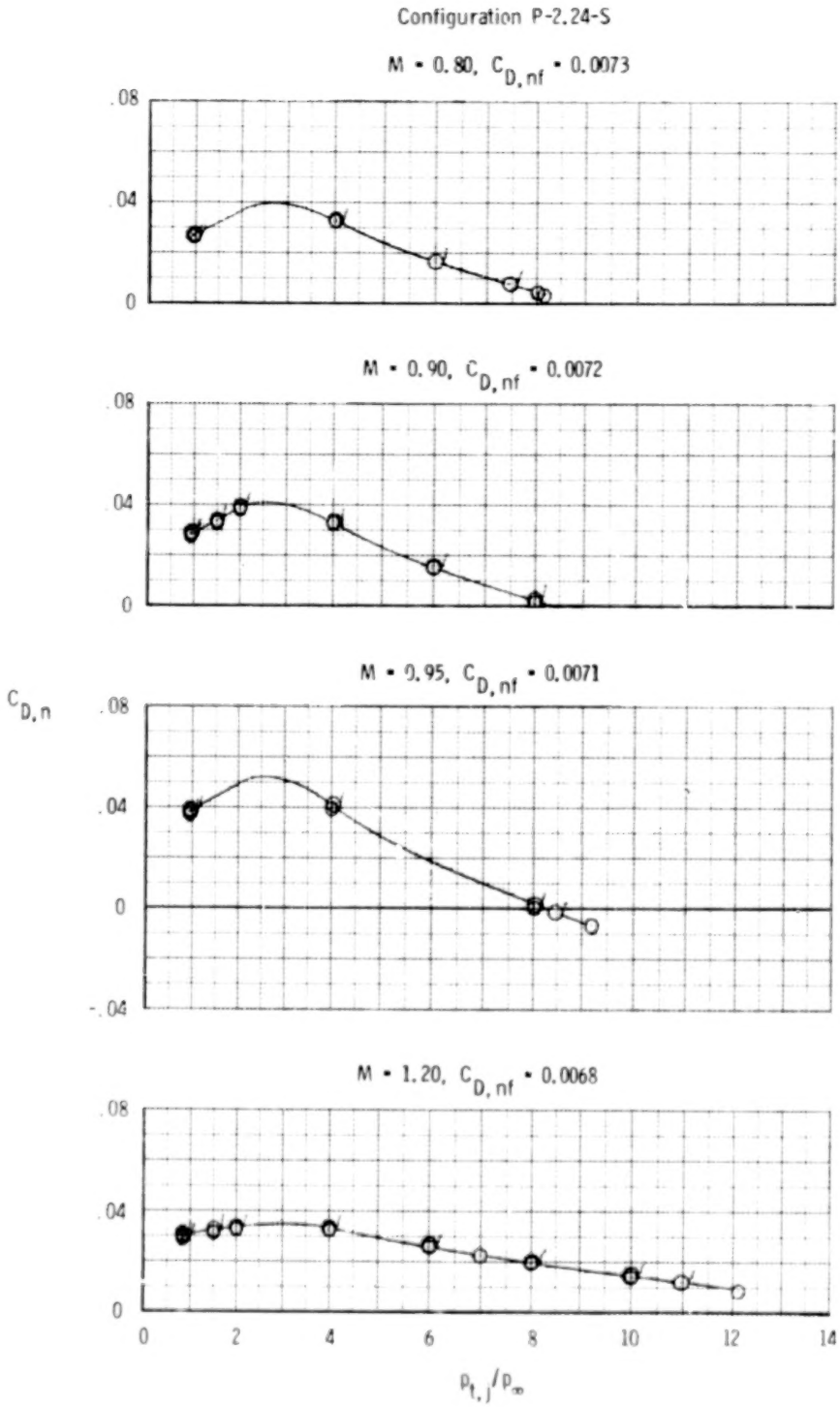

(a) Variation of nozzle drag coefficient.

Figure 12.- Variation of nozzle drag coefficient, thrust-minus-drag ratio, thrust ratio, and mass-flow ratio with nozzle pressure ratio for configuration P-2.24-S. Dashed line indicates theoretical values. Flagged symbols indicate data used to determine F/F_i.

BLANK PAGE

BLANK PAGE

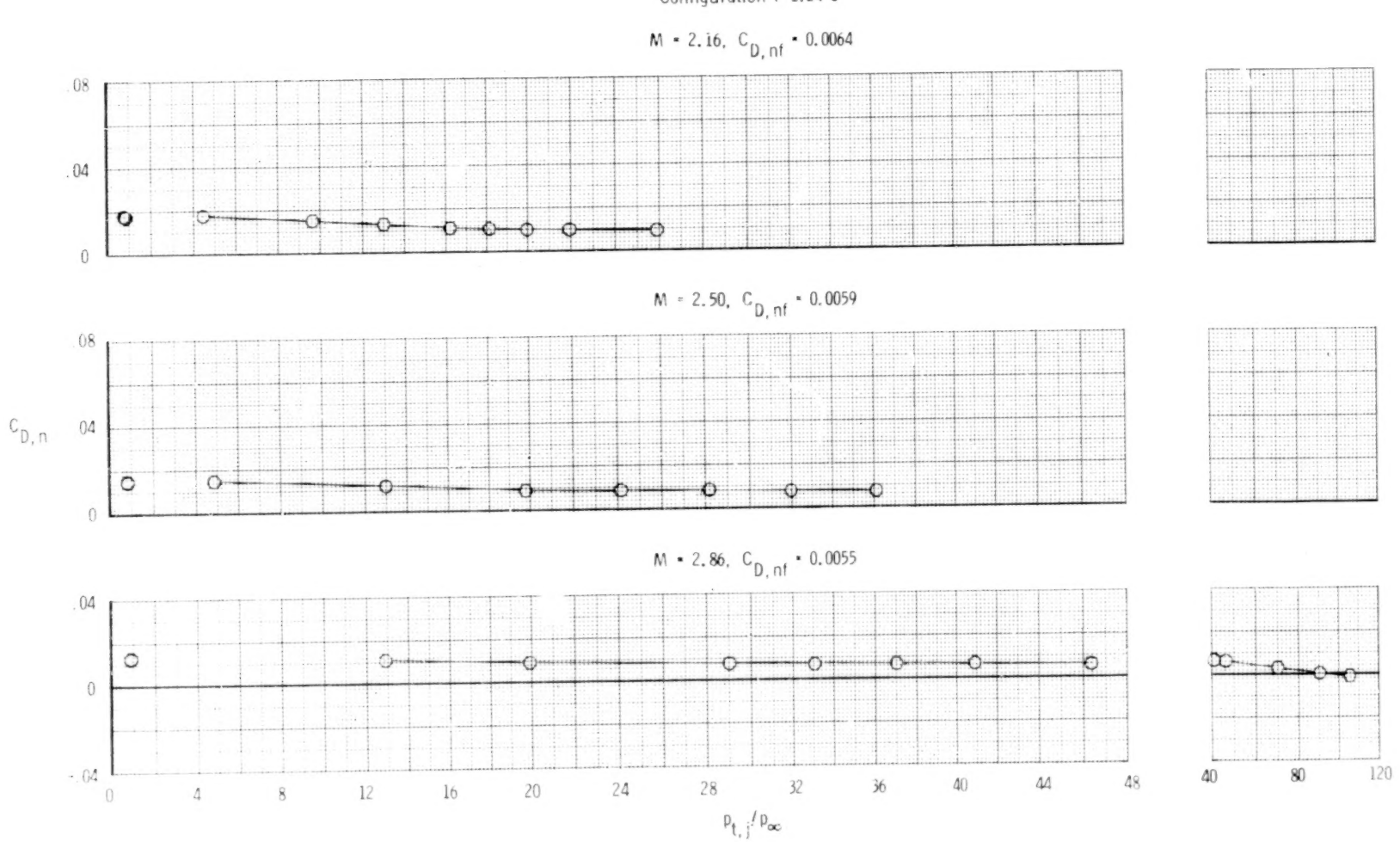

(a) Concluded.

Figure 12.- Continued.

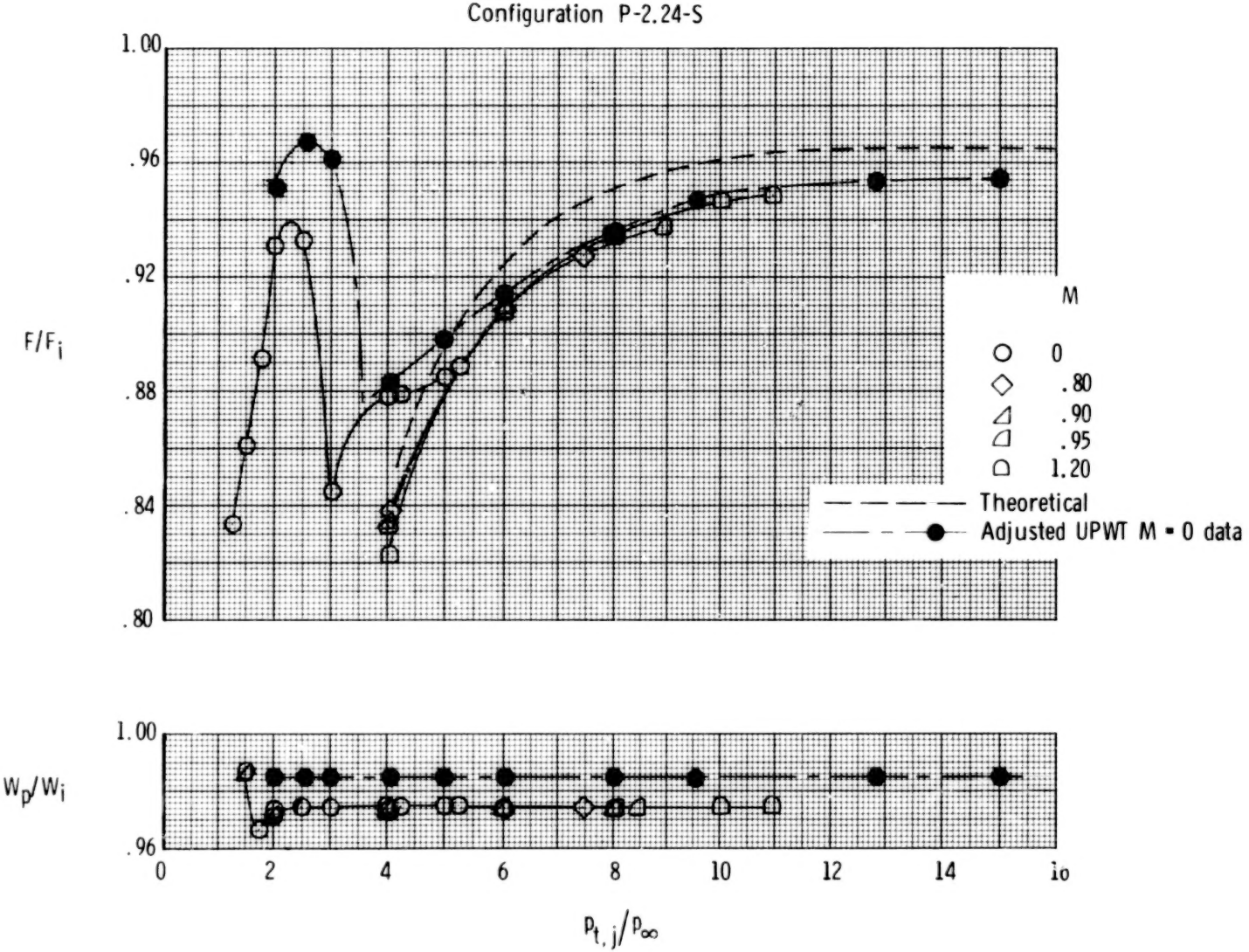

(b) Variation of thrust ratio and mass-flow ratio at subsonic and transonic speeds (16FTT).

Figure 12.- Continued.

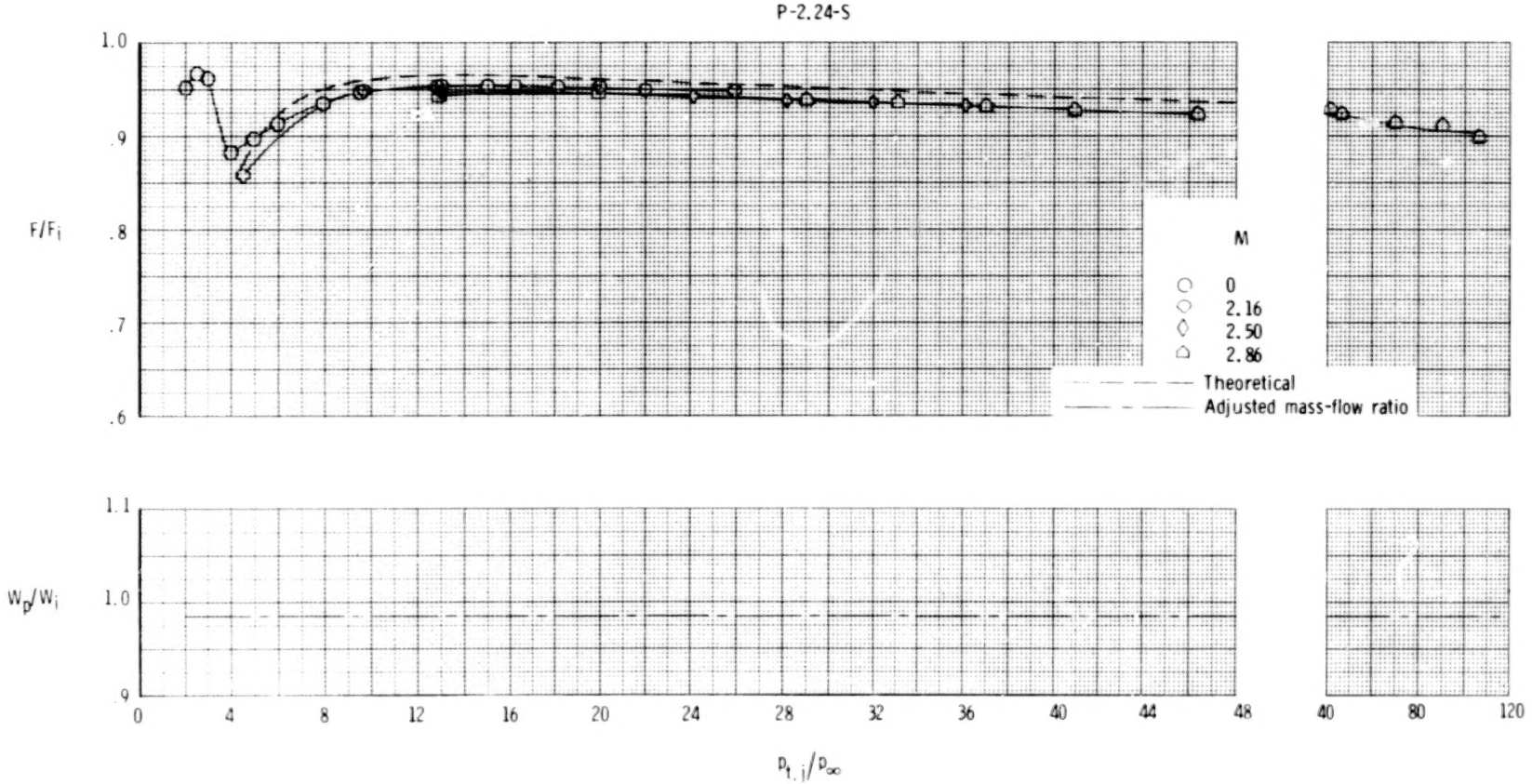

(c) Variation of thrust ratio and mass-flow ratio at supersonic speeds (UPWT).

Figure 12.- Continued.

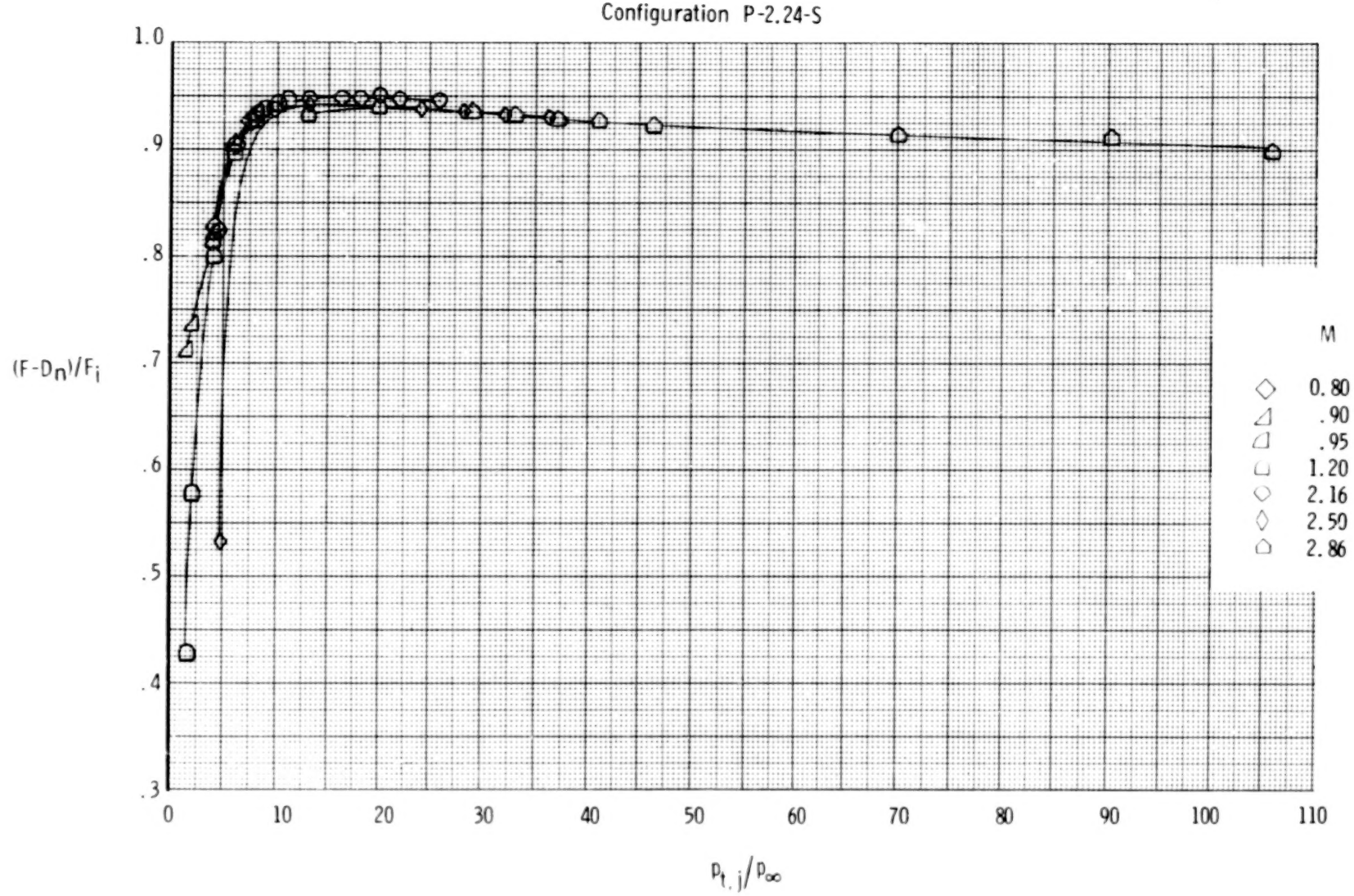

(d) Variation of thrust-minus-drag ratio.

Figure 12.- Concluded.

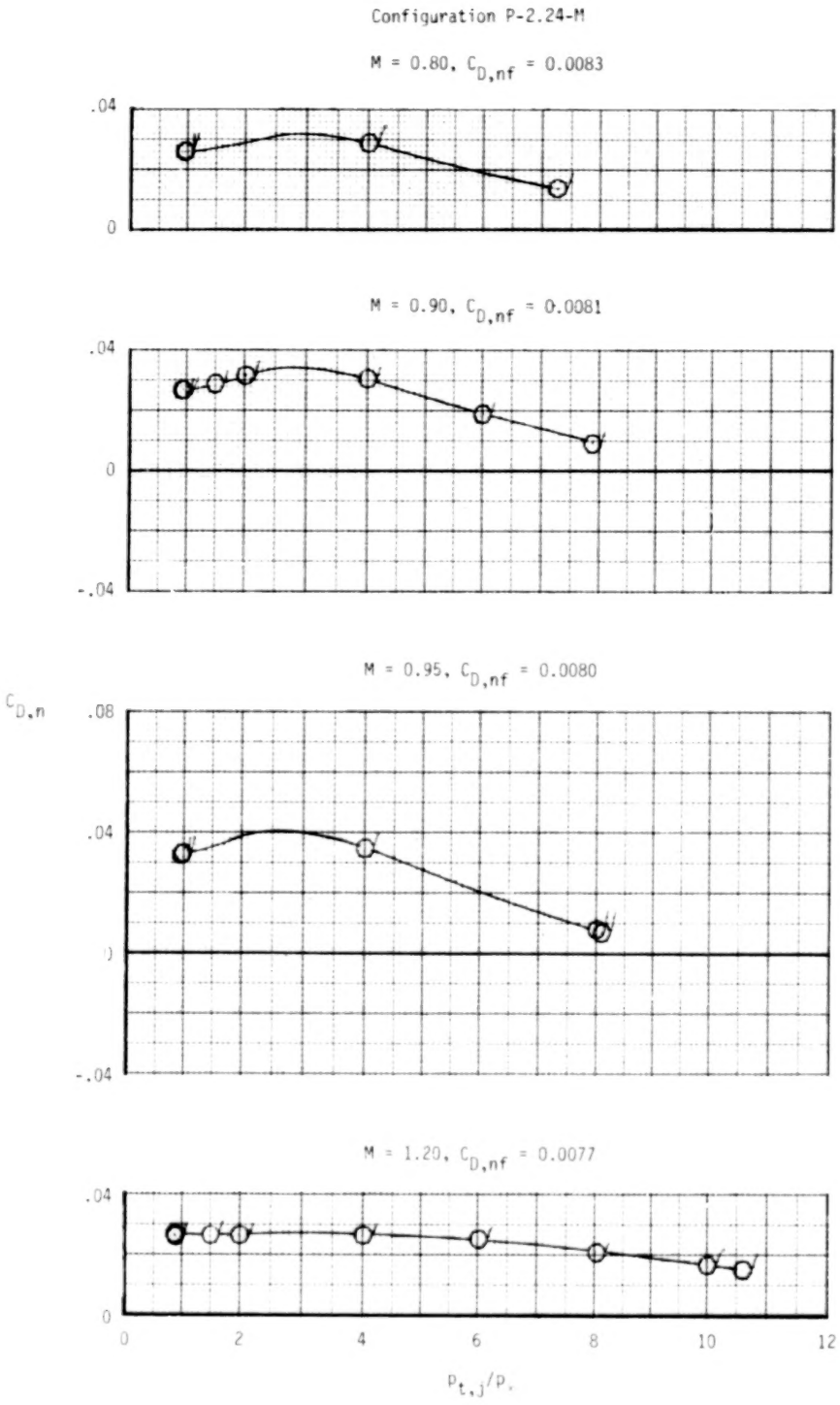

(a) Variation of nozzle drag coefficient.

Figure 13.- Variation of nozzle drag coefficient, thrust-minus-drag ratio, thrust ratio, and mass-flow ratio with nozzle pressure ratio for configuration P-2.24-M. Dashed line indicates theoretical values. Flagged symbols indicate data used to determine F/F_i.

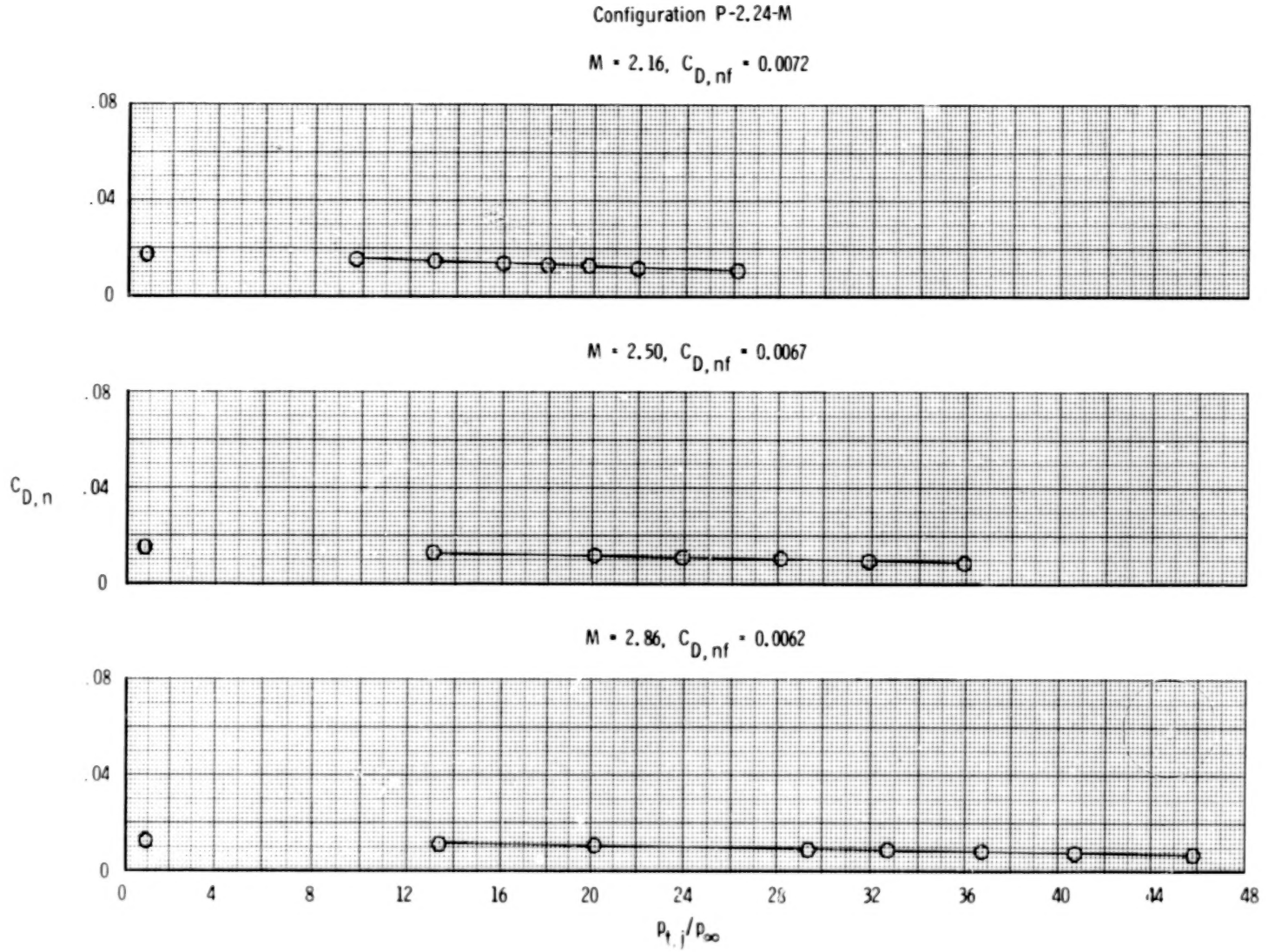

(a) Concluded.

Figure 13.- Continued.

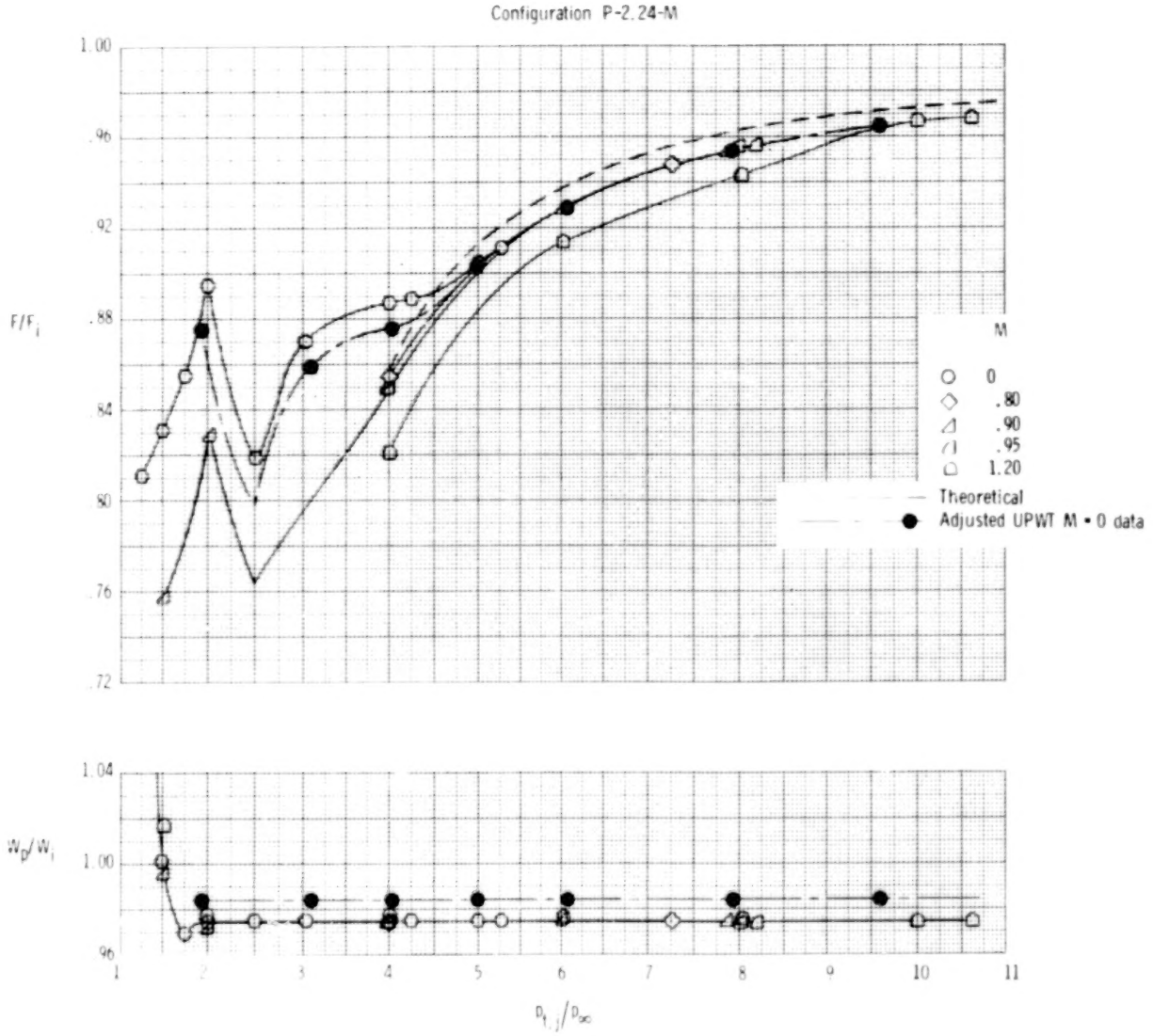

(b) Variation of thrust ratio and mass-flow ratio at subsonic and transonic speeds (16FTT).

Figure 13.- Continued.

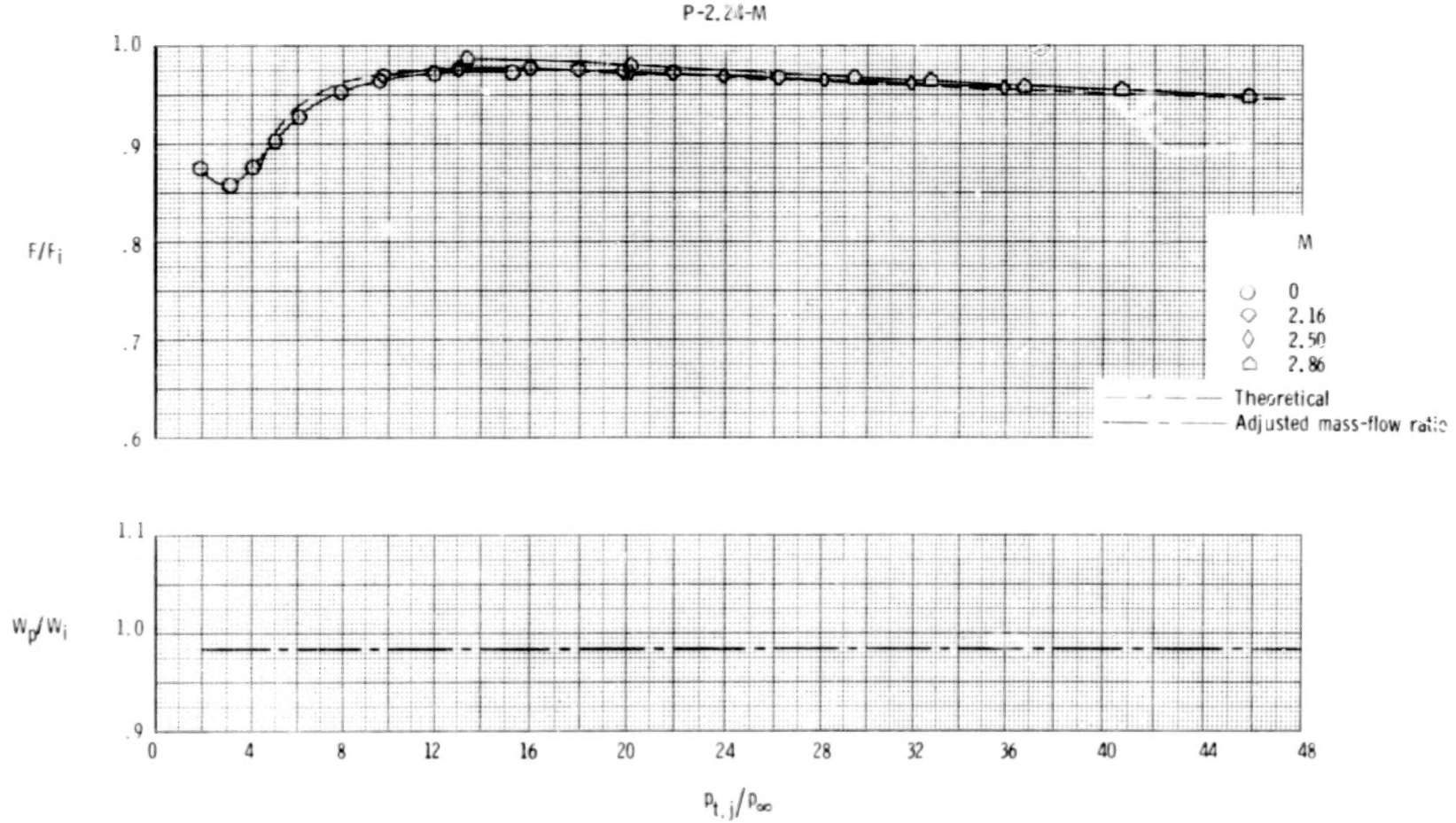

(c) Variation of thrust ratio and mass-flow ratio at supersonic speeds (UPWT).

Figure 13.- Continued.

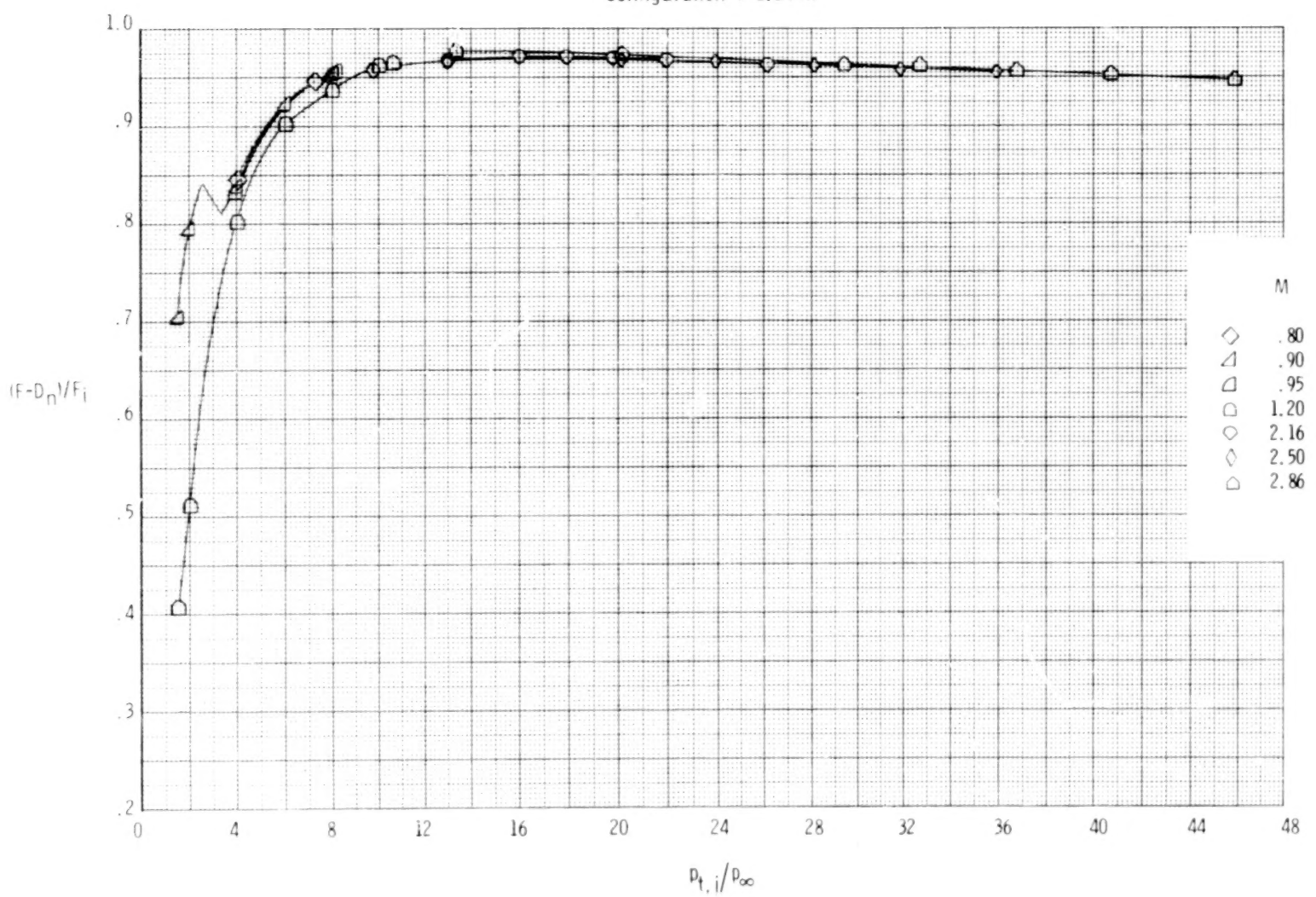

(d) Variation of thrust-minus-drag ratio.

Figure 13.- Concluded.

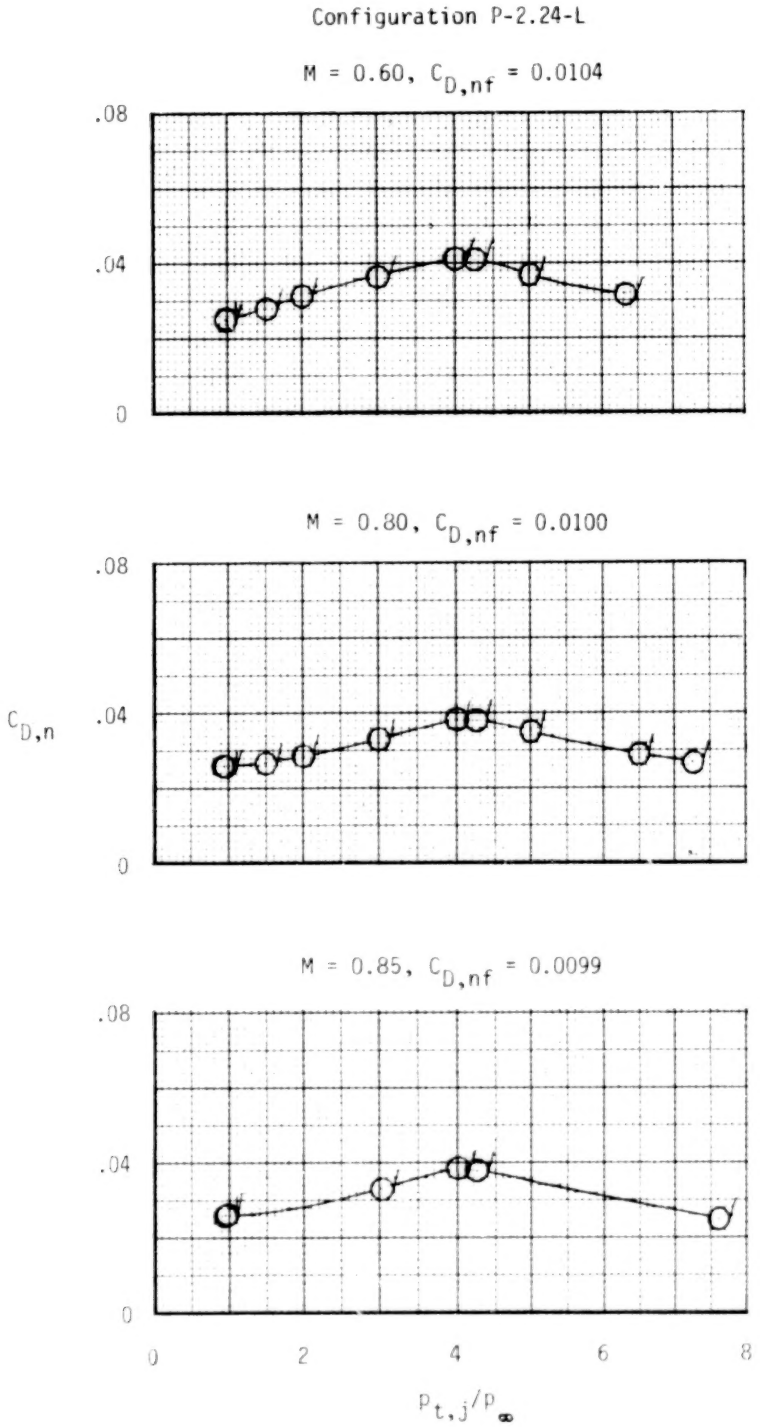

(a) Variation of nozzle drag coefficient.

Figure 14.- Variation of nozzle drag coefficient, thrust-minus-drag ratio, thrust ratio, and mass-flow ratio with nozzle pressure ratio for configuration P-2.24-L. Dashed line indicates theoretical values. Flagged symbols indicate data used to determine F/F_i.

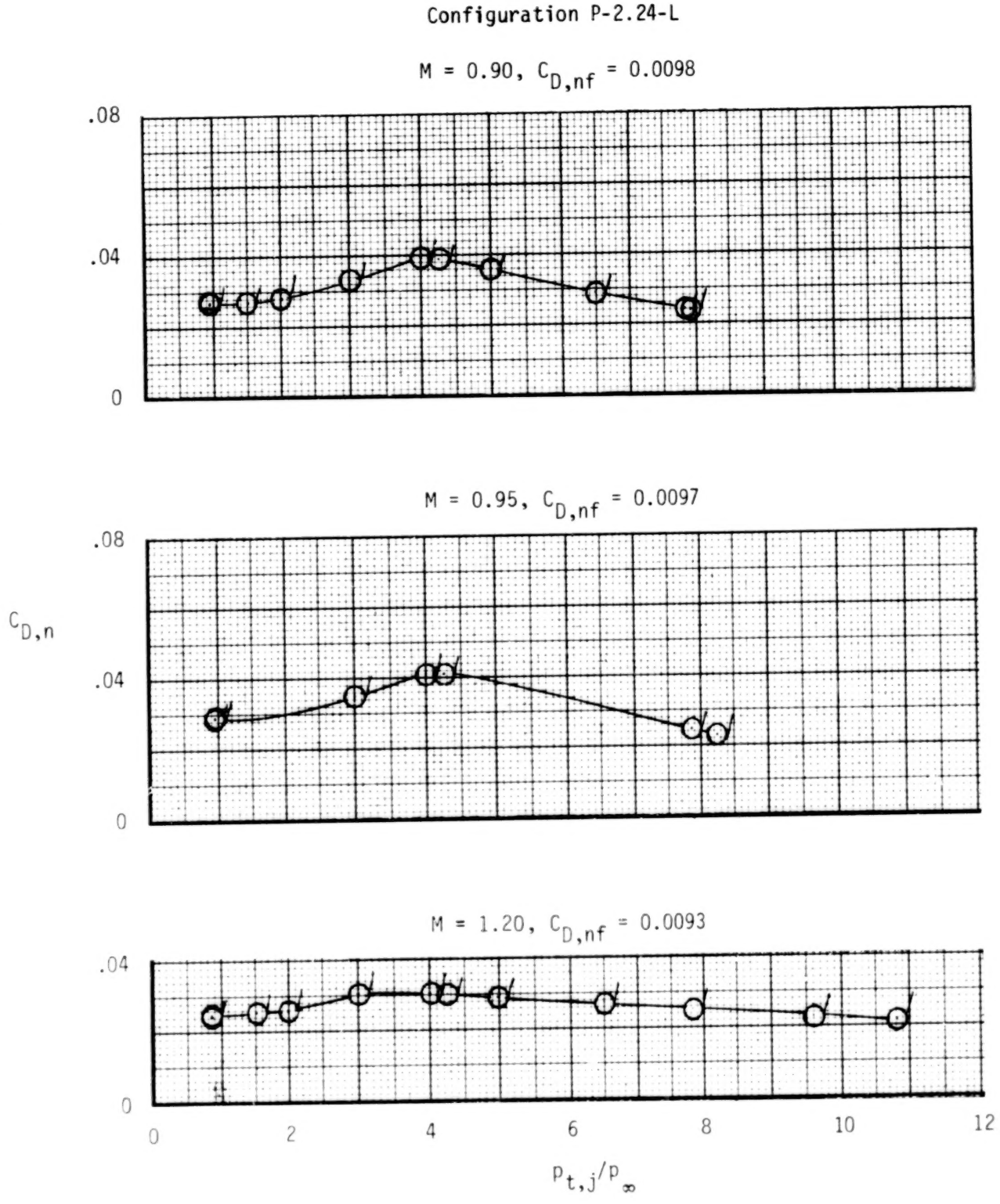

(a) Continued.

Figure 14.- Continued.

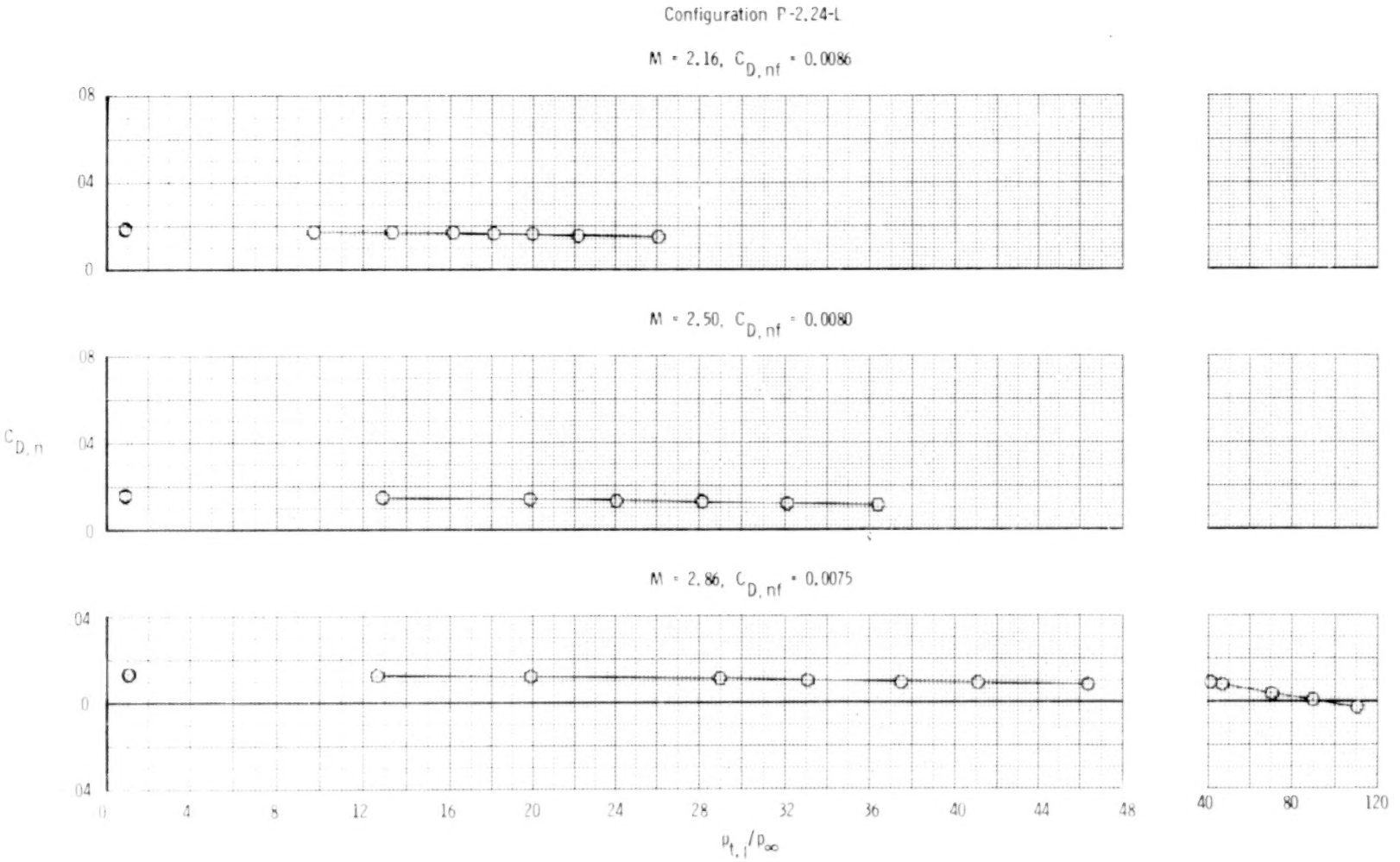

(a) Concluded.

Figure 14.- Continued.

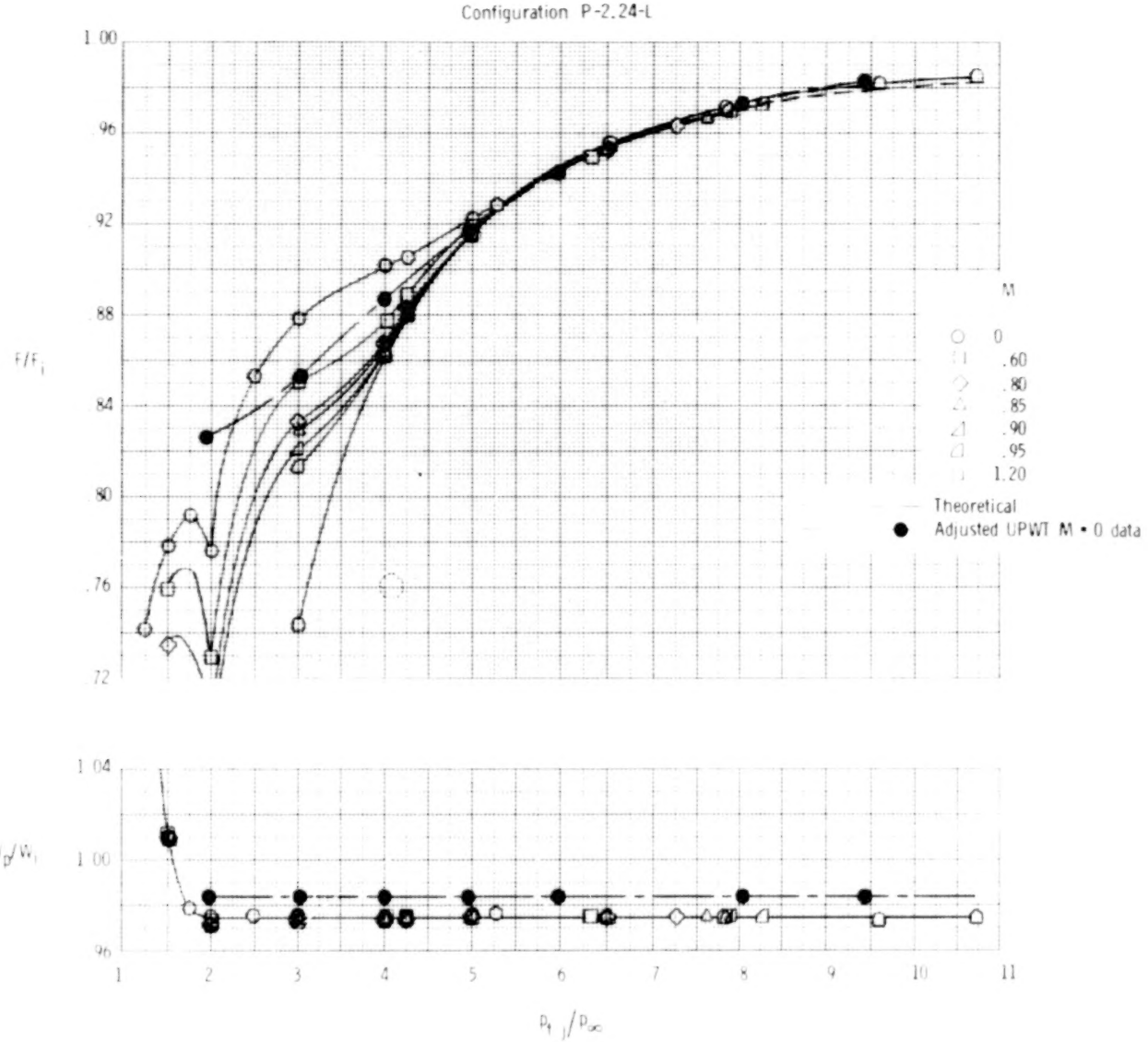

(b) Variation of thrust ratio and mass-flow ratio at subsonic and transonic speeds (16FTT).

Figure 14.- Continued.

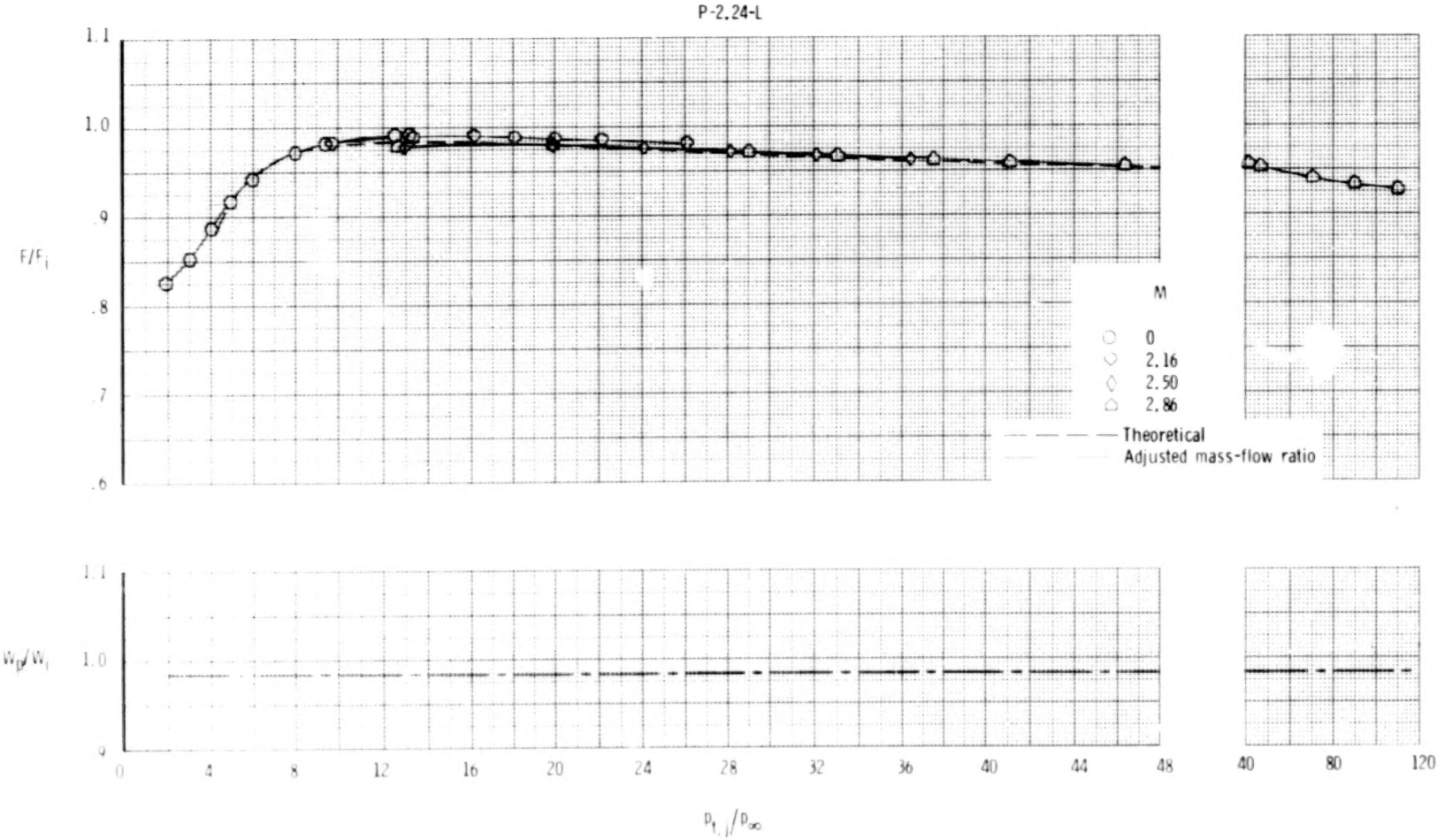

(c) Variation of thrust ratio and mass-flow ratio at supersonic speeds (UPWT).

Figure 14.- Continued.

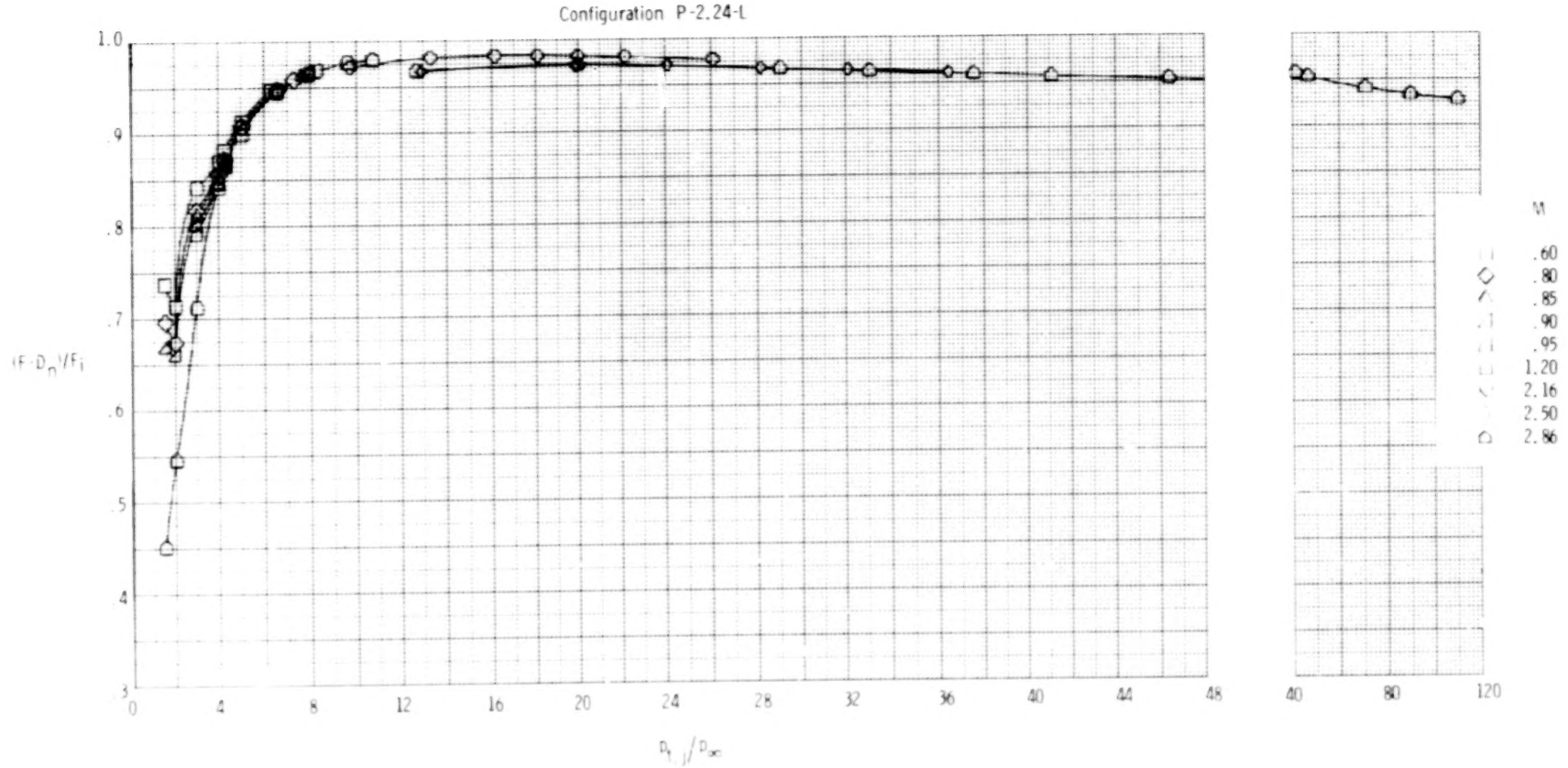

(d) Variation of thrust-minus-drag ratio.

Figure 14.- Concluded.

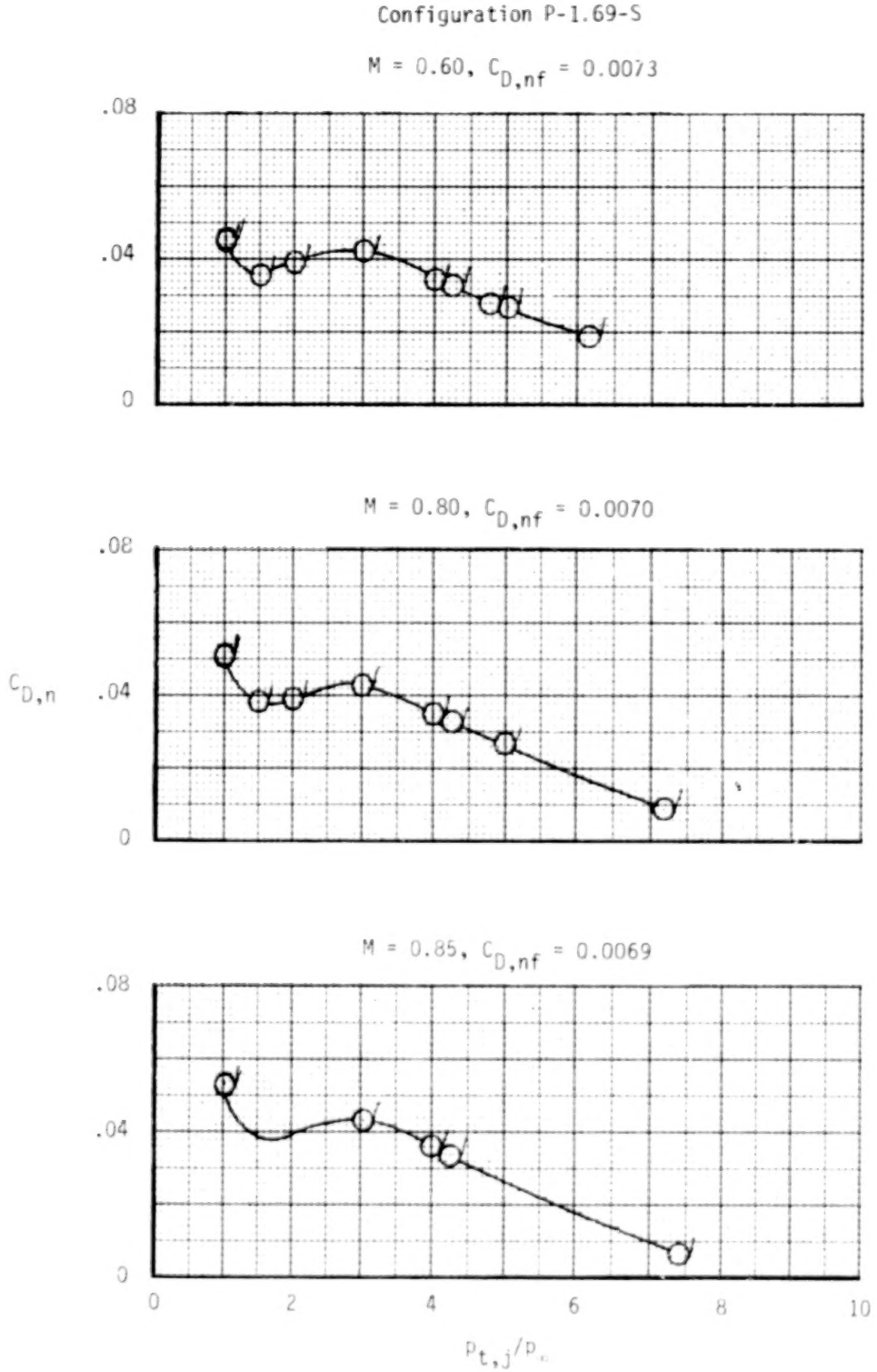

(a) Variation of nozzle drag coefficient.

Figure 15.- Variation of nozzle drag coefficient, thrust-minus-drag ratio, thrust ratio, and mass-flow ratio with nozzle pressure ratio for configuration P-1.69-S. Dashed line indicates theoretical values. Flagged symbols indicate data used to determine F/F_i.

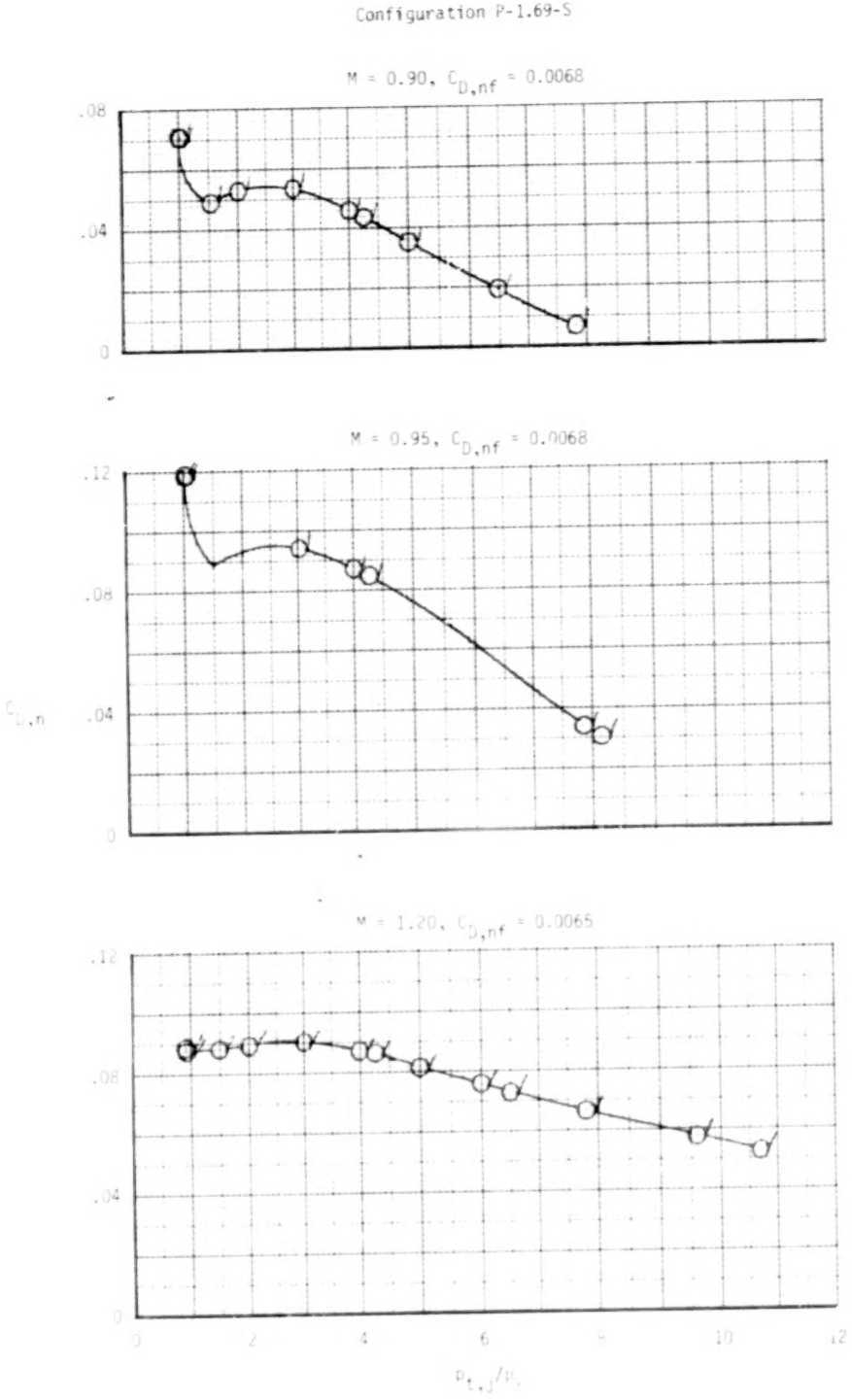

(a) Continued.

Figure 15.- Continued.

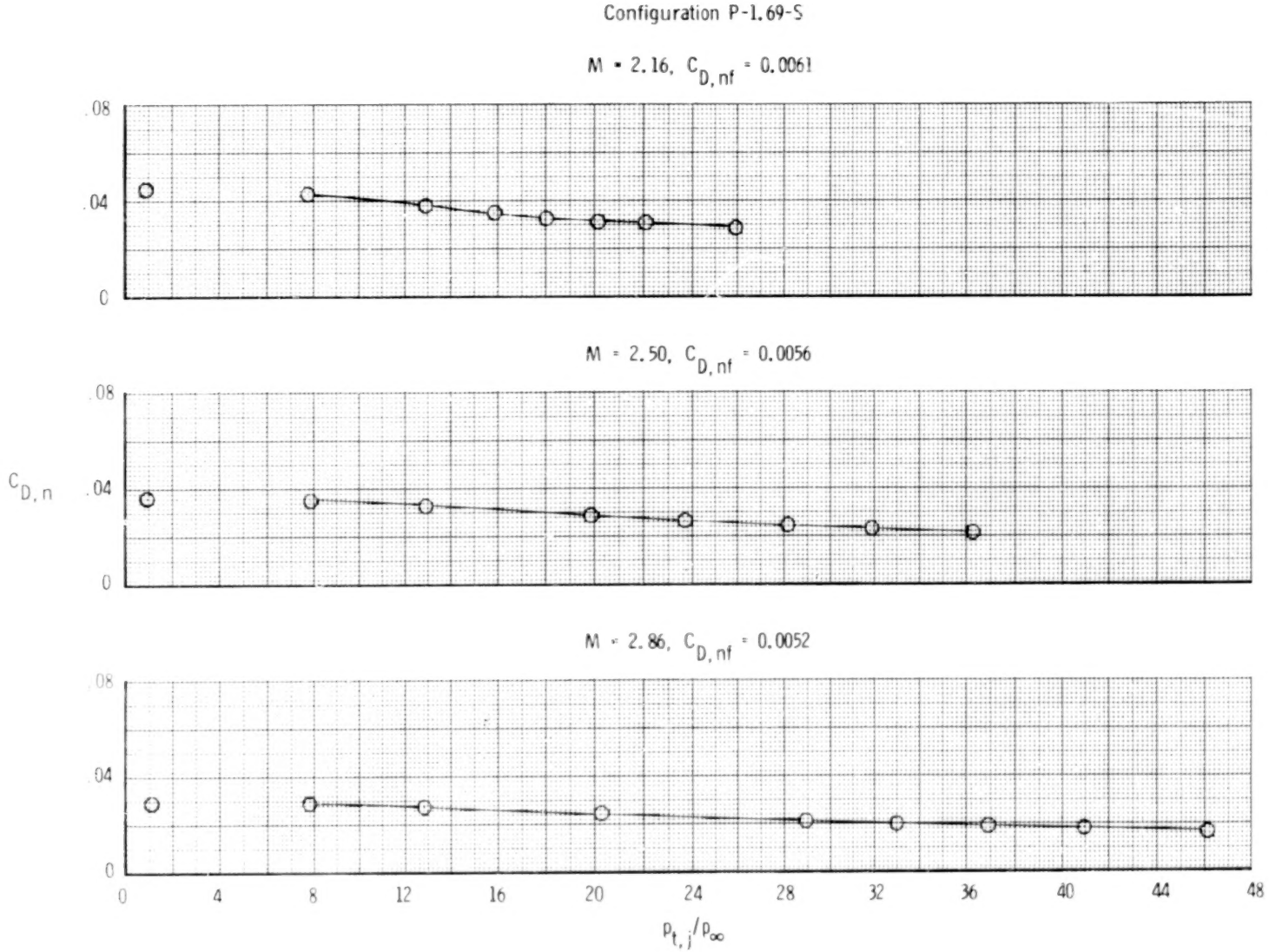

(a) Concluded.

Figure 15.- Continued.

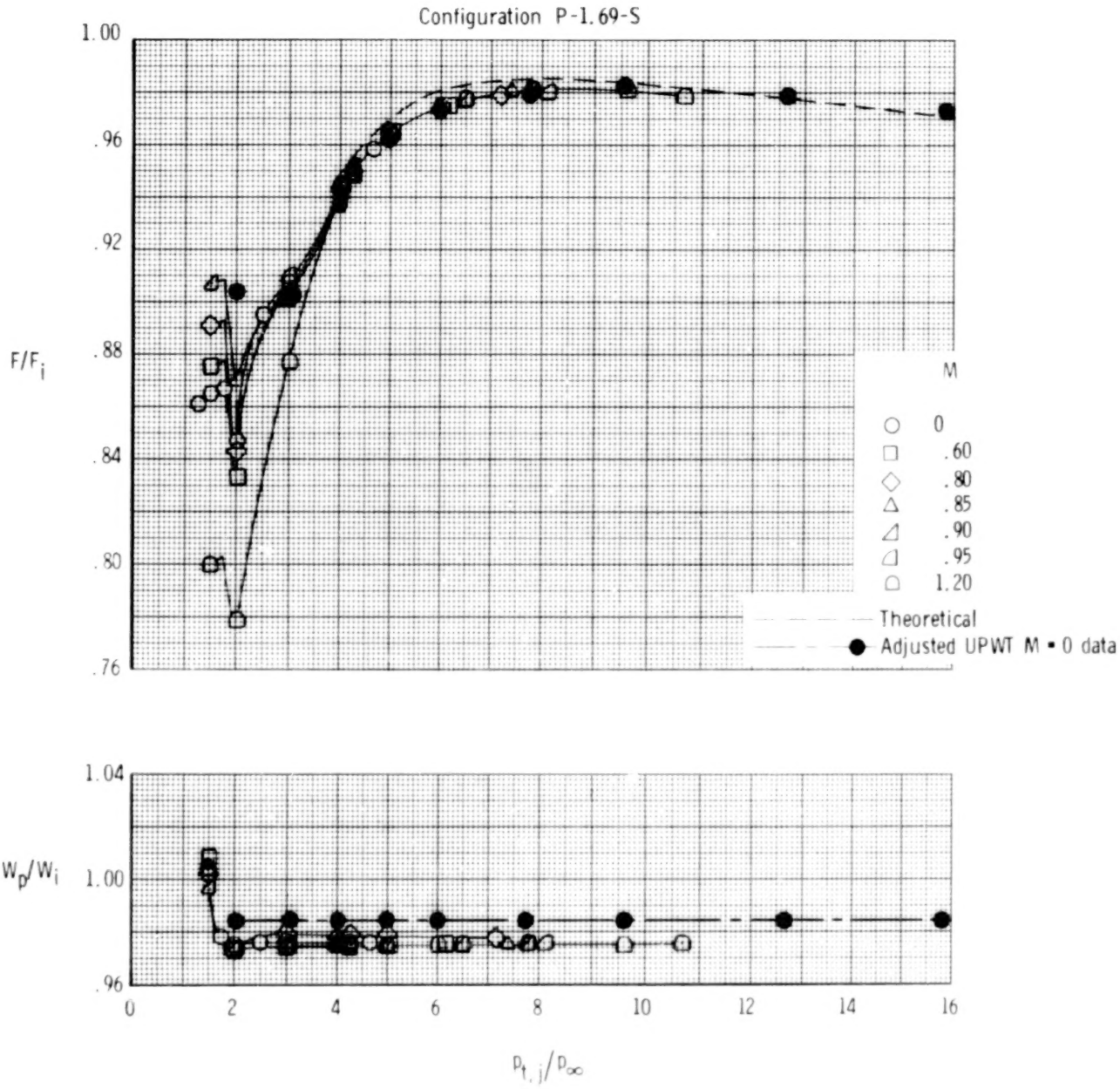

(b) Variation of thrust ratio and mass-flow ratio at subsonic and transonic speeds (16FTT).

Figure 15.- Continued.

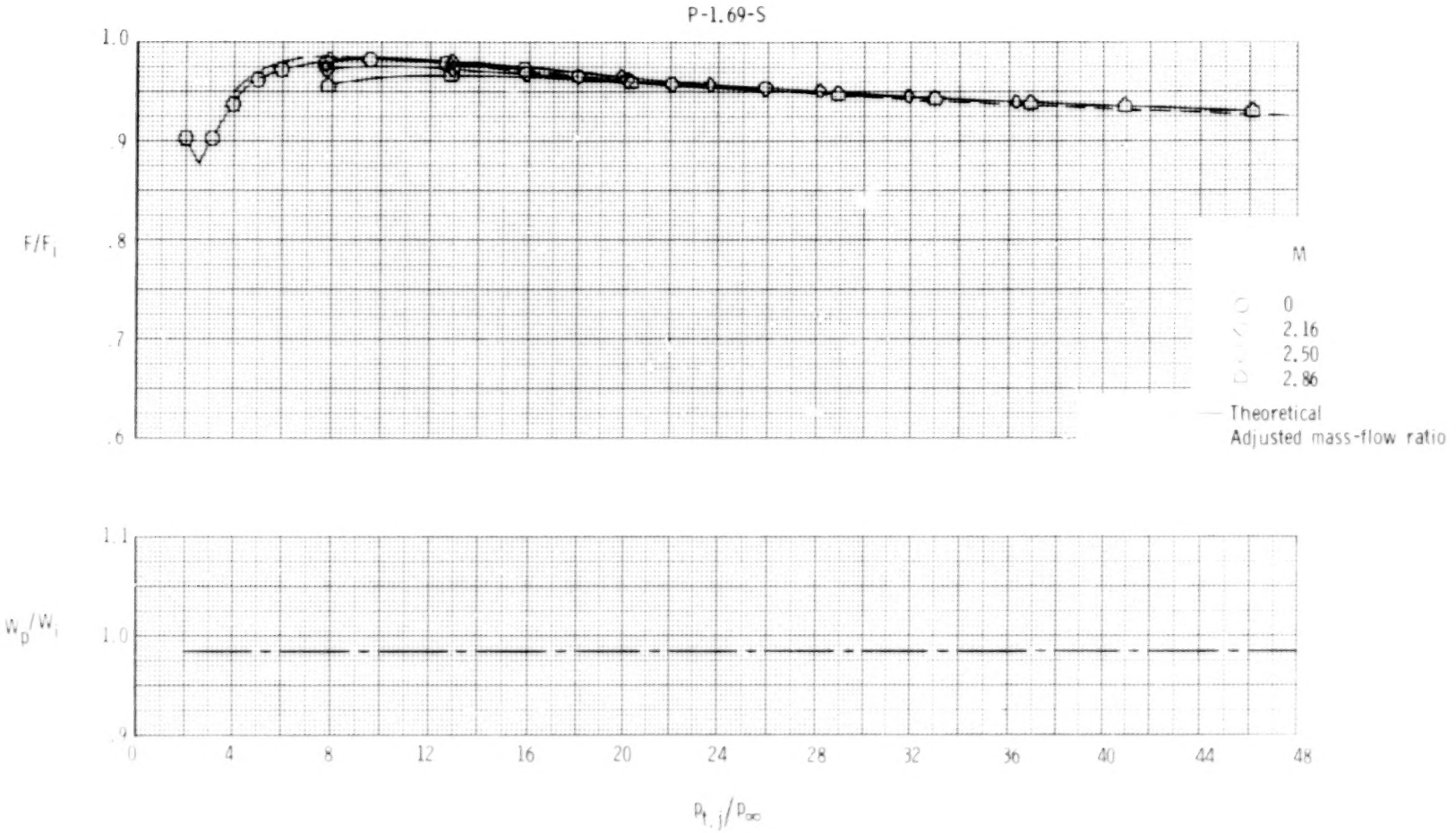

(c) Variation of thrust ratio and mass-flow ratio at supersonic speeds (UPWT).

Figure 15.- Continued.

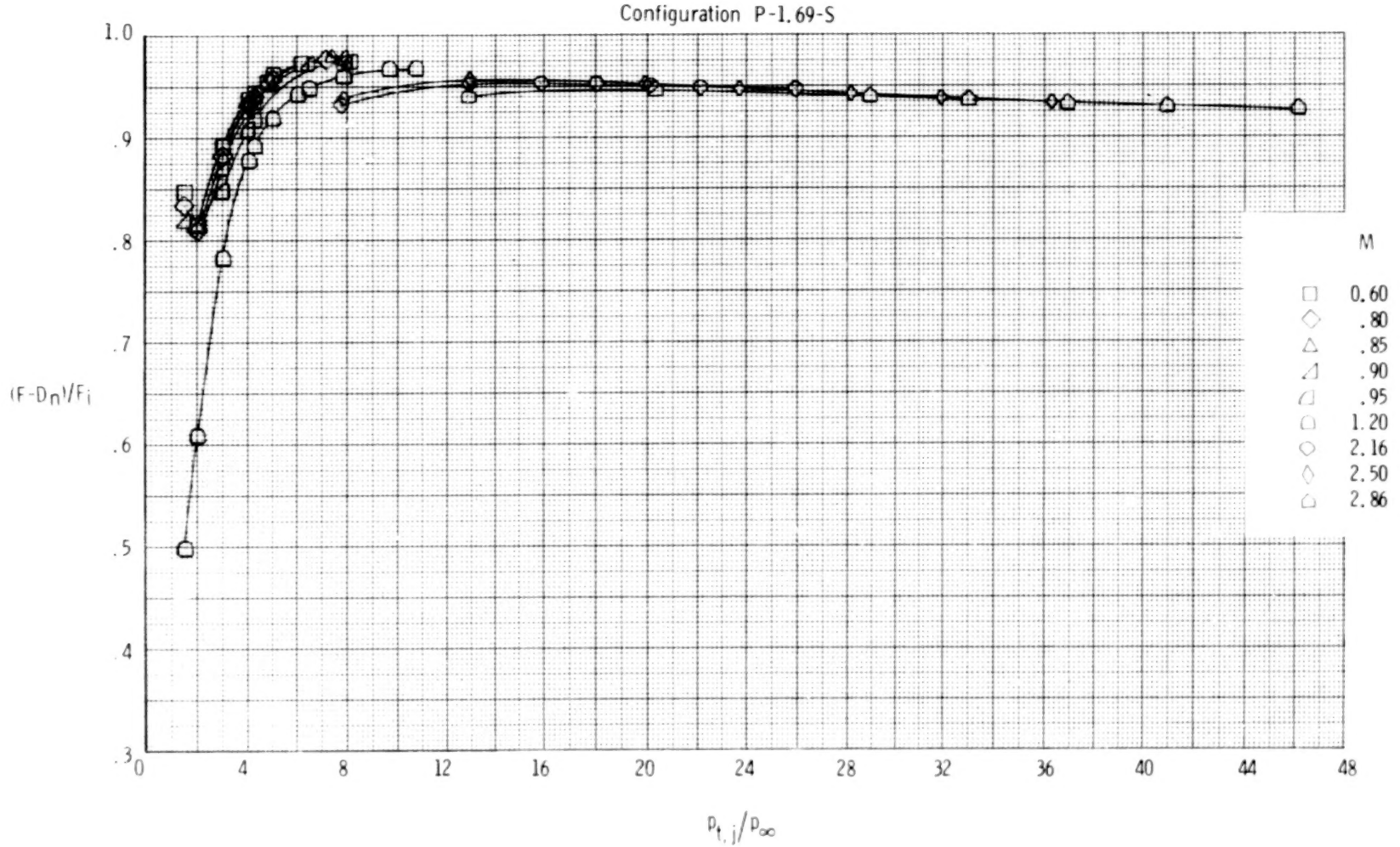

(d) Variation of thrust-minus-drag ratio.

Figure 15.- Concluded.

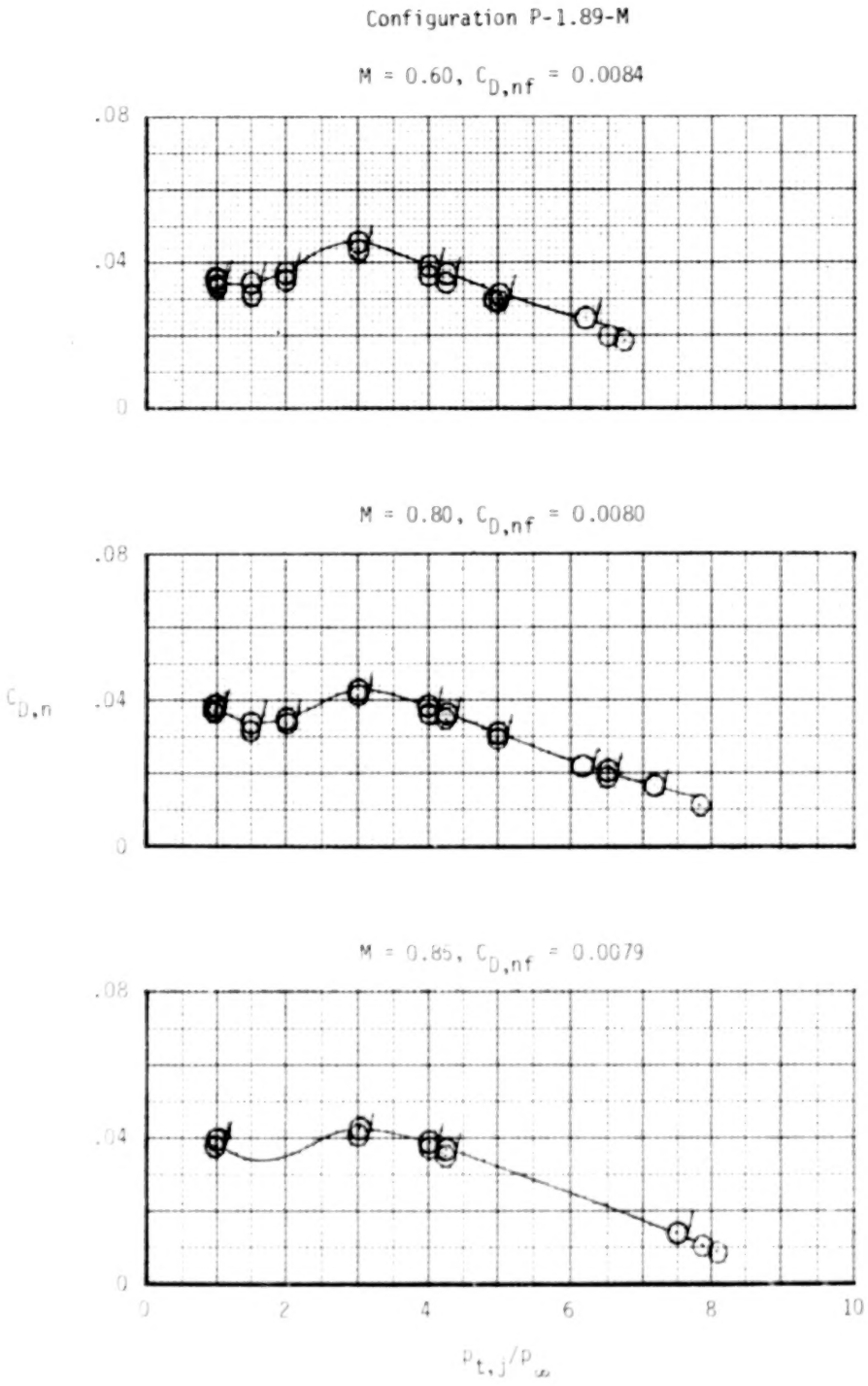

(a) Variation of nozzle drag coefficient.

Figure 16.- Variation of nozzle drag coefficient, thrust-minus-drag ratio, thrust ratio, and mass-flow ratio with nozzle pressure ratio for configuration P-1.89-M. Dashed line indicates theoretical values. Flagged symbols indicate data used to determine F/F_i.

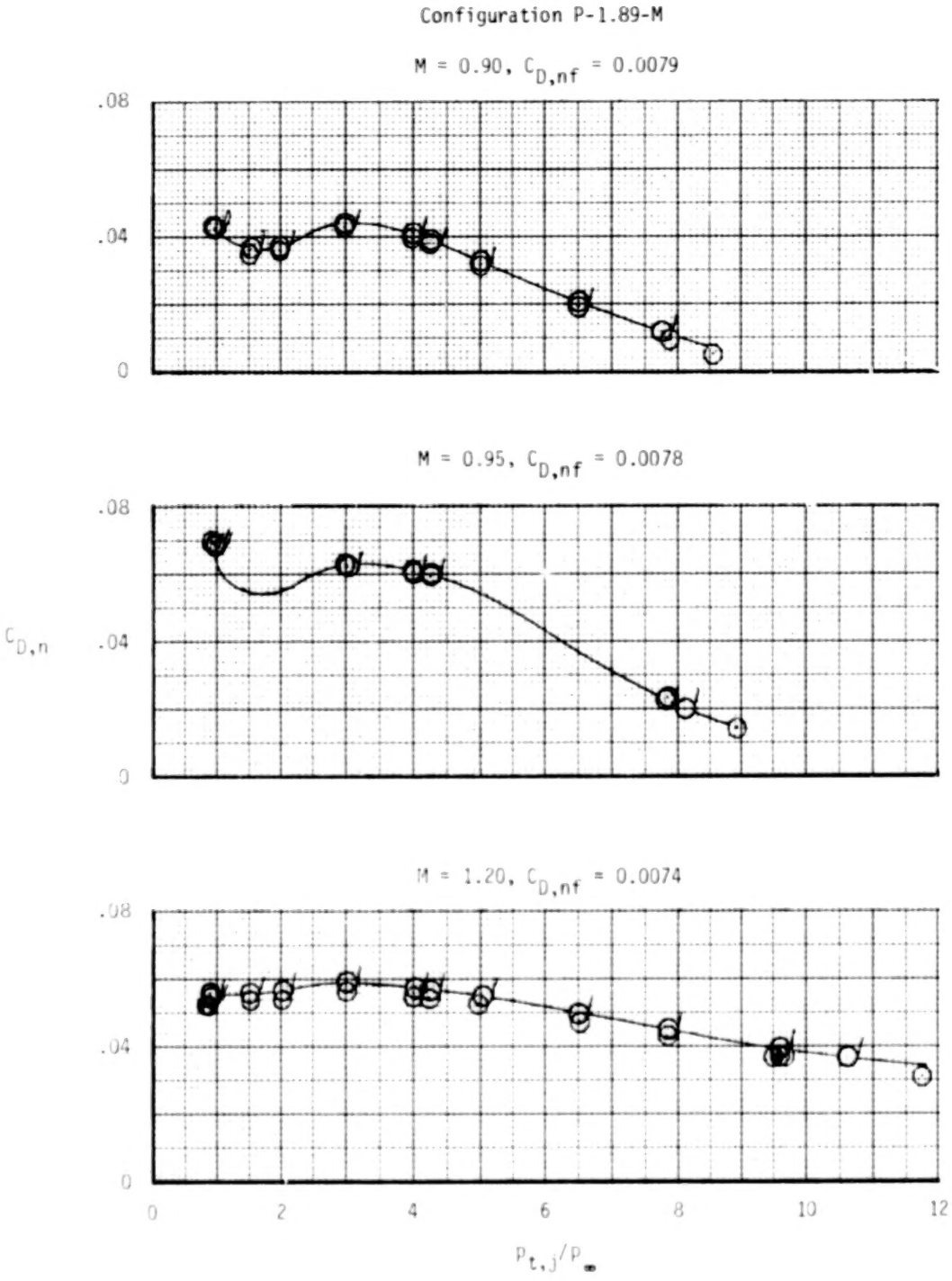

(a) Continued.

Figure 16.- Continued.

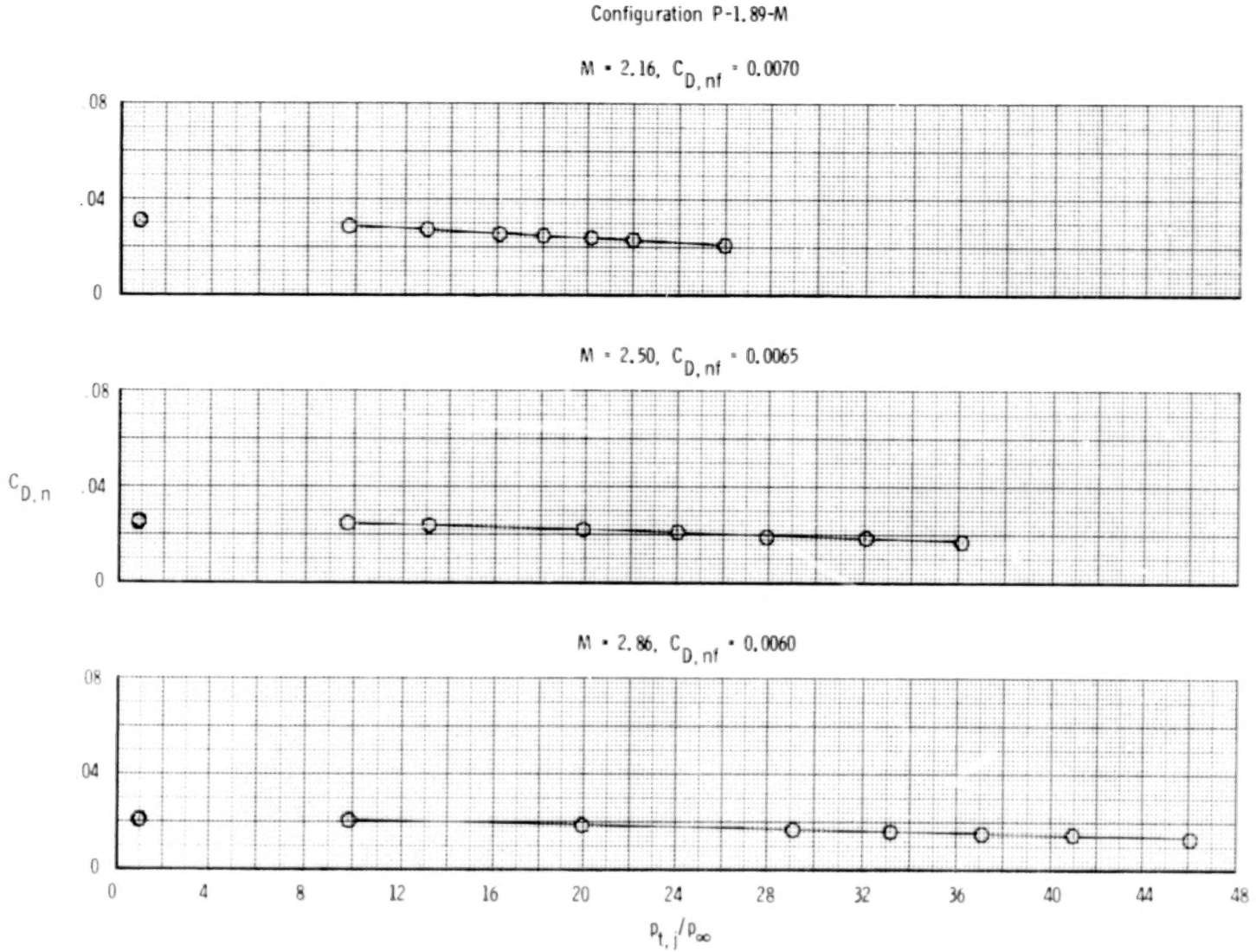

(a) Concluded.

Figure 16.- Continued.

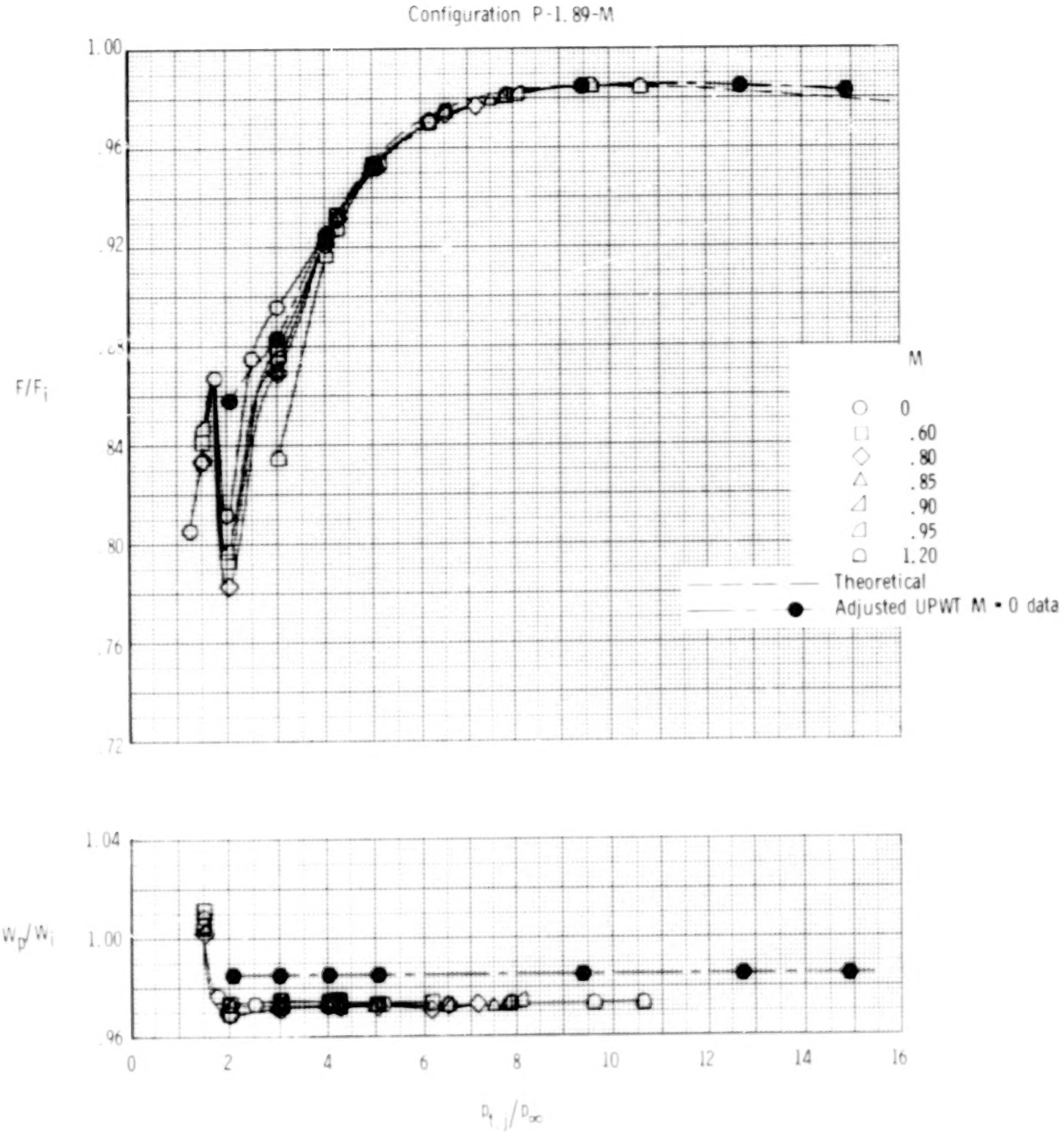

(b) Variation of thrust ratio and mass-flow ratio at subsonic and transonic speeds (16FTT).

Figure 16.- Continued.

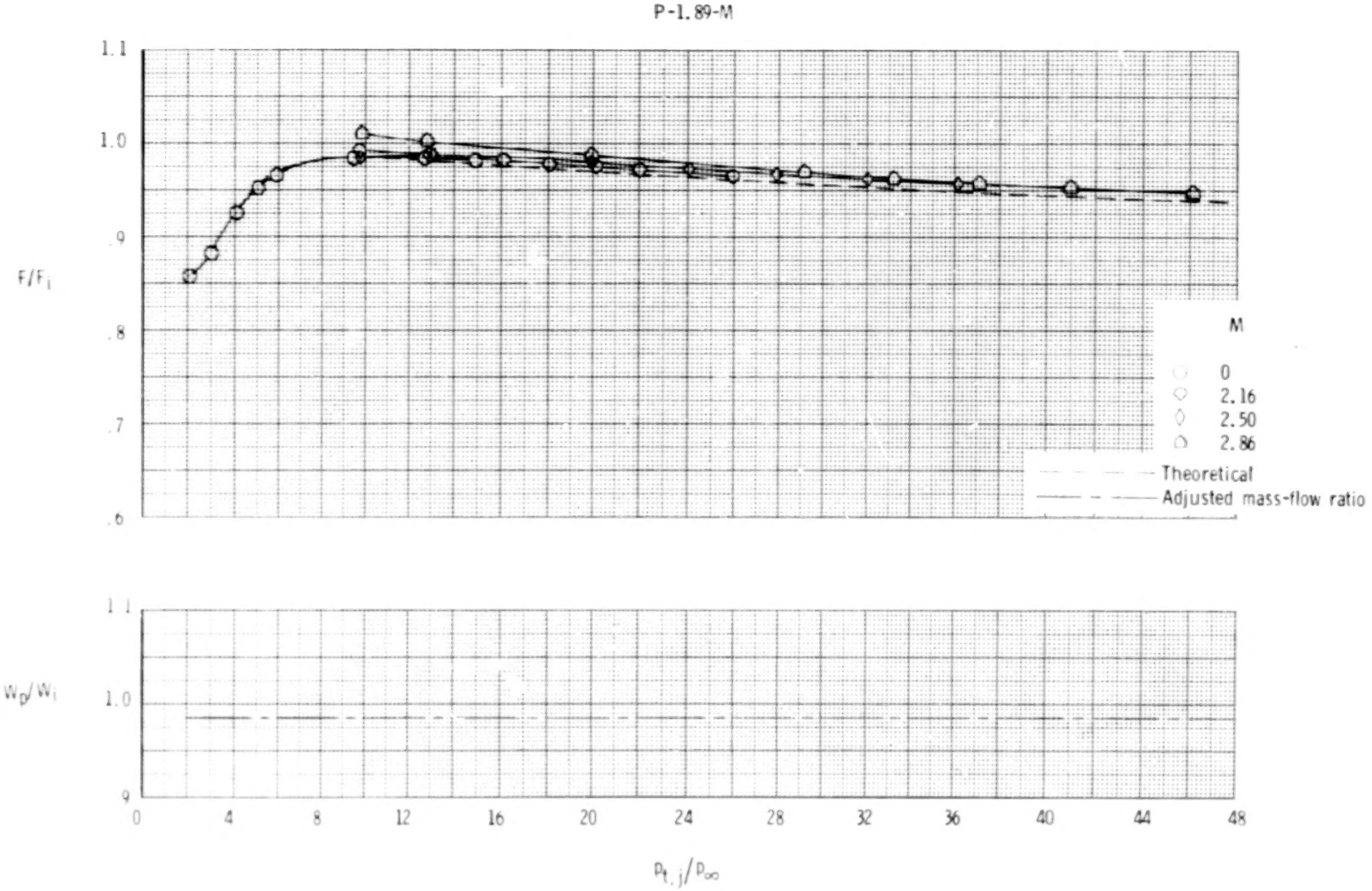

(c) Variation of thrust ratio and mass-flow ratio at supersonic speeds (UPWT).

Figure 16.- Continued.

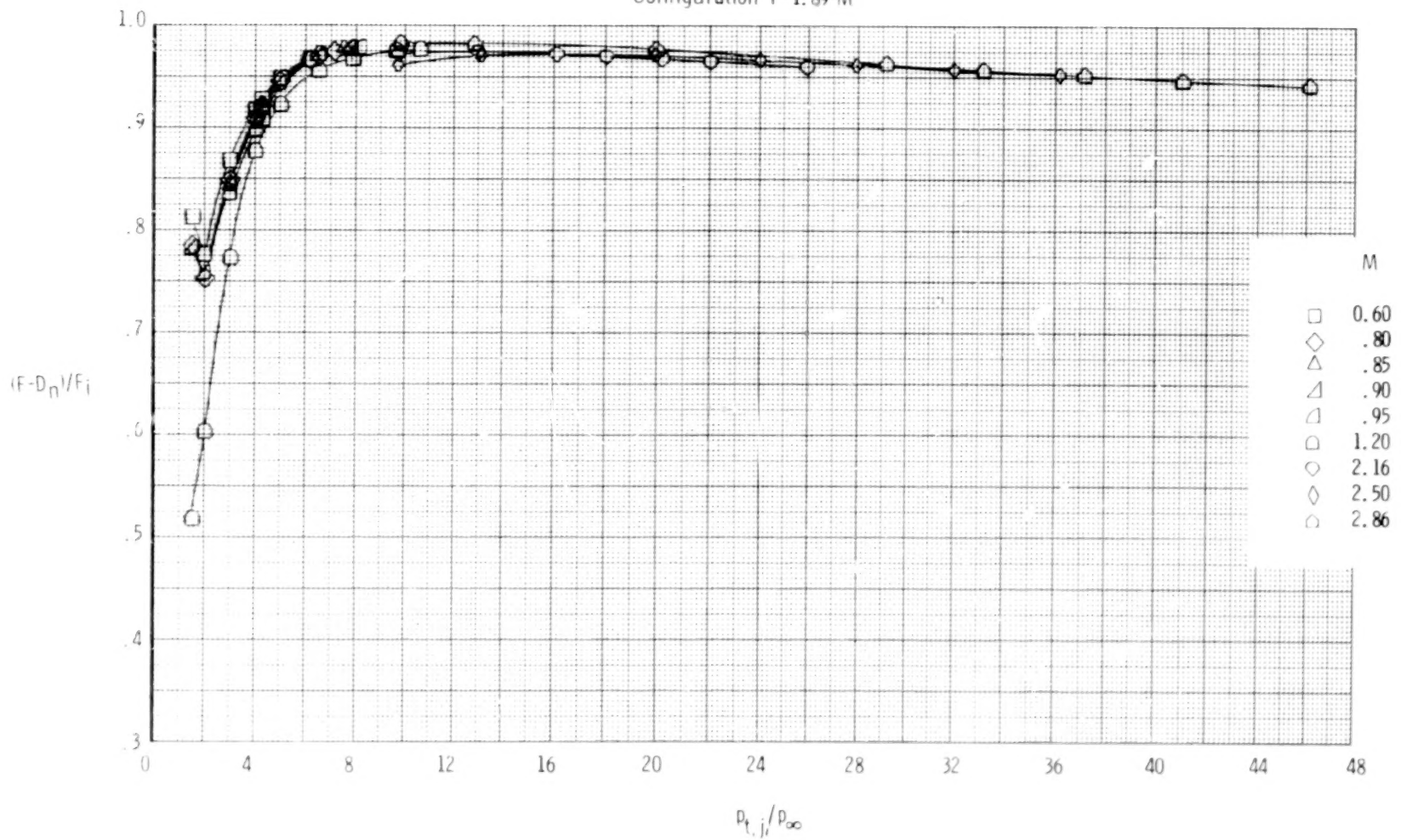

(d) Variation of thrust-minus-drag ratio.

Figure 16.- Concluded.

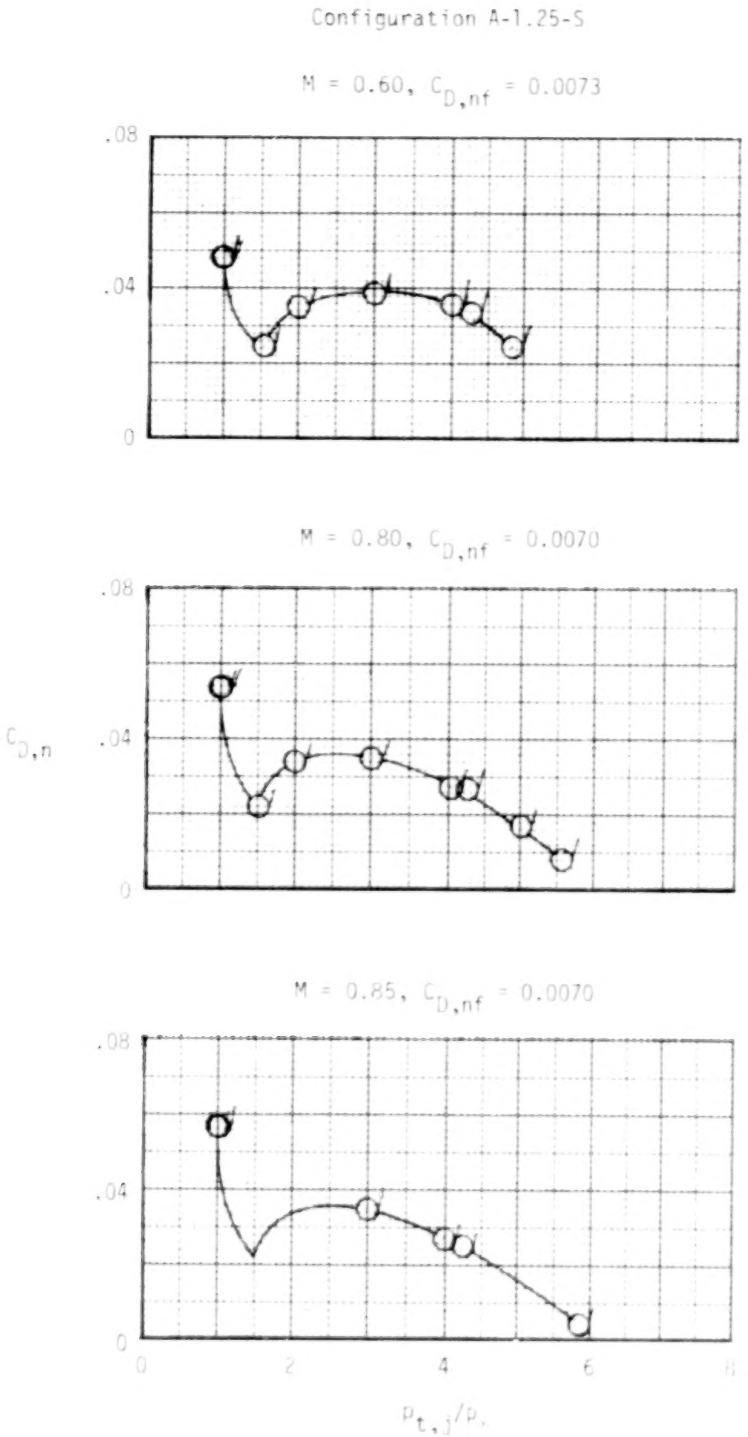

(a) Variation of nozzle drag coefficient.

Figure 17.- Variation of nozzle drag coefficient, thrust-minus-drag ratio, thrust ratio, and mass-flow ratio with nozzle pressure ratio for configuration A-1.25-S. Dashed line indicates theoretical values. Flagged symbols indicate data used to determine F/F_i.

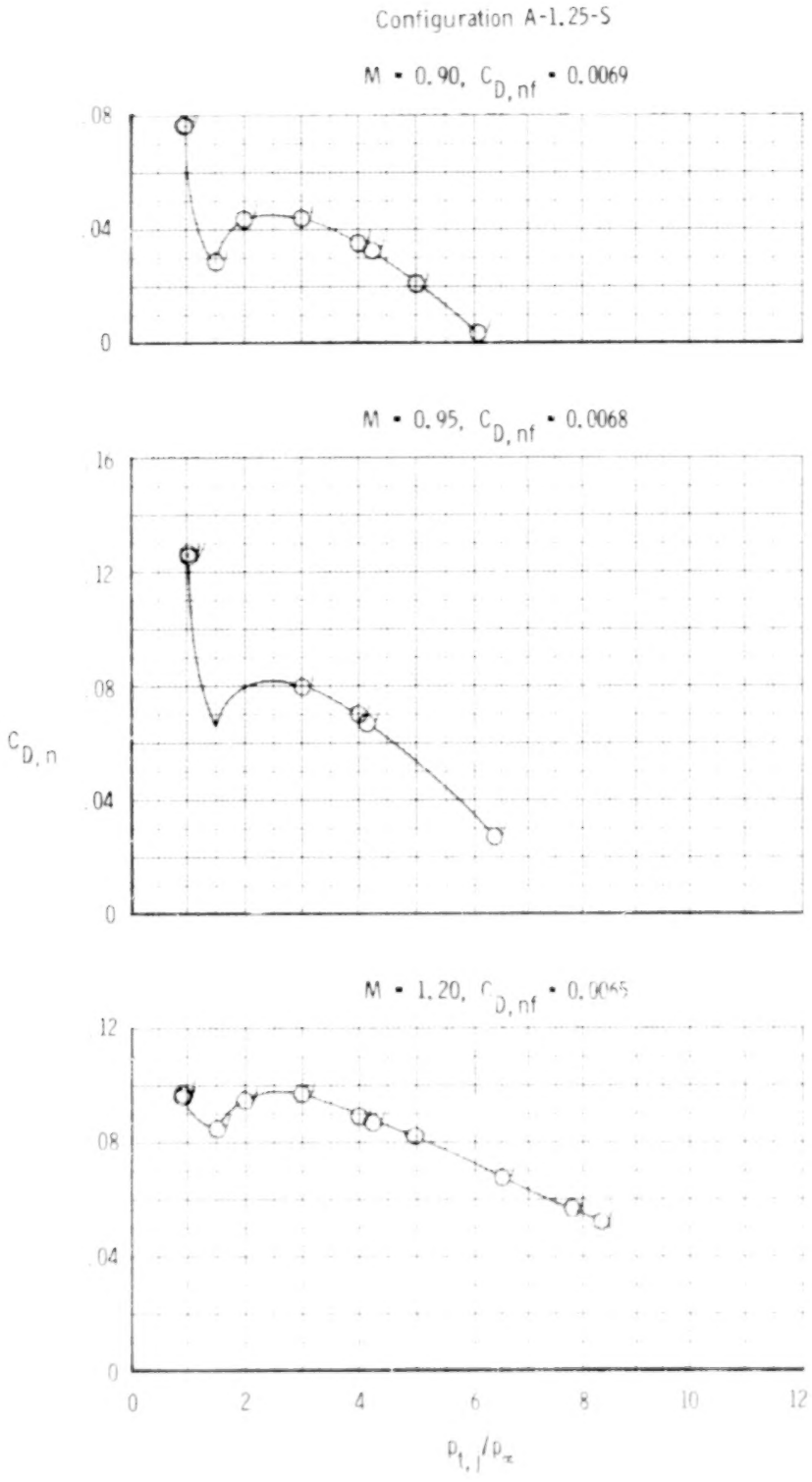

(a) Continued.

Figure 17.- Continued.

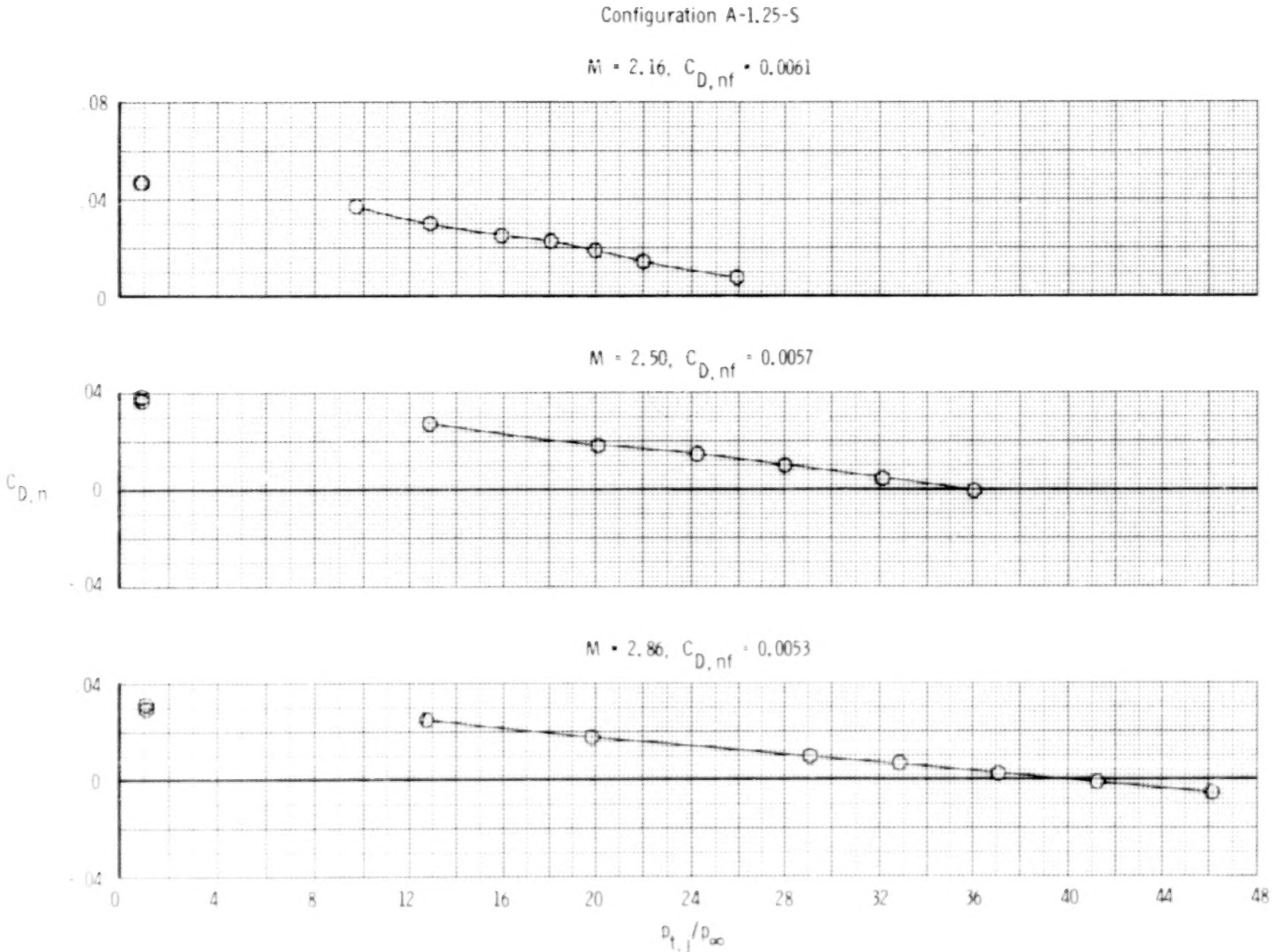

(a) Concluded.

Figure 17.- Continued.

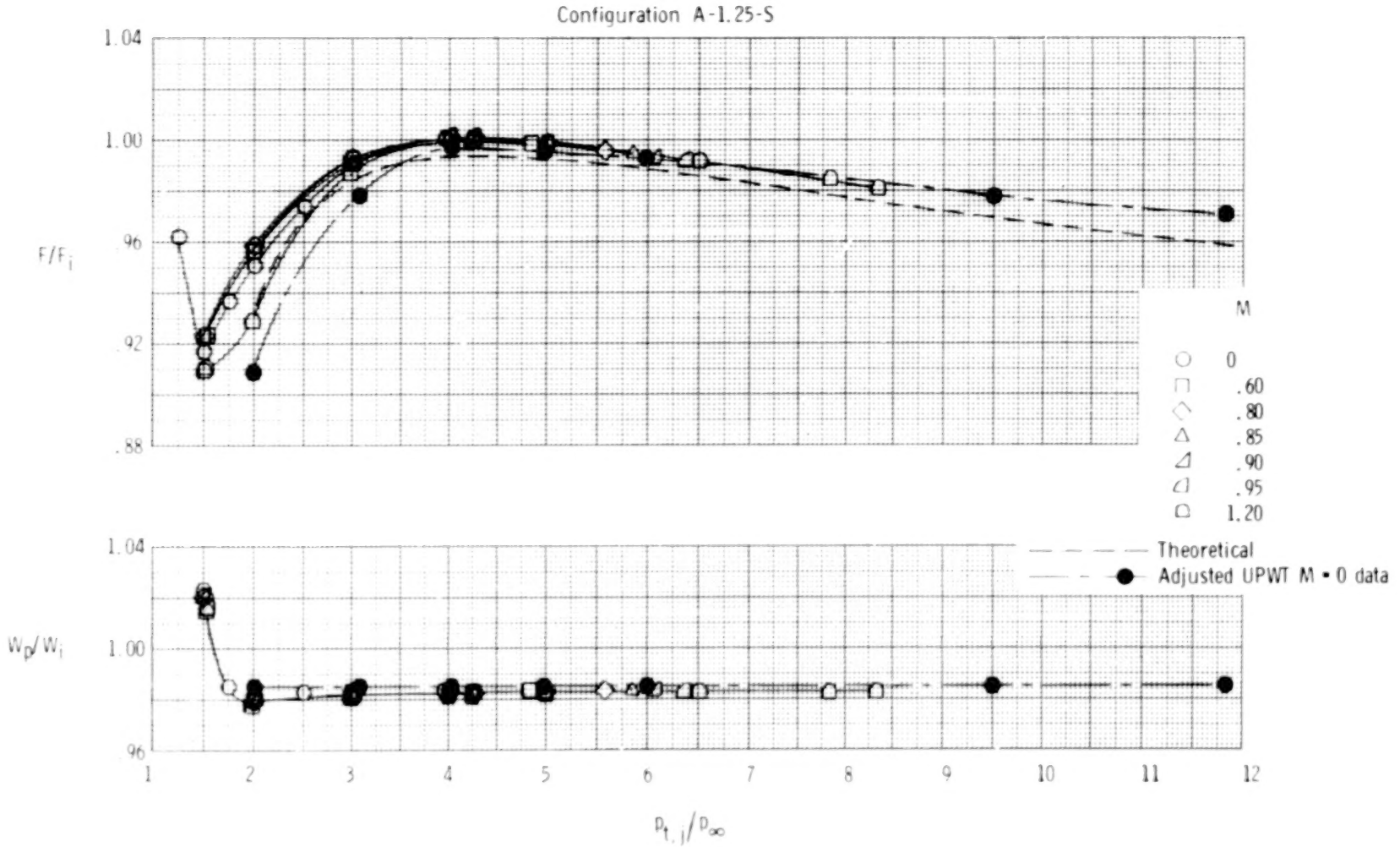

(b) Variation of thrust ratio and mass-flow ratio at subsonic and transonic speeds (16FTT).

Figure 17.- Continued.

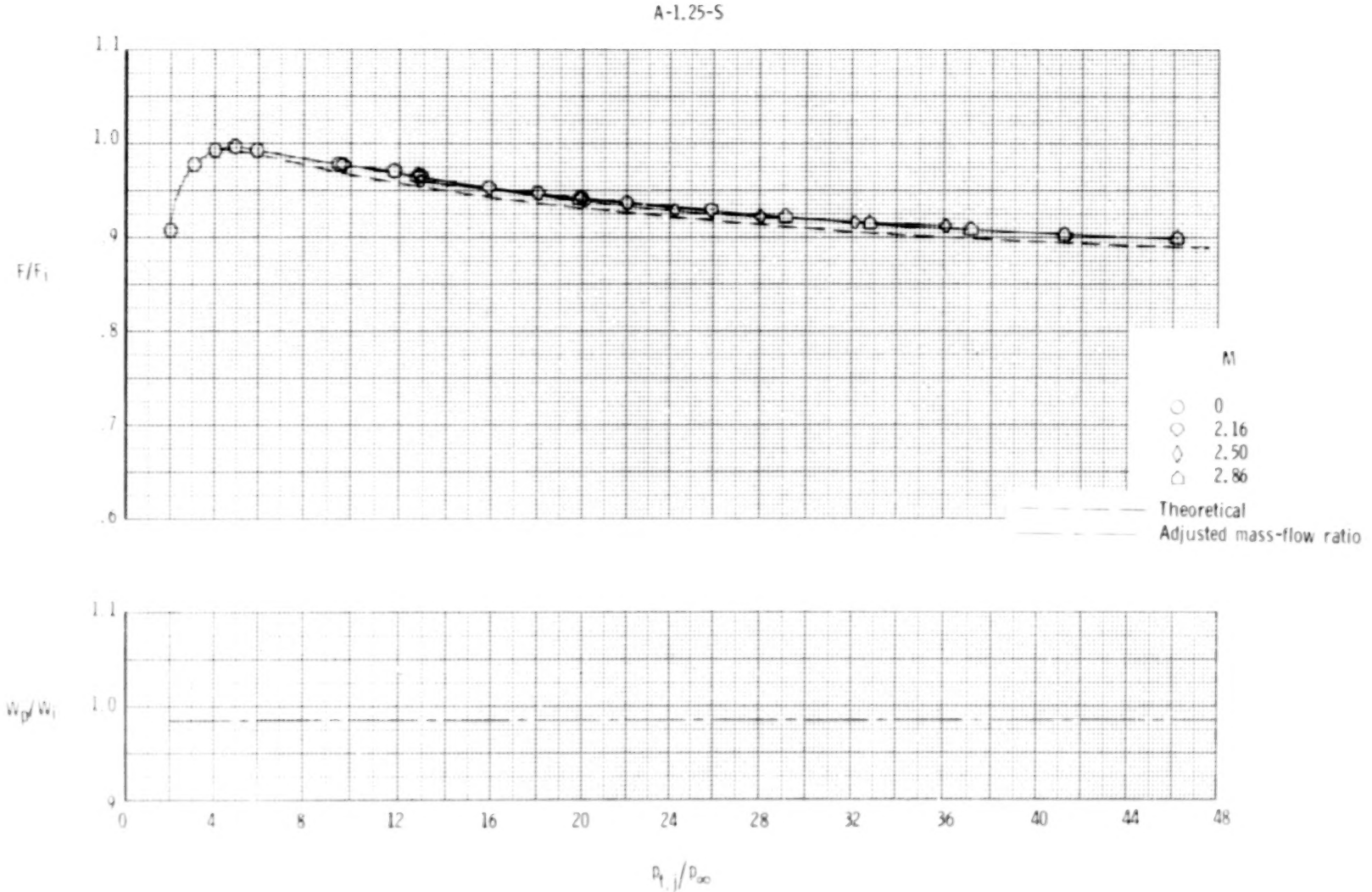

(c) Variation of thrust ratio and mass-flow ratio at supersonic speeds (UPWT).

Figure 17.- Continued.

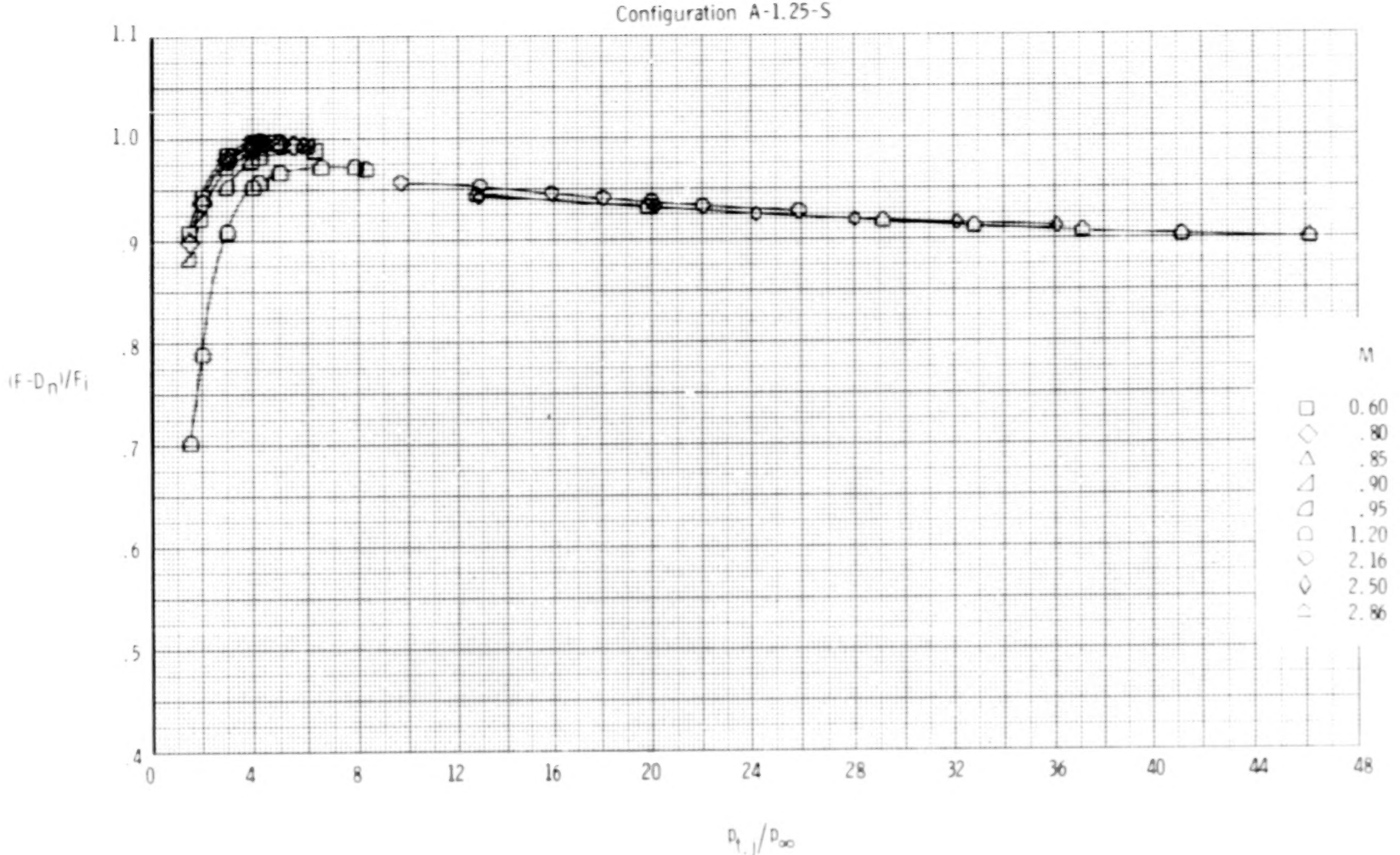

(d) Variation of thrust-minus-drag ratio.

Figure 17.- Concluded.

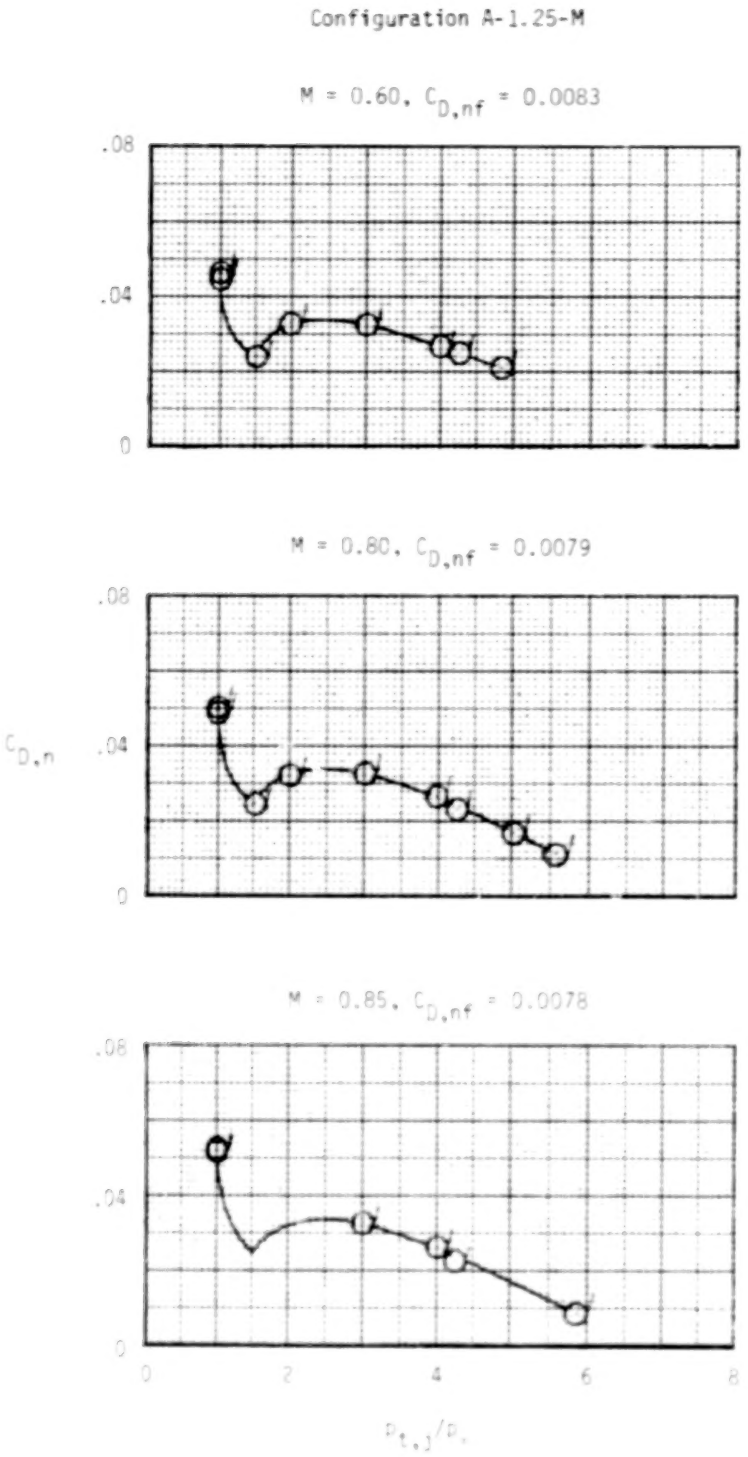

(a) Variation of nozzle drag coefficient.

Figure 18.- Variation of nozzle drag coefficient, thrust-minus-drag ratio, thrust ratio, and mass-flow ratio with nozzle pressure ratio for configuration A-1.25-M. Dashed line indicates theoretical values. Flagged symbols indicate data used to determine F/F_i.

Configuration A-1.25-M

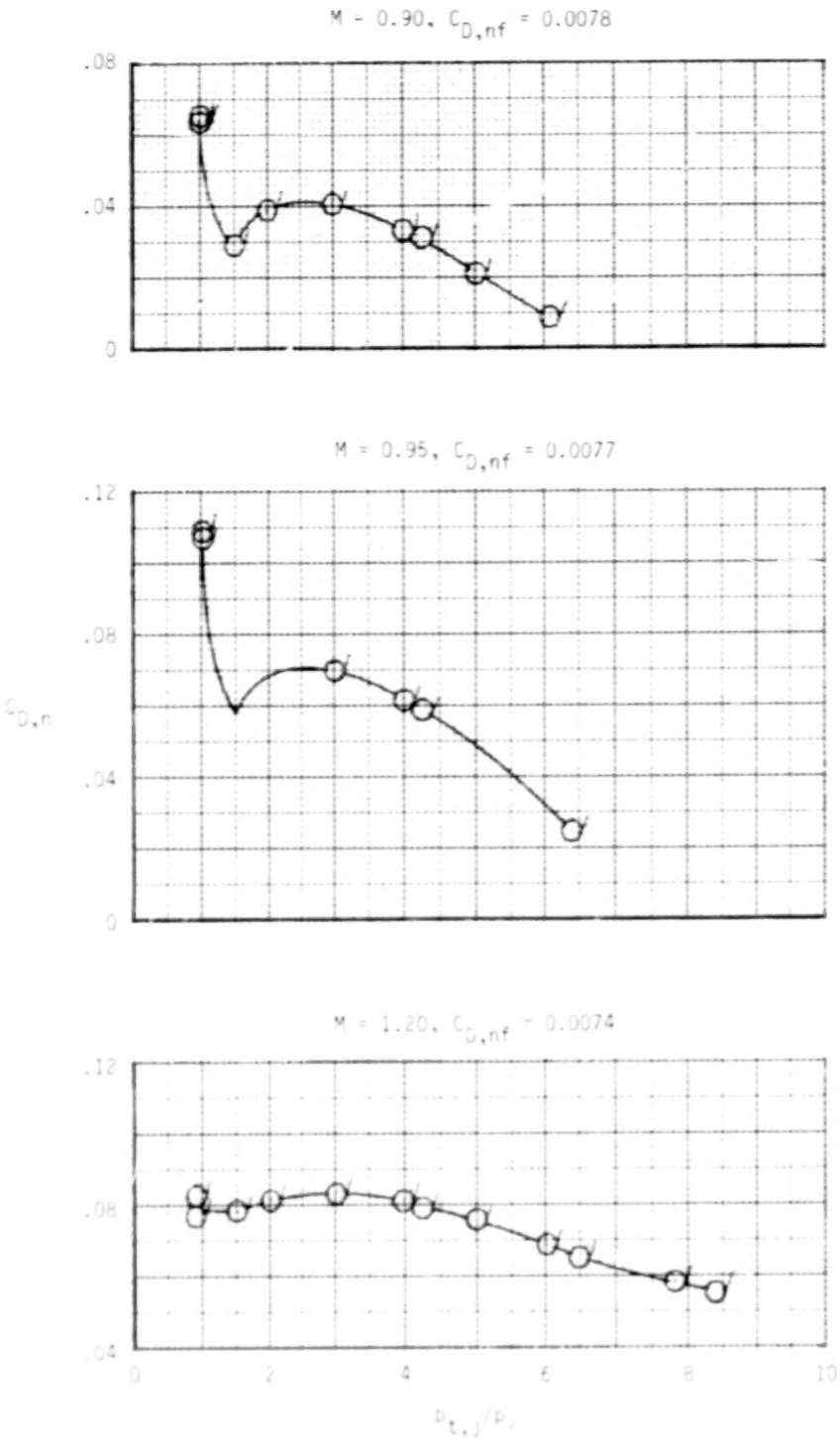

(a) Continued.

Figure 18.- Continued.

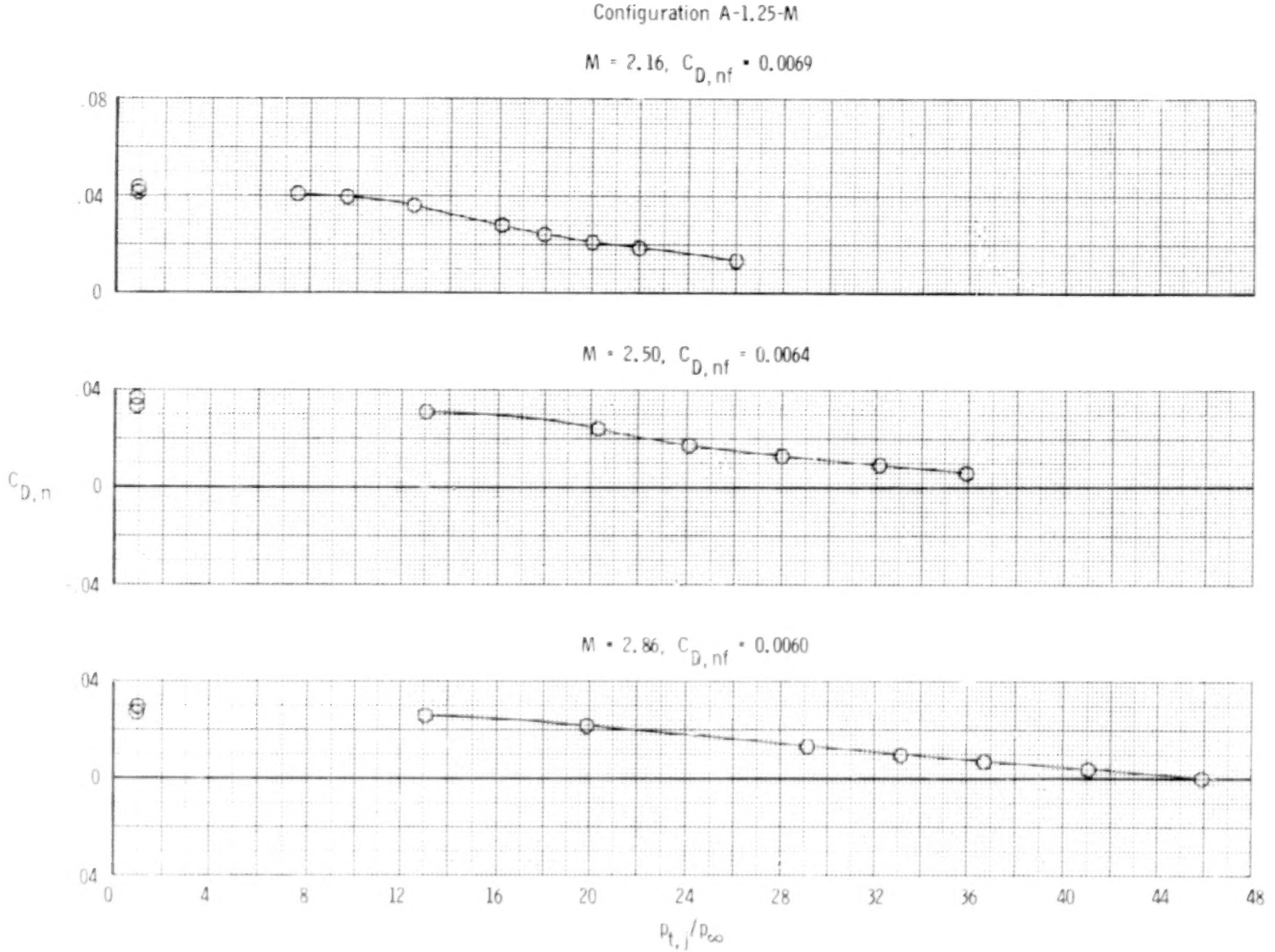

(a) Concluded.

Figure 18.- Continued.

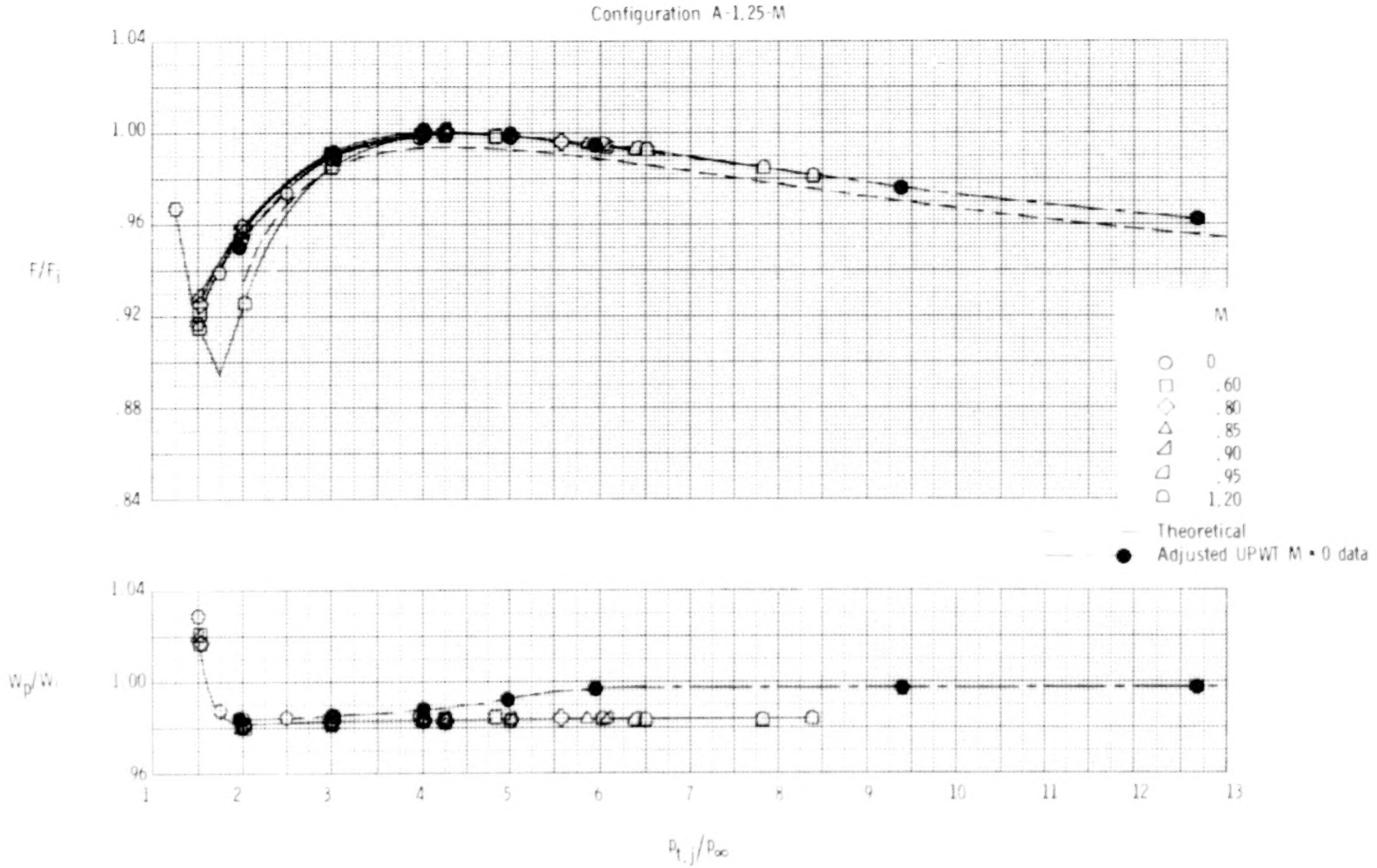

(b) Variation of thrust ratio and mass-flow ratio at subsonic and transonic speeds (16FTT).

Figure 18.- Continued.

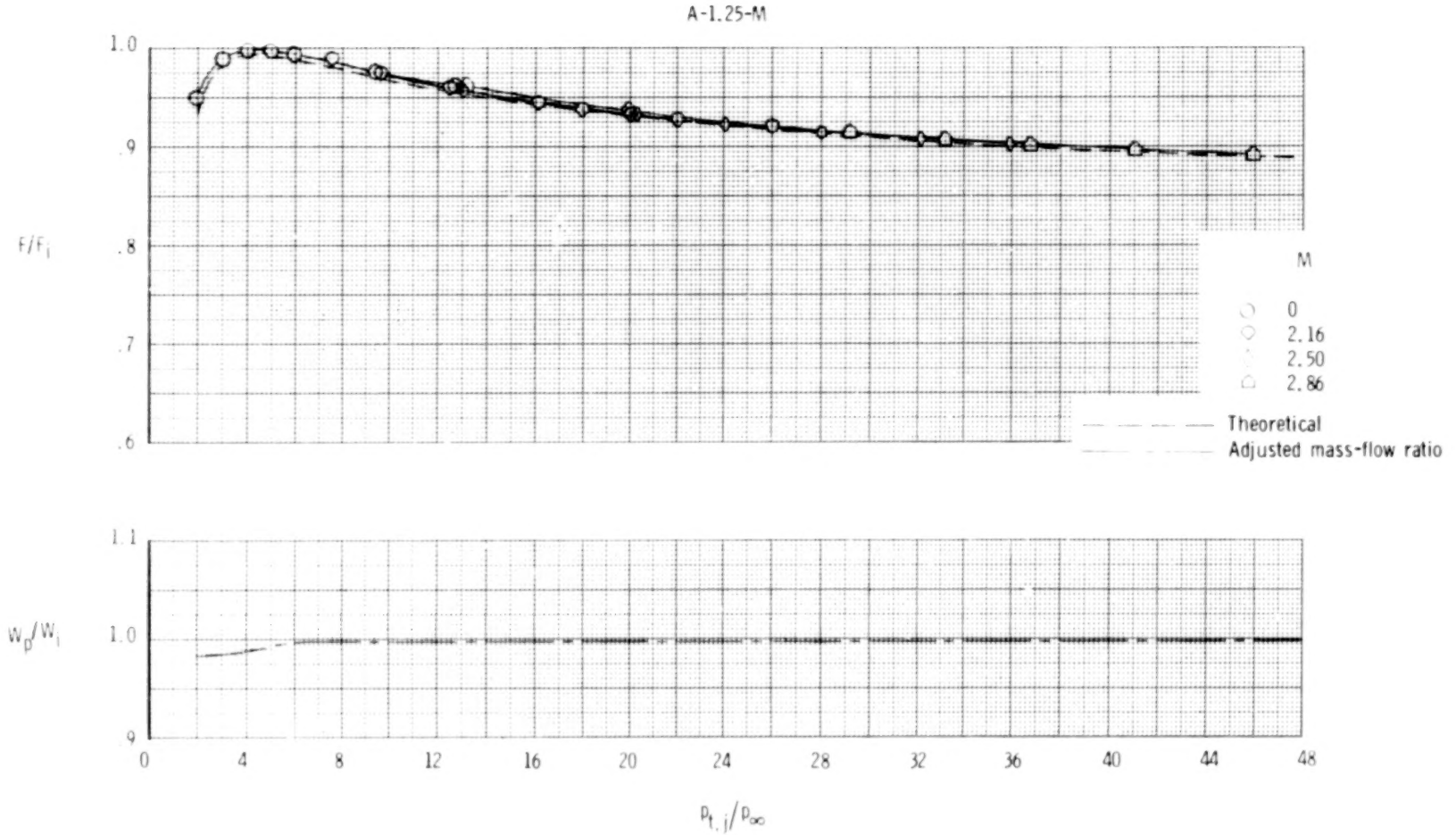

(c) Variation of thrust ratio and mass-flow ratio at supersonic speeds (UPWT).

Figure 18.- Continued.

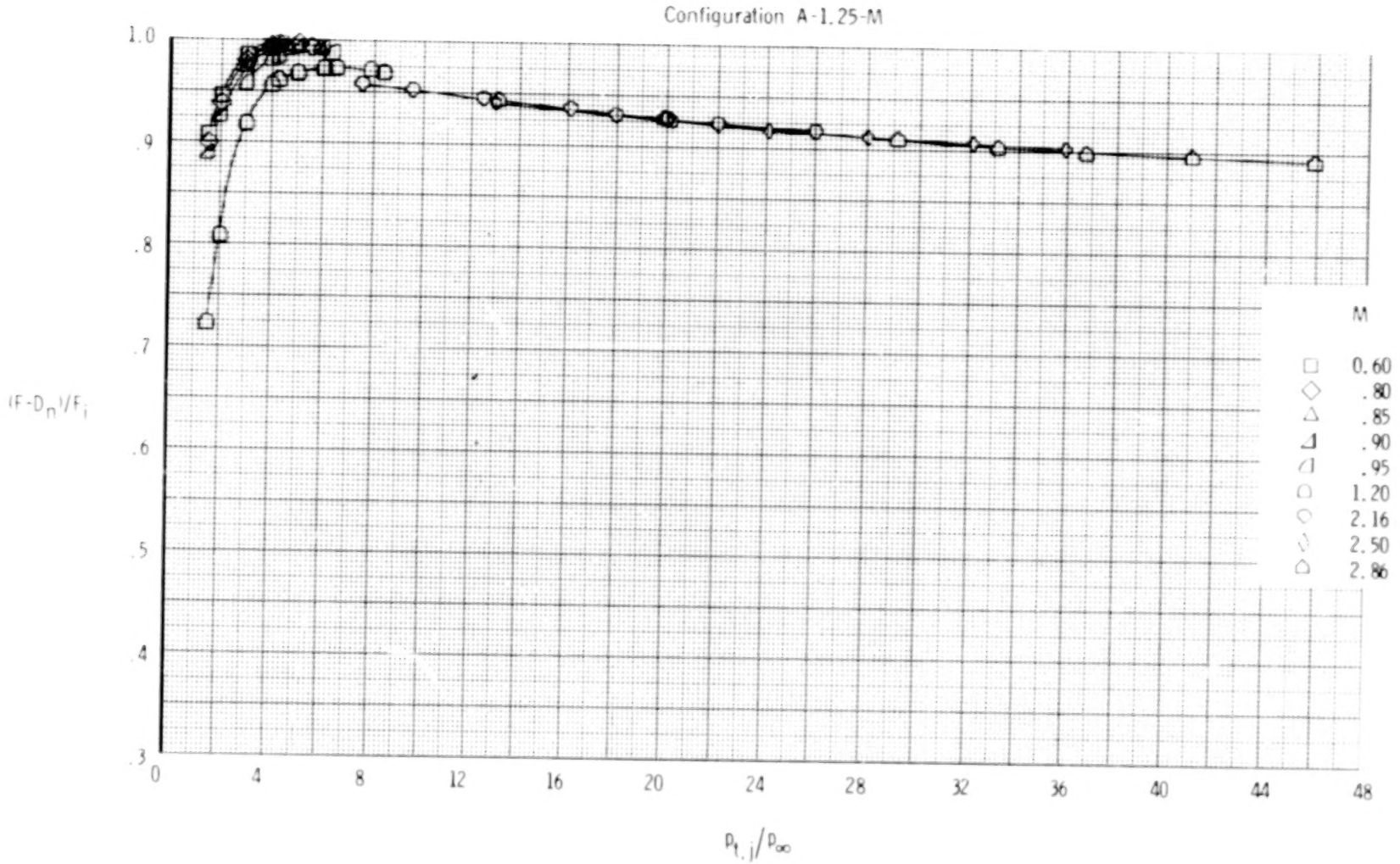

(d) Variation of thrust-minus-drag ratio.

Figure 18.- Concluded.

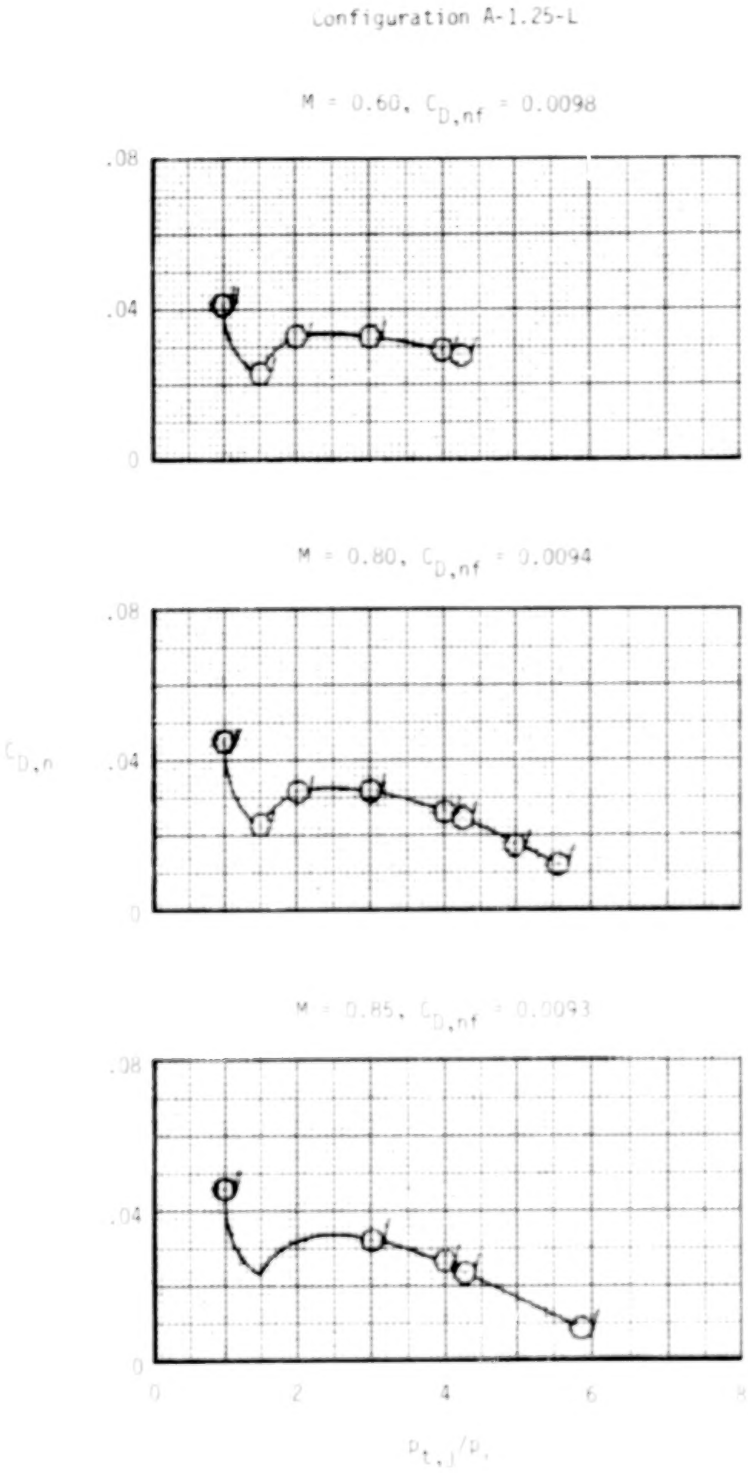

(a) Variation of nozzle drag coefficient.

Figure 19.- Variation of nozzle drag coefficient, thrust-minus-drag ratio, thrust ratio, and mass-flow ratio with nozzle pressure ratio for configuration A-1.25-L. Dashed line indicates theoretical values. Flagged symbols indicate data used to determine F/F_i.

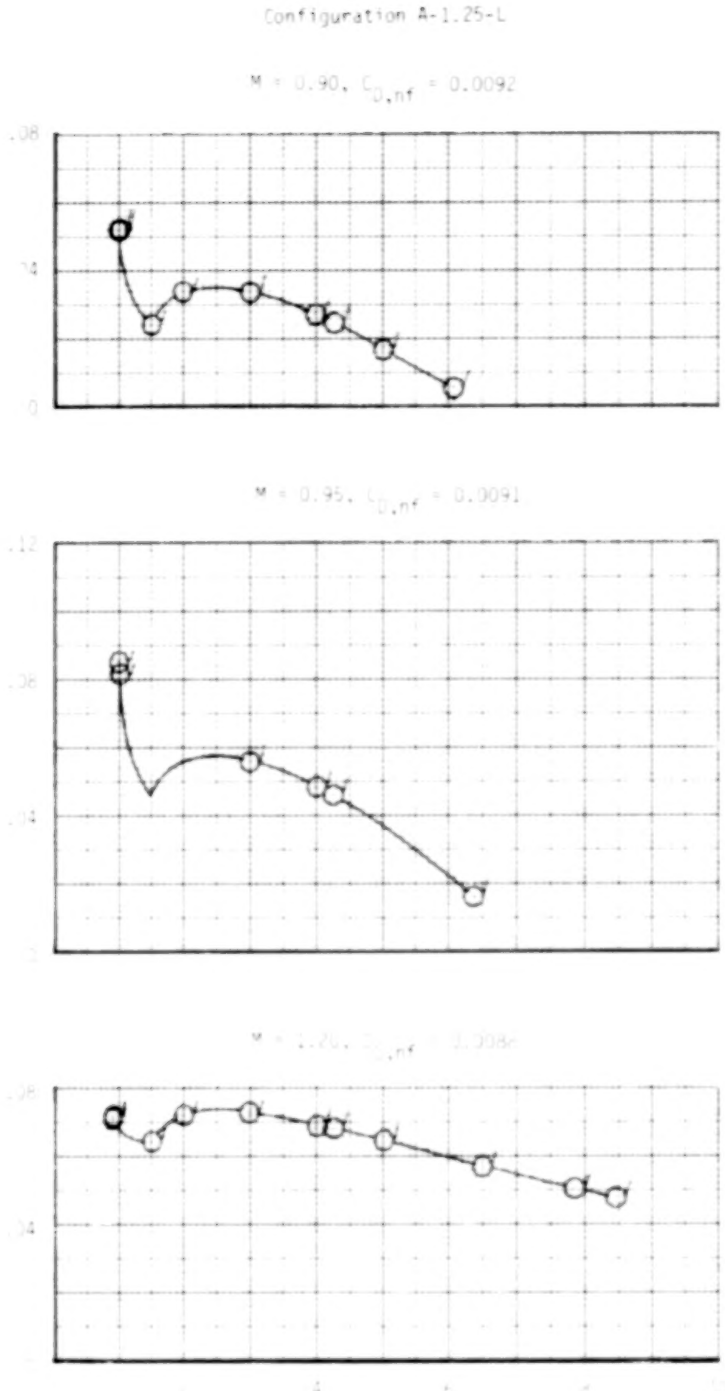

(a) Continued.

Figure 19.- Continued.

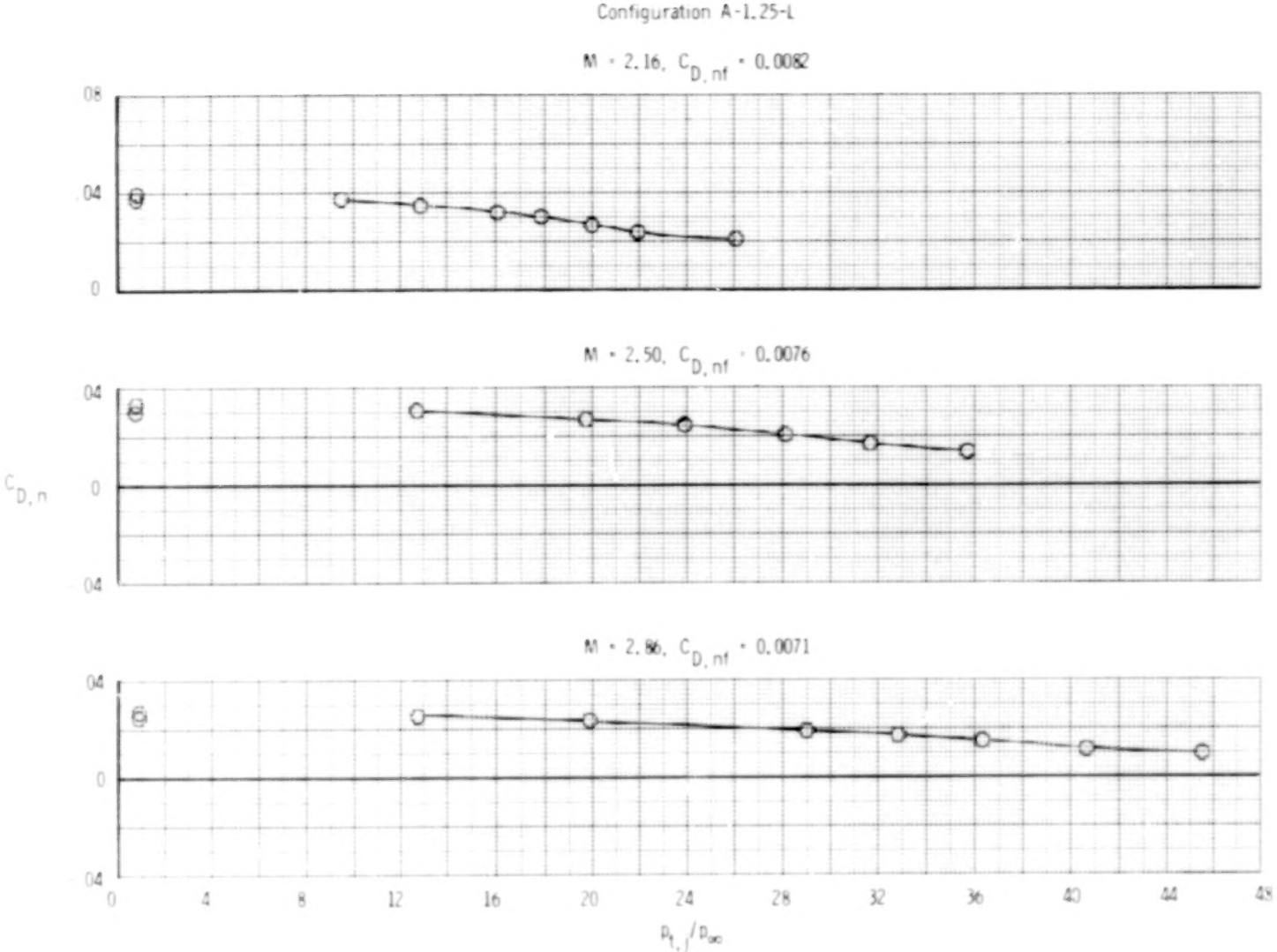

(a) Concluded.

Figure 19.- Continued.

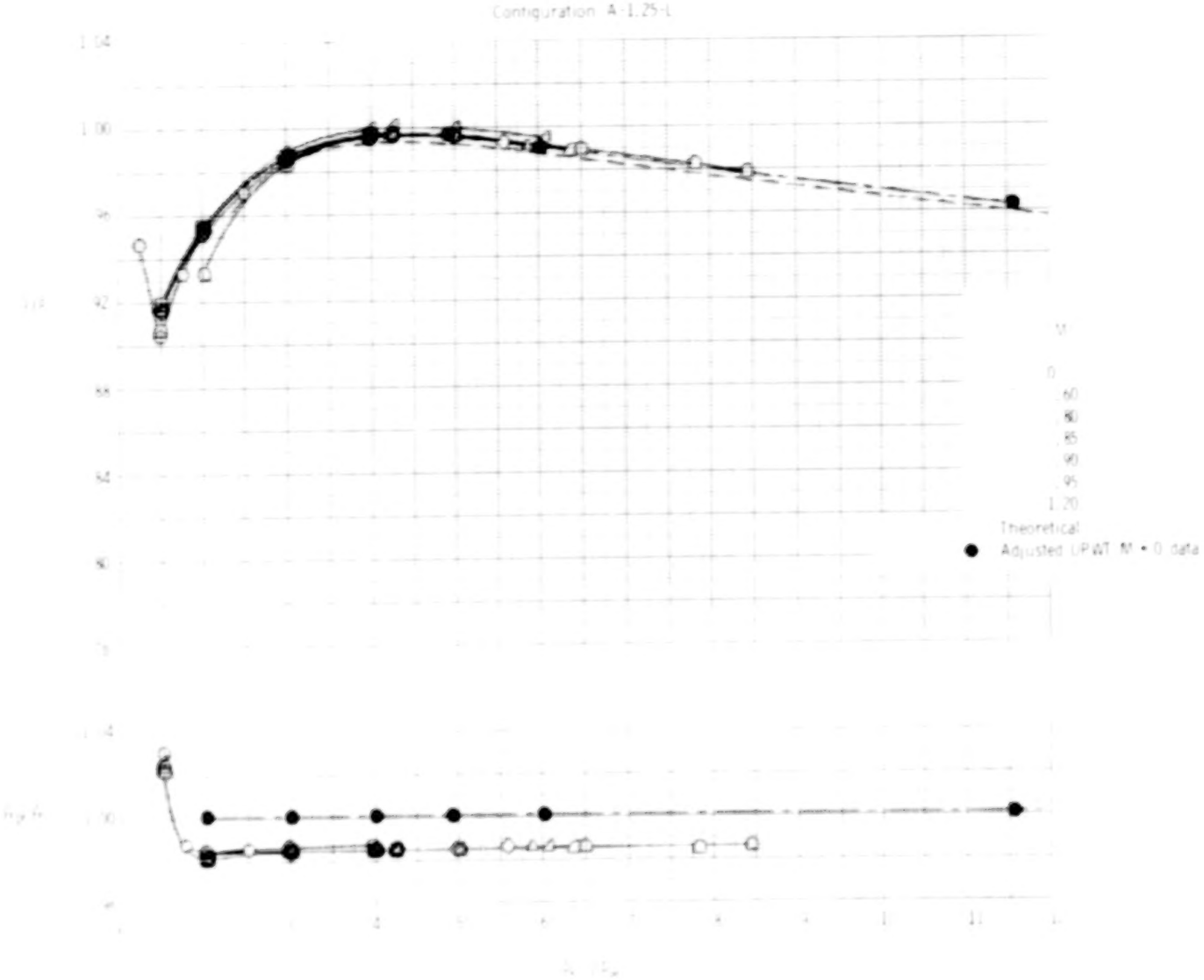

(b) Variation of thrust ratio and mass-flow ratio at subsonic and transonic speeds (16FTT).

Figure 19.- Continued.

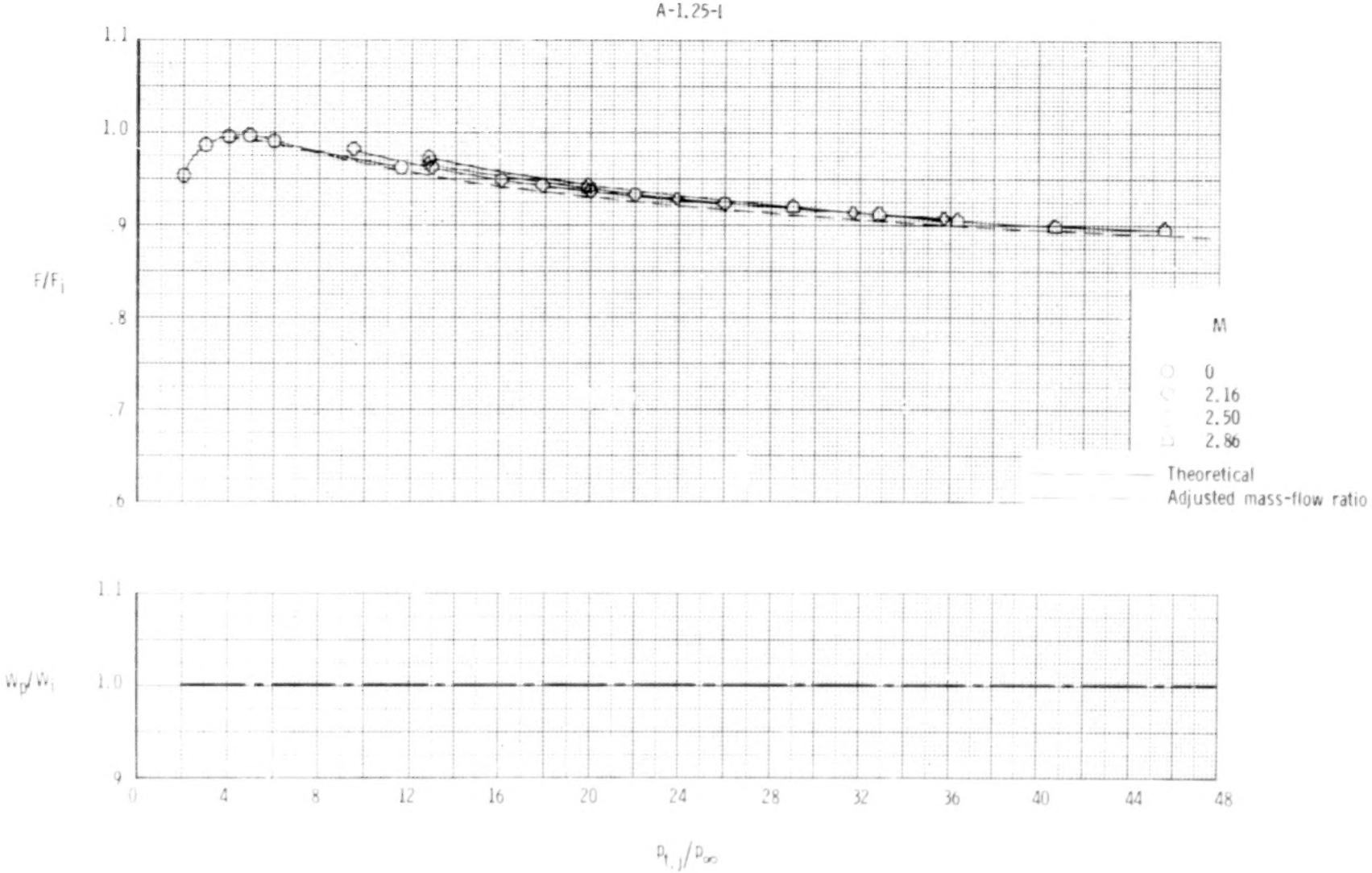

(c) Variation of thrust ratio and mass-flow ratio at supersonic speeds (UPWT).

Figure 19.- Continued.

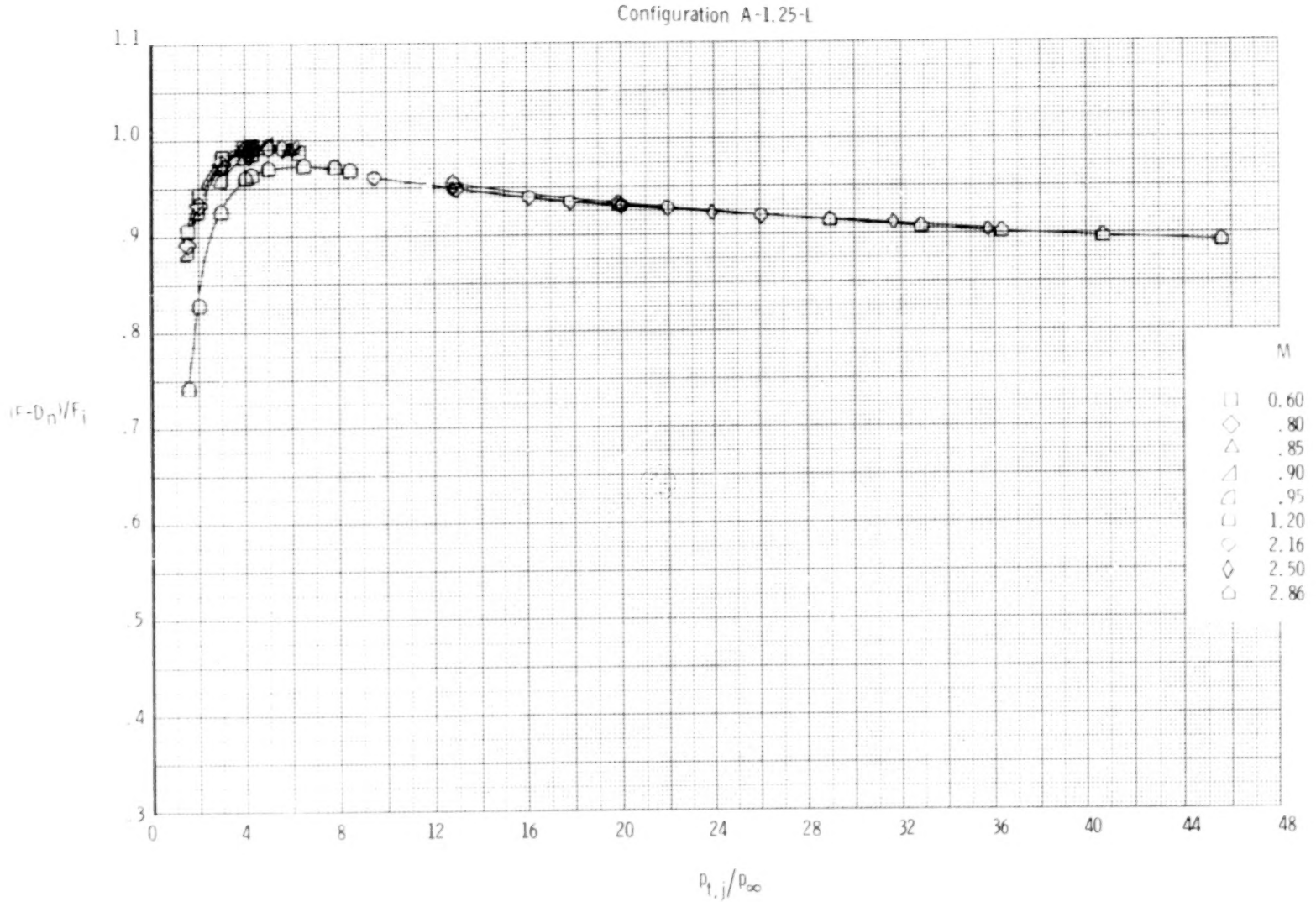

(d) Variation of thrust-minus-drag ratio.

Figure 19.- Concluded.

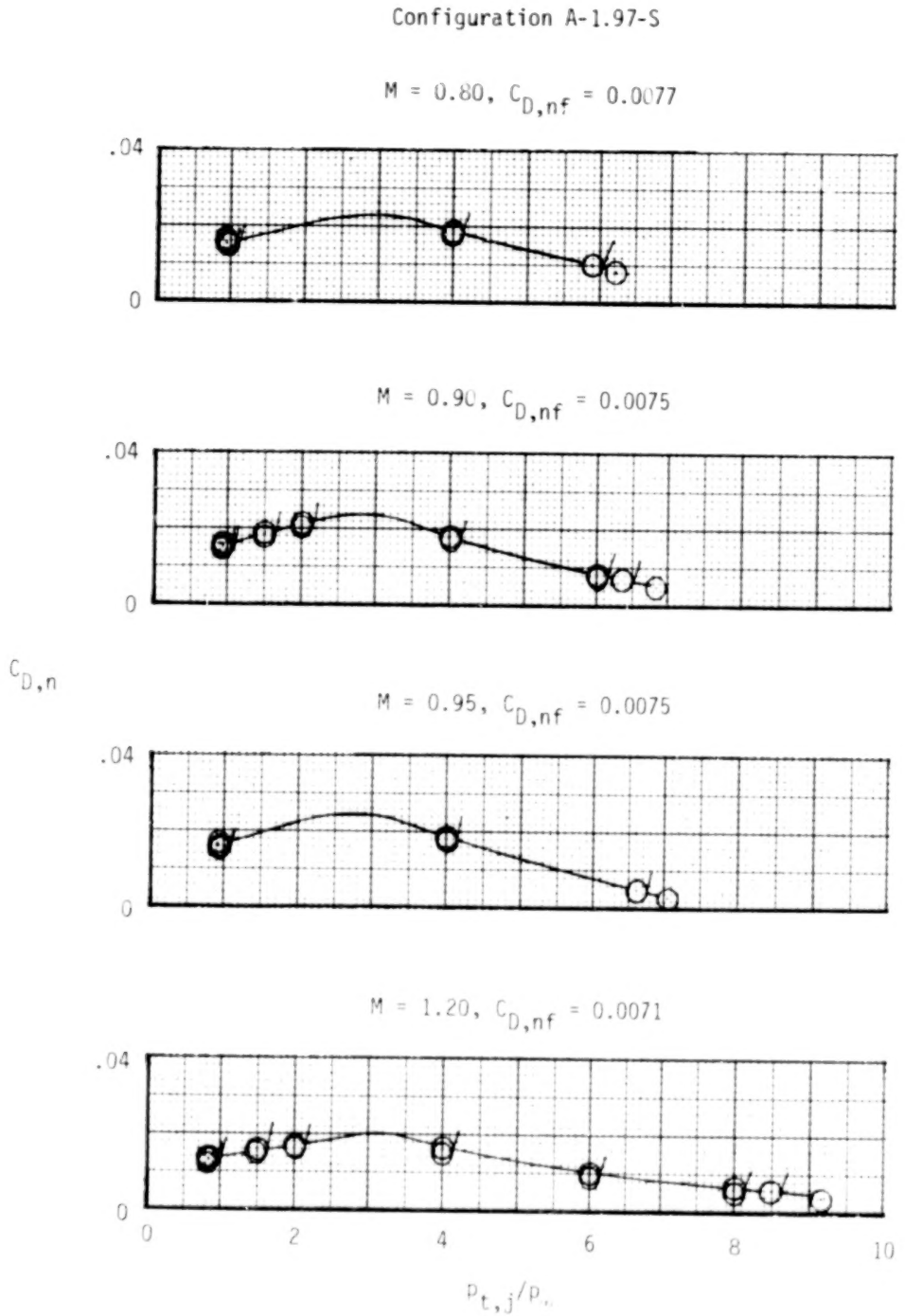

(a) Variation of nozzle drag coefficient.

Figure 20.- Variation of nozzle drag coefficient, thrust-minus-drag ratio, thrust ratio, and mass-flow ratio with nozzle pressure ratio for configuration A-1.97-S. Dashed line indicates theoretical values. Flagged symbols indicate data used to determine F/F_i.

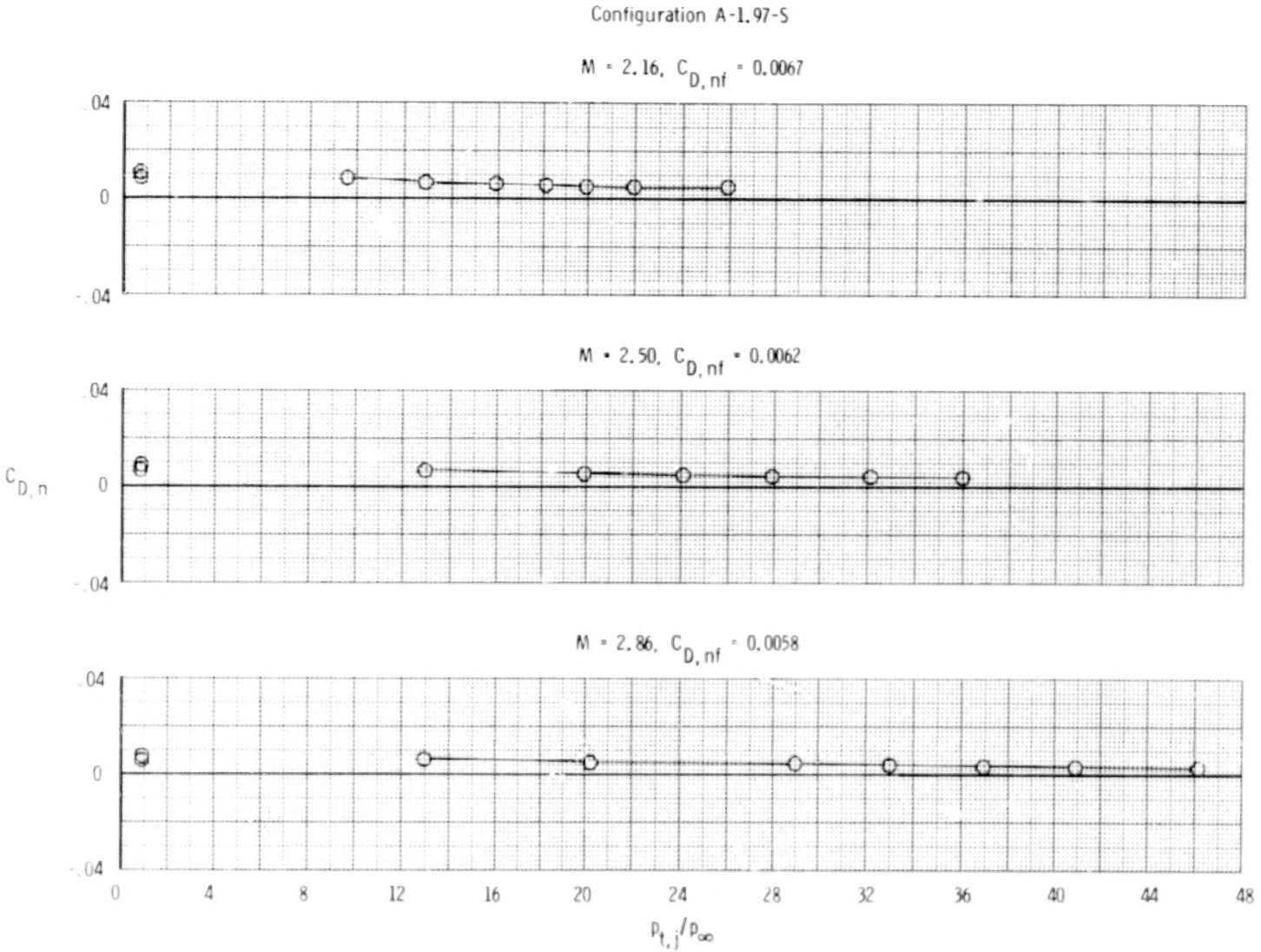

(a) Concluded.

Figure 20.- Continued.

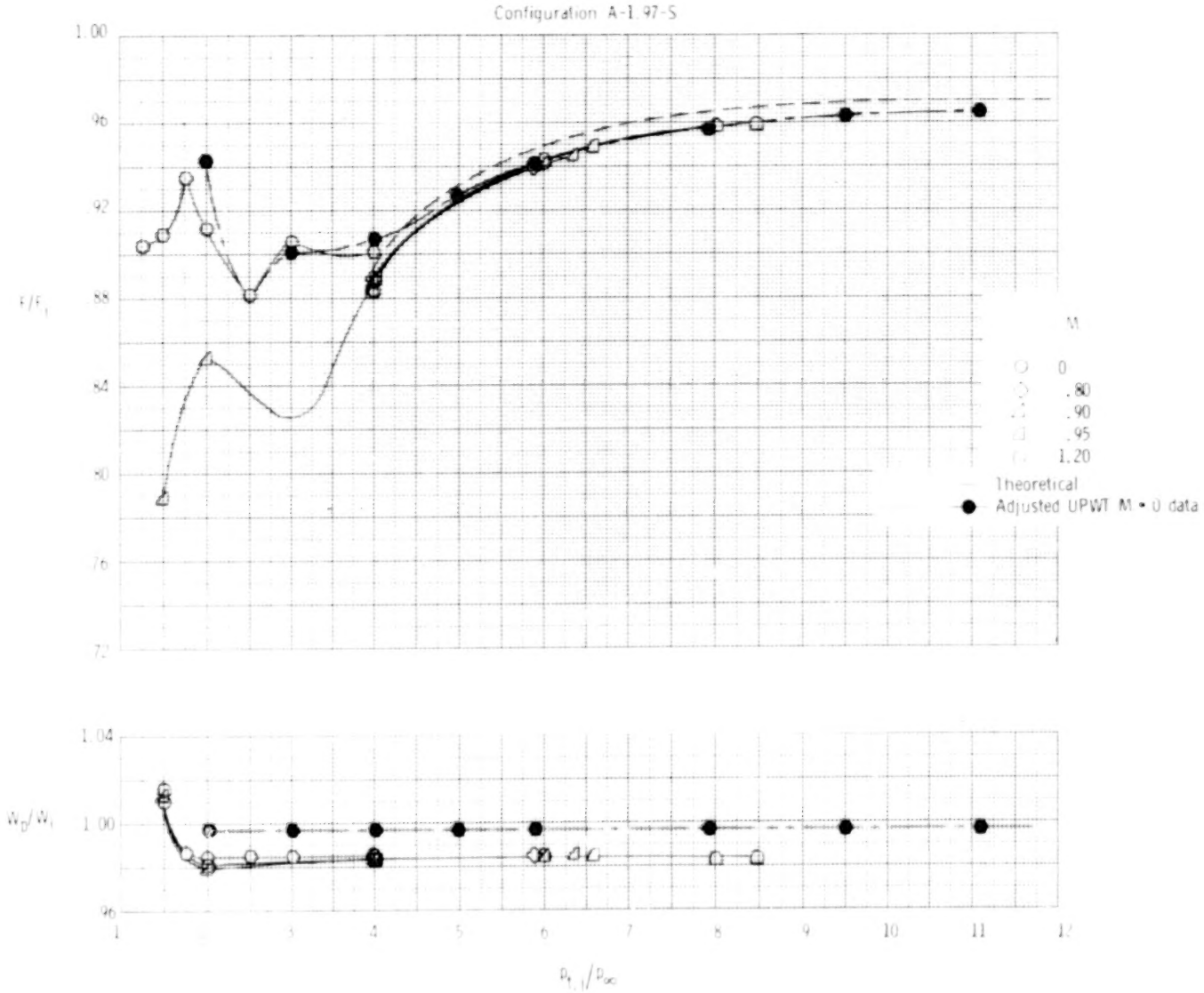

(b) Variation of thrust ratio and mass-flow ratio at subsonic and transonic speeds (16FTT).

Figure 20.- Continued.

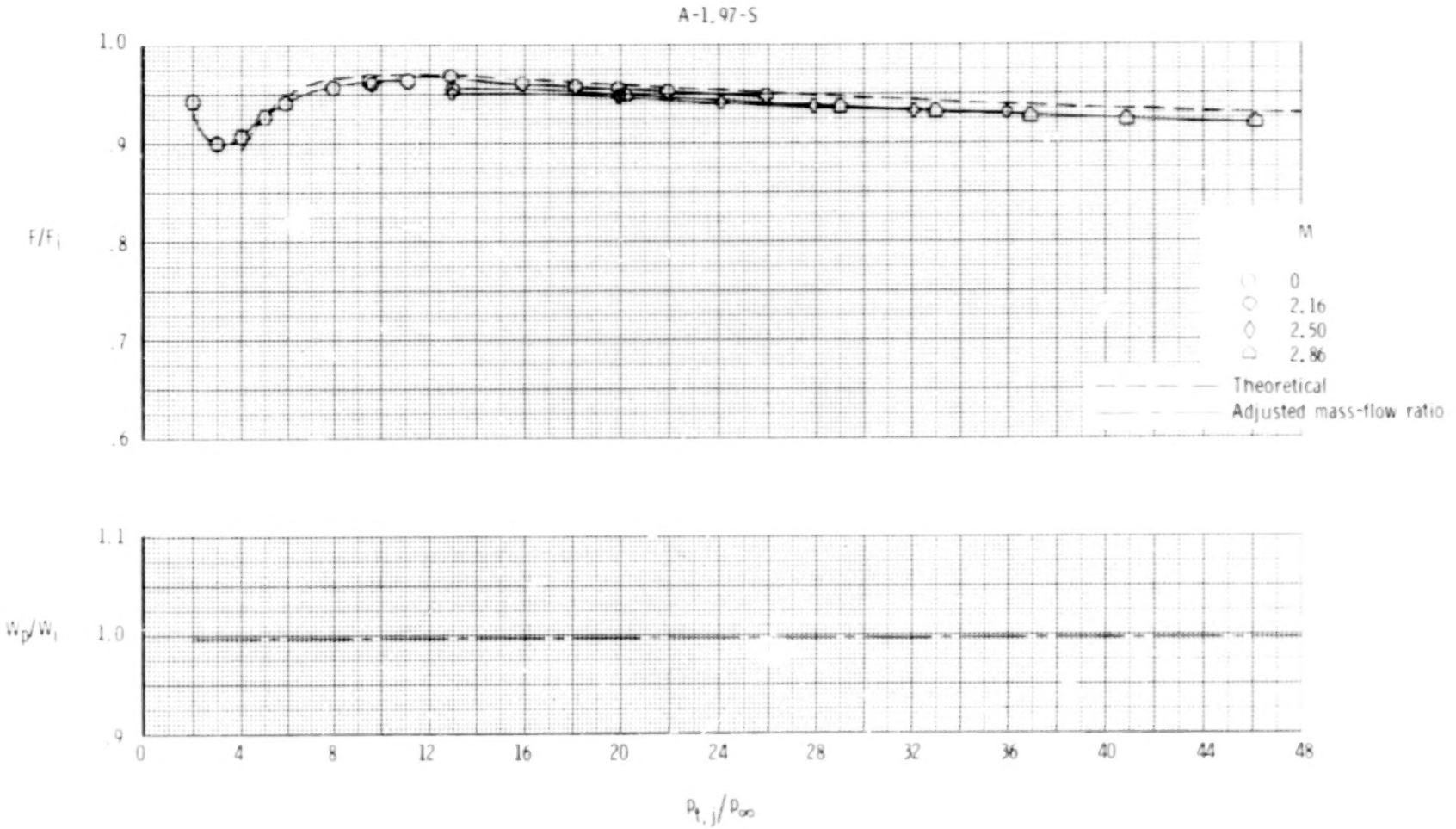

(c) Variation of thrust ratio and mass-flow ratio at supersonic speeds (UPWT).

Figure 20.- Continued.

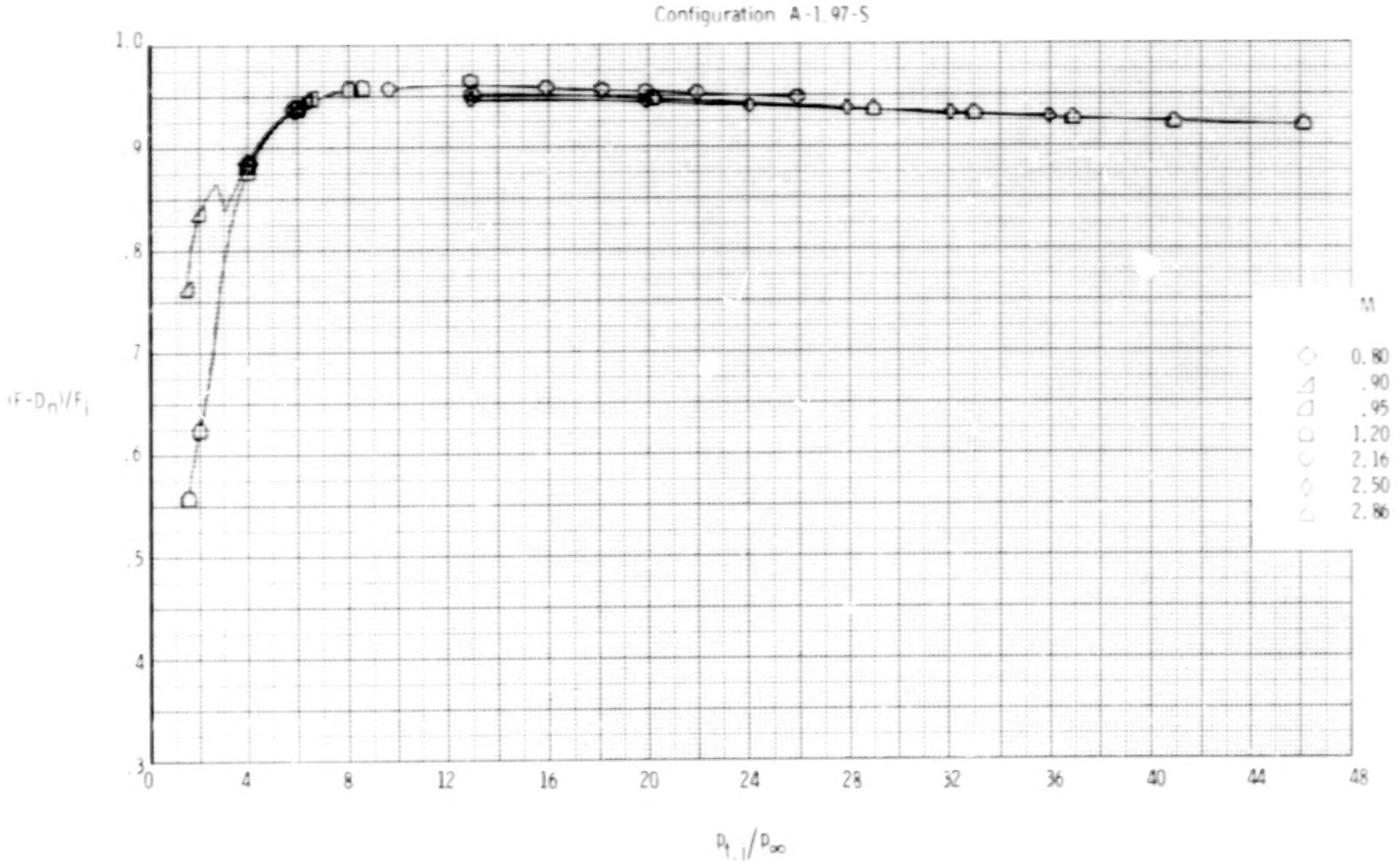

(d) Variation of thrust-minus-drag ratio.

Figure 20.- Concluded.

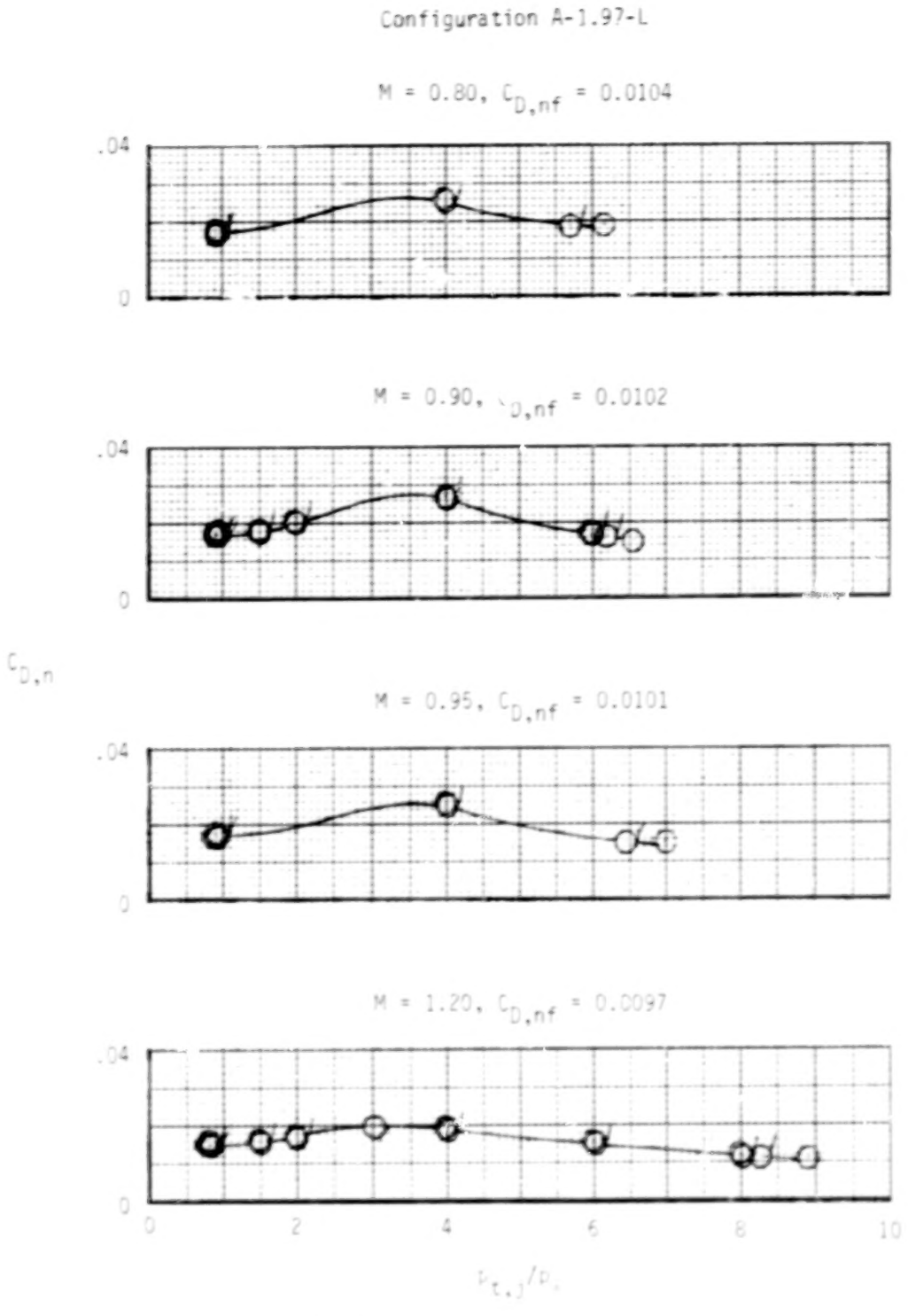

(a) Variation of nozzle drag coefficient.

Figure 21.- Variation of nozzle drag coefficient, thrust-minus-drag ratio, thrust ratio, and mass-flow ratio with nozzle pressure ratio for configuration A-1.97-L. Dashed line indicates theoretical values. Flagged symbols indicate data used to determine F/F_i.

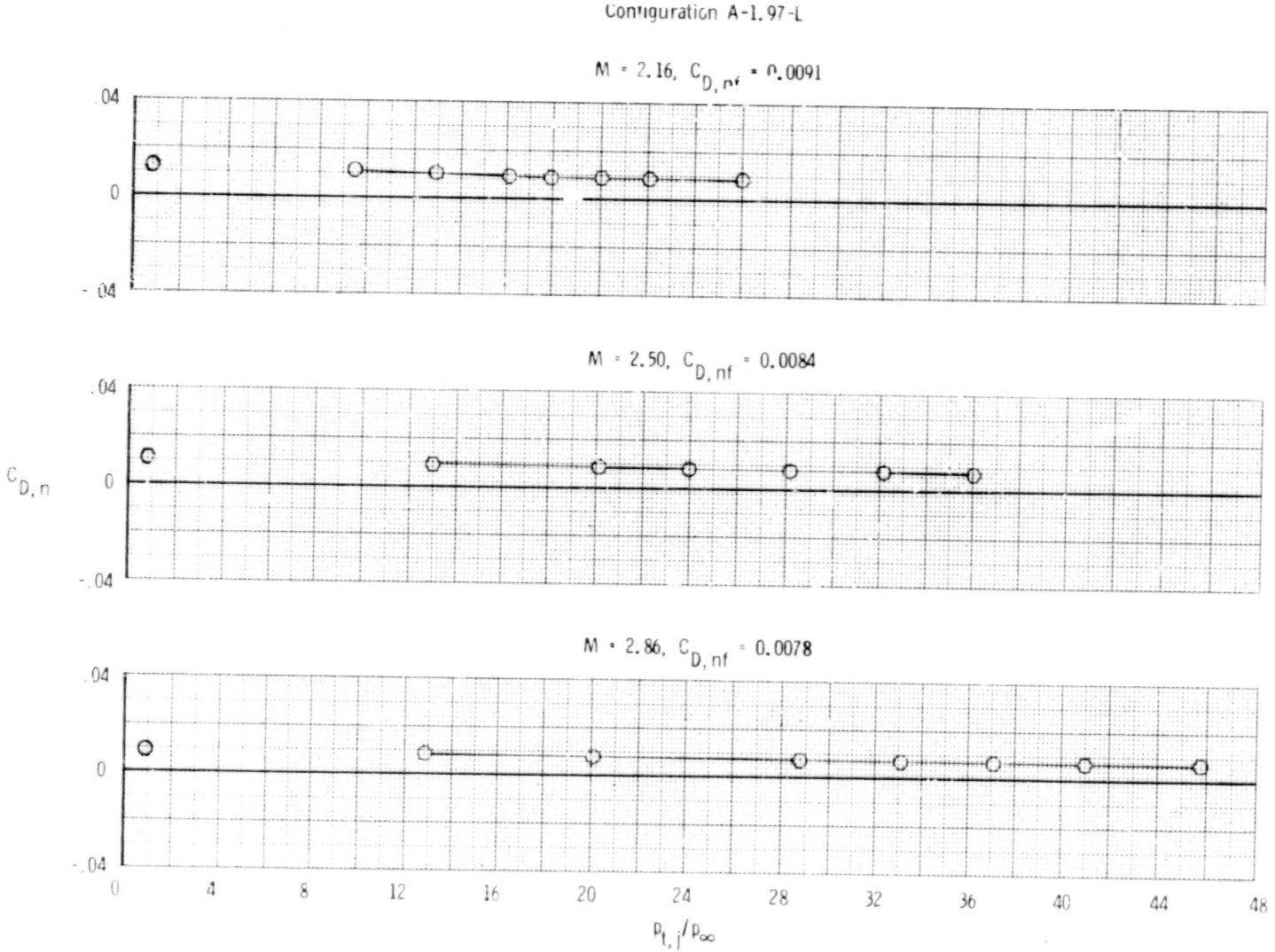

(a) Concluded.

Figure 21.- Continued.

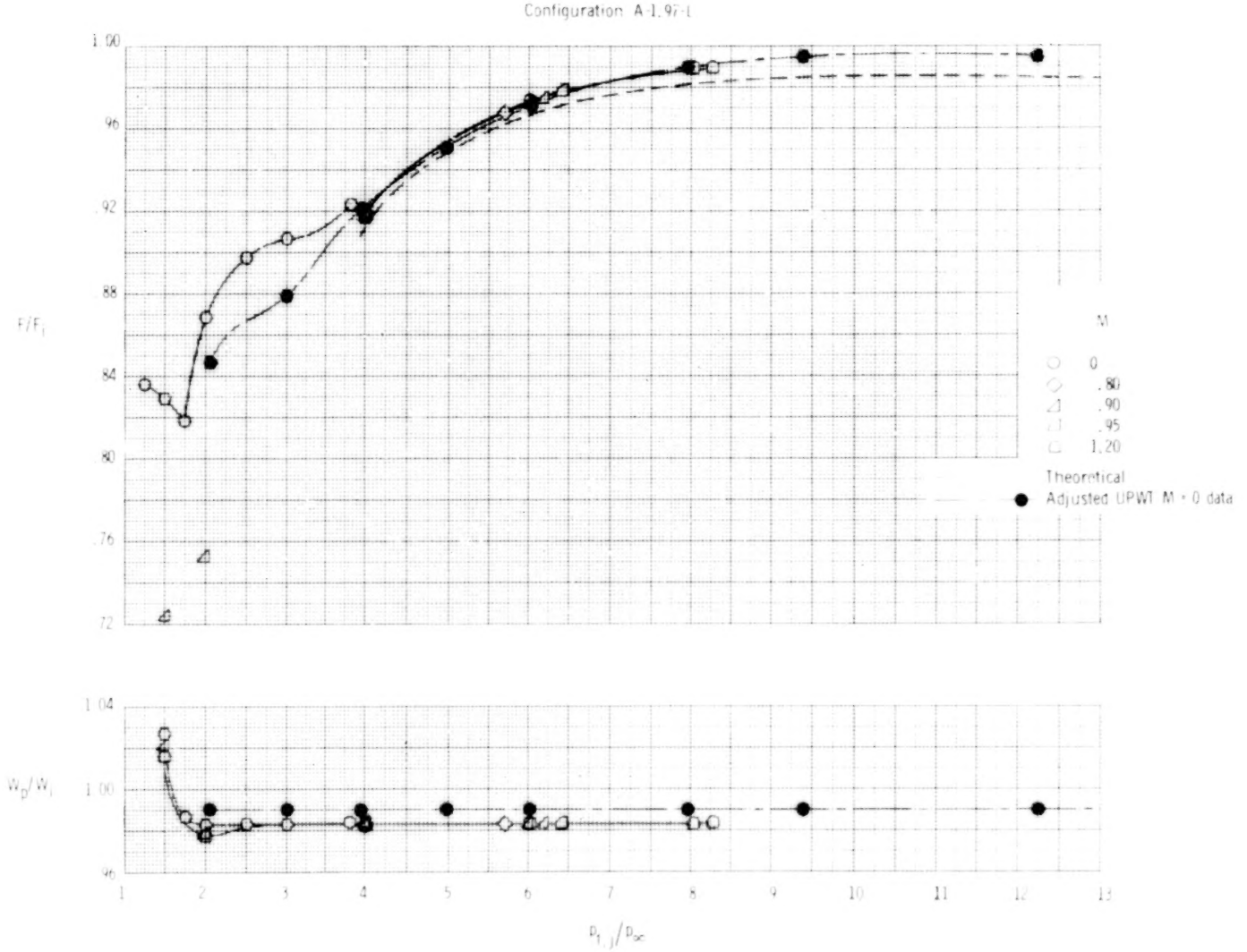

(b) Variation of thrust ratio and mass-flow ratio at subsonic and transonic speeds (16FTT).

Figure 21.- Continued.

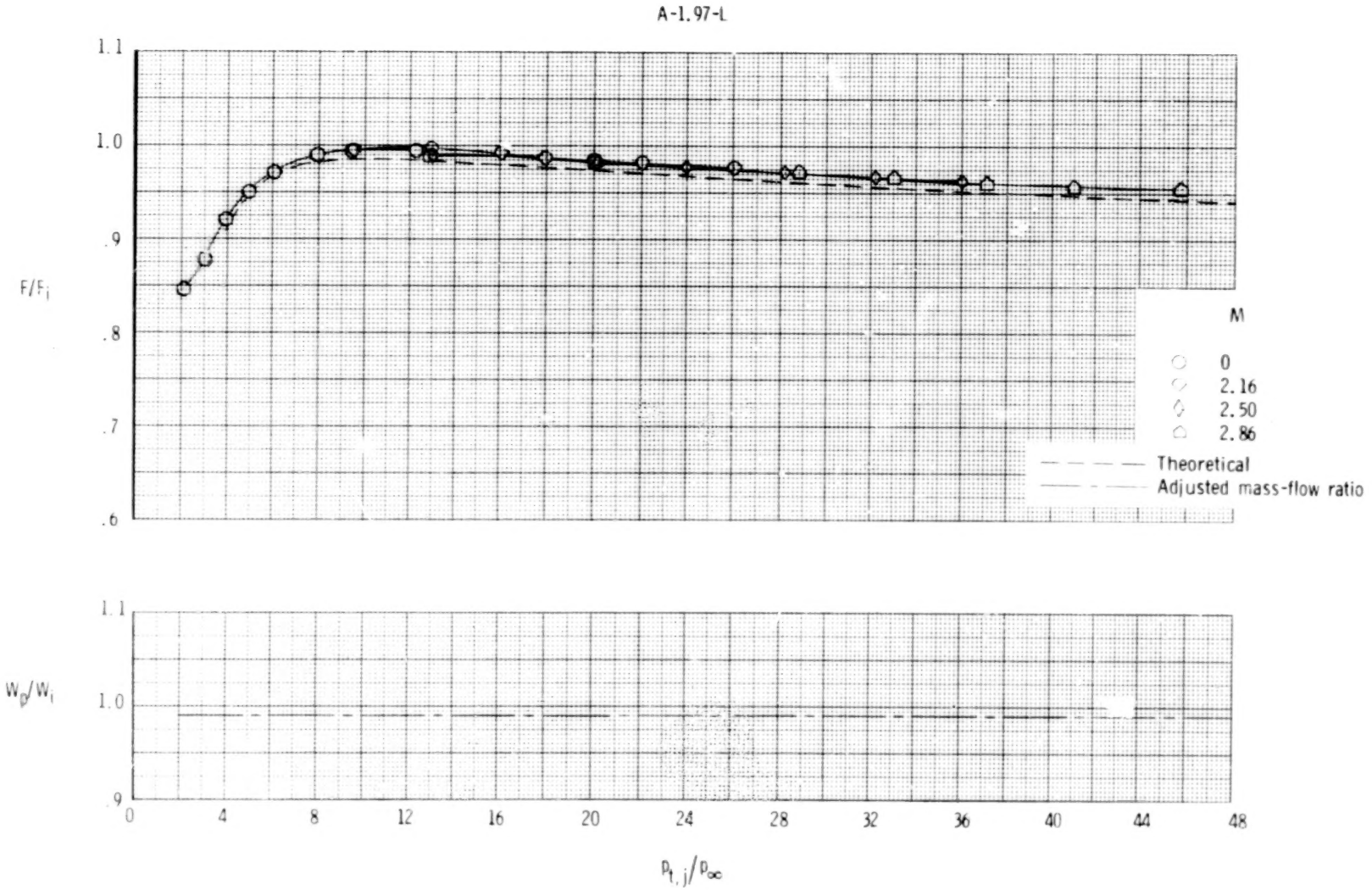

(c) Variation of thrust ratio and mass-flow ratio at supersonic speeds (UPWT).

Figure 21.- Continued.

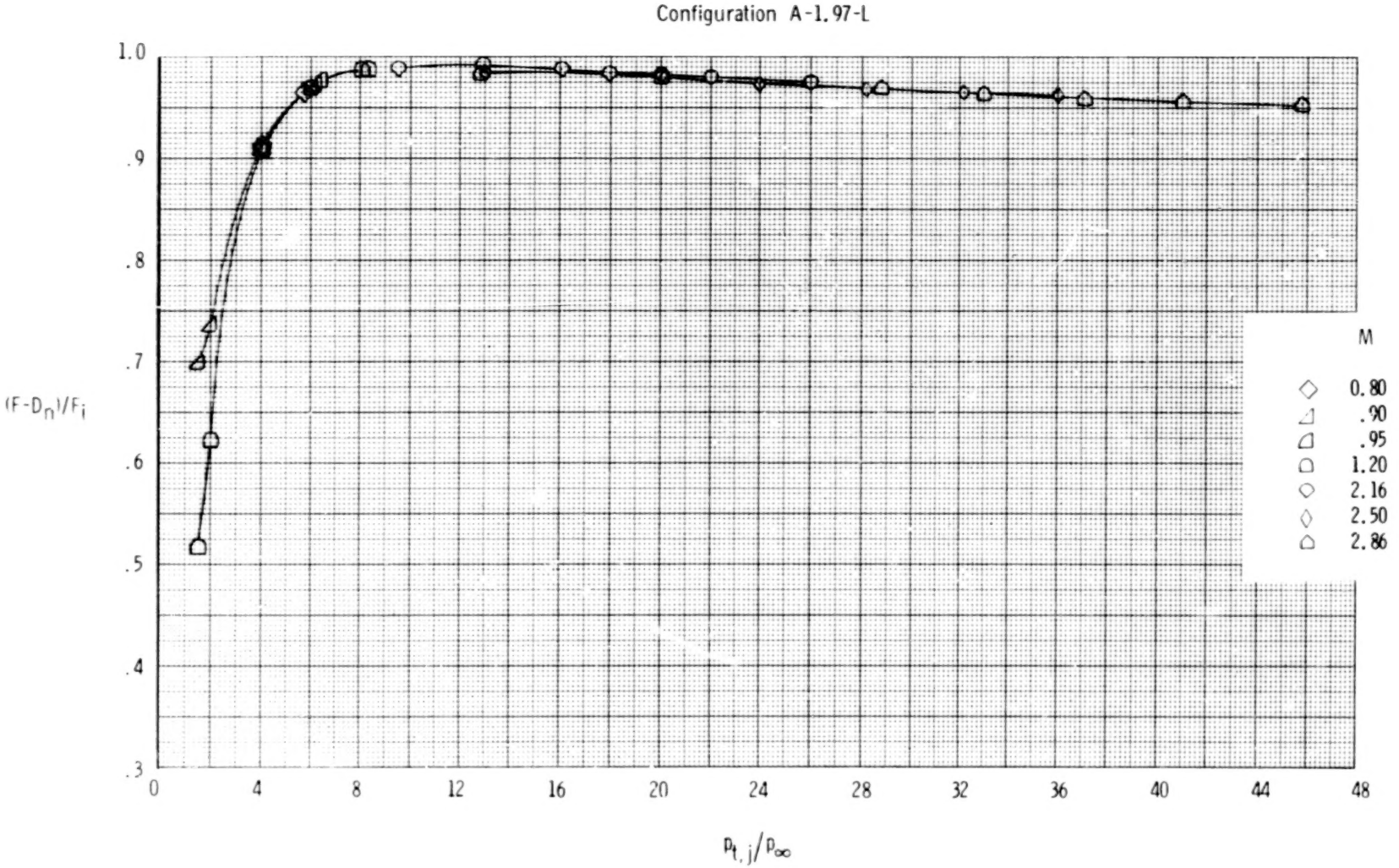

(d) Variation of thrust-minus-drag ratio.

Figure 21.- Concluded.

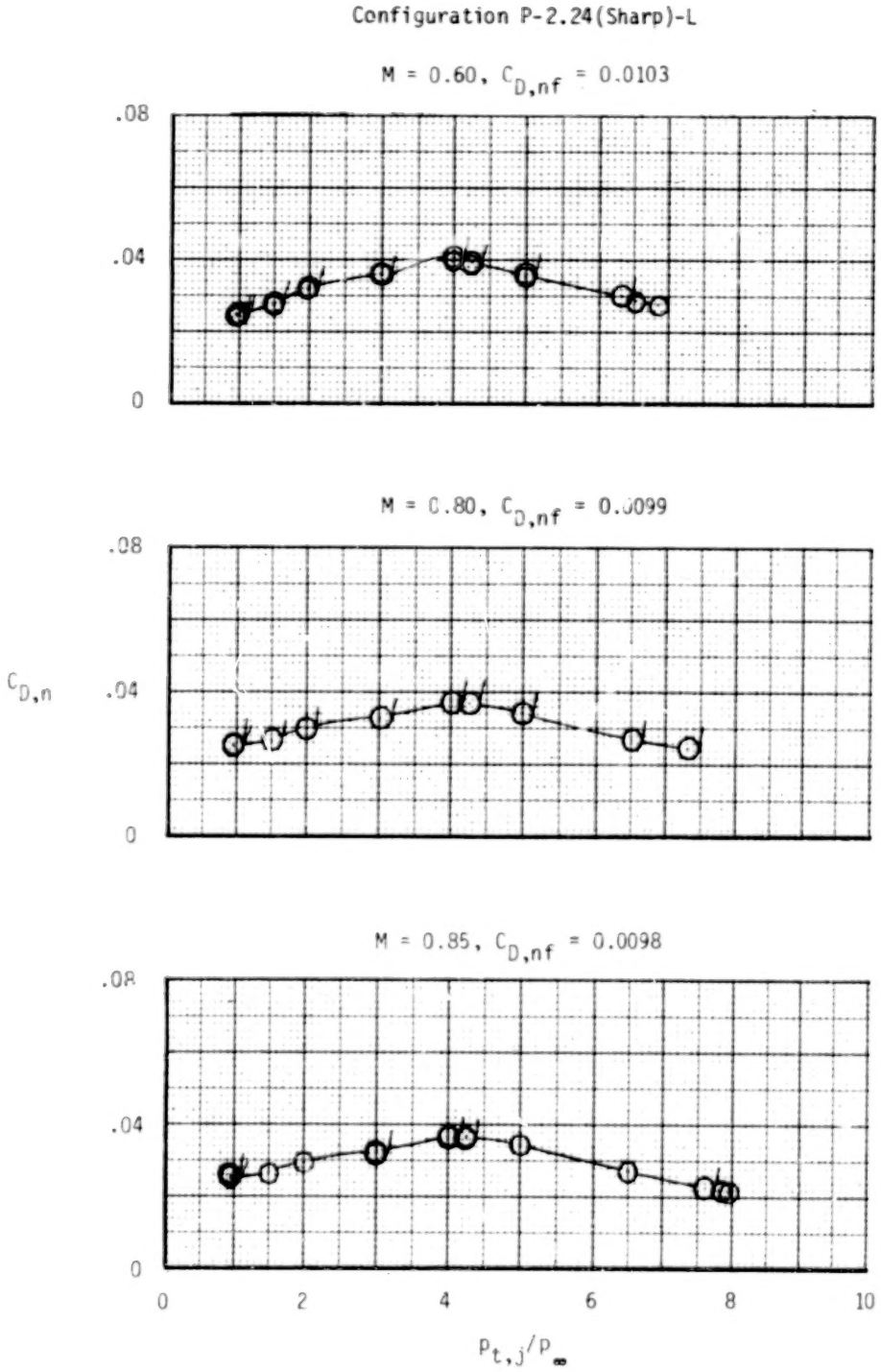

(a) Variation of nozzle drag coefficient.

Figure 22.- Variation of nozzle drag coefficient, thrust-minus-drag ratio, thrust ratio, and mass-flow ratio with nozzle pressure ratio for configuration P-2.24(Sharp)-L. Dashed line indicates theoretical values. Flagged symbols indicate data used to determine F/F_i.

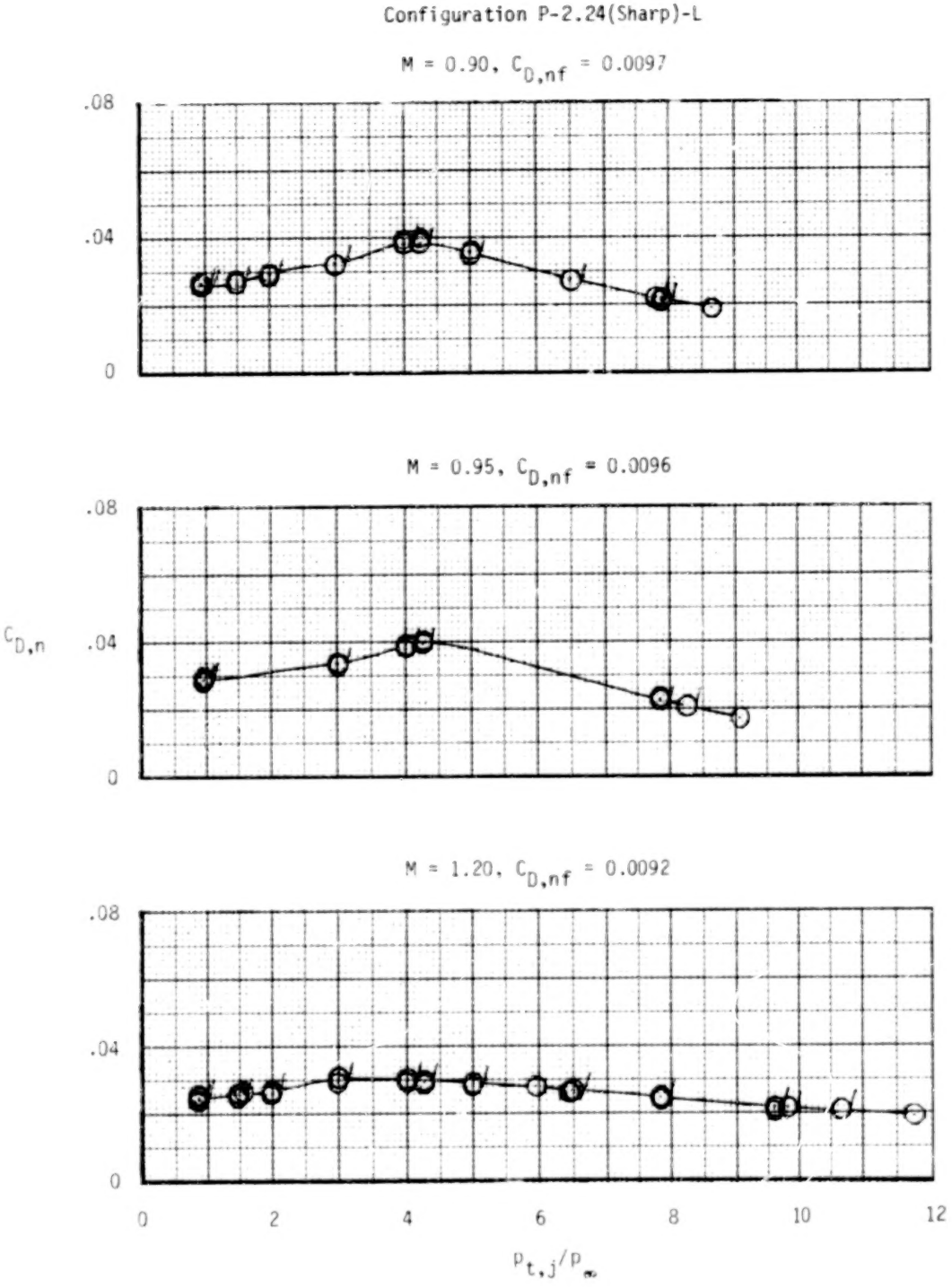

(a) Concluded.

Figure 22.- Continued.

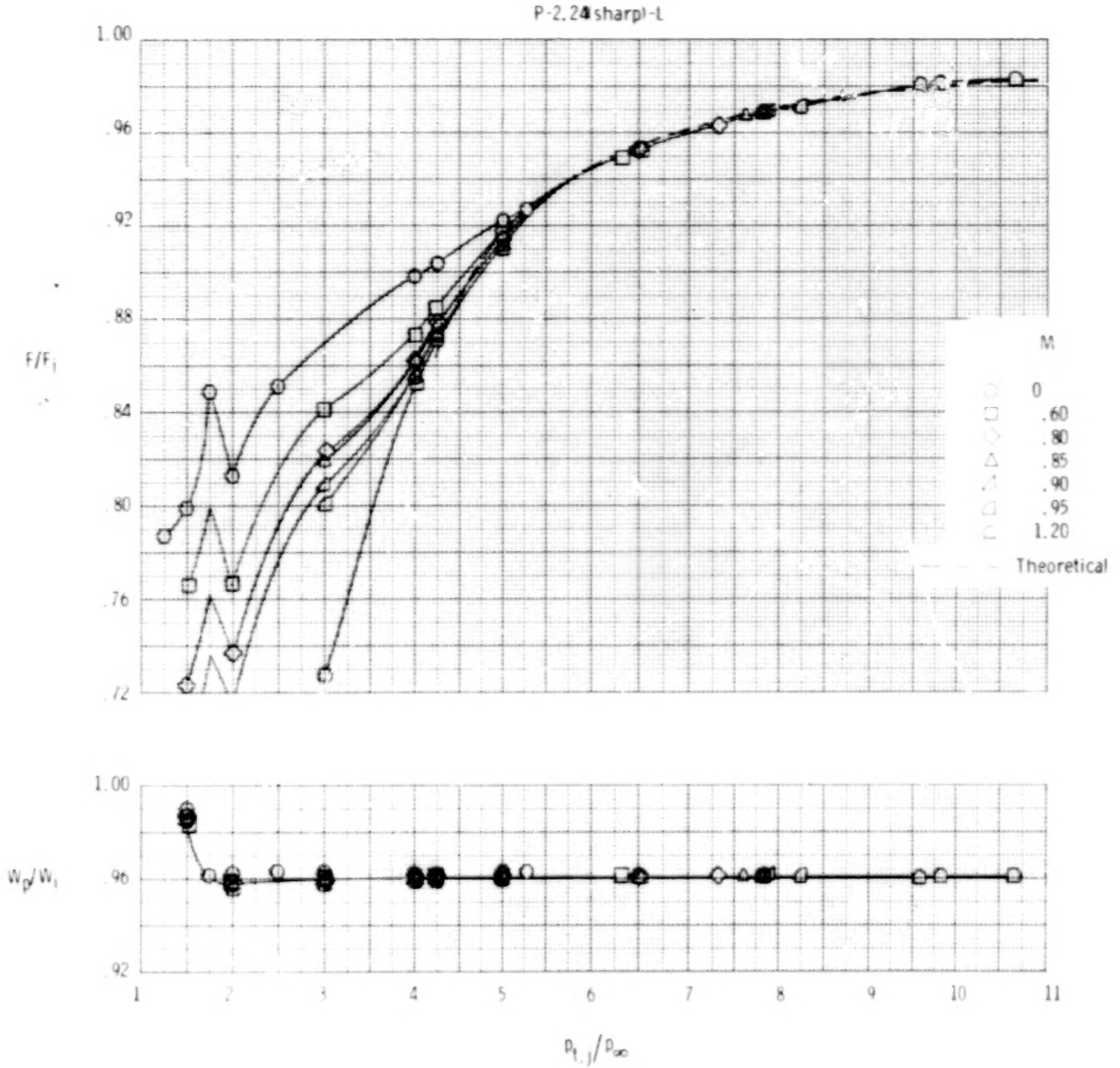

(b) Variation of thrust ratio and mass-flow ratio at subsonic and transonic speeds (16FTT).

Figure 22.- Continued.

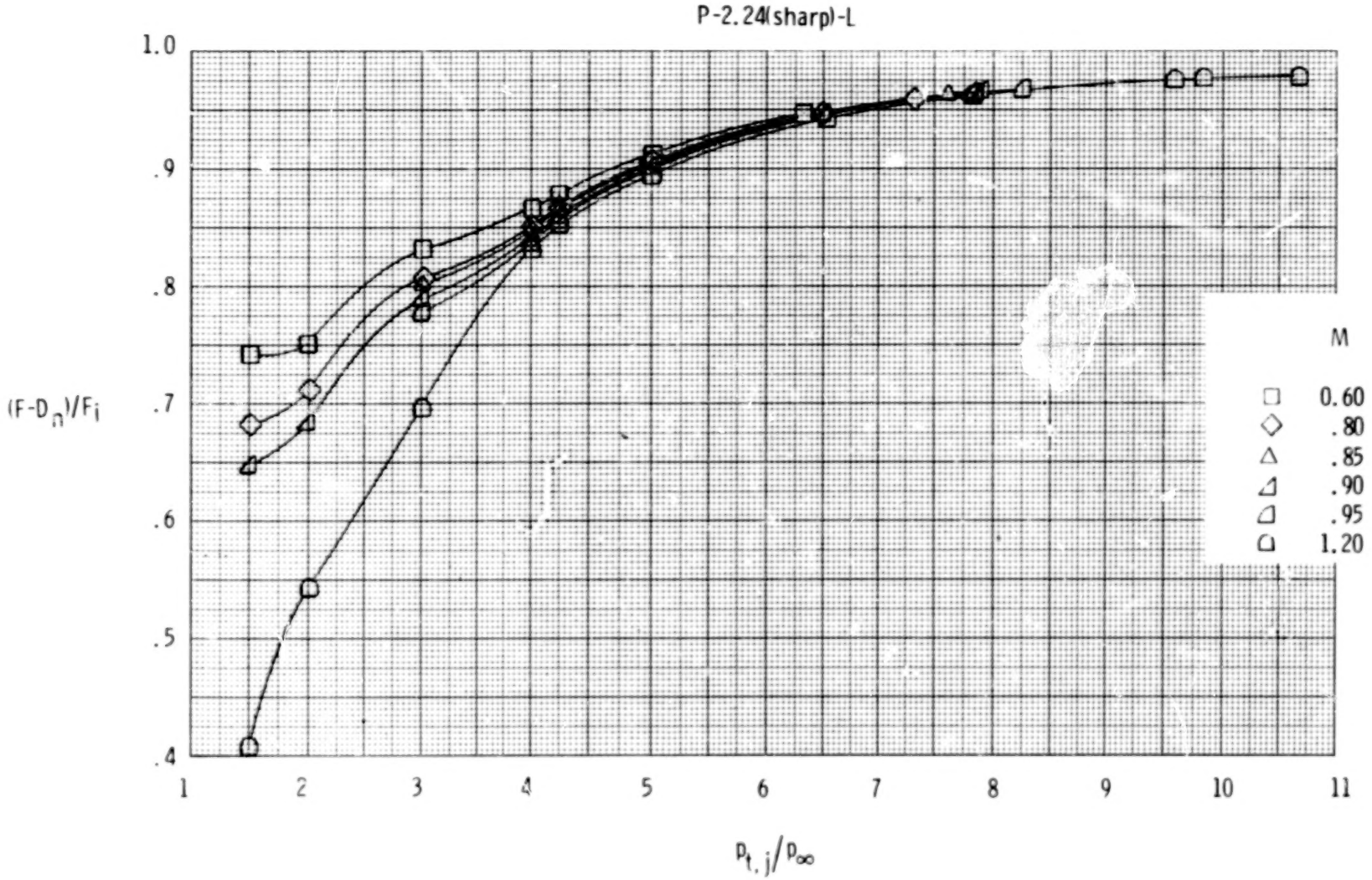

(c) Variation of thrust-minus-drag ratio.

Figure 22.- Concluded.

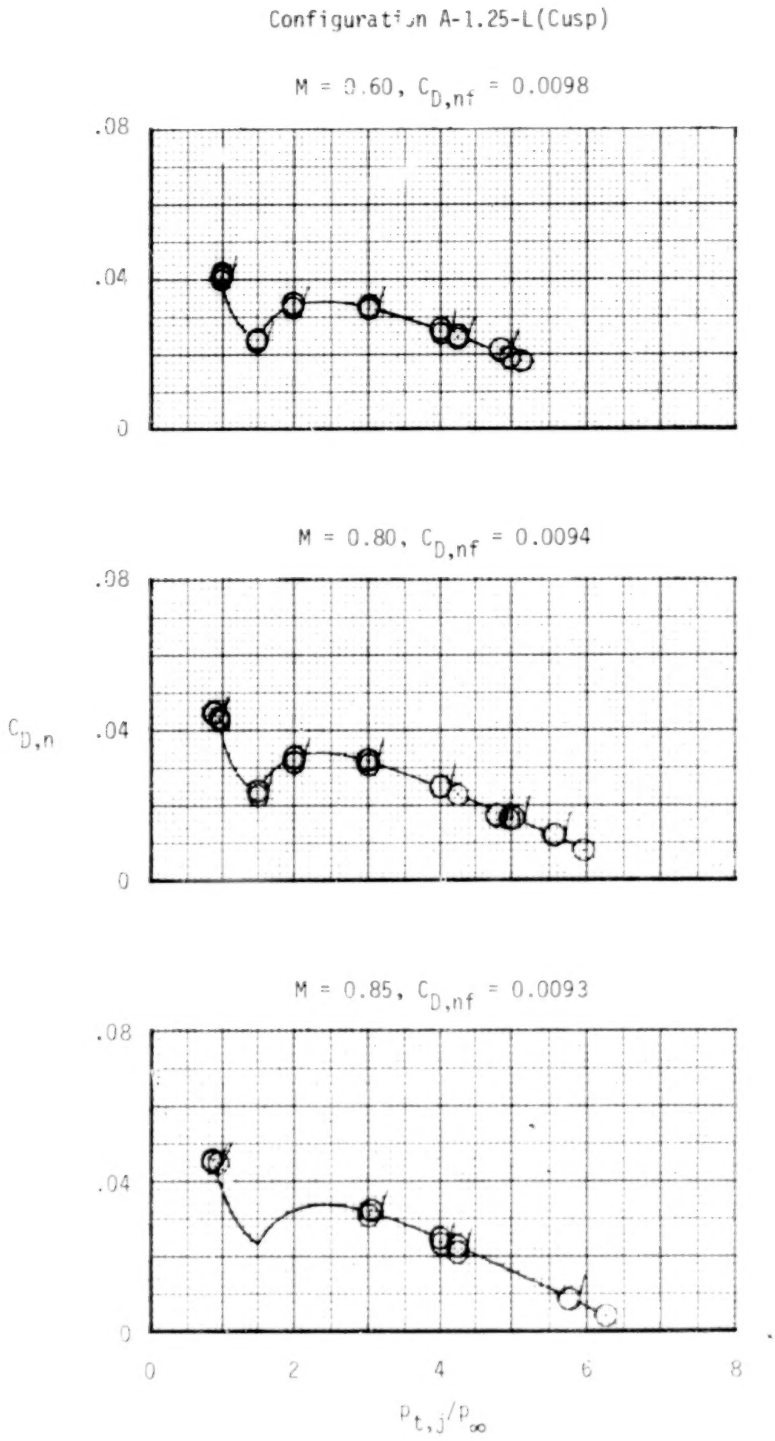

(a) Variation of nozzle drag coefficient.

Figure 23.- Variation of nozzle drag coefficient, thrust-minus-drag ratio, thrust ratio, and mass-flow ratio with nozzle pressure ratio for configuration A-1.25-L(Cusp). Dashed line indicates theoretical values. Flagged symbols indicate data used to determine F/F_i.

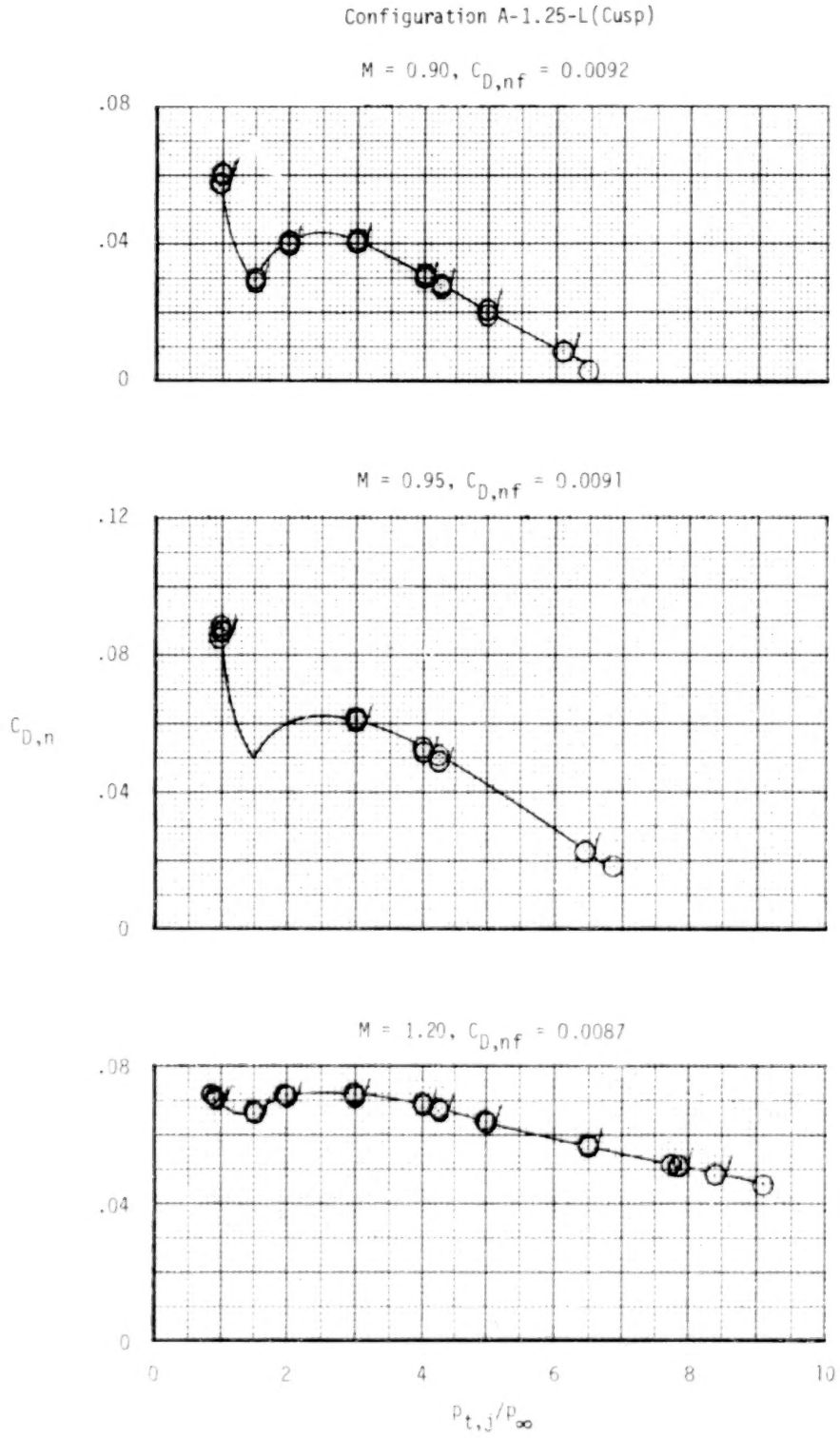

(a) Continued.

Figure 23.- Continued.

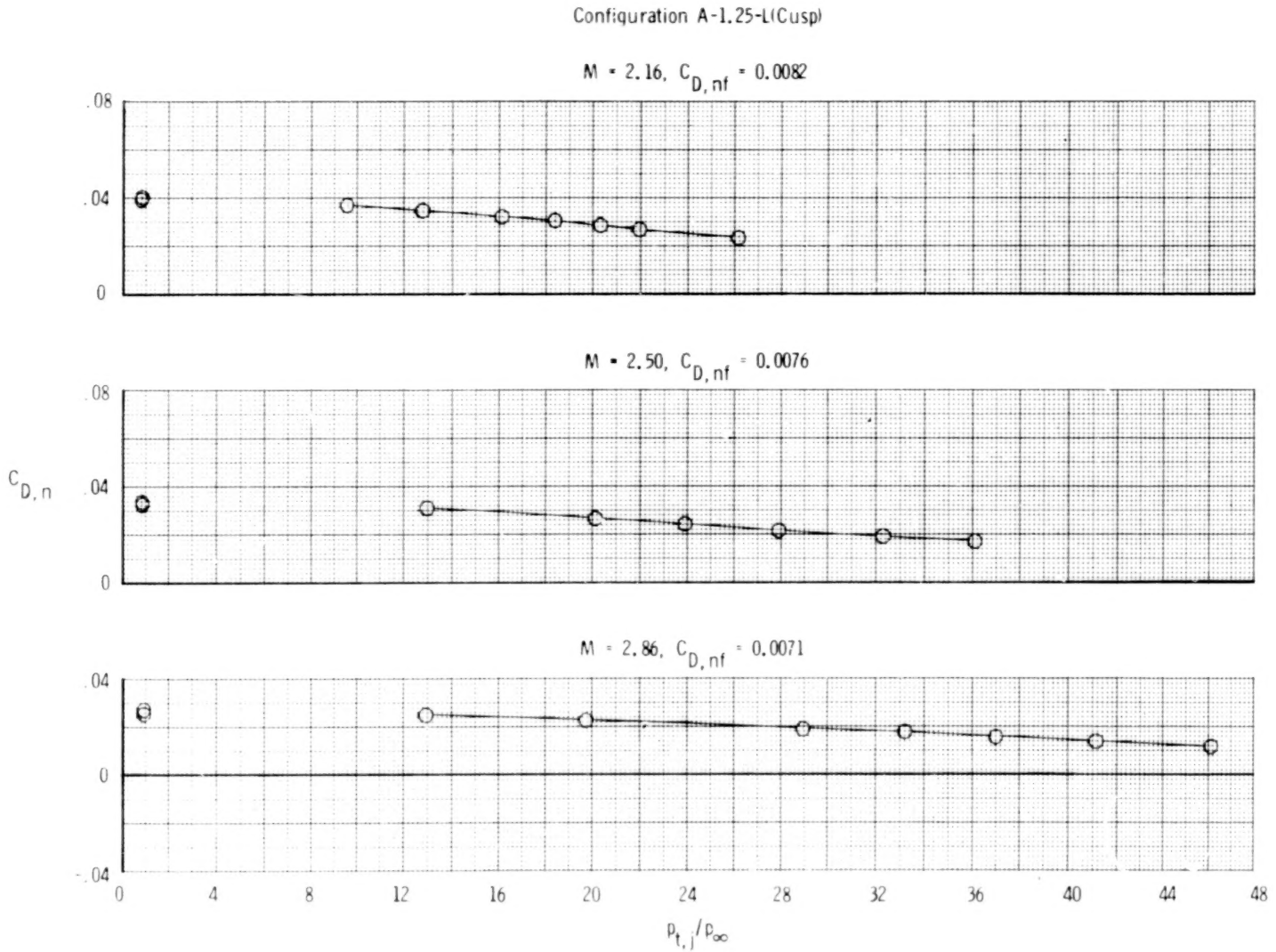

(a) Concluded.

Figure 23.- Continued.

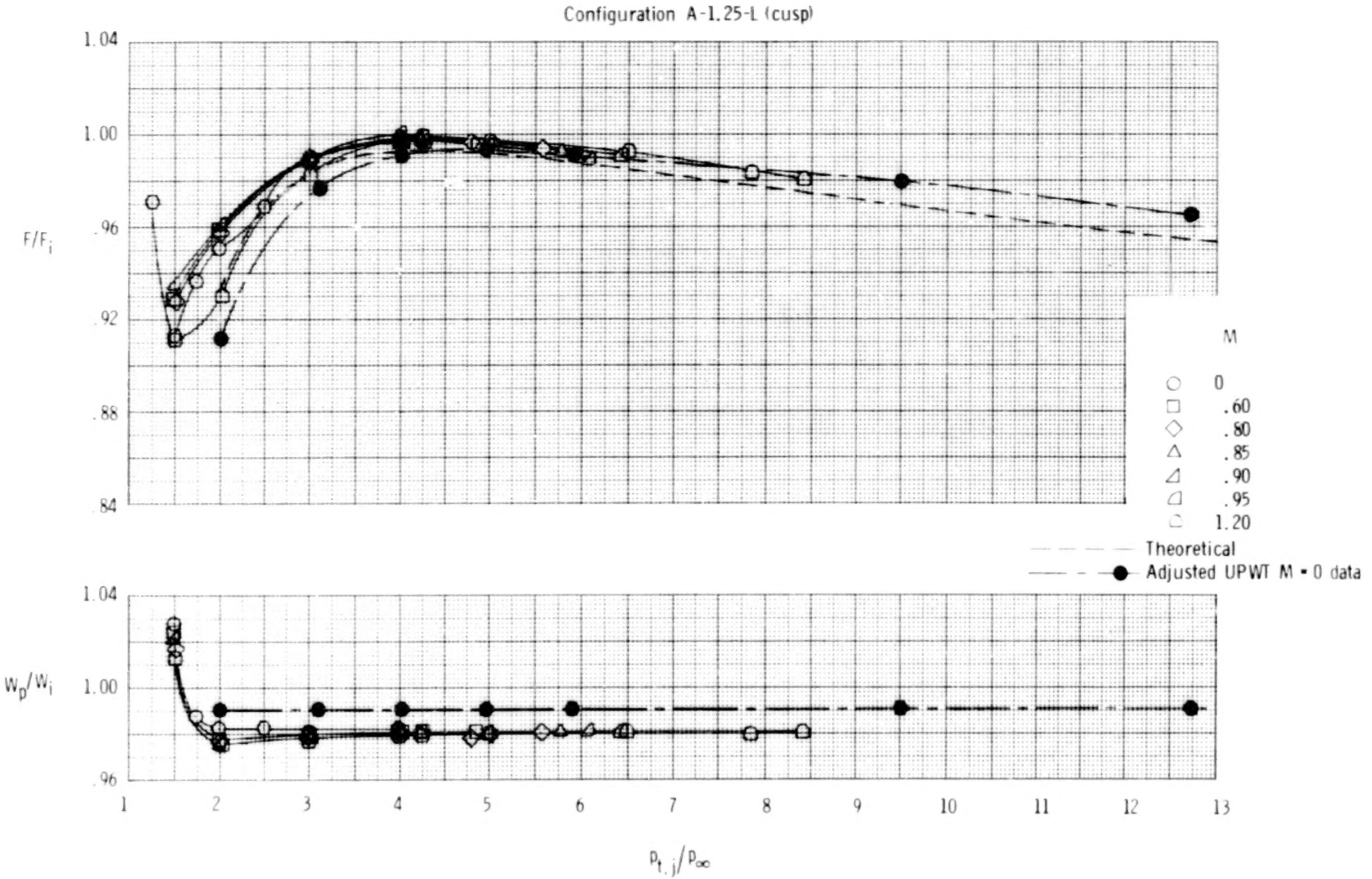

(b) Variation of thrust ratio and mass-flow ratio at subsonic and transonic speeds (16FTT).

Figure 23.- Continued.

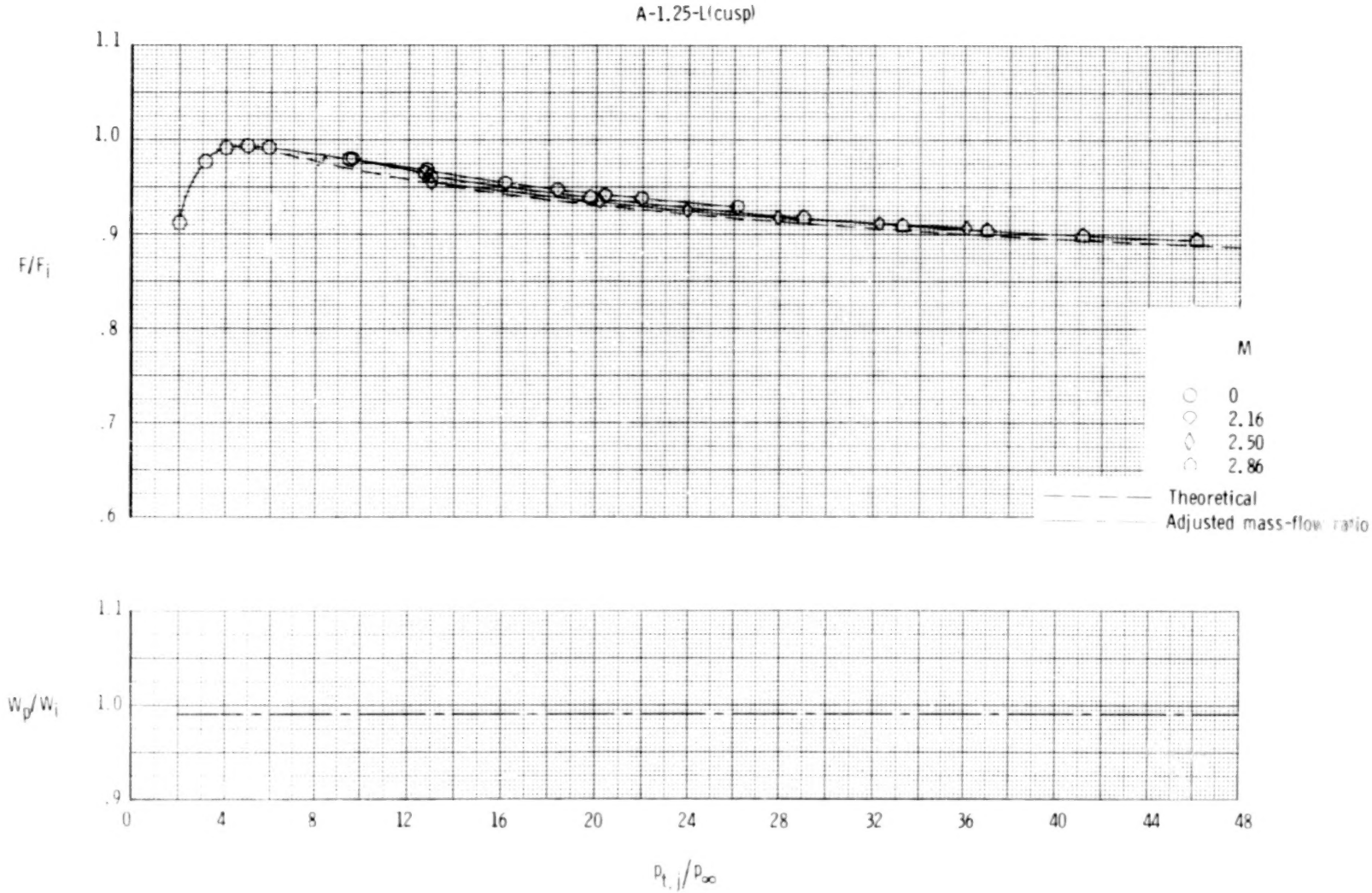

(c) Variation of thrust ratio and mass-flow ratio at supersonic speeds (UPWT).

Figure 23.- Continued.

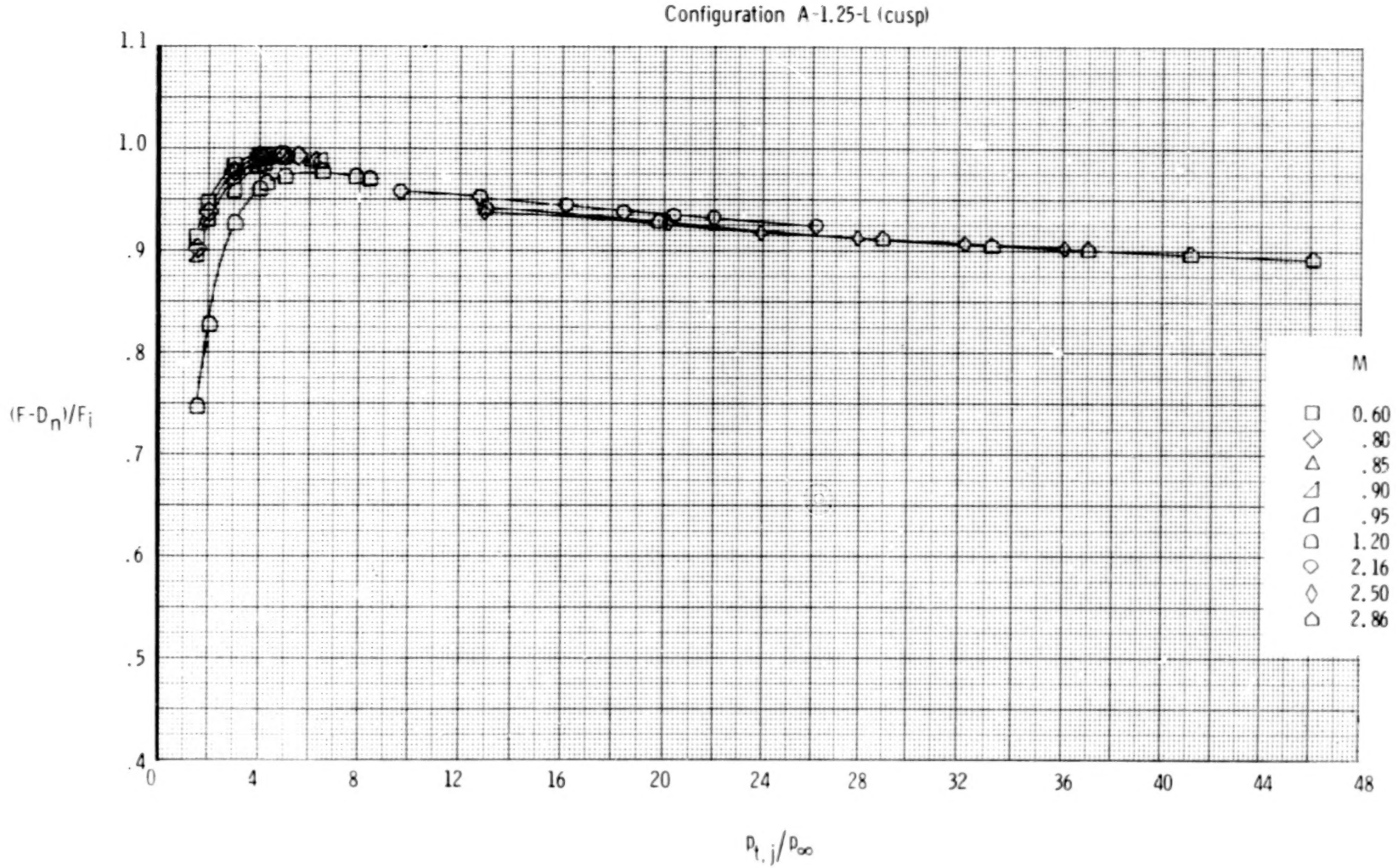

(d) Variation of thrust-minus-drag ratio.

Figure 23.- Concluded.

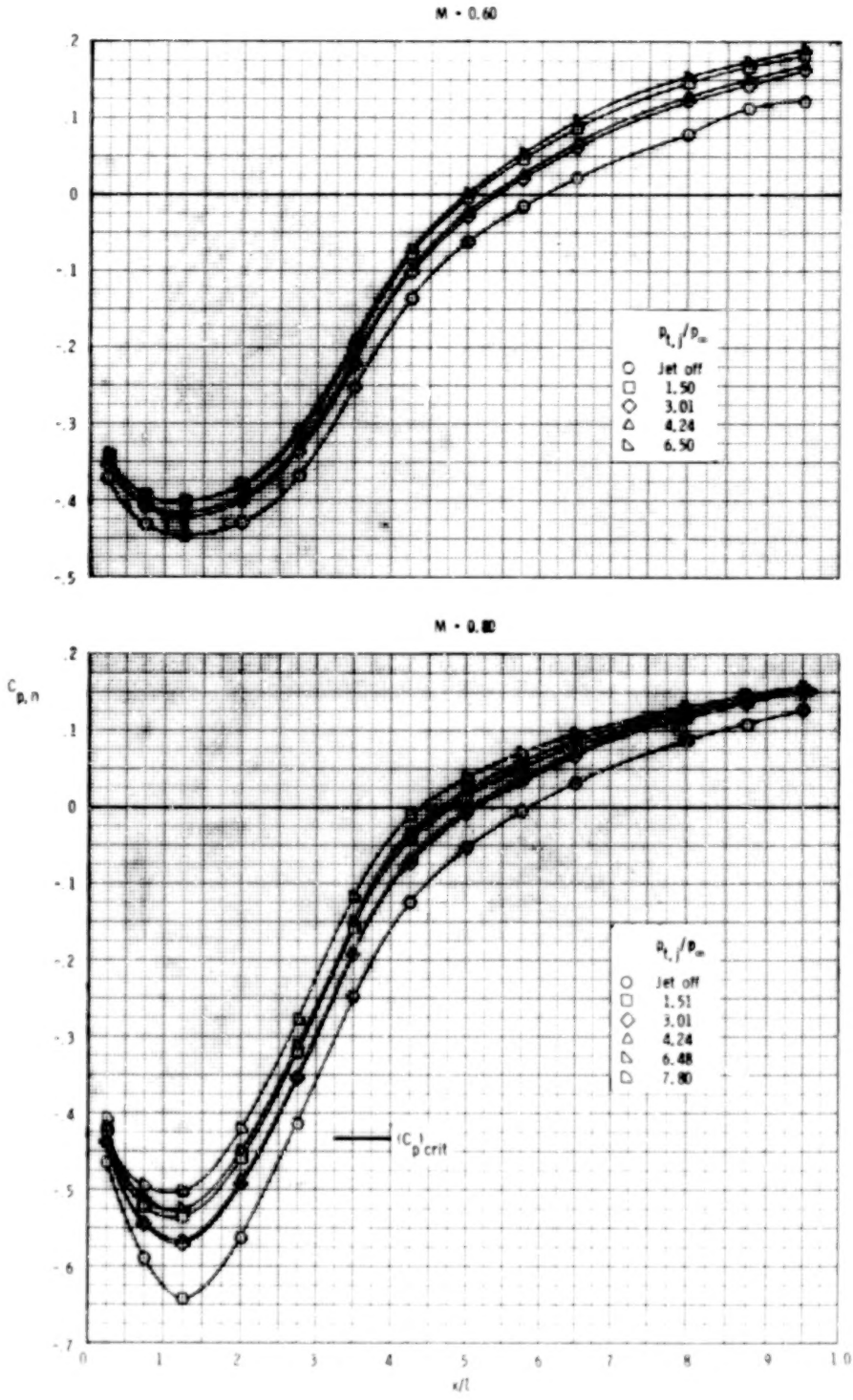

(a) M = 0.60 and 0.80.

Figure 24.- Nozzle pressure-coefficient distributions for configuration D-1.22-S. Dashed line indicates theoretical values.

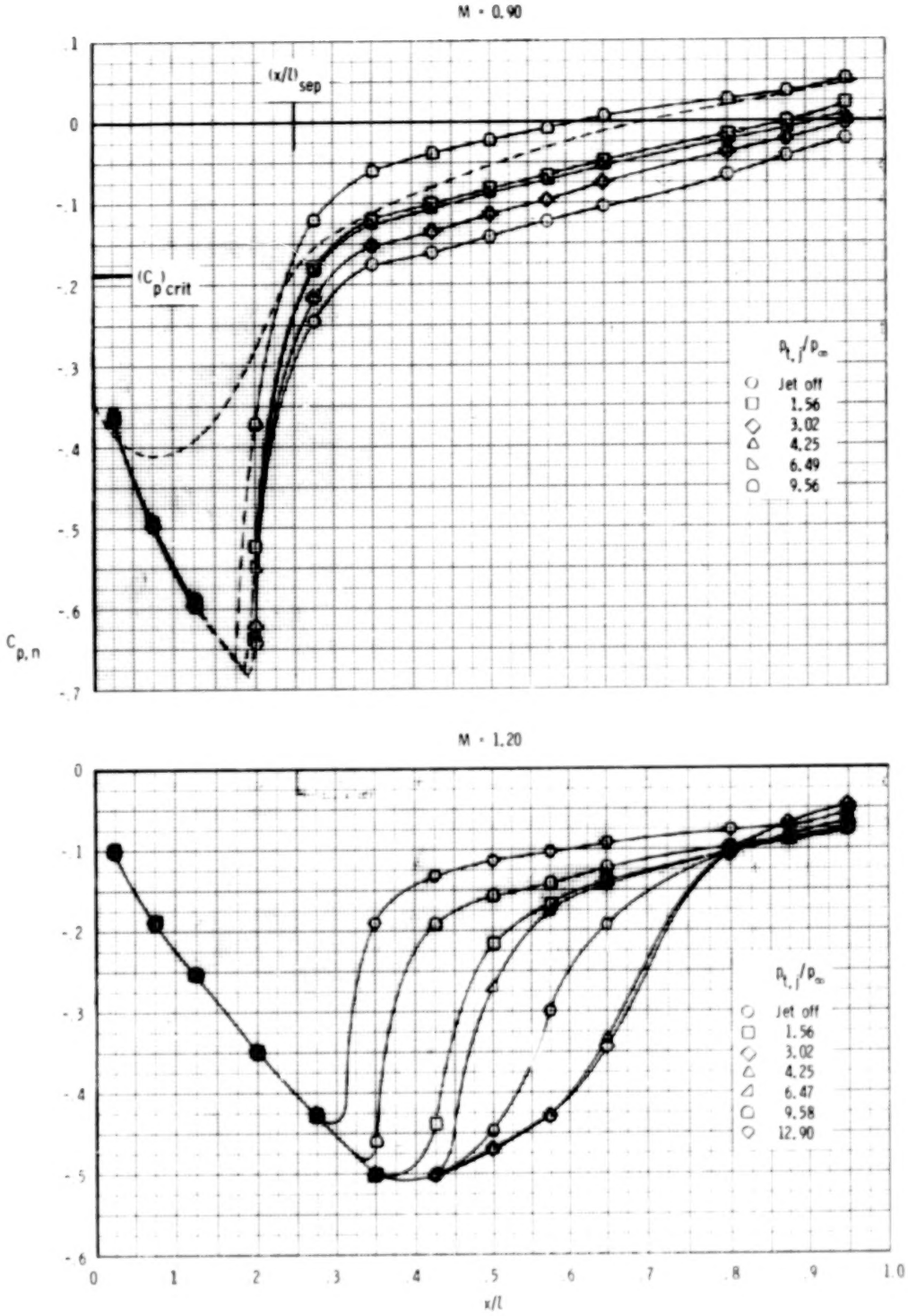

(b) M = 0.90 and 1.20.

Figure 24.- Continued.

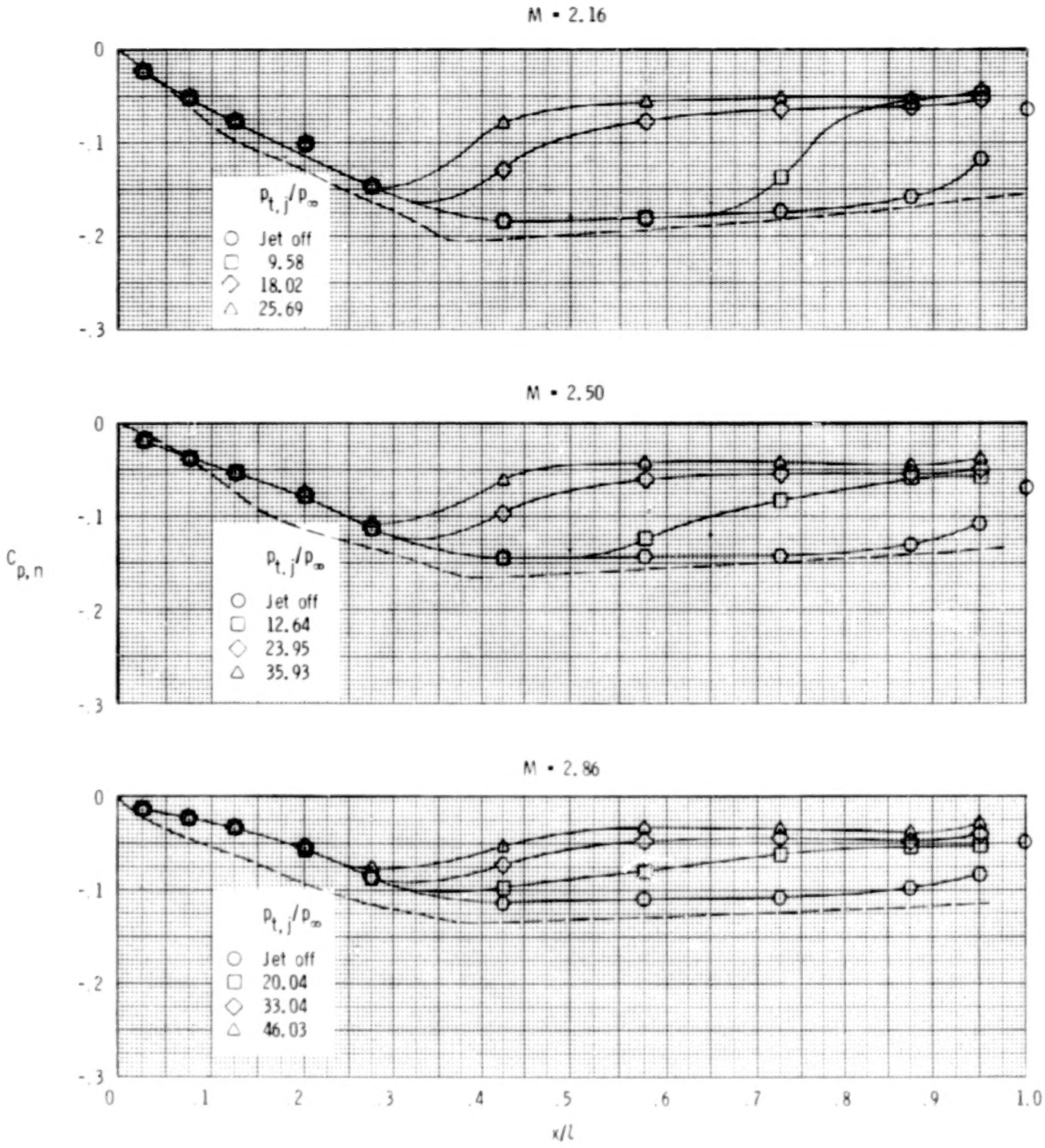

(c) M = 2.16 to 2.86.

Figure 24.- Concluded.

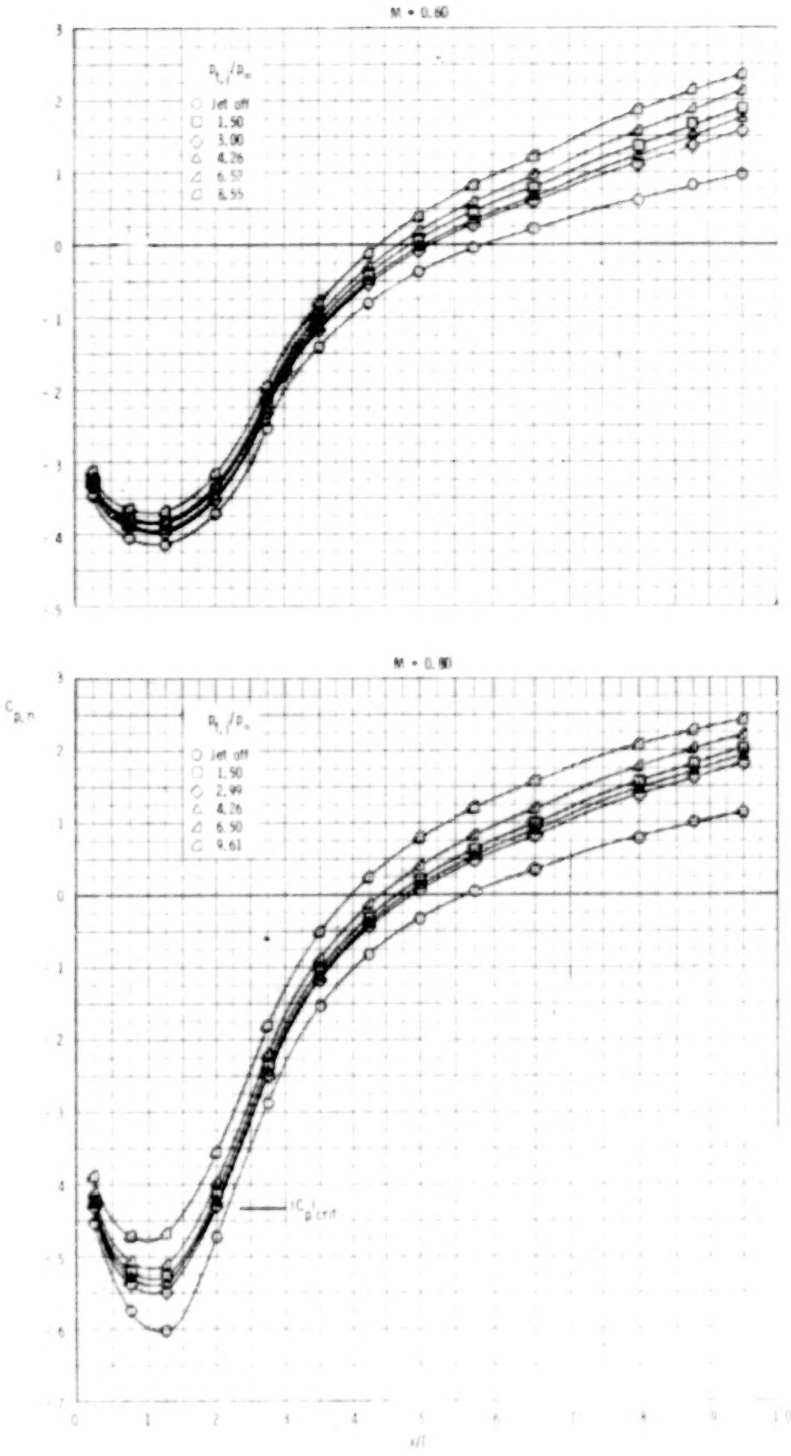

(a) M = 0.60 and 0.80.

Figure 25.- Nozzle pressure-coefficient distributions for configuration D-1.22-M. Dashed line indicates theoretical values.

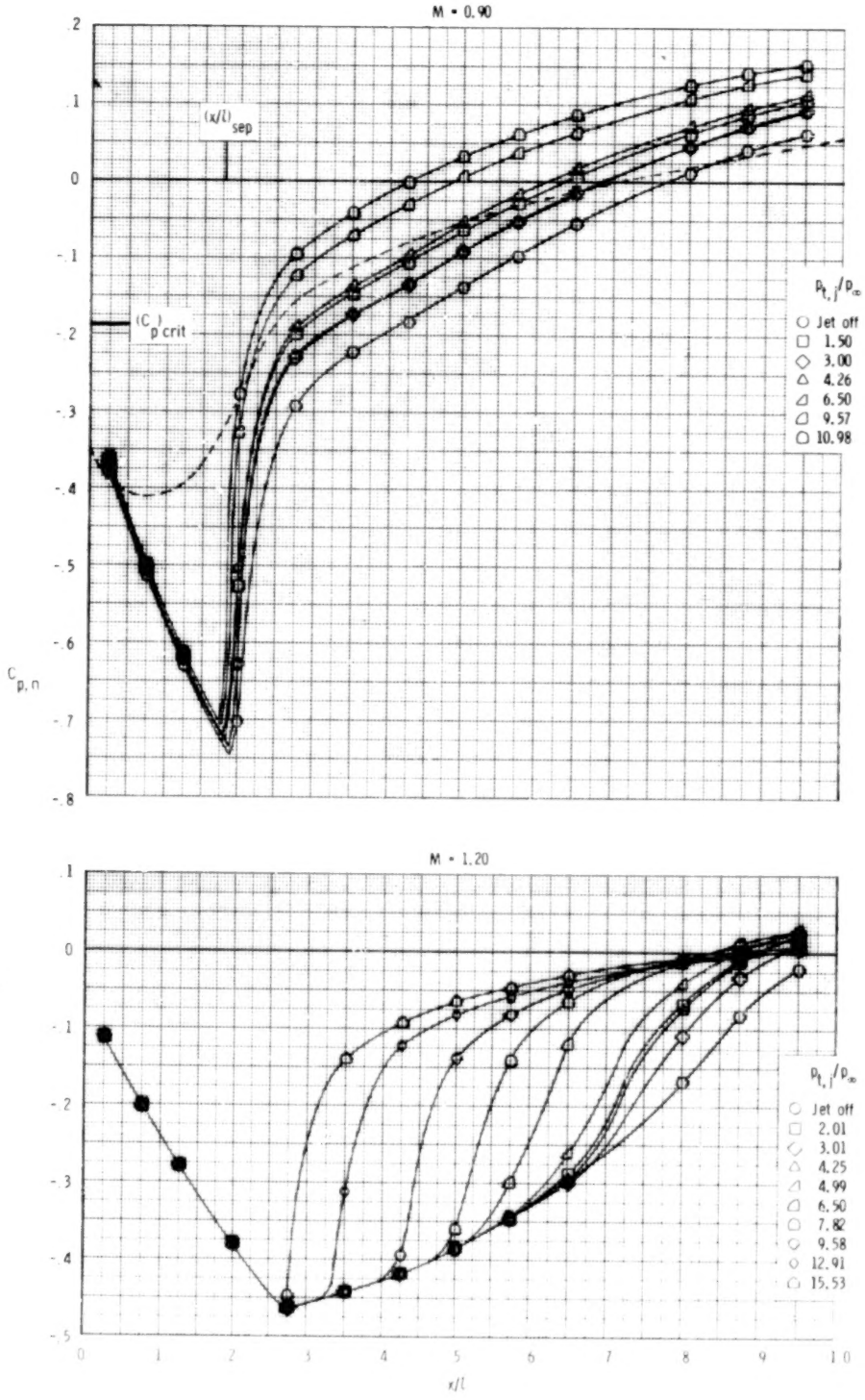

(b) M = 0.90 and 1.20.

Figure 25.- Continued.

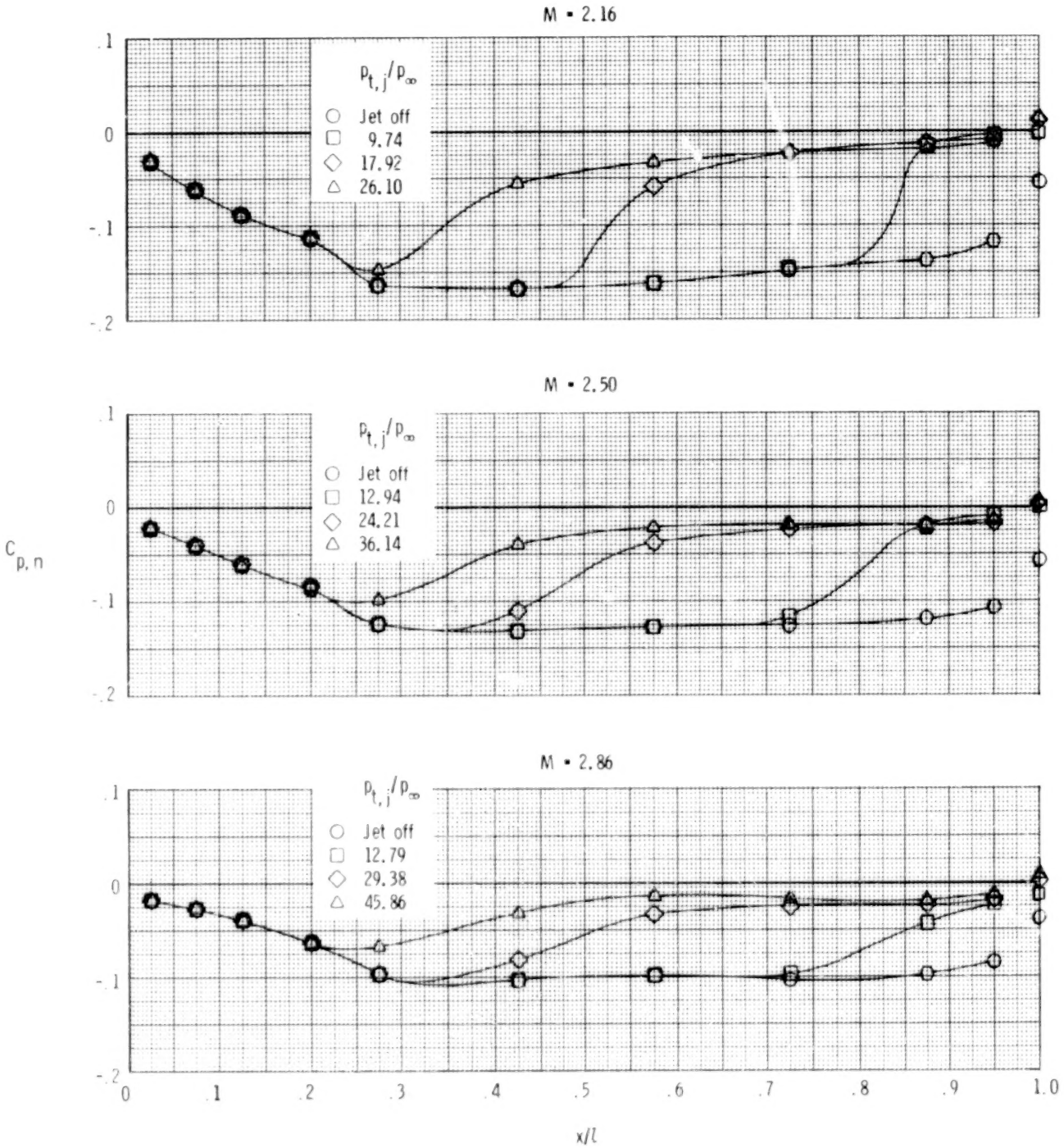

(c) M = 2.16 to 2.86.

Figure 25.- Concluded.

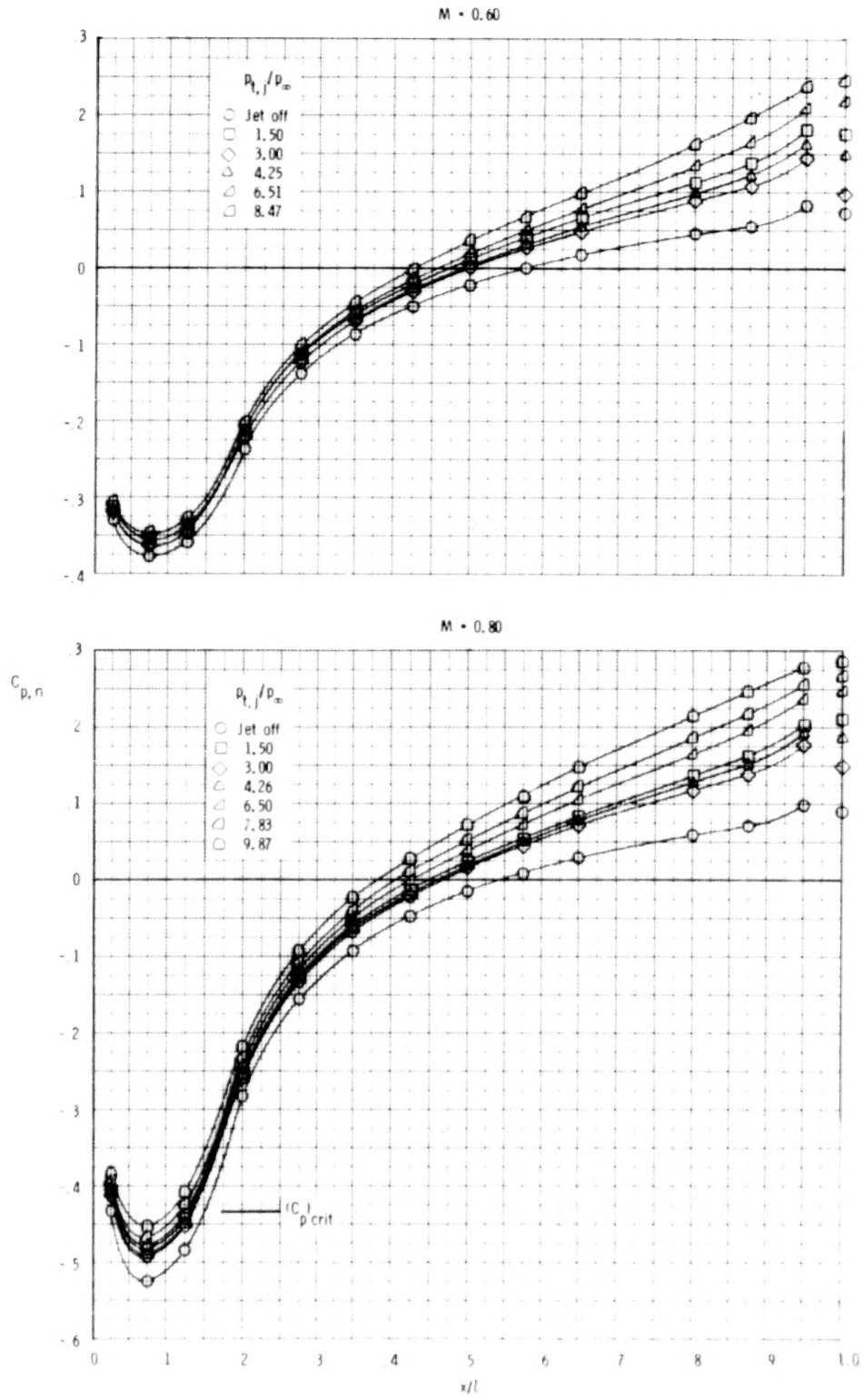

(a) M = 0.60 and 0.80.

Figure 26.- Nozzle pressure-coefficient distributions for configuration D-1.22-L. Dashed line indicates theoretical values.

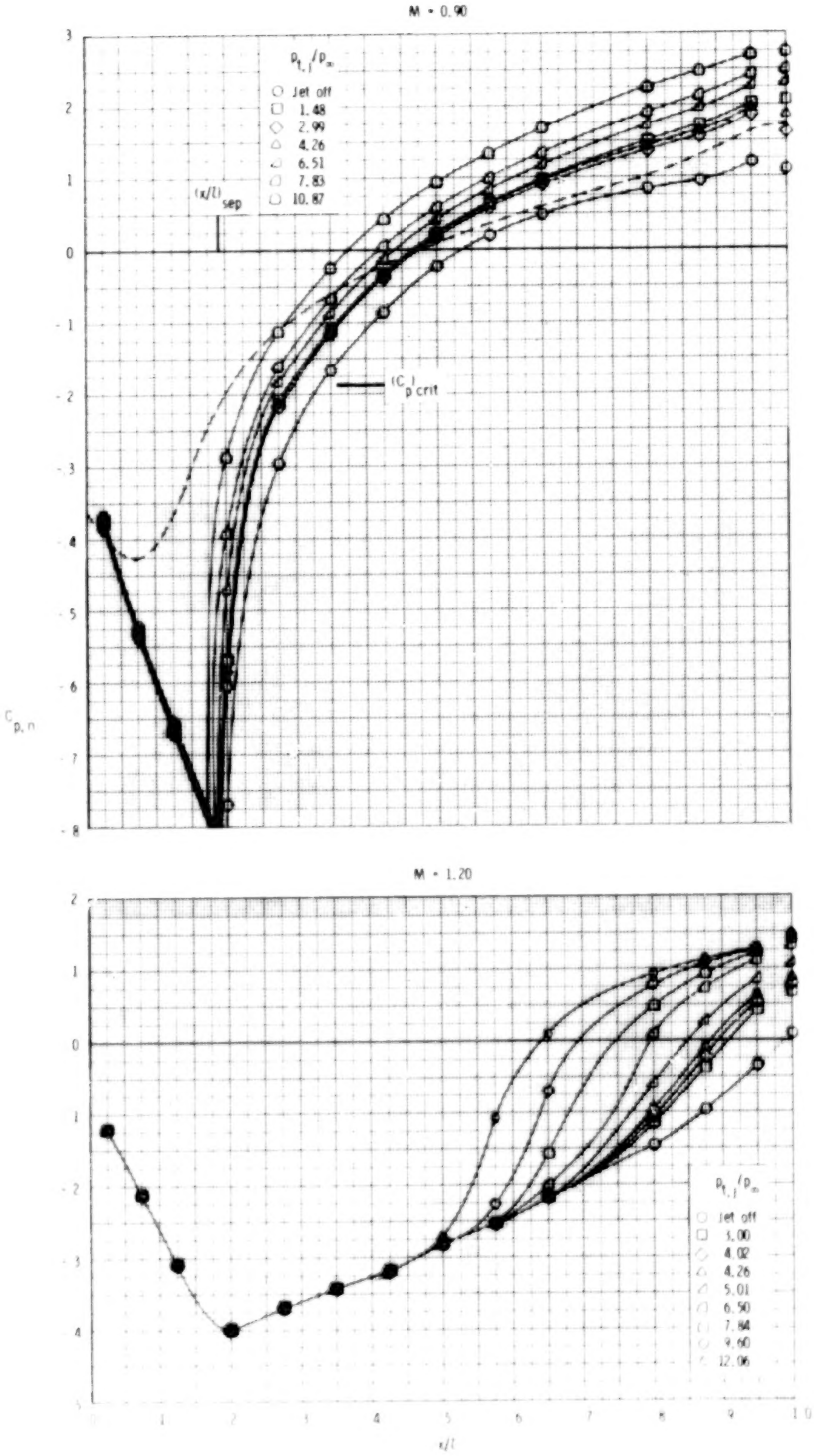

(b) M = 0.90 and 1.20.

Figure 26.- Continued.

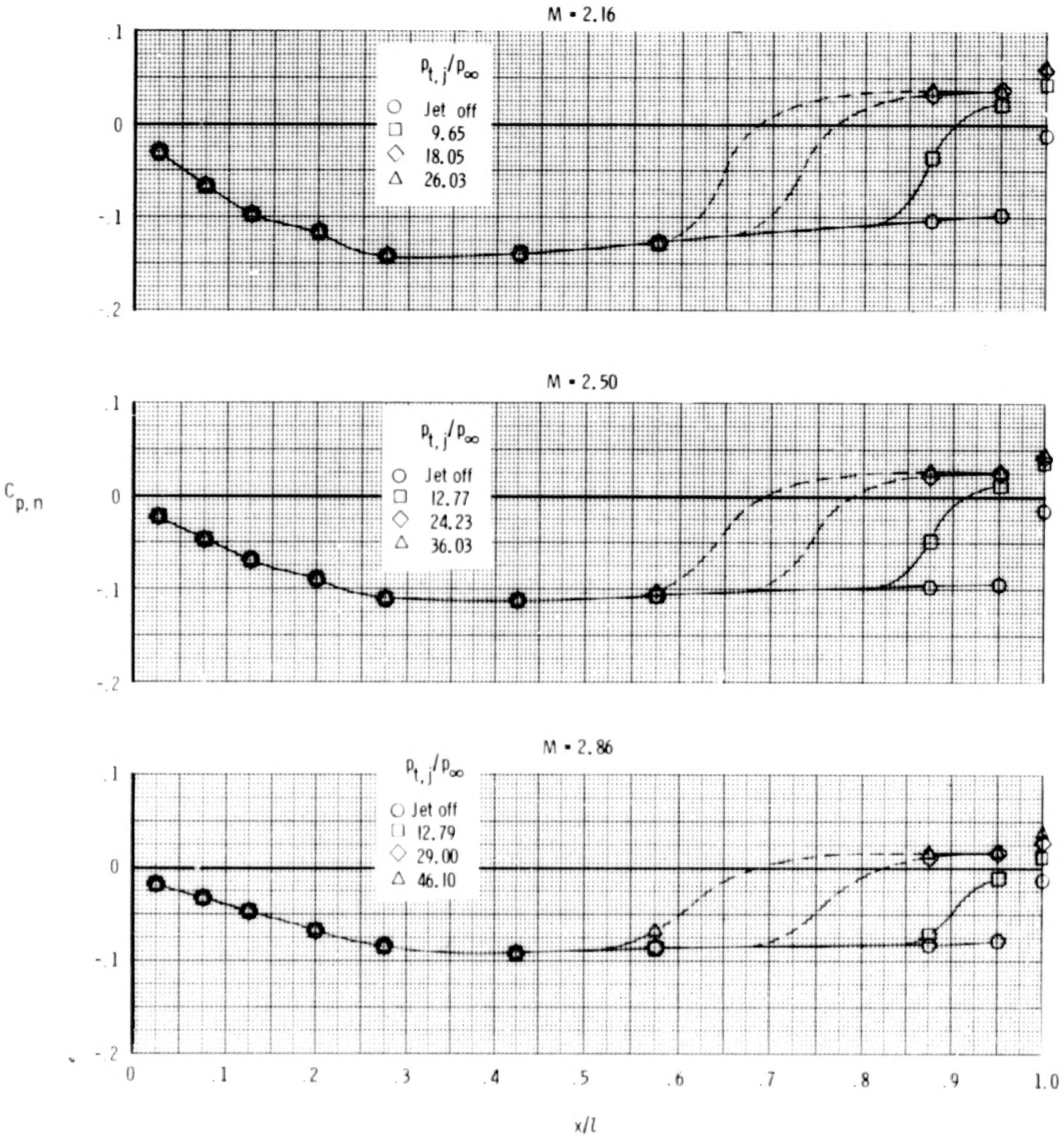

(c) M = 2.16 to 2.86.

Figure 26.- Concluded.

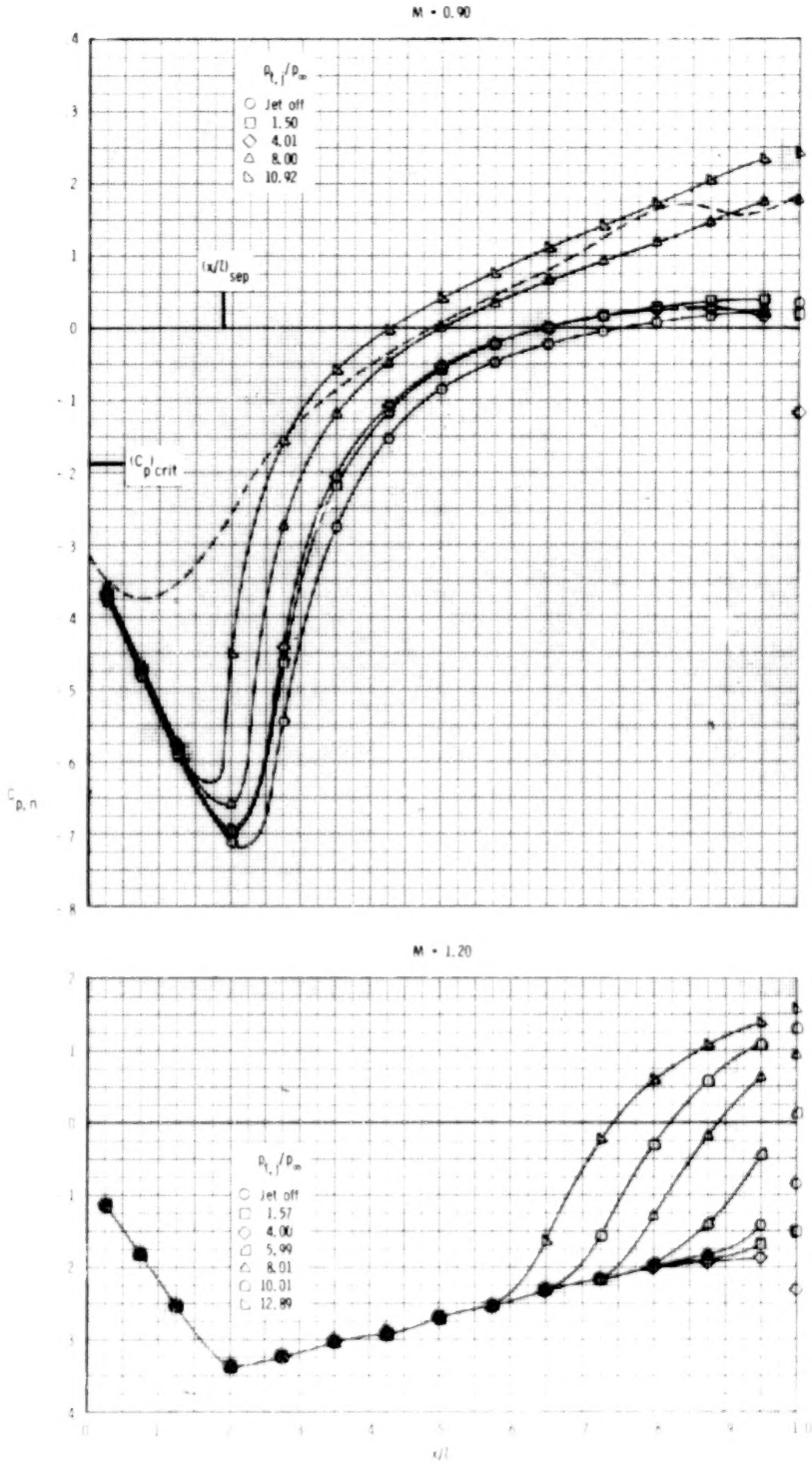

(a) M = 0.90 and 1.20.

Figure 27.- Nozzle pressure-coefficient distributions for configuration D-2.24-S. Dashed line indicates theoretical values.

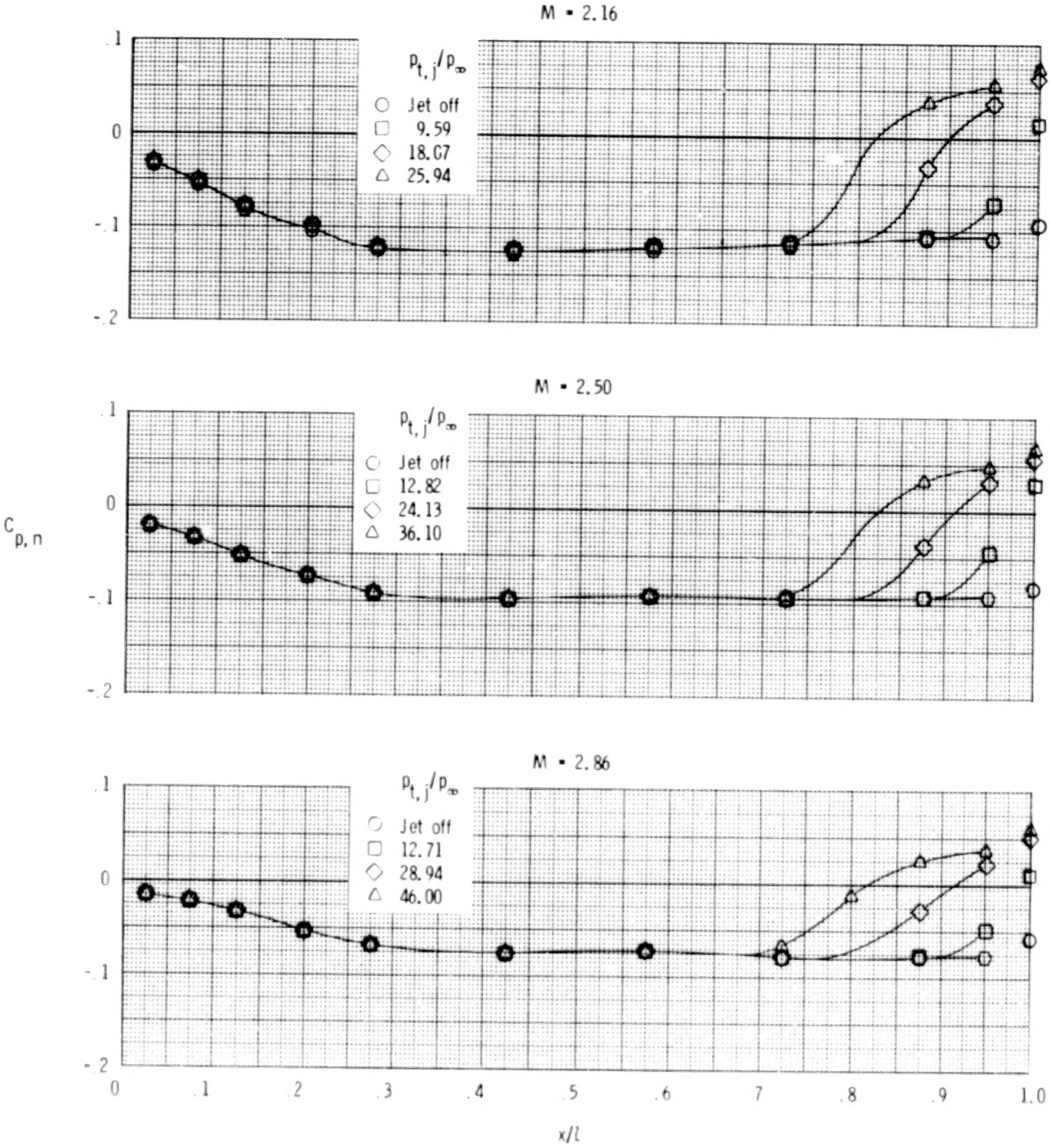

(b) M = 2.16 to 2.86.

Figure 27.- Concluded.

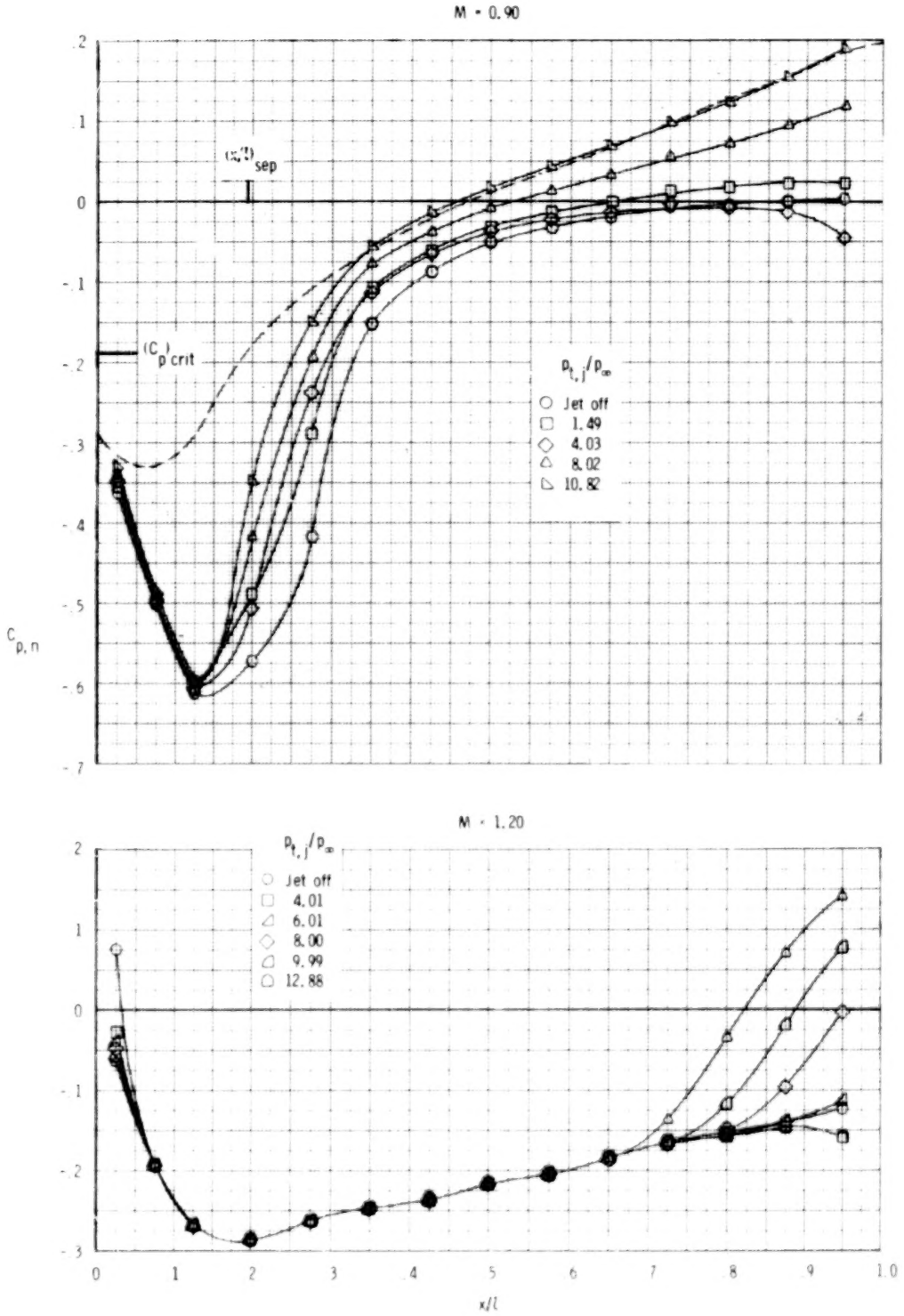

(a) M = 0.90 and 1.20.

Figure 28.- Nozzle pressure-coefficient distributions for configuration D-2.24-M. Dashed line indicates theoretical values.

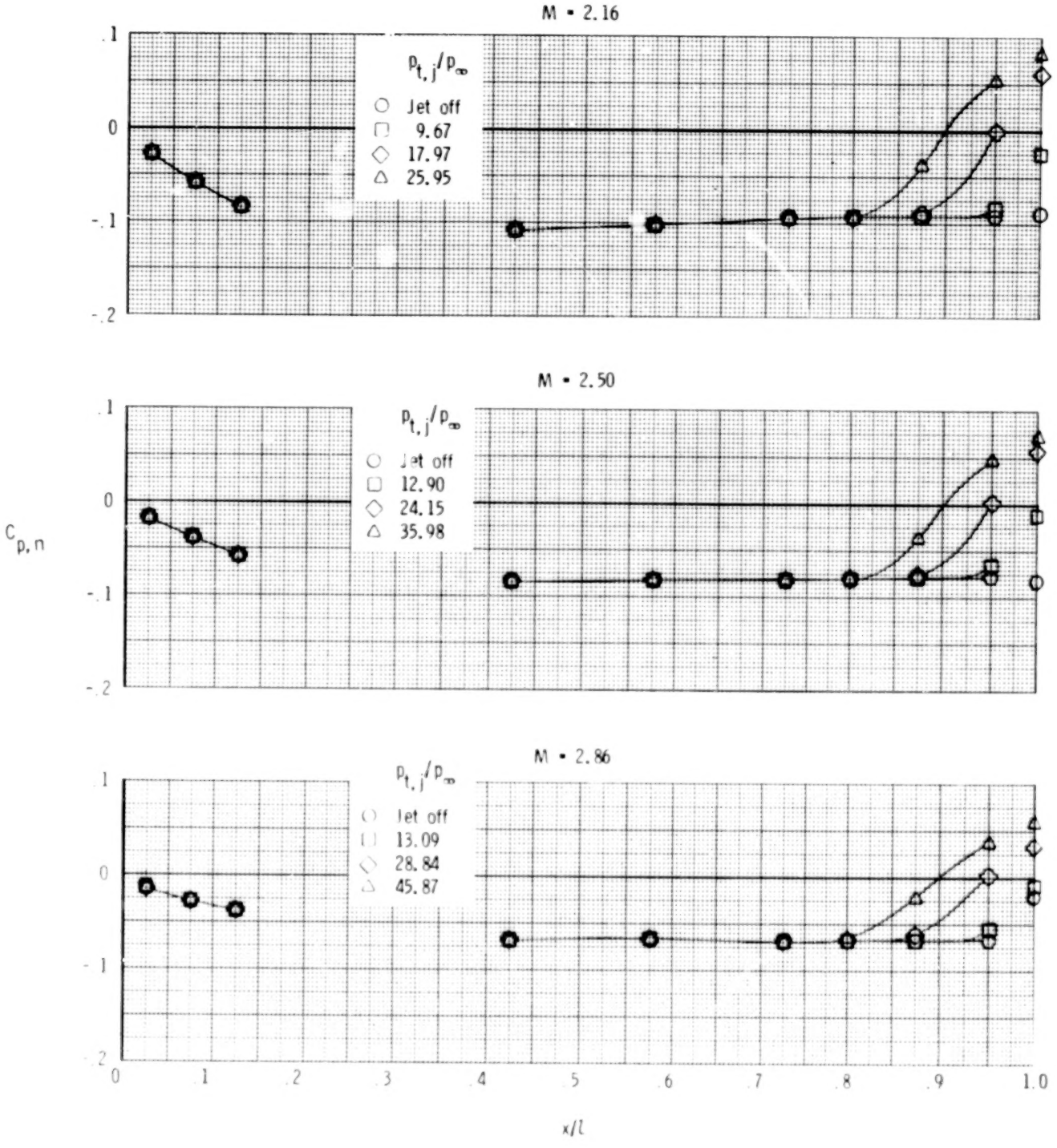

(b) M = 2.16 to 2.86.

Figure 28.- Concluded.

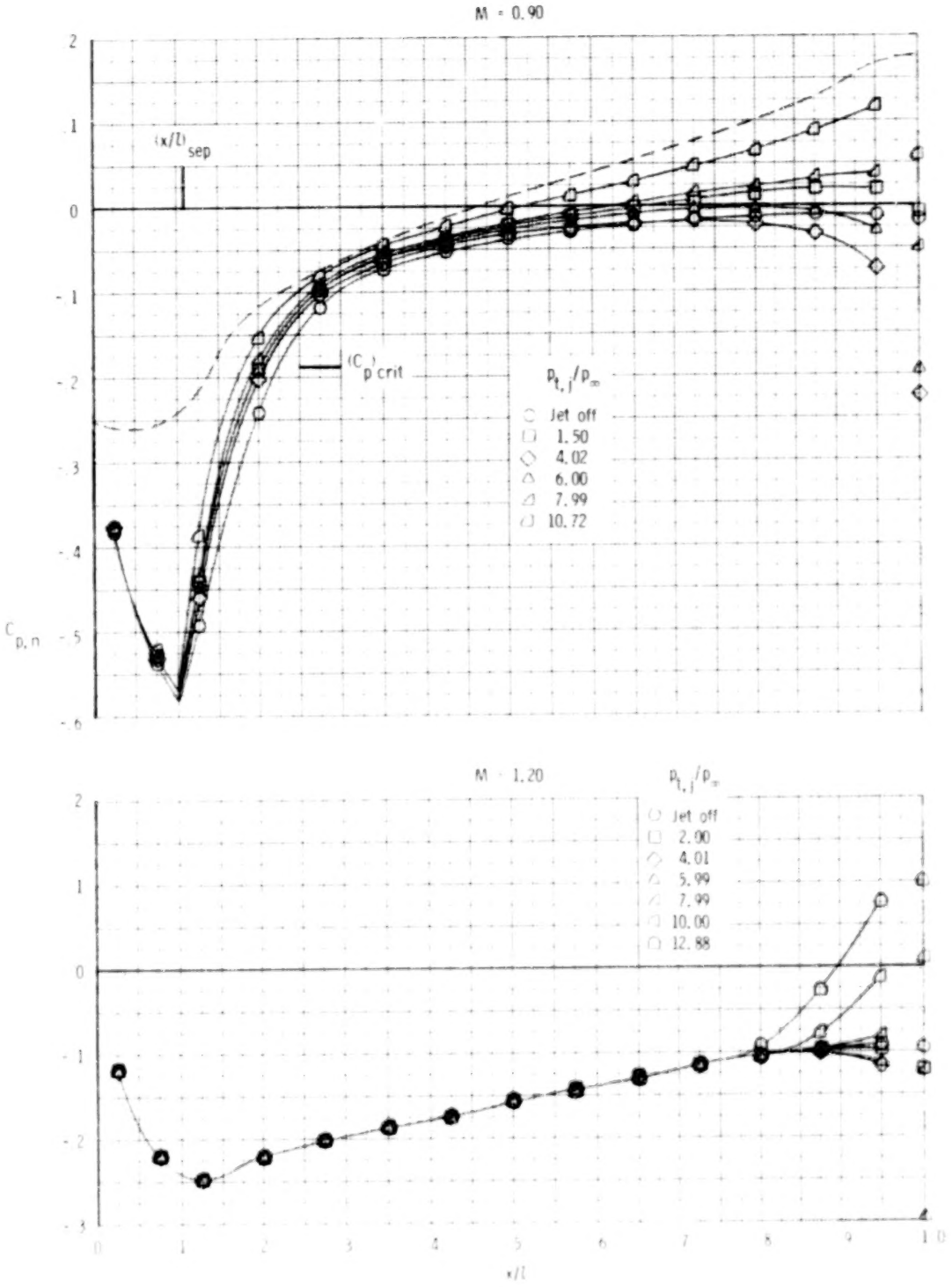

(a) M = 0.90 and 1.20.

Figure 29.- Nozzle pressure-coefficient distributions for configuration D-2.24-L. Dashed line indicates theoretical values.

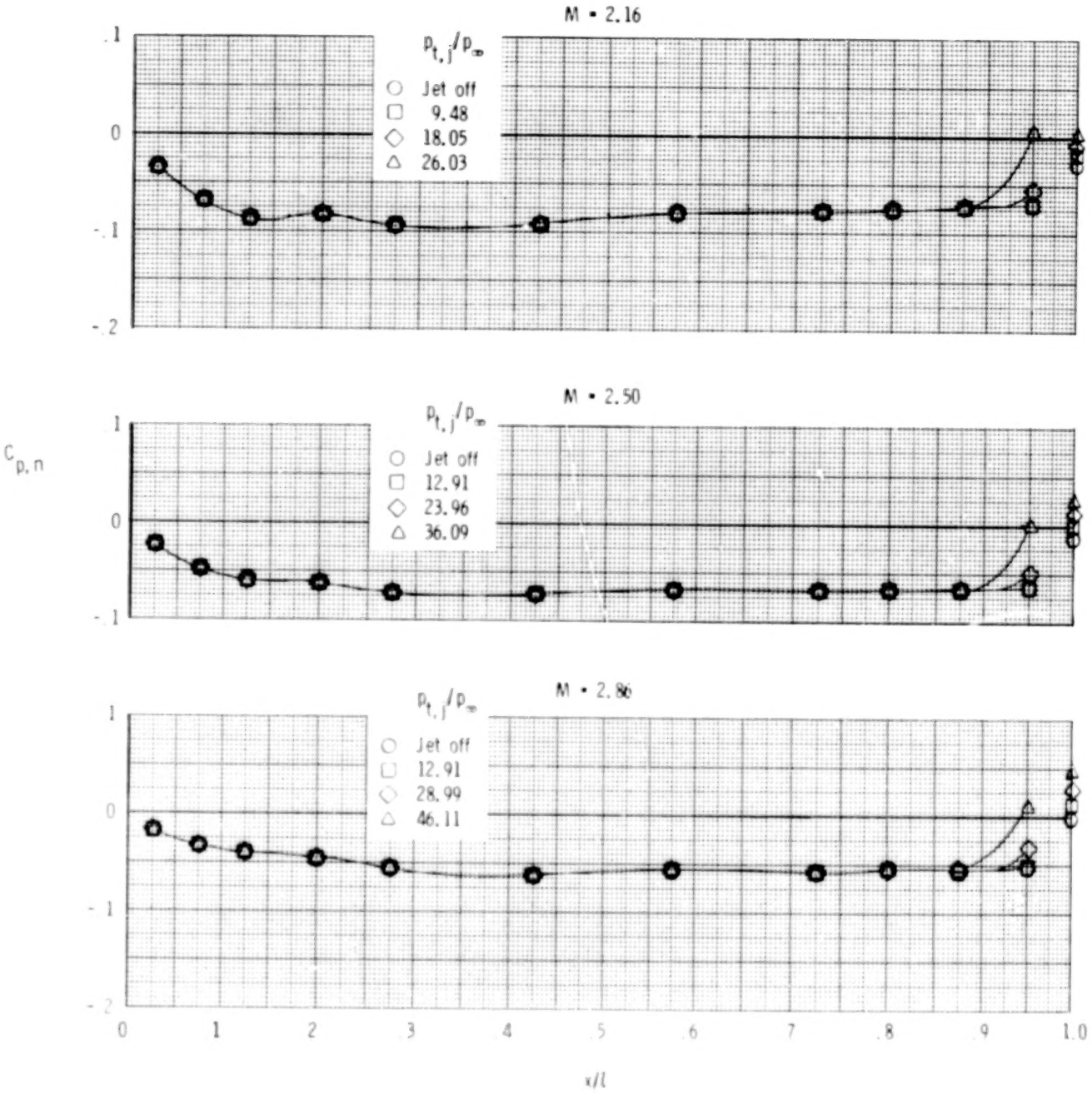

(b) M = 2.16 to 2.86.

Figure 29.- Concluded.

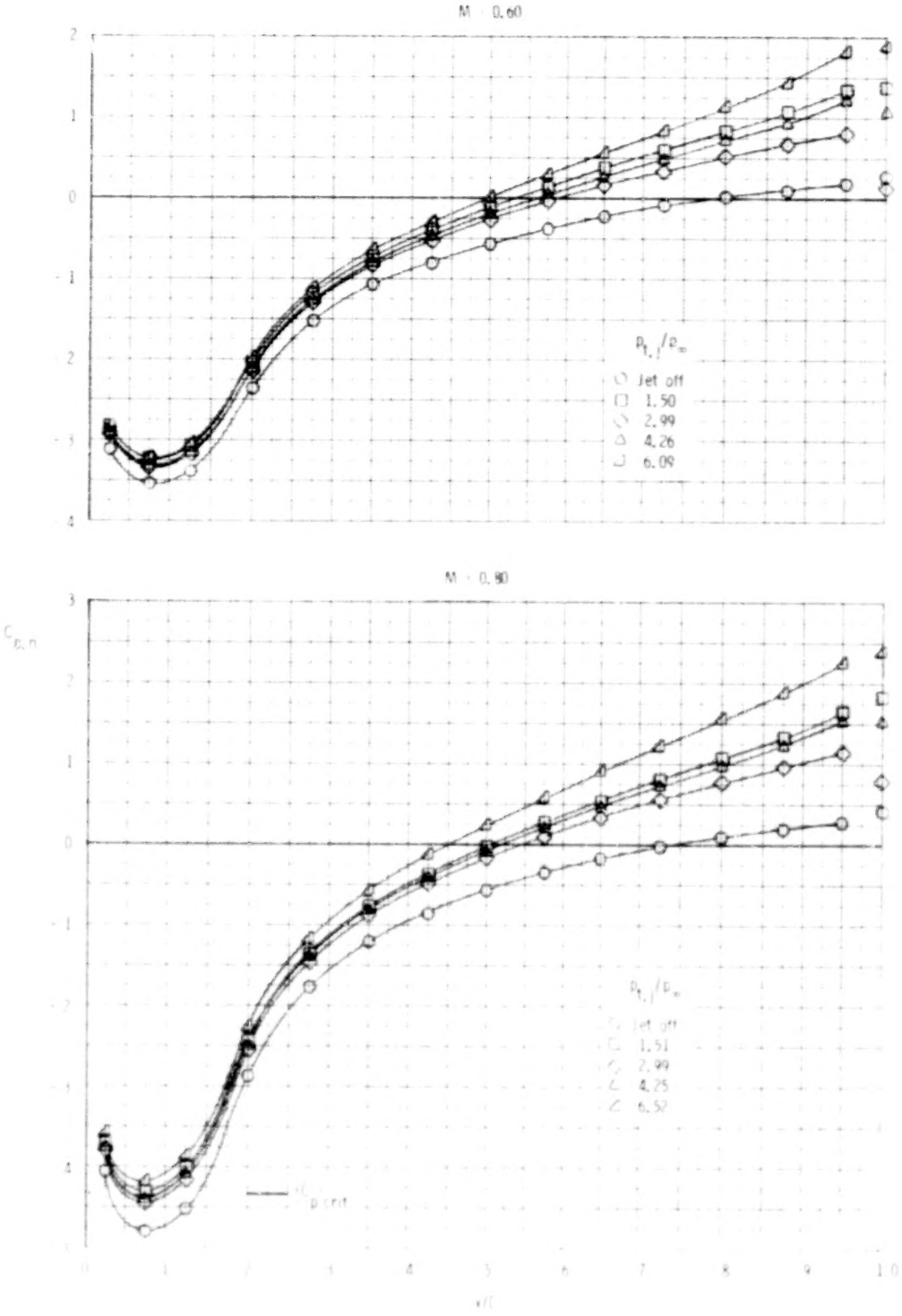

(a) M = 0.60 and 0.80.

Figure 30.- Nozzle pressure-coefficient distributions for configuration P-1.25-M. Dashed line indicates theoretical values.

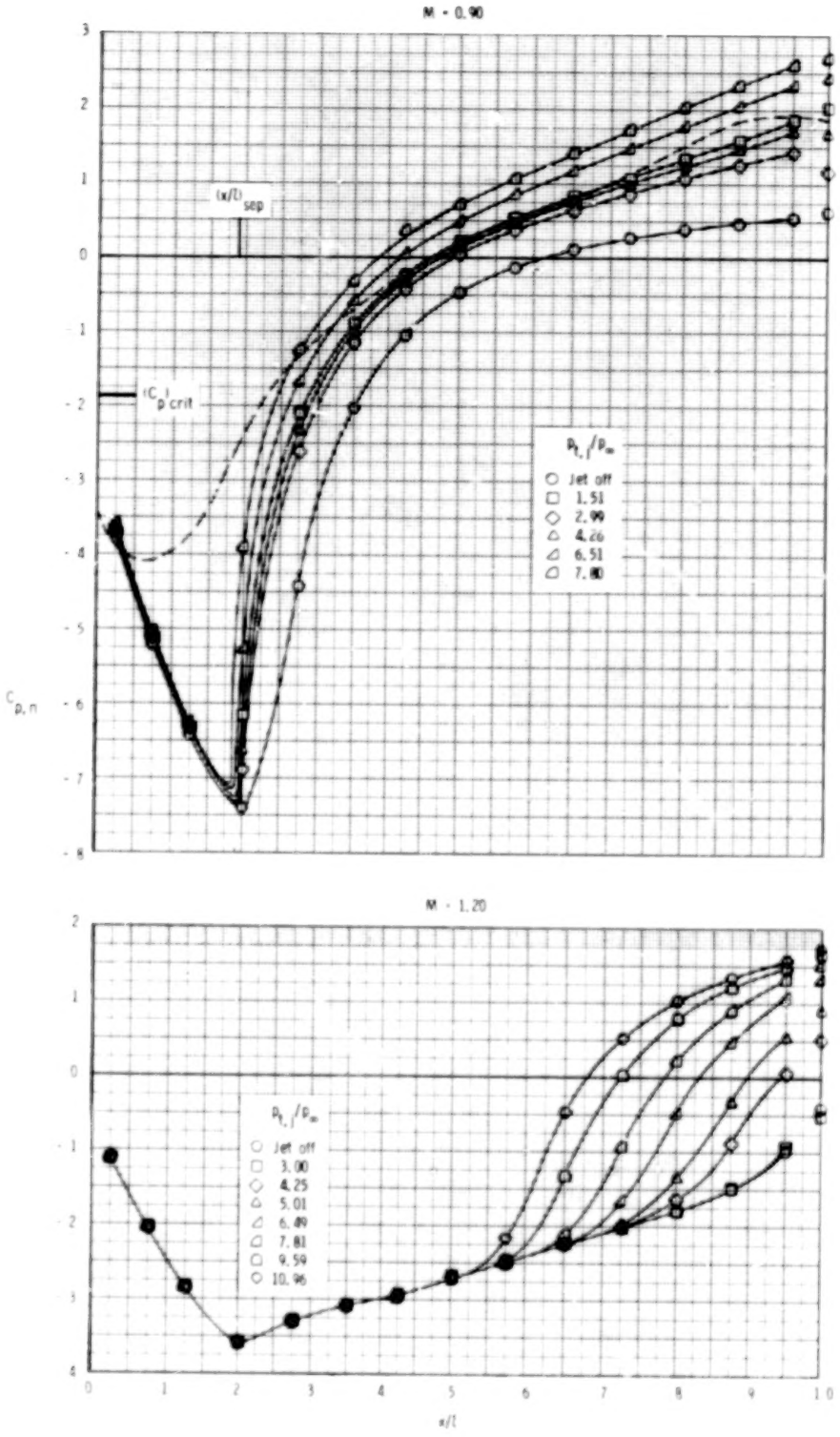

(b) M = 0.90 and 1.20.

Figure 30.- Continued.

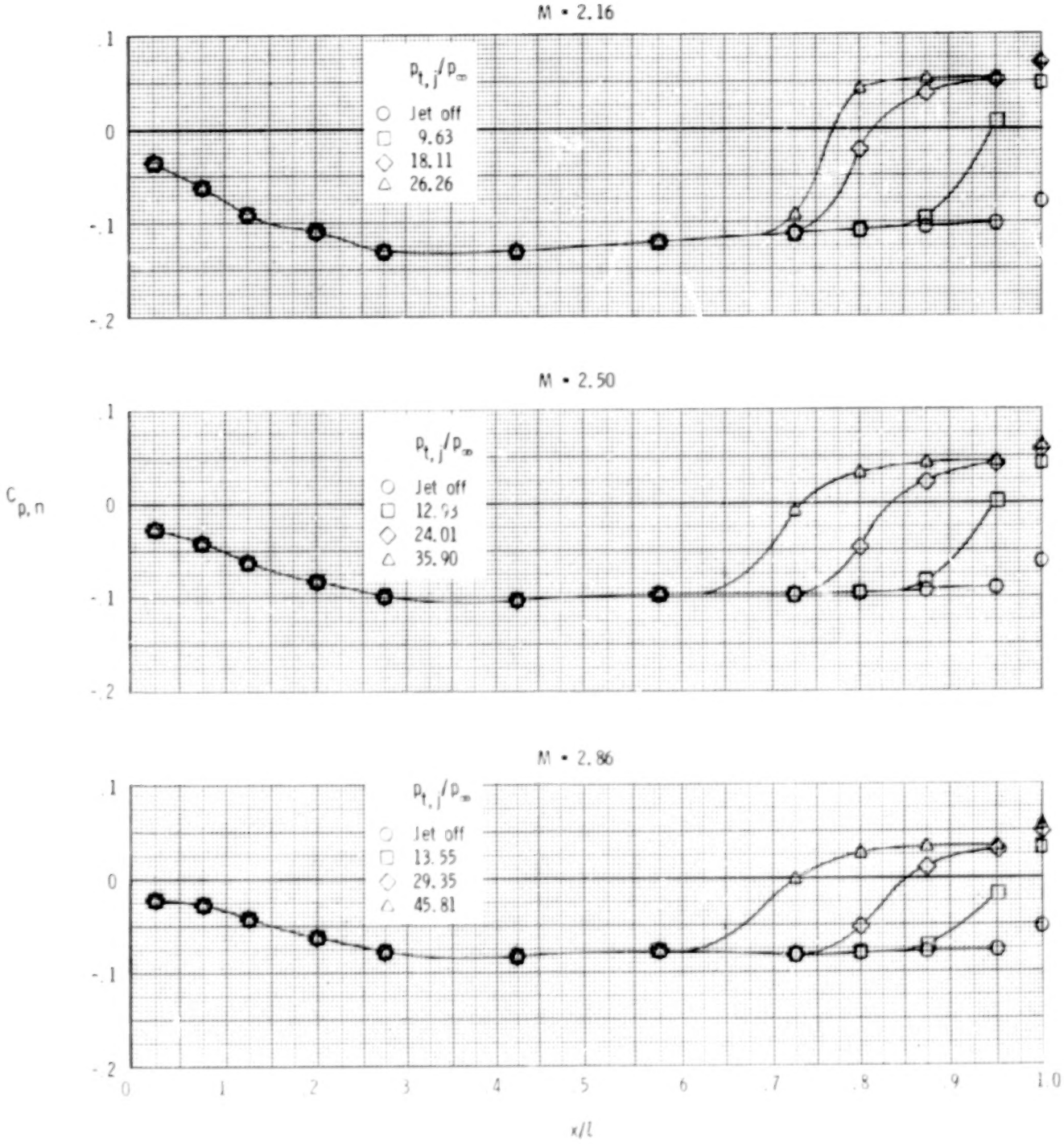

(c) M = 2.16 to 2.86.

Figure 30.- Concluded.

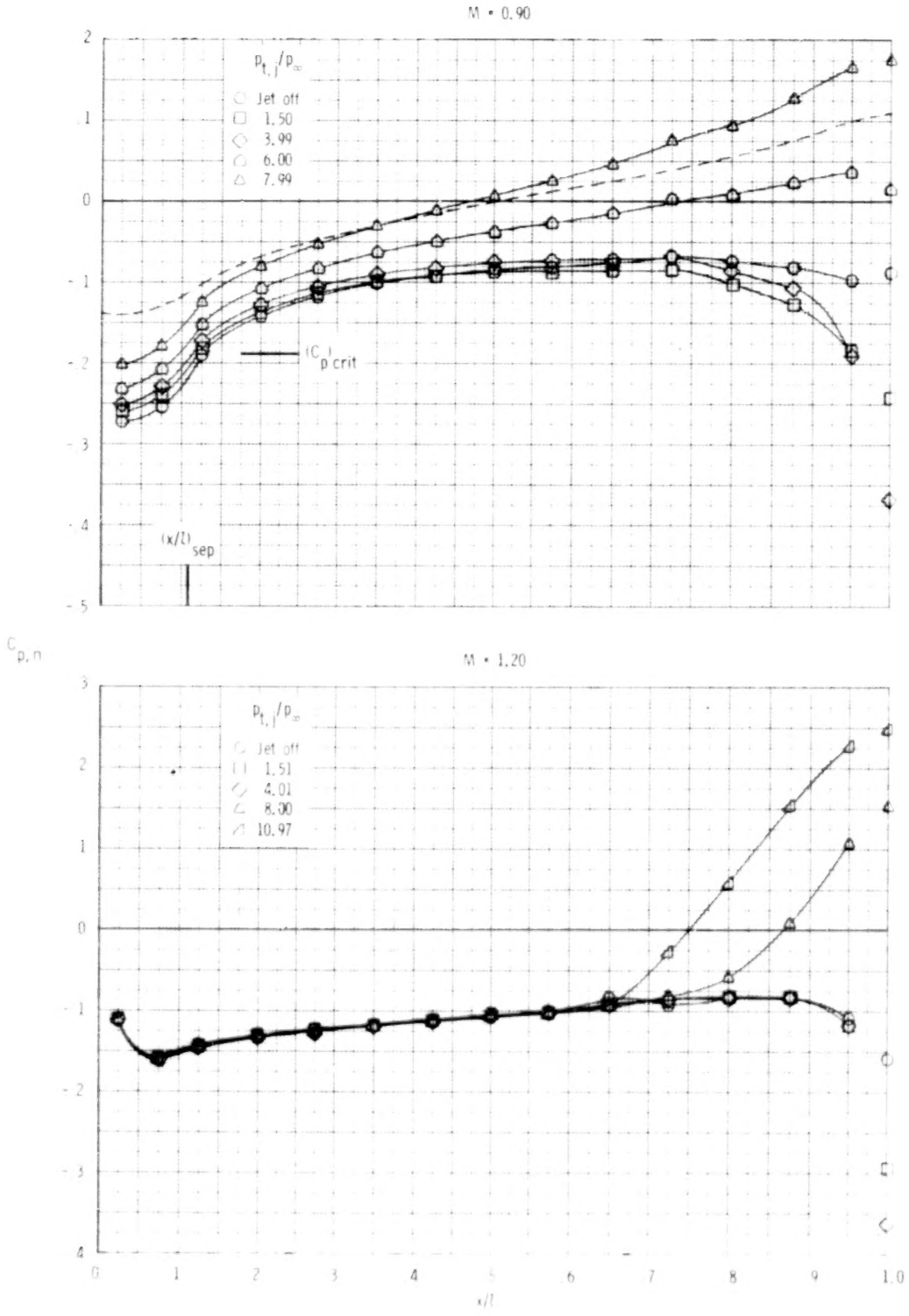

(a) M = 0.90 and 1.20.

Figure 31.- Nozzle pressure-coefficient distributions for configuration P-2.24-S. Dashed line indicates theoretical values.

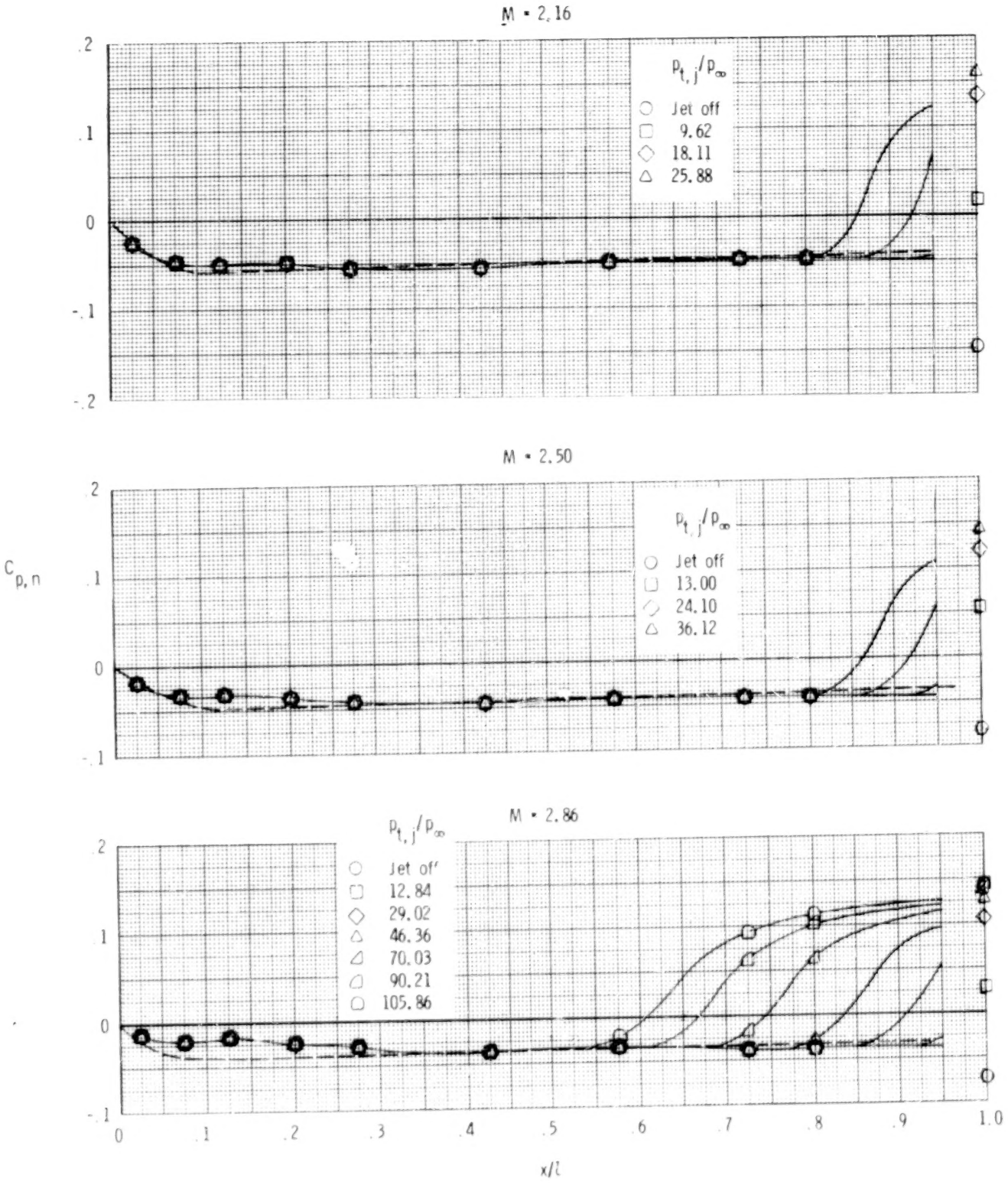

(b) M = 2.16 to 2.86.

Figure 31.- Concluded.

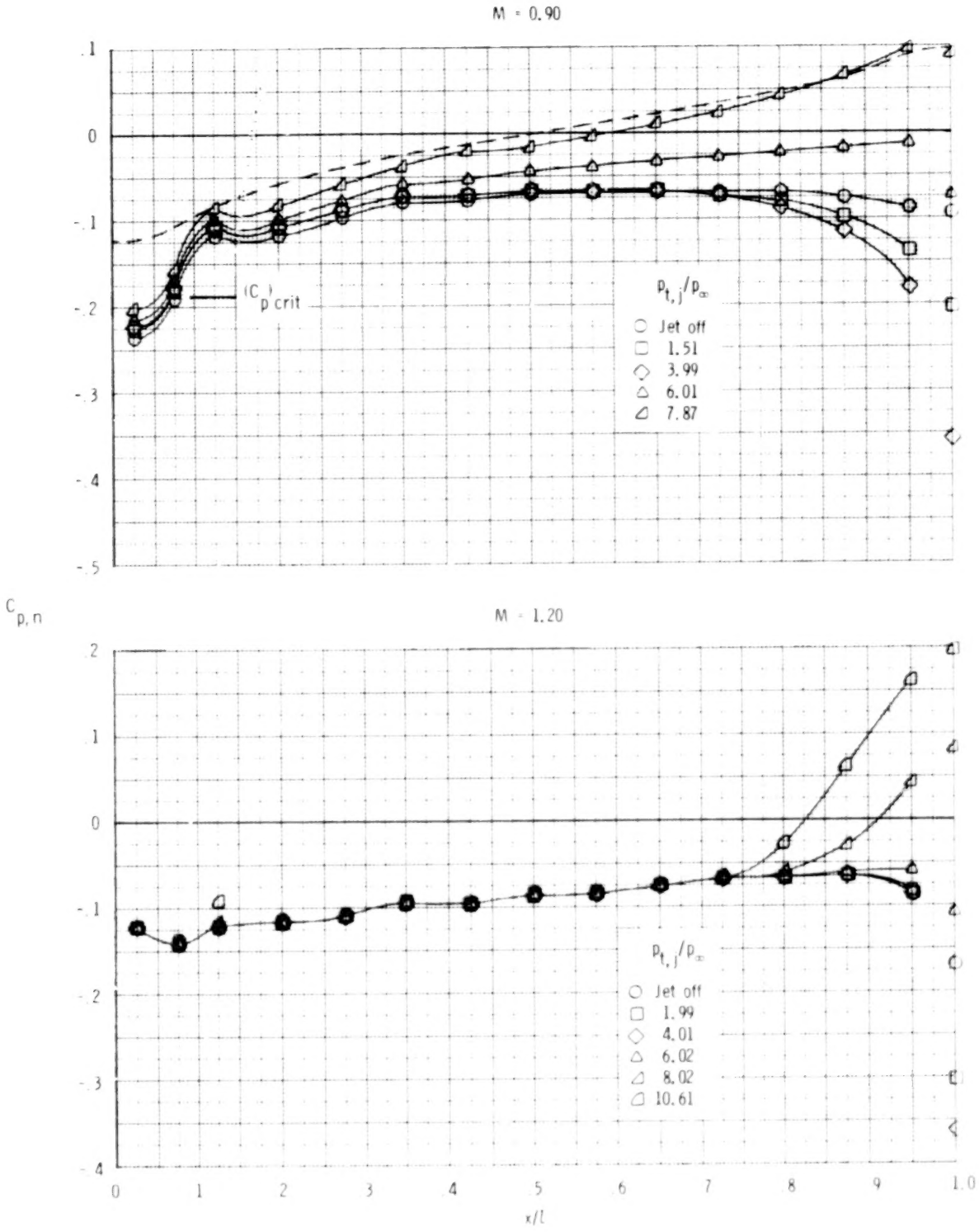

(a) M = 0.90 and 1.20.

Figure 32.- Nozzle pressure-coefficient distributions for configuration P-2.24-M. Dashed line indicates theoretical values.

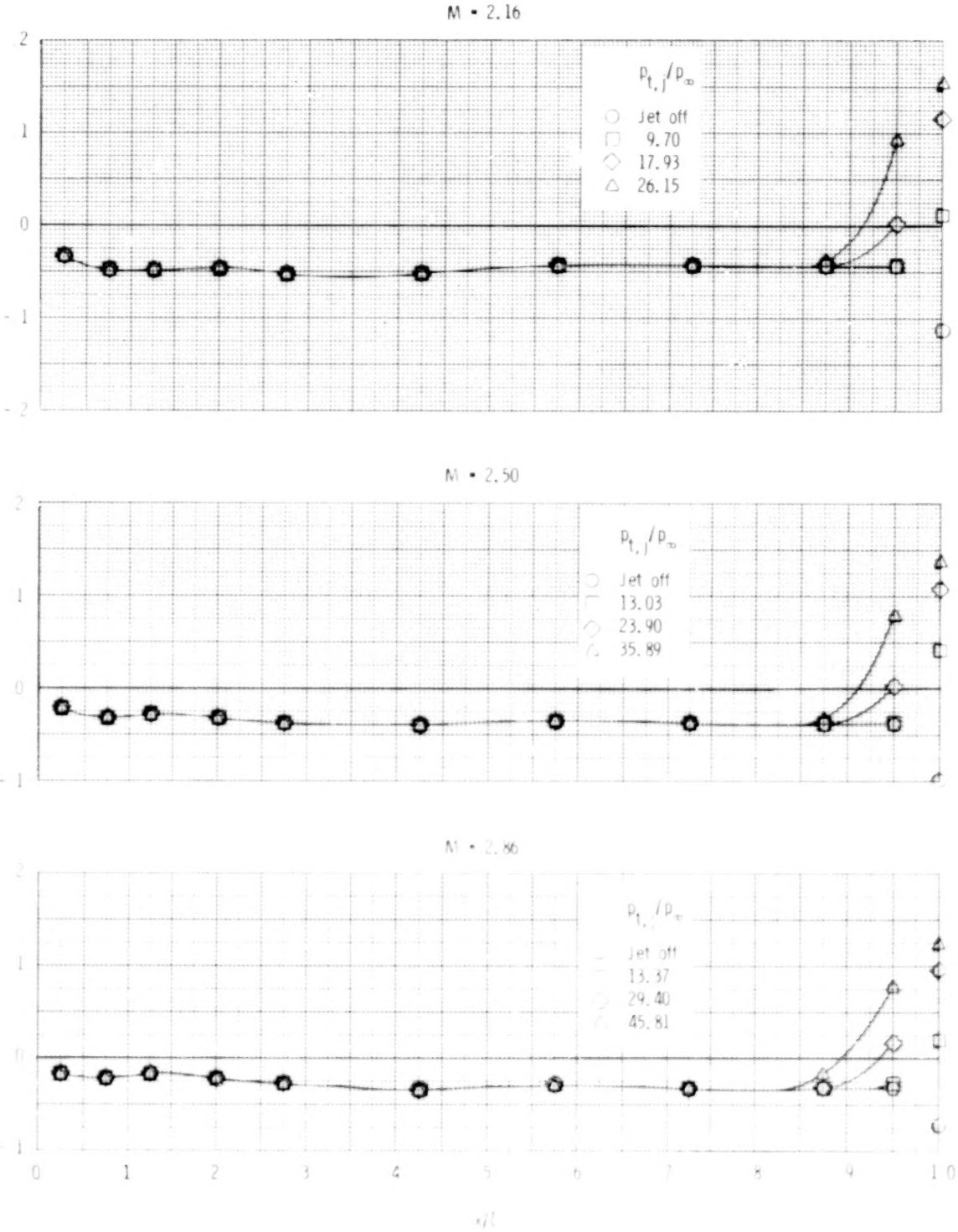

(b) M = 2.16 to 2.86.

Figure 32.- Concluded.

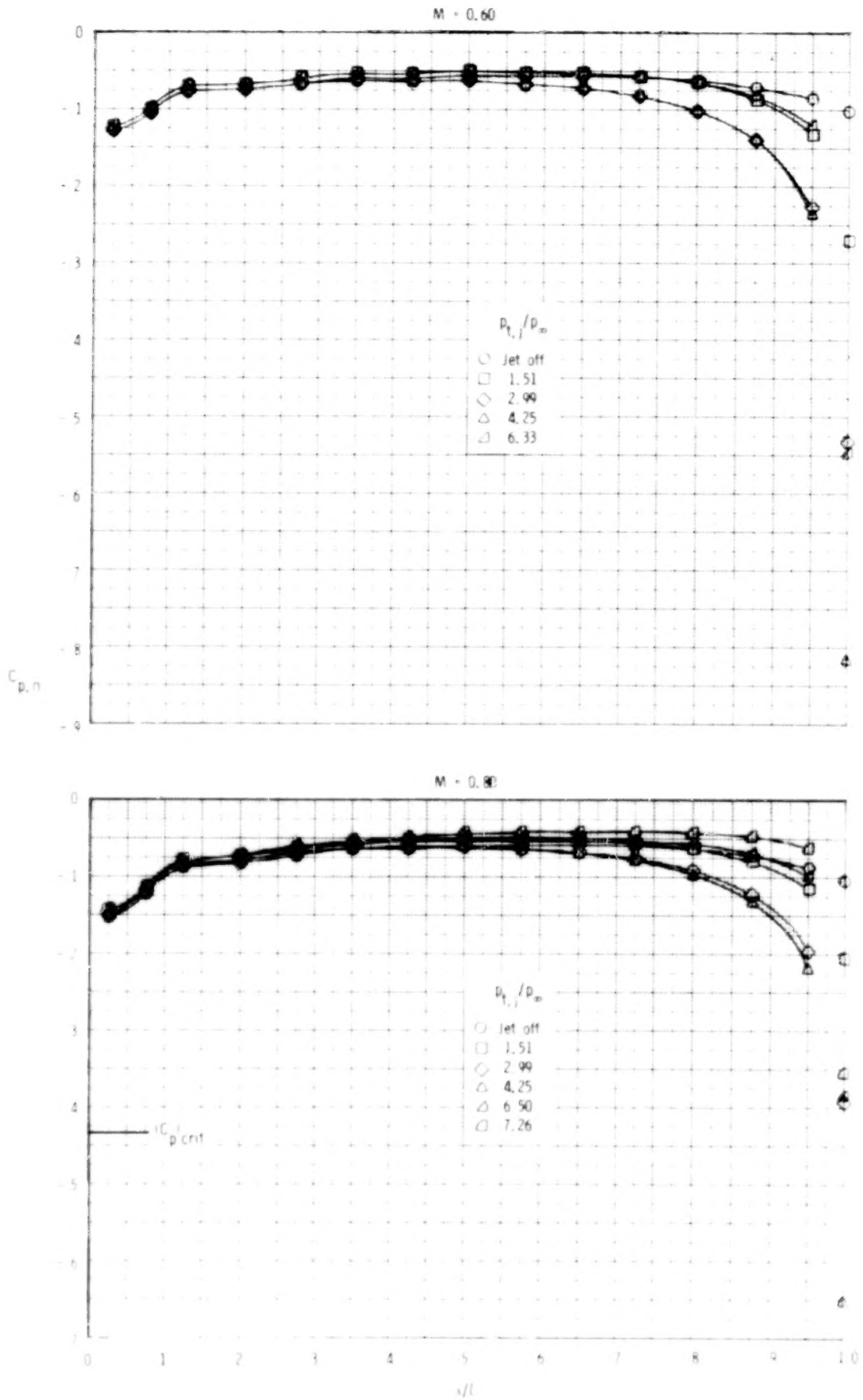

(a) M = 0.60 and 0.80.

Figure 33.- Nozzle pressure-coefficient distributions for configuration P-2.24-L. Dashed line indicates theoretical values.

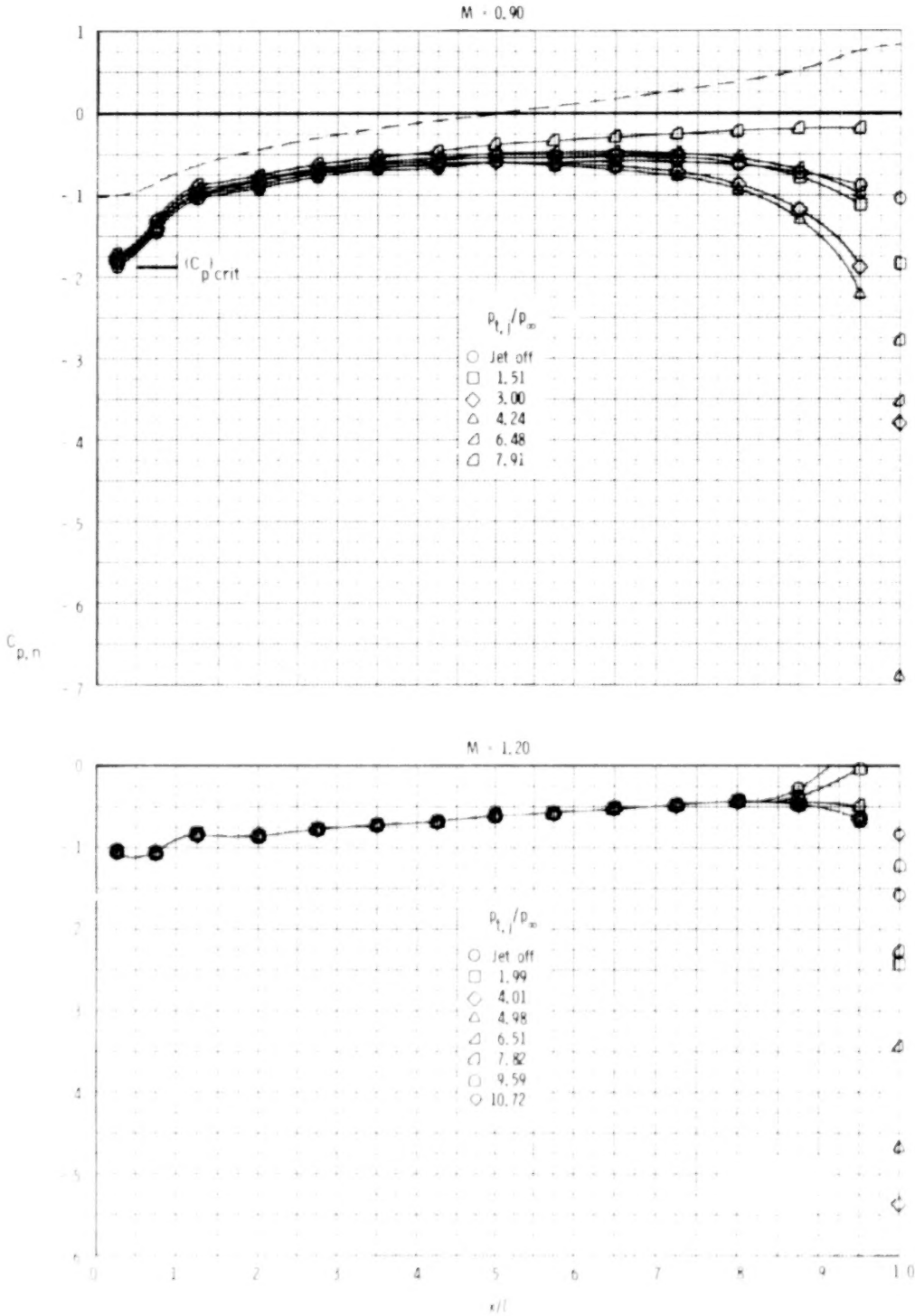

(b) M = 0.90 and 1.20.

Figure 33.- Continued.

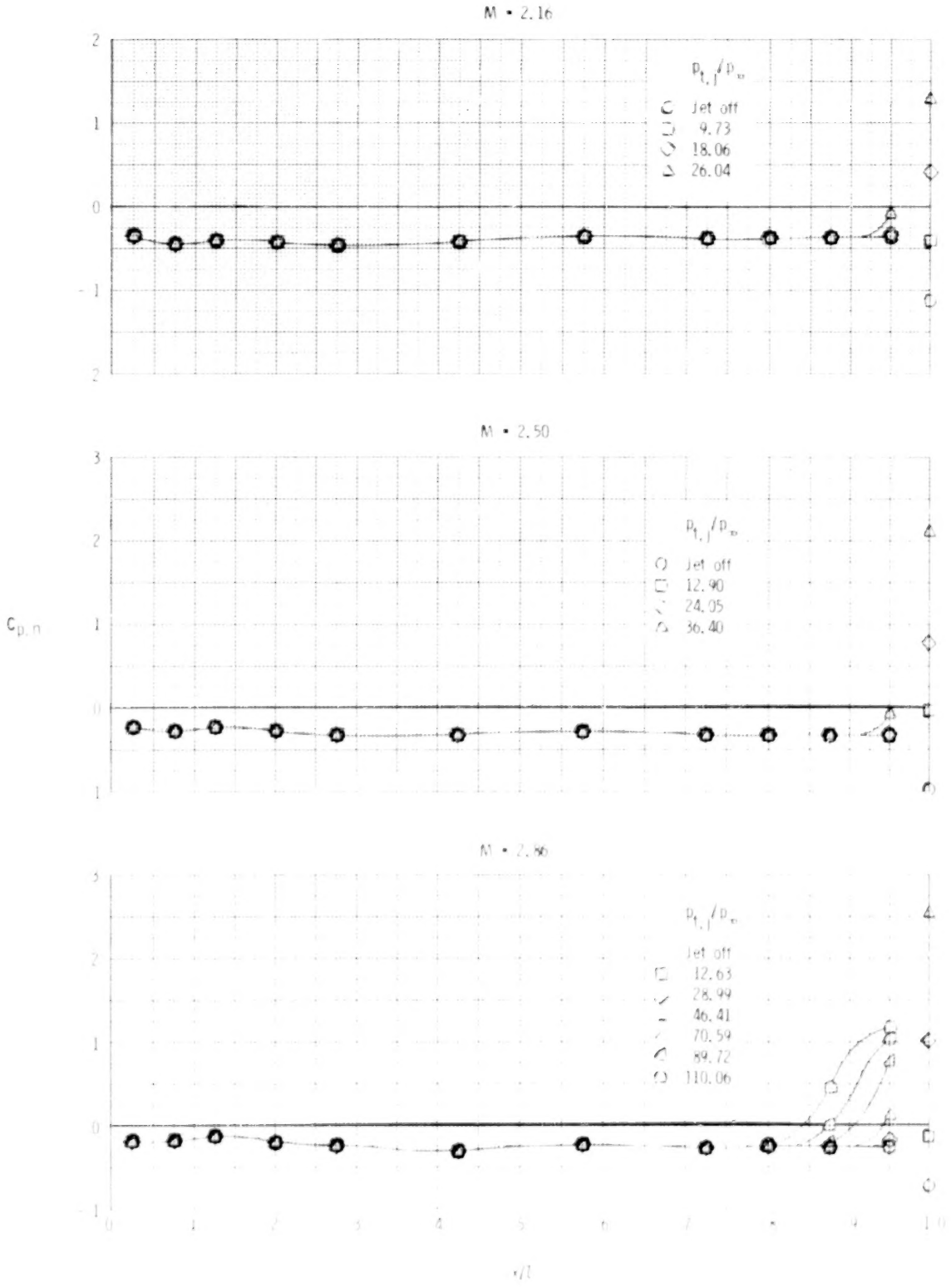

(c) M = 2.16 to 2.86.

Figure 33.- Concluded.

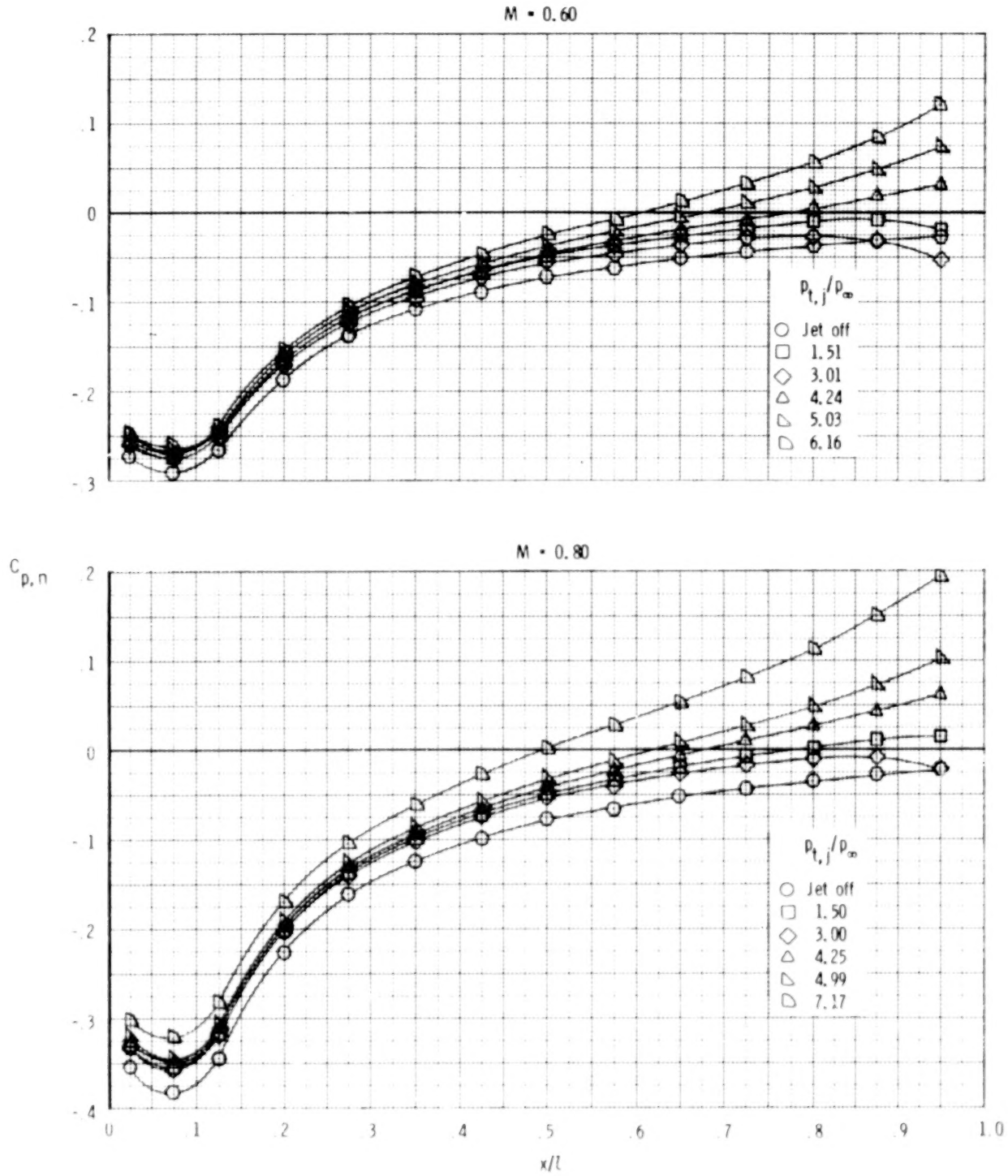

(a) M = 0.60 and 0.80.

Figure 34.- Nozzle pressure-coefficient distributions for configuration P-1.69-S. Dashed line indicates theoretical values.

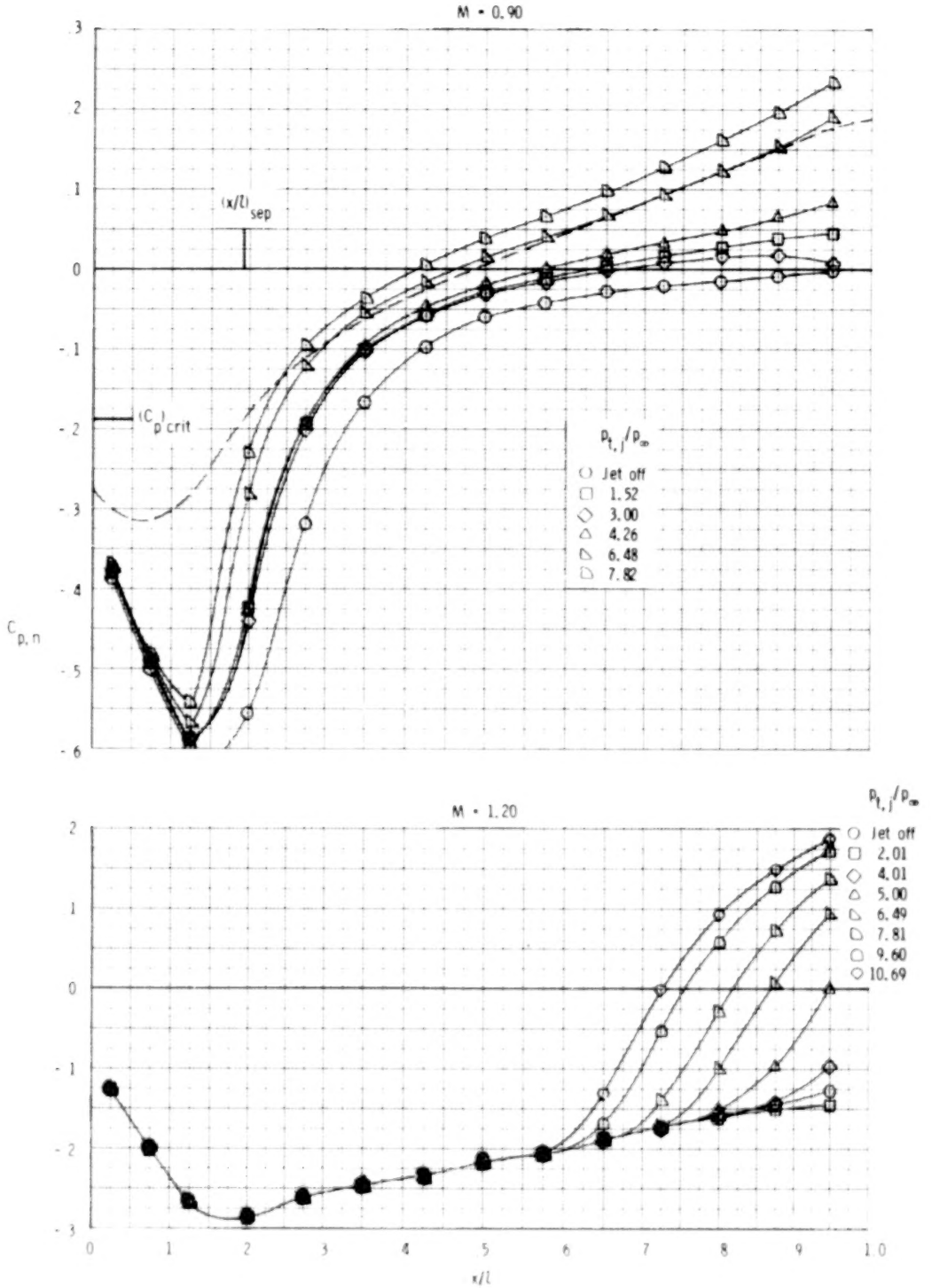

(b) M = 0.90 and 1.20.

Figure 34.- Continued.

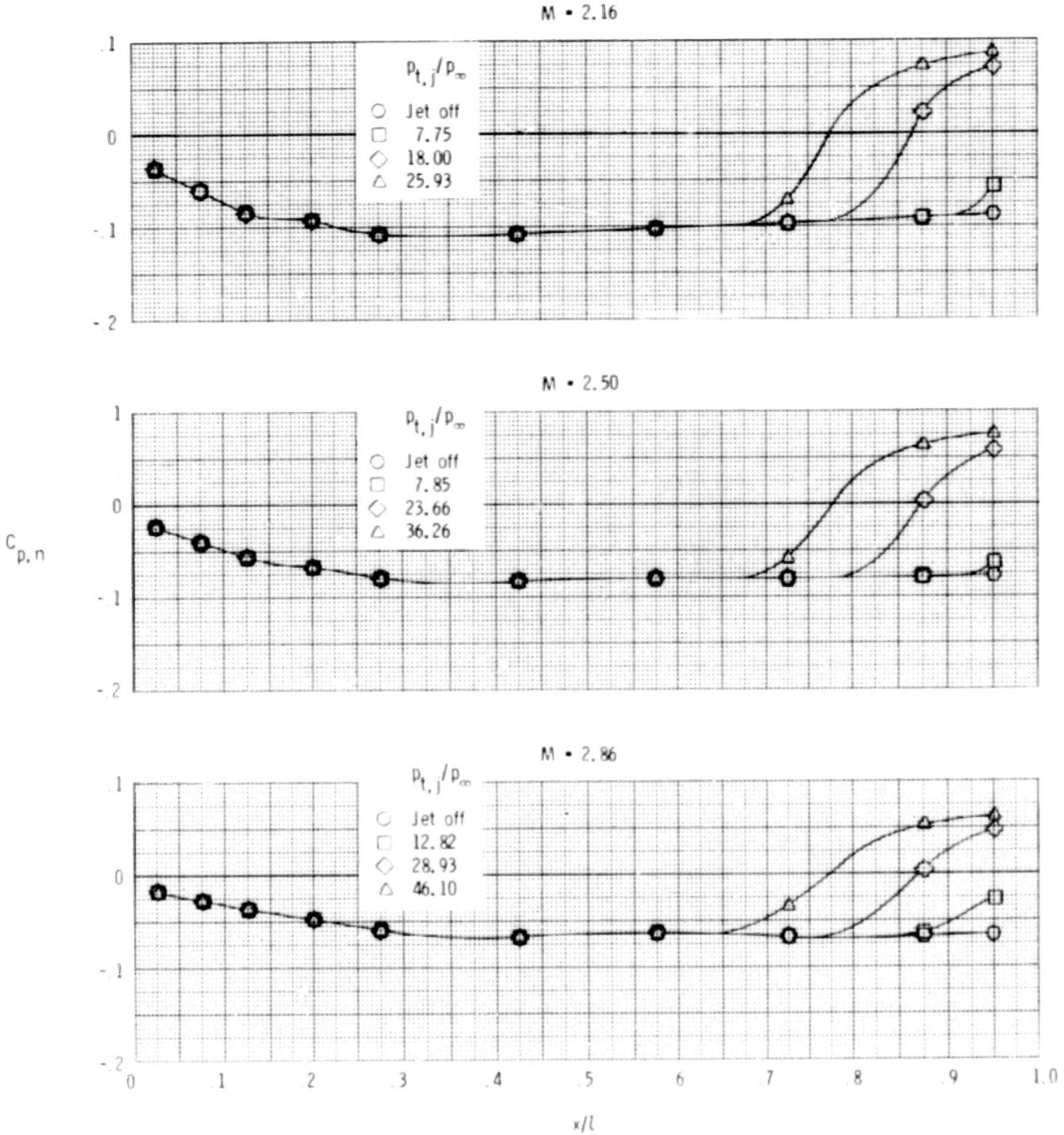

(c) M = 2.16 to 2.86.

Figure 34.- Concluded.

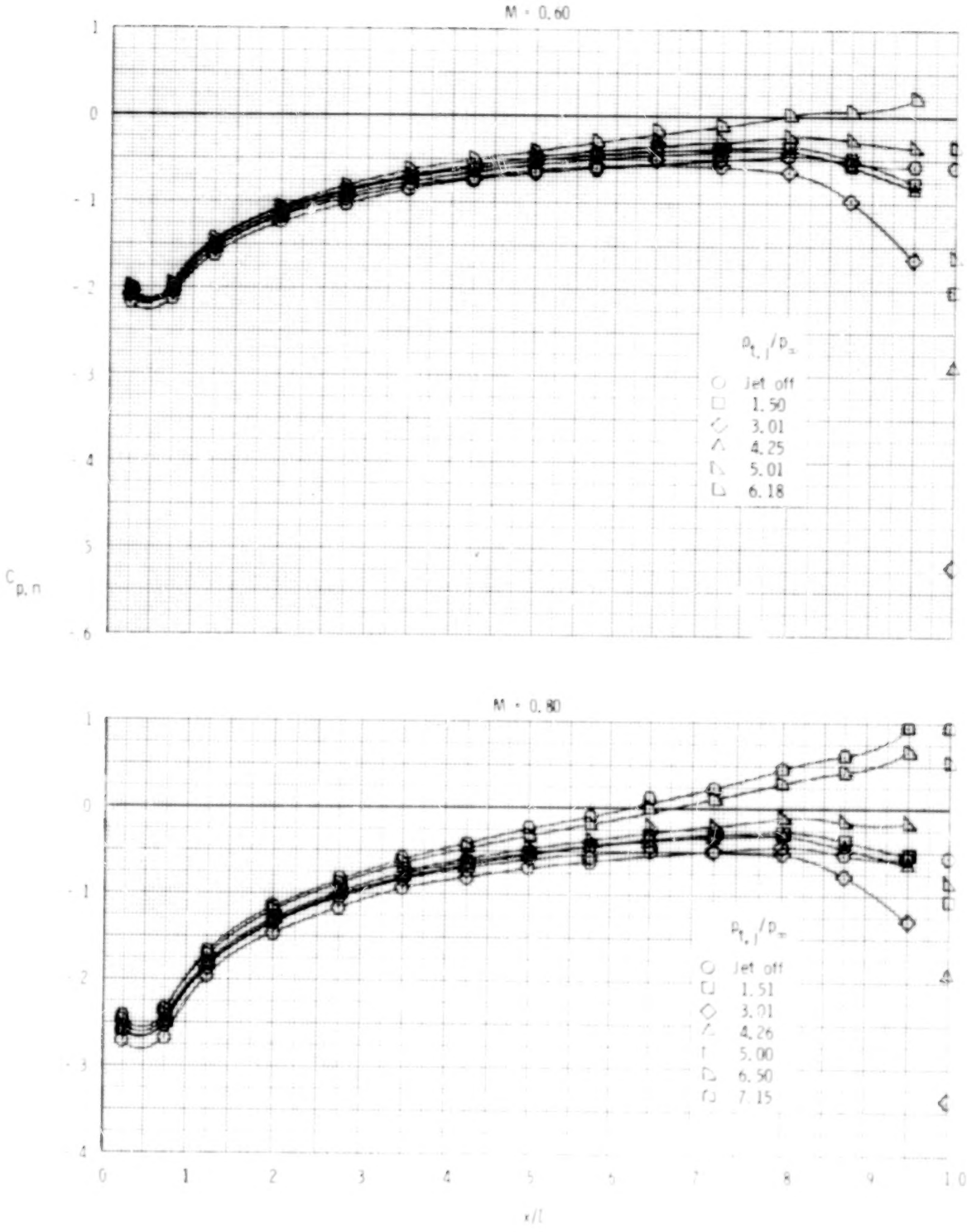

(a) M = 0.60 and 0.80.

Figure 35.- Nozzle pressure-coefficient distributions for configuration P-1.89-M. Dashed line indicates theoretical values.

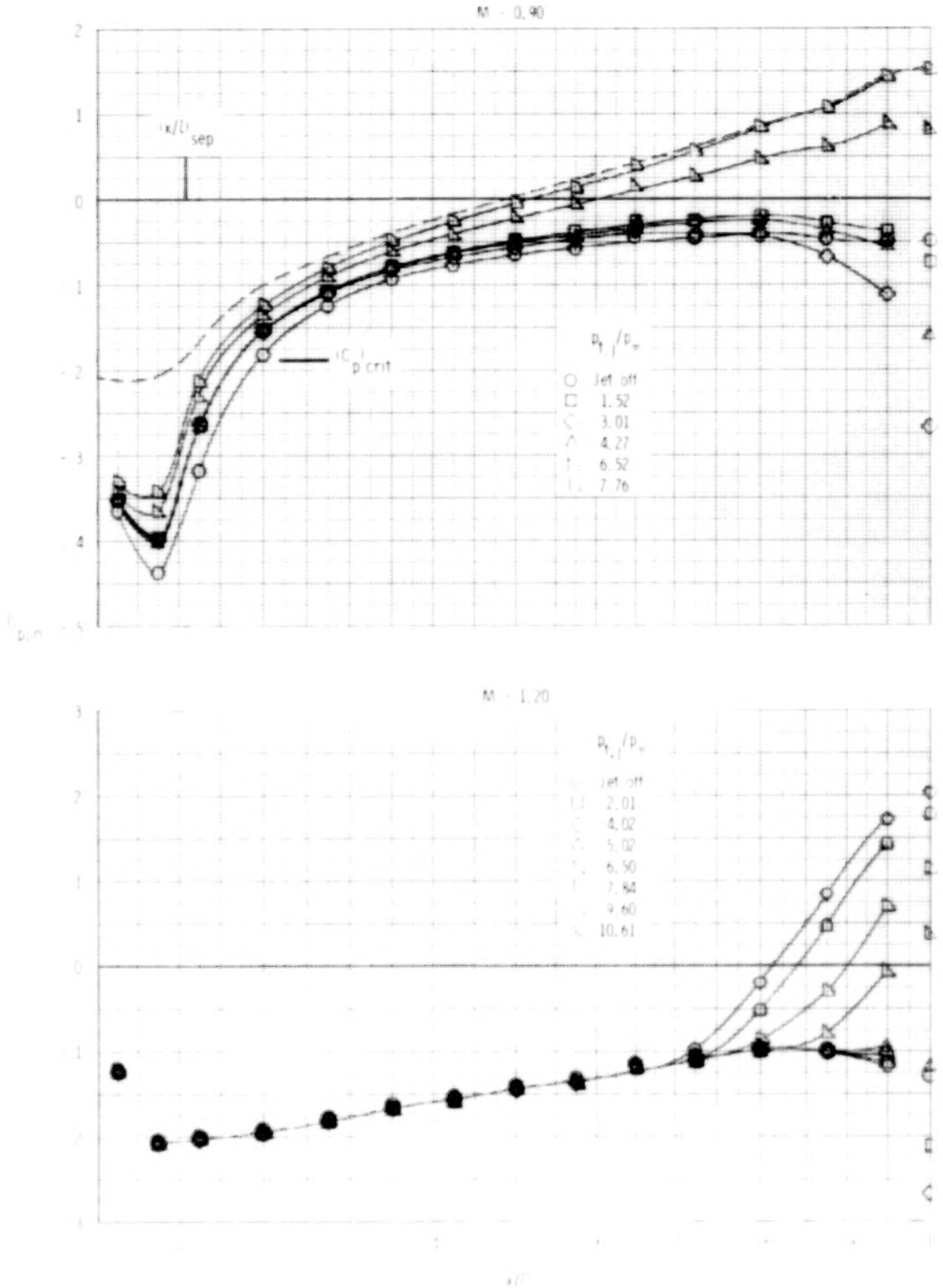

(b) M = 0.90 and 1.20.

Figure 35.- Continued.

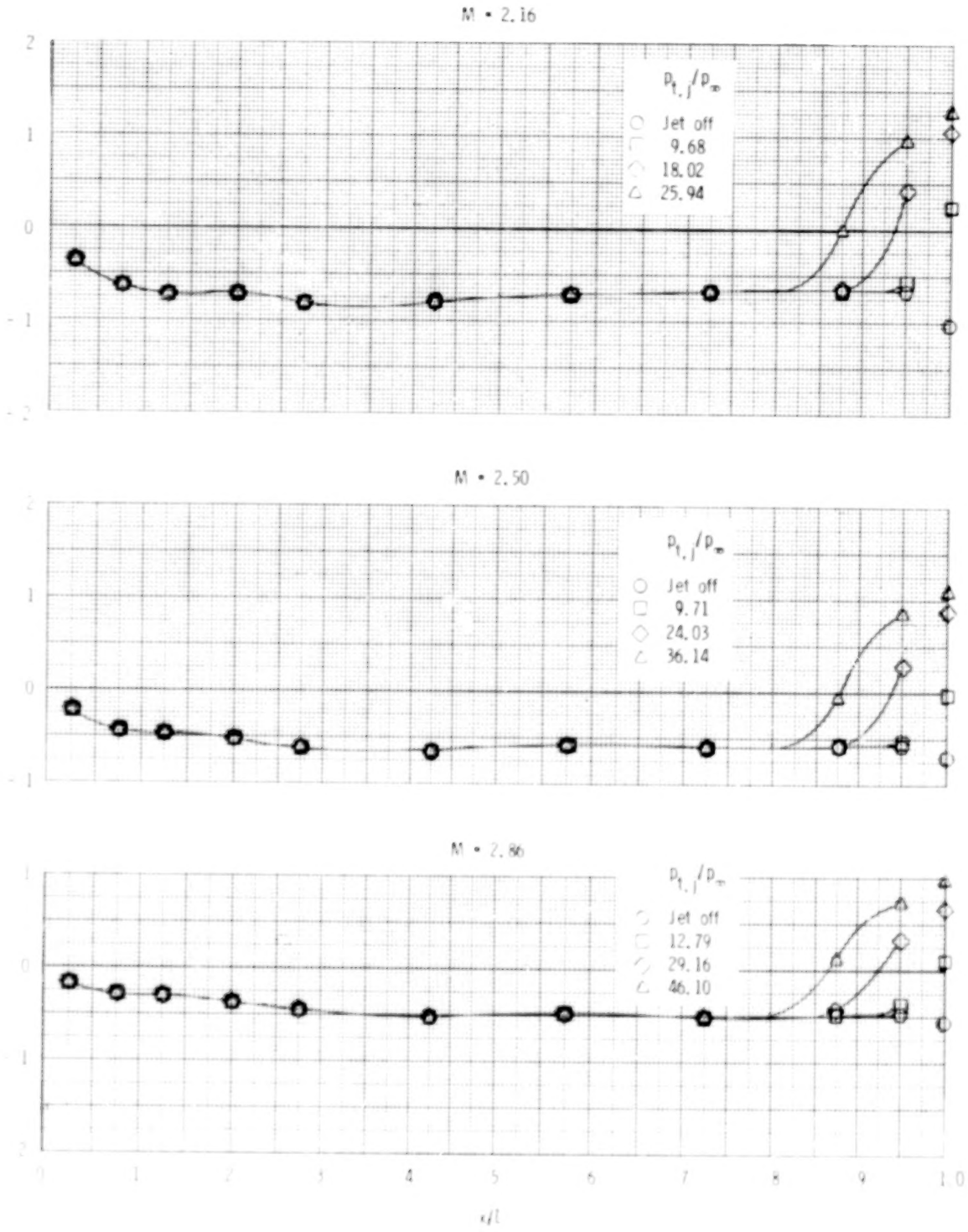

(c) M = 2.16 to 2.86.

Figure 35.- Concluded.

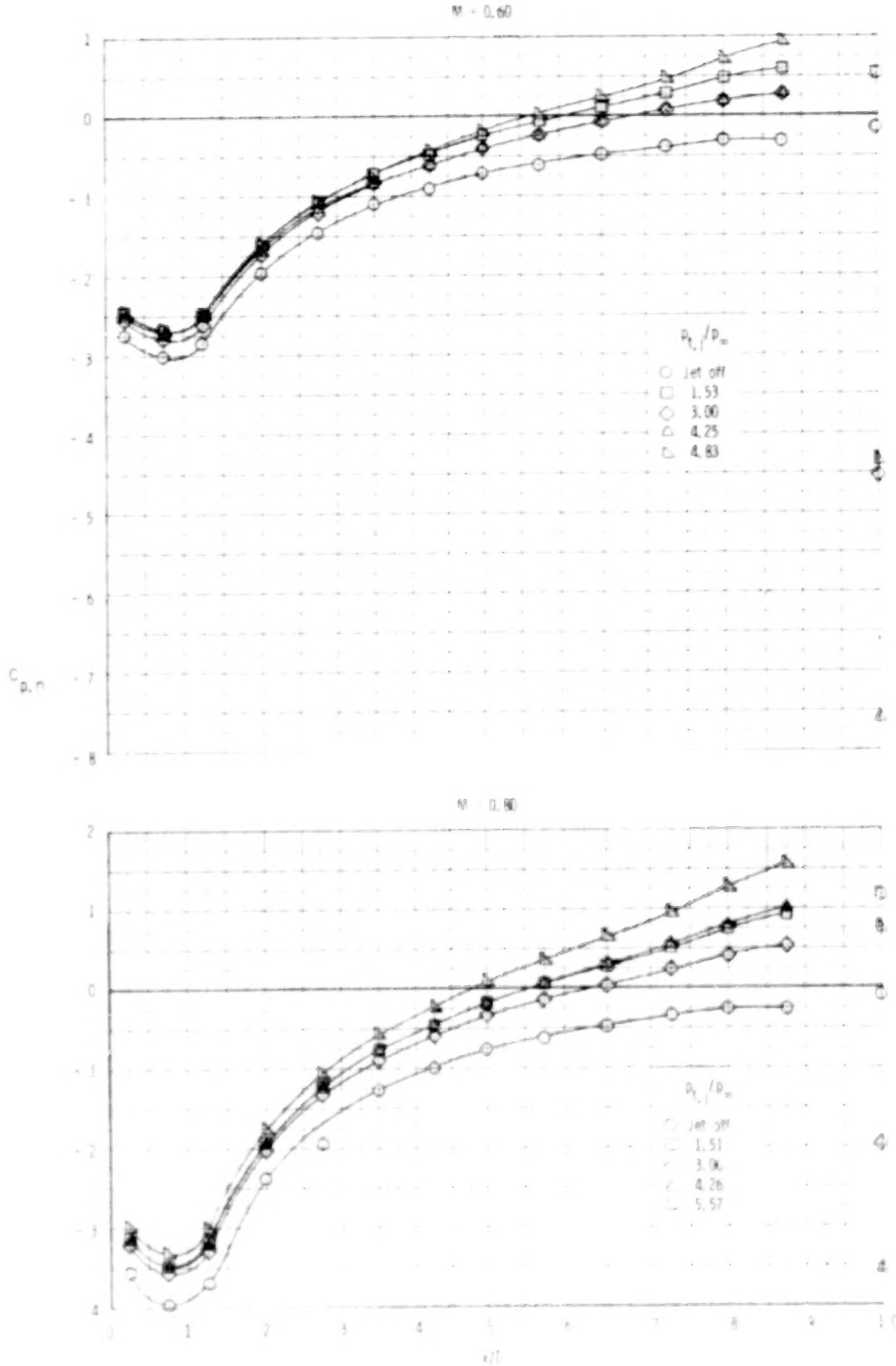

(a) M = 0.60 and 0.80.

Figure 36.- Nozzle pressure-coefficient distributions for configuration A-1.25-S. Dashed line indicates theoretical values.

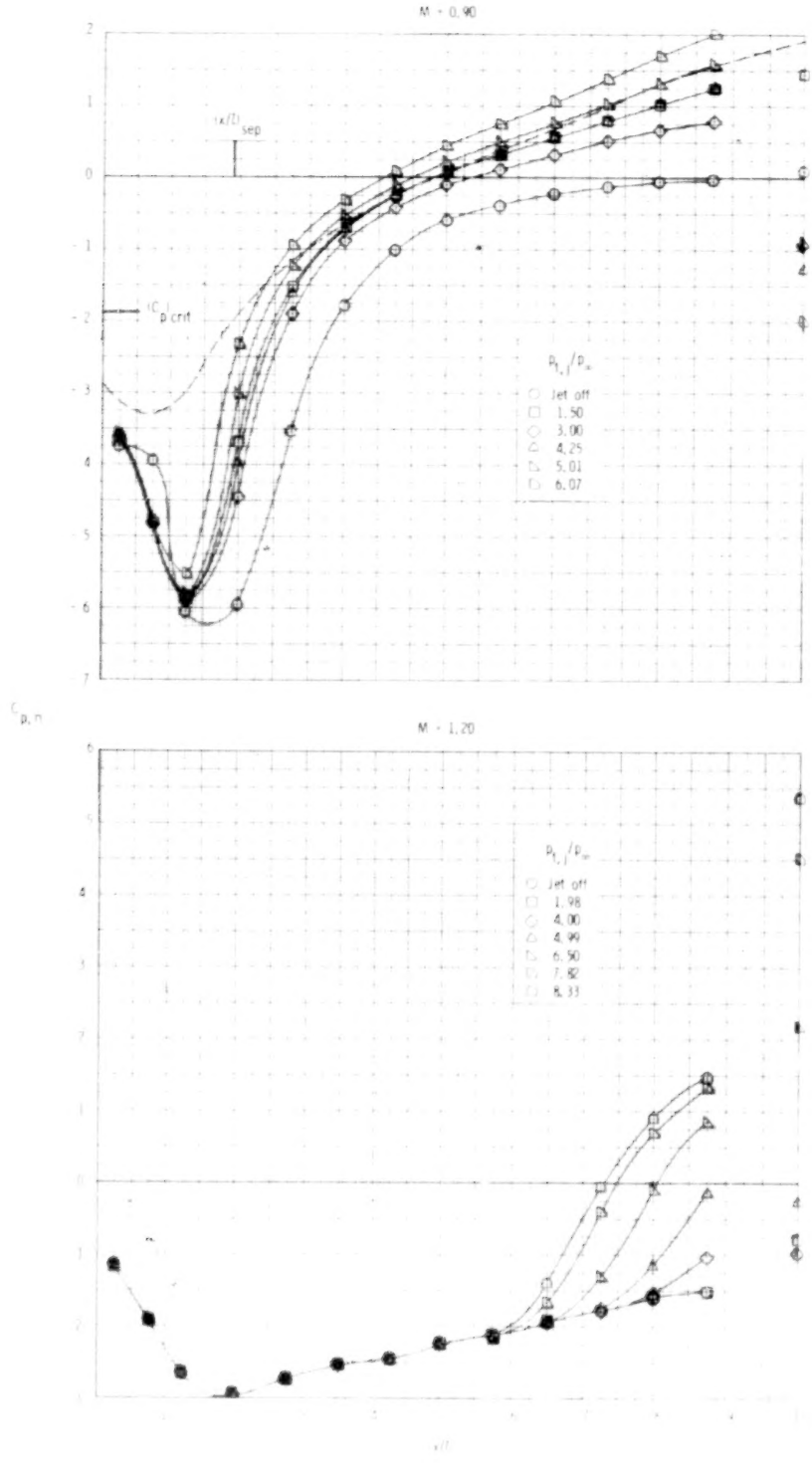

(b) M = 0.90 and 1.20.

Figure 36.- Continued.

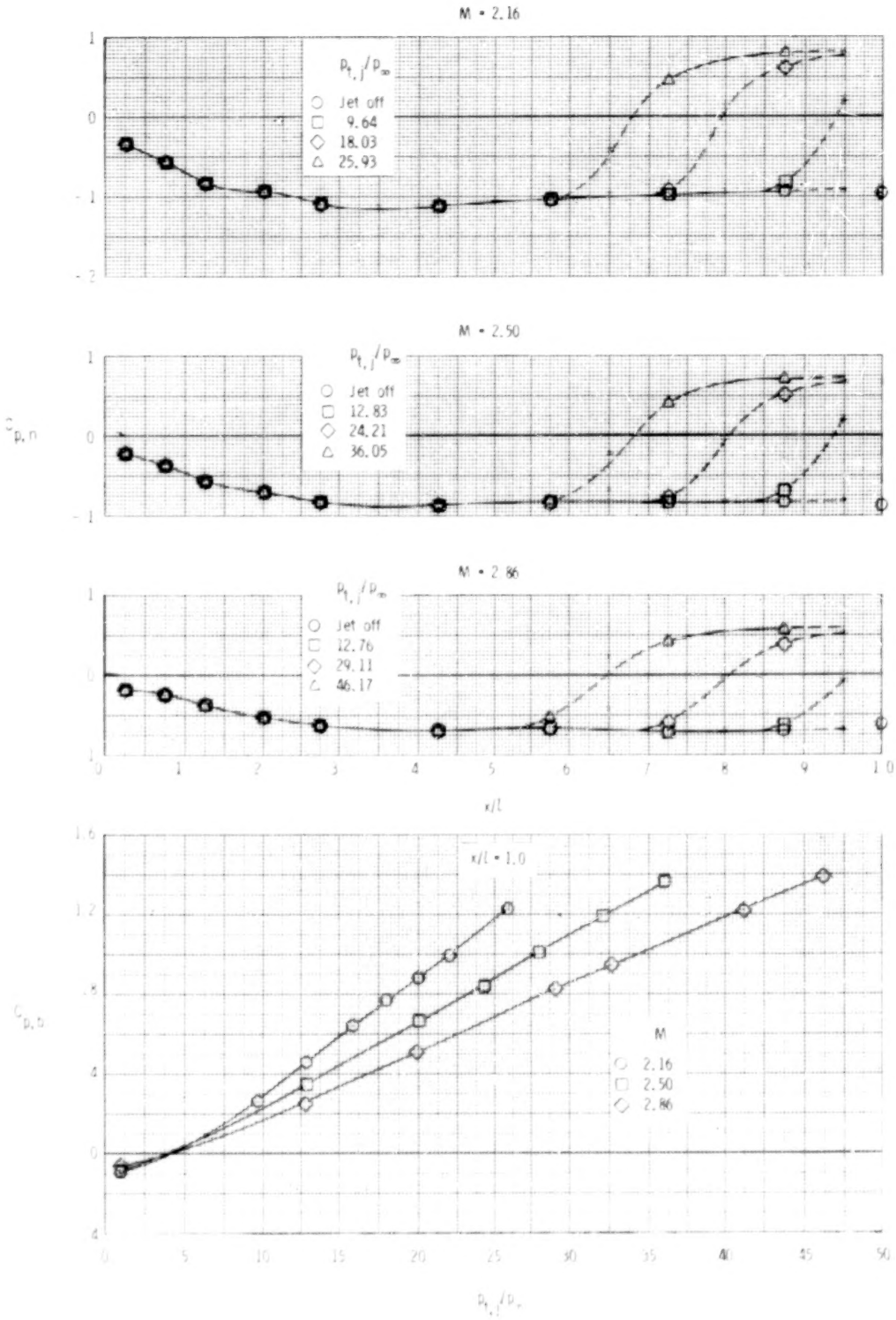

(c) M = 2.16 to 2.86.

Figure 36.- Concluded.

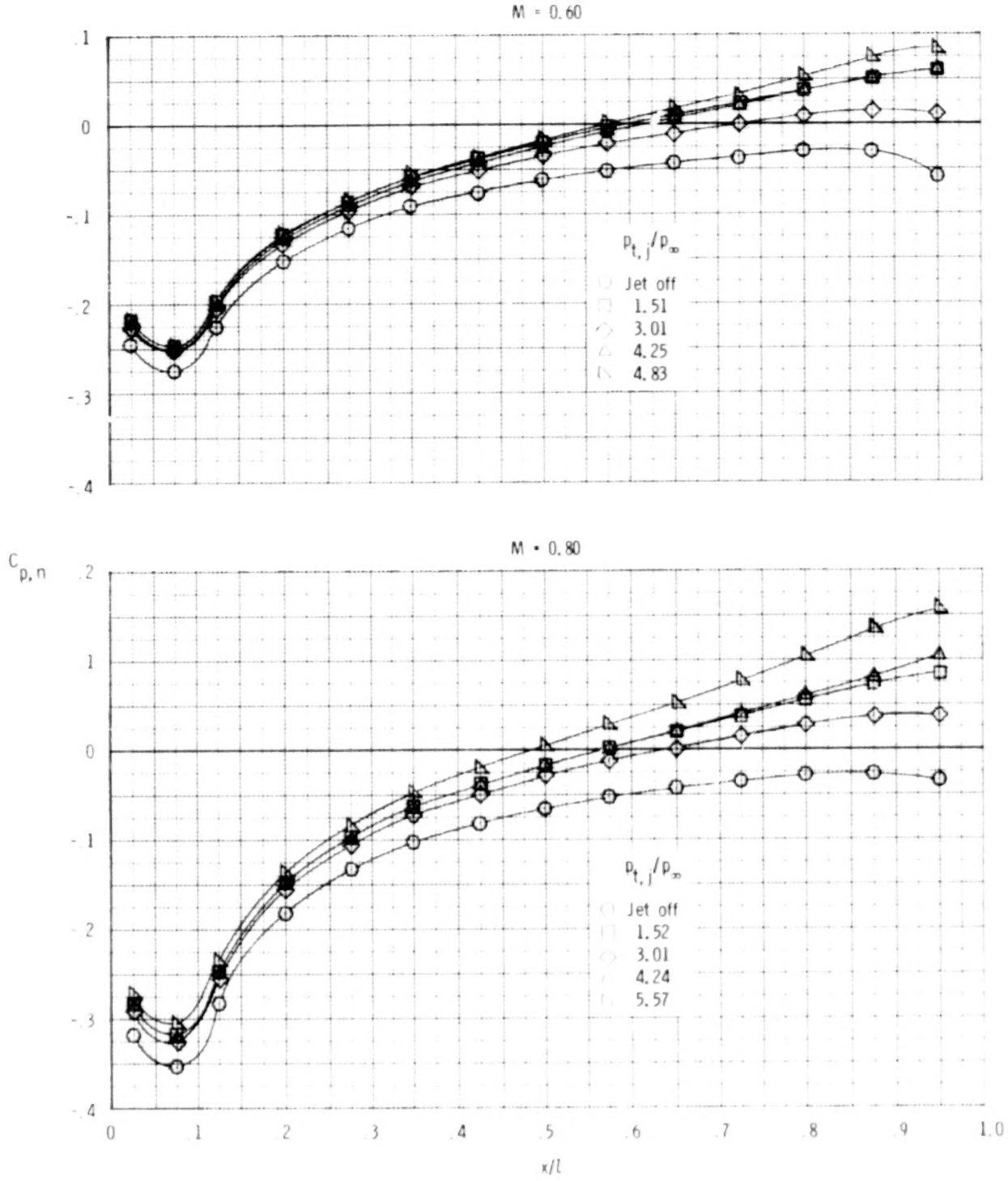

(a) M = 0.60 and 0.80.

Figure 37.- Nozzle pressure-coefficient distributions for configuration A-1.25-M. Dashed line indicates theoretical values.

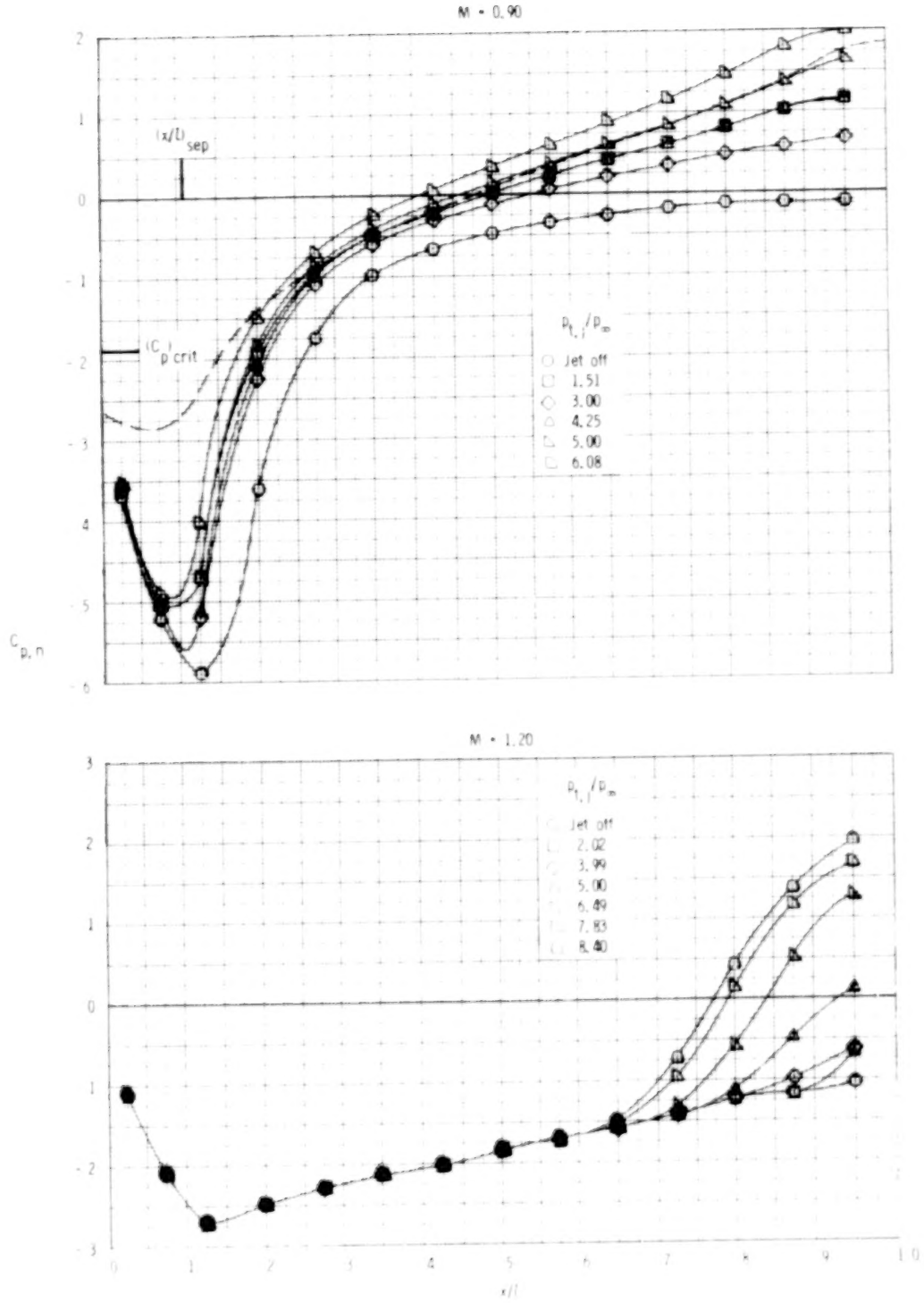

(b) M = 0.90 and 1.20.

Figure 37.- Continued.

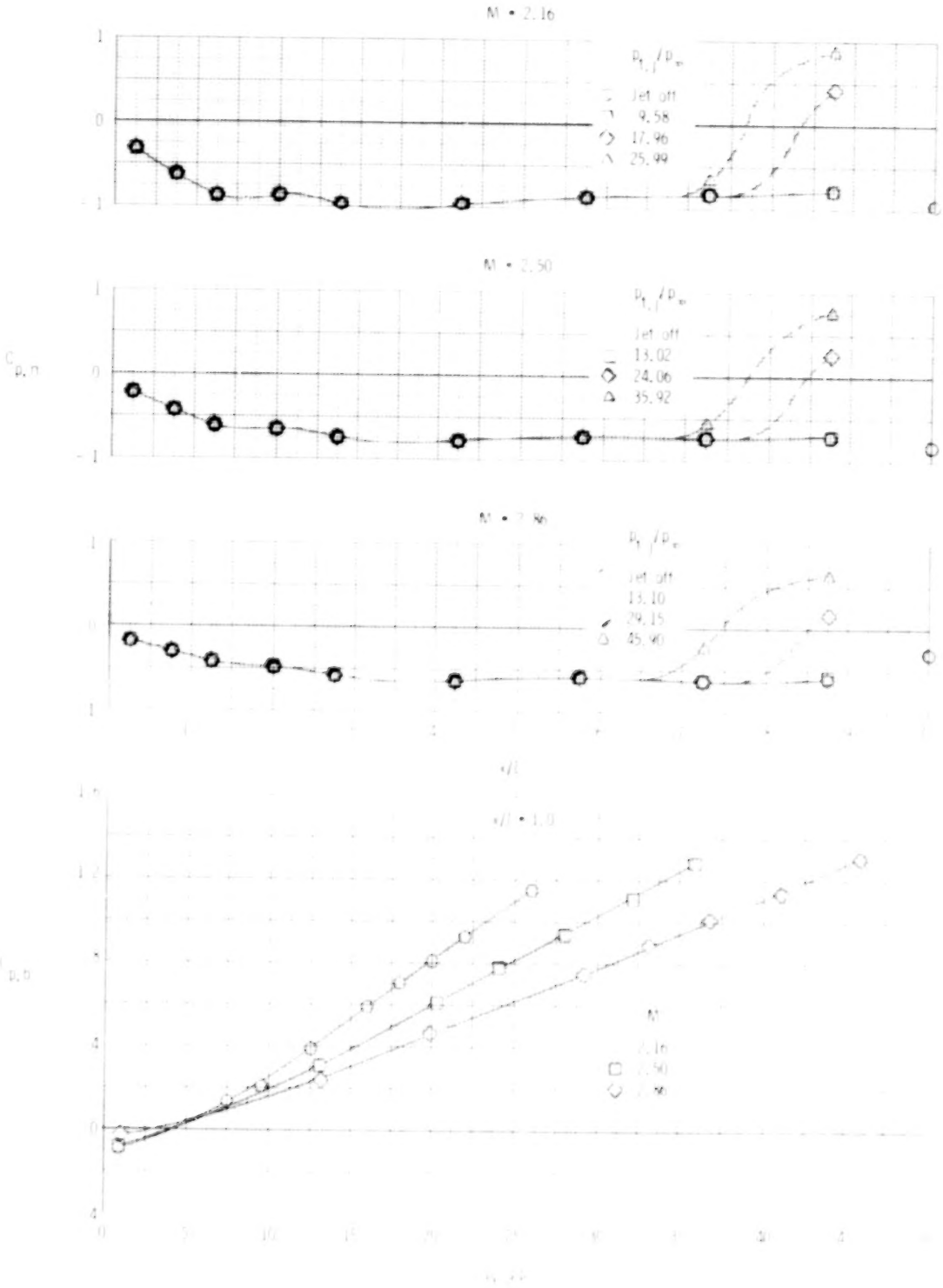

(c) M = 2.16 to 2.86.

Figure 37.- Concluded.

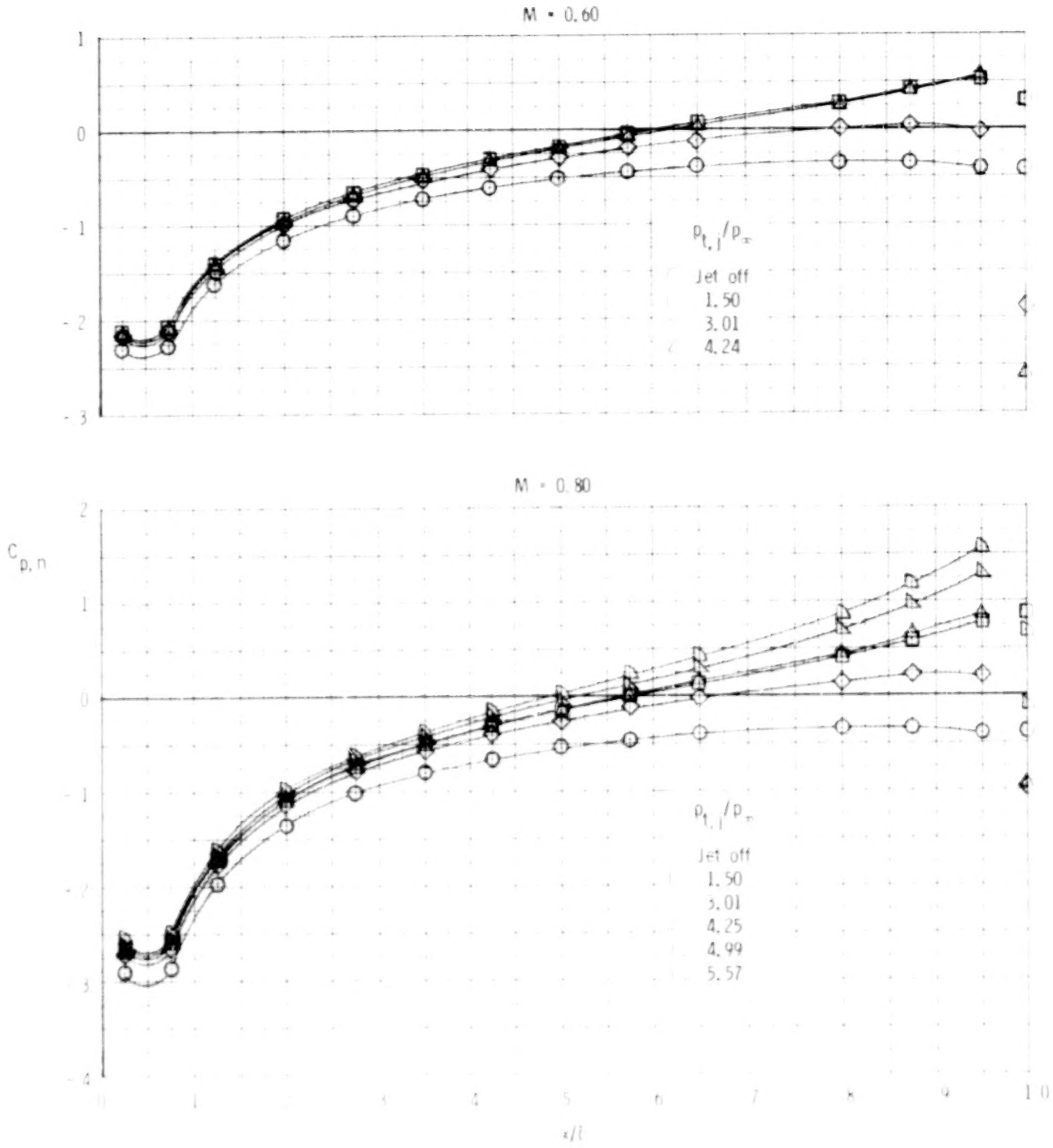

(a) M = 0.60 and 0.80.

Figure 38.- Nozzle pressure-coefficient distributions for configuration A-1.25-L. Dashed line indicates theoretical values.

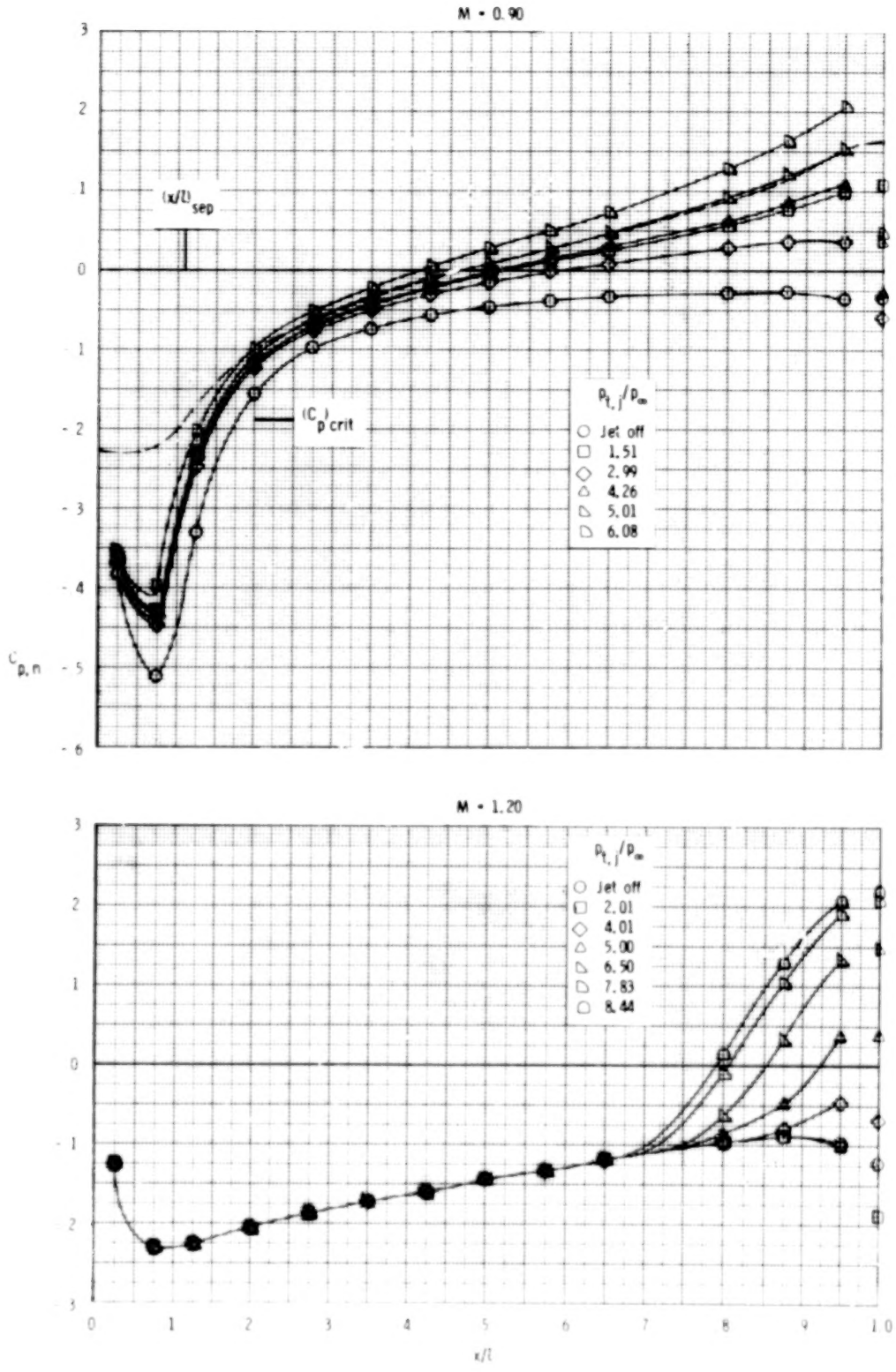

(b) M = 0.90 and 1.20.

Figure 38.- Continued.

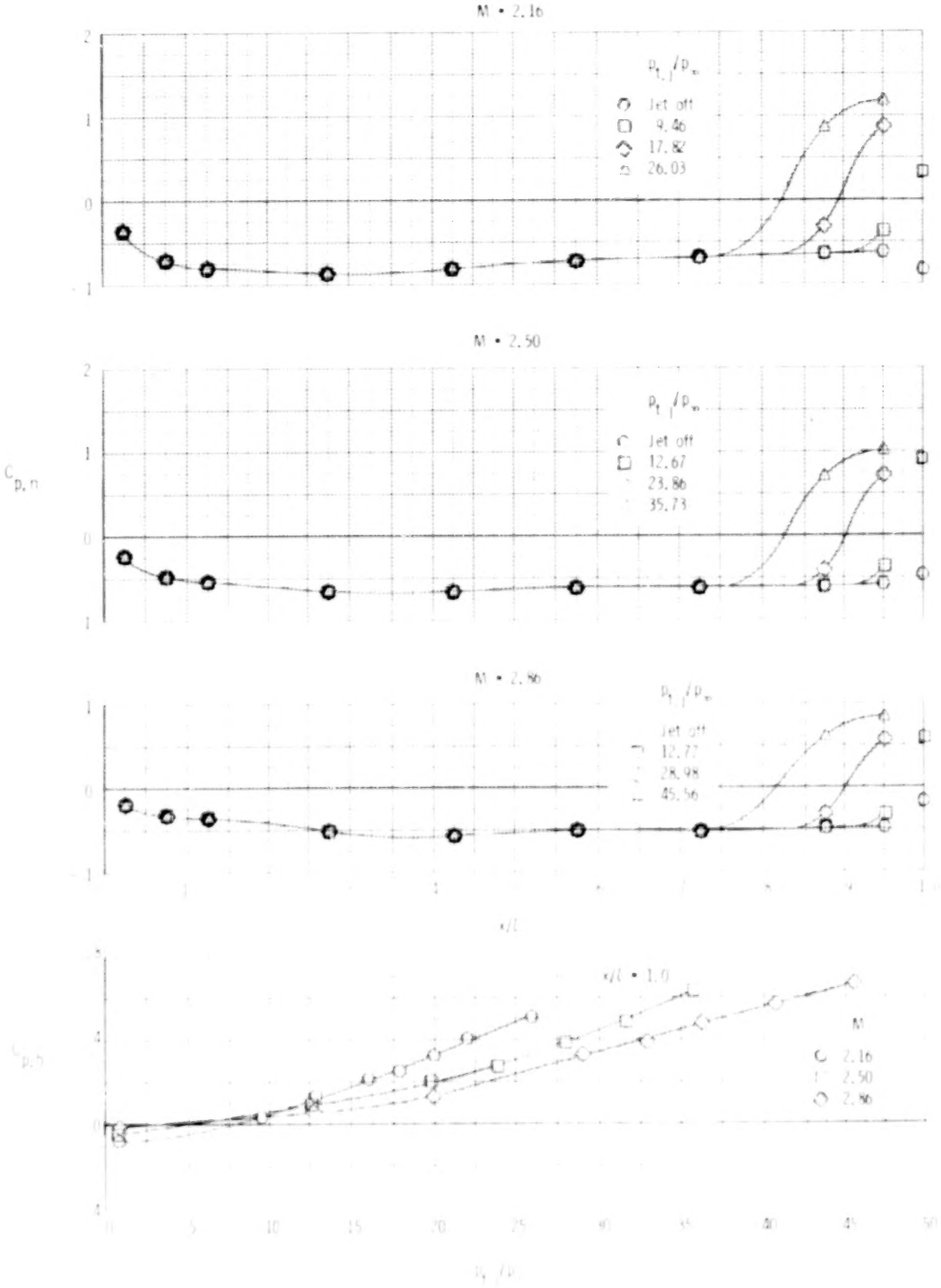

(c) M = 2.16 to 2.86.

Figure 38.- Concluded.

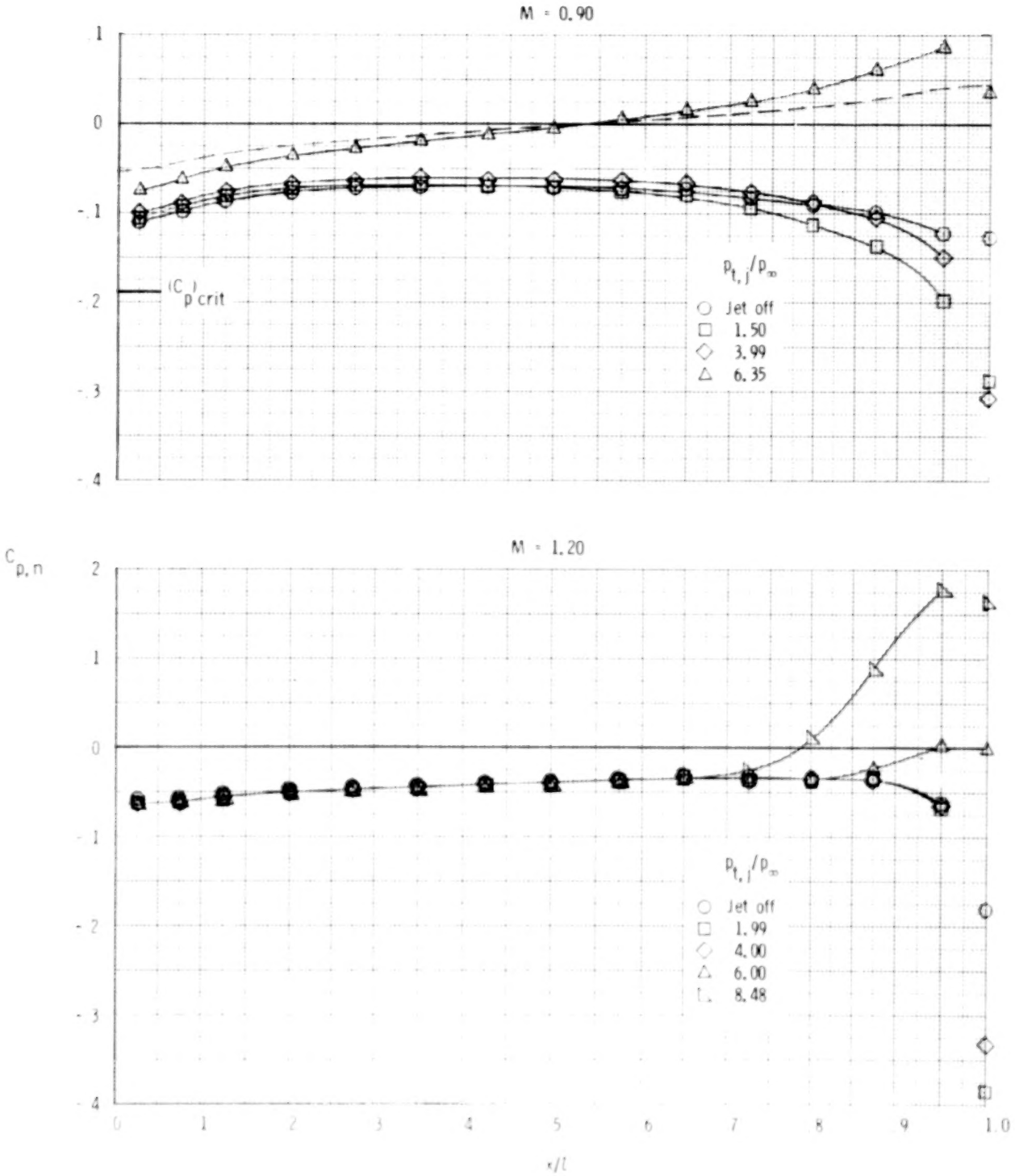

(a) M = 0.90 and 1.20.

Figure 39.- Nozzle pressure-coefficient distributions for configuration A-1.97-S. Dashed line indicates theoretical values.

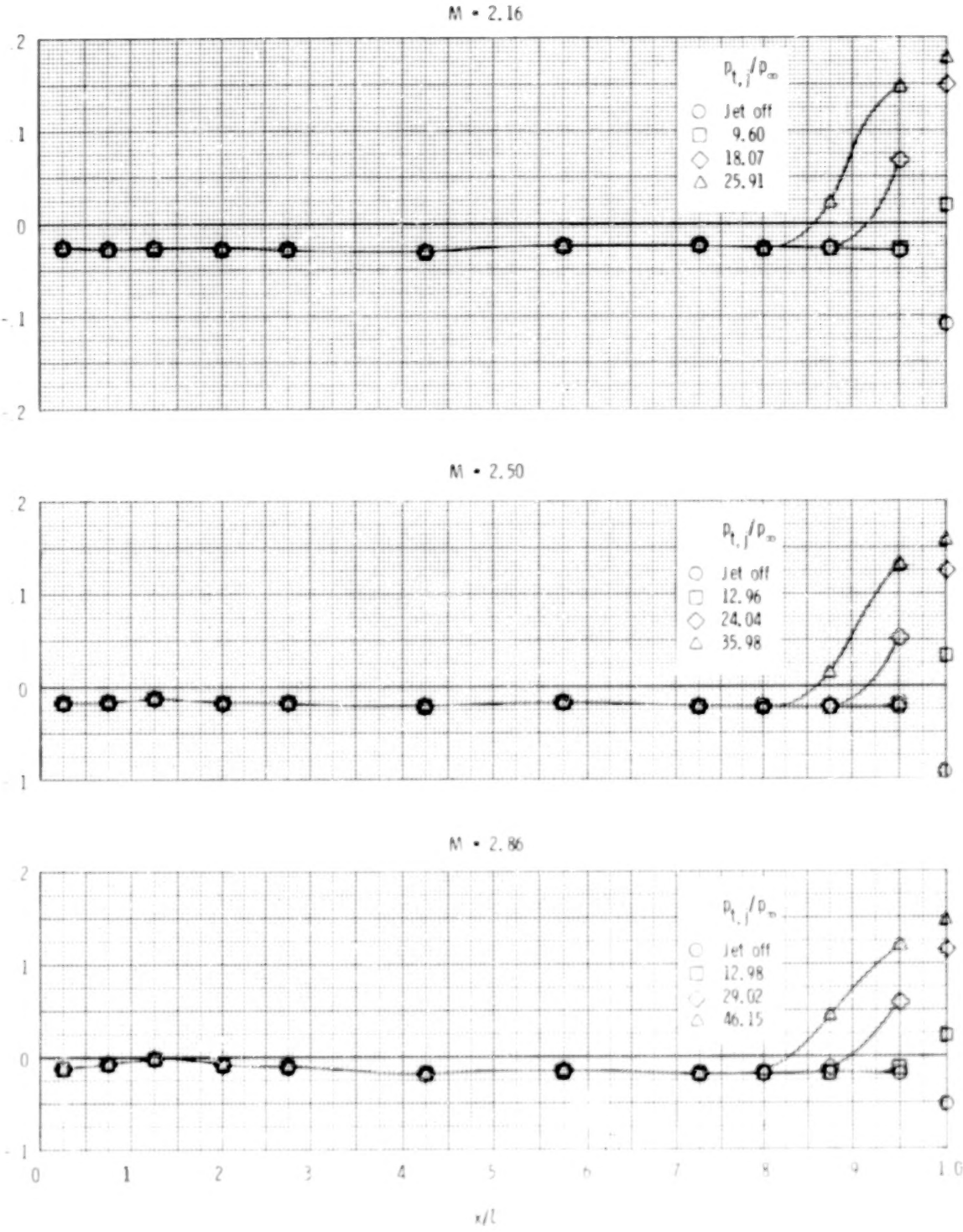

(b) M = 2.16 to 2.86.

Figure 39.- Concluded.

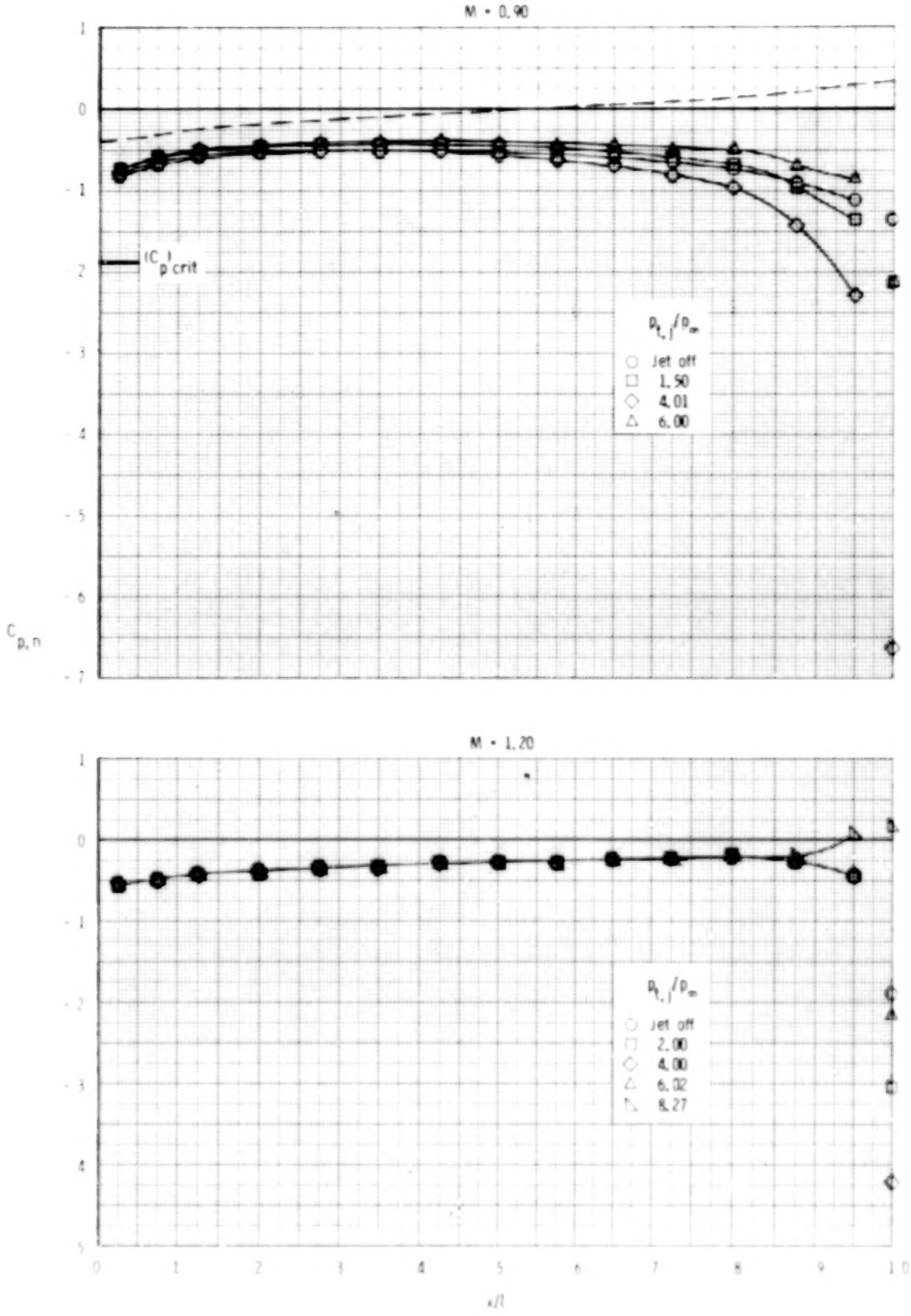

(a) M = 0.90 and 1.20.

Figure 40.- Nozzle pressure-coefficient distributions for configuration A-1.97-L. Dashed line indicates theoretical values.

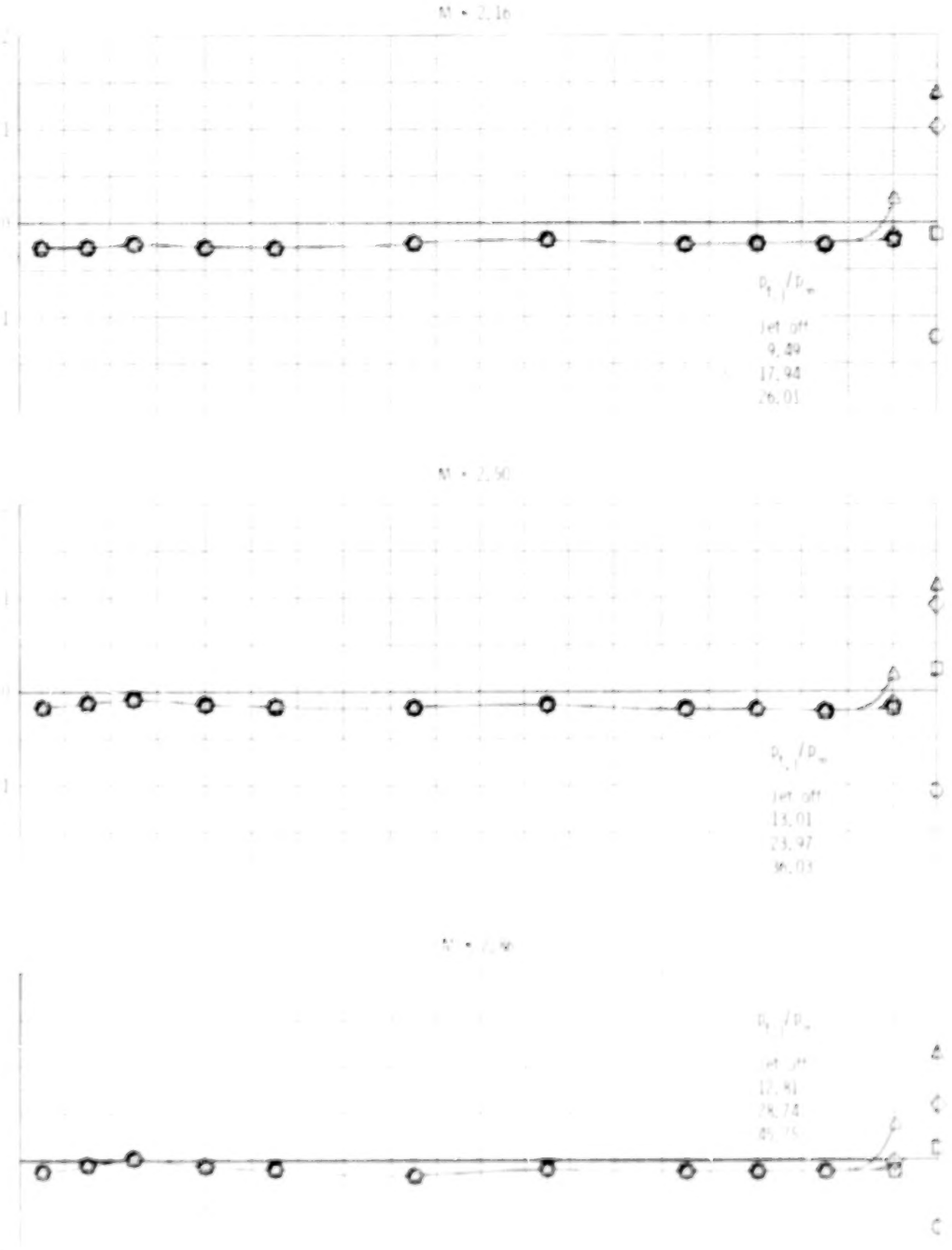

(b) M = 2.16 to 2.86.

Figure 40.- Concluded.

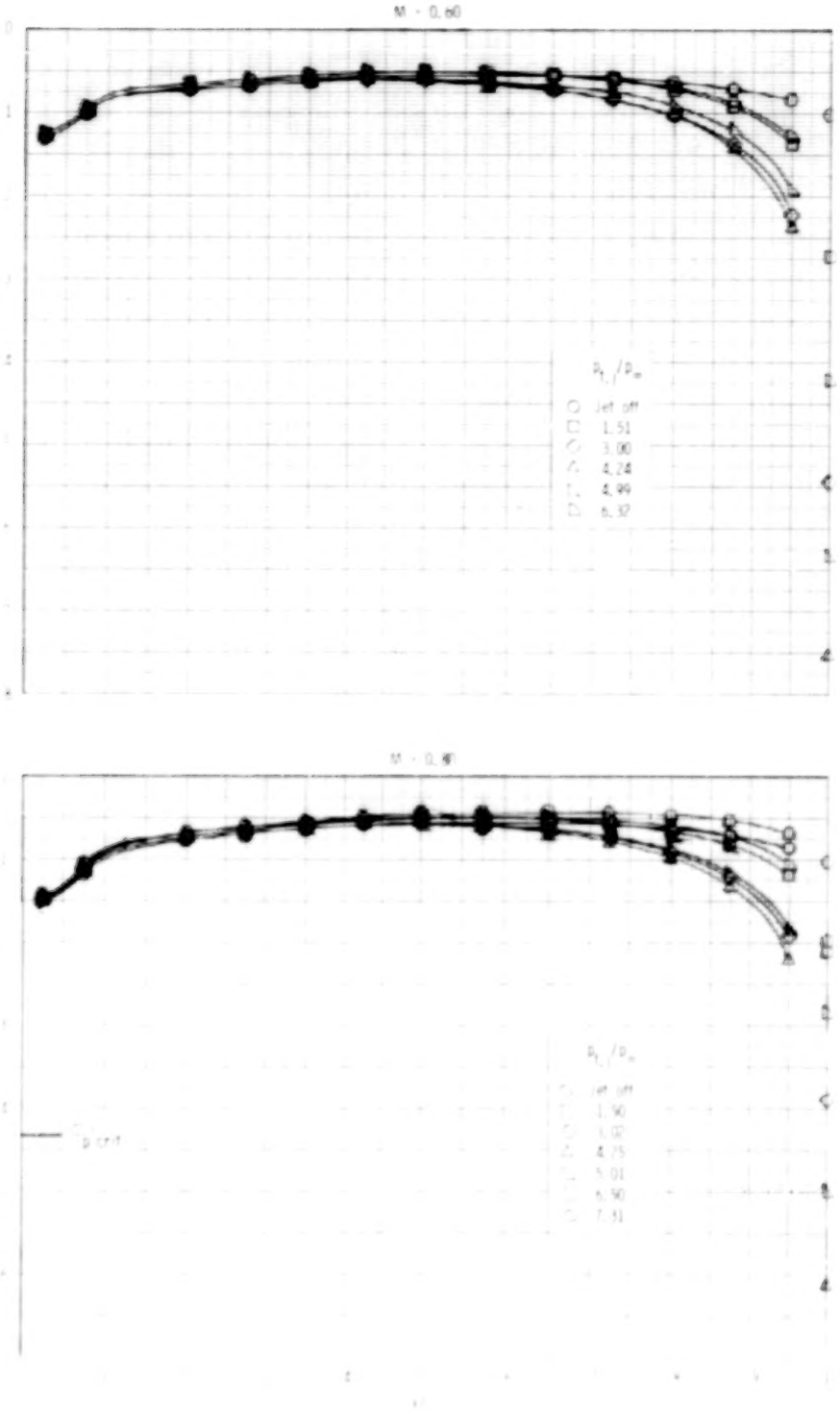

(a) M = 0.60 and 0.80.

Figure 41.- Nozzle pressure-coefficient distributions for configuration P-2.24(Sharp)-L.

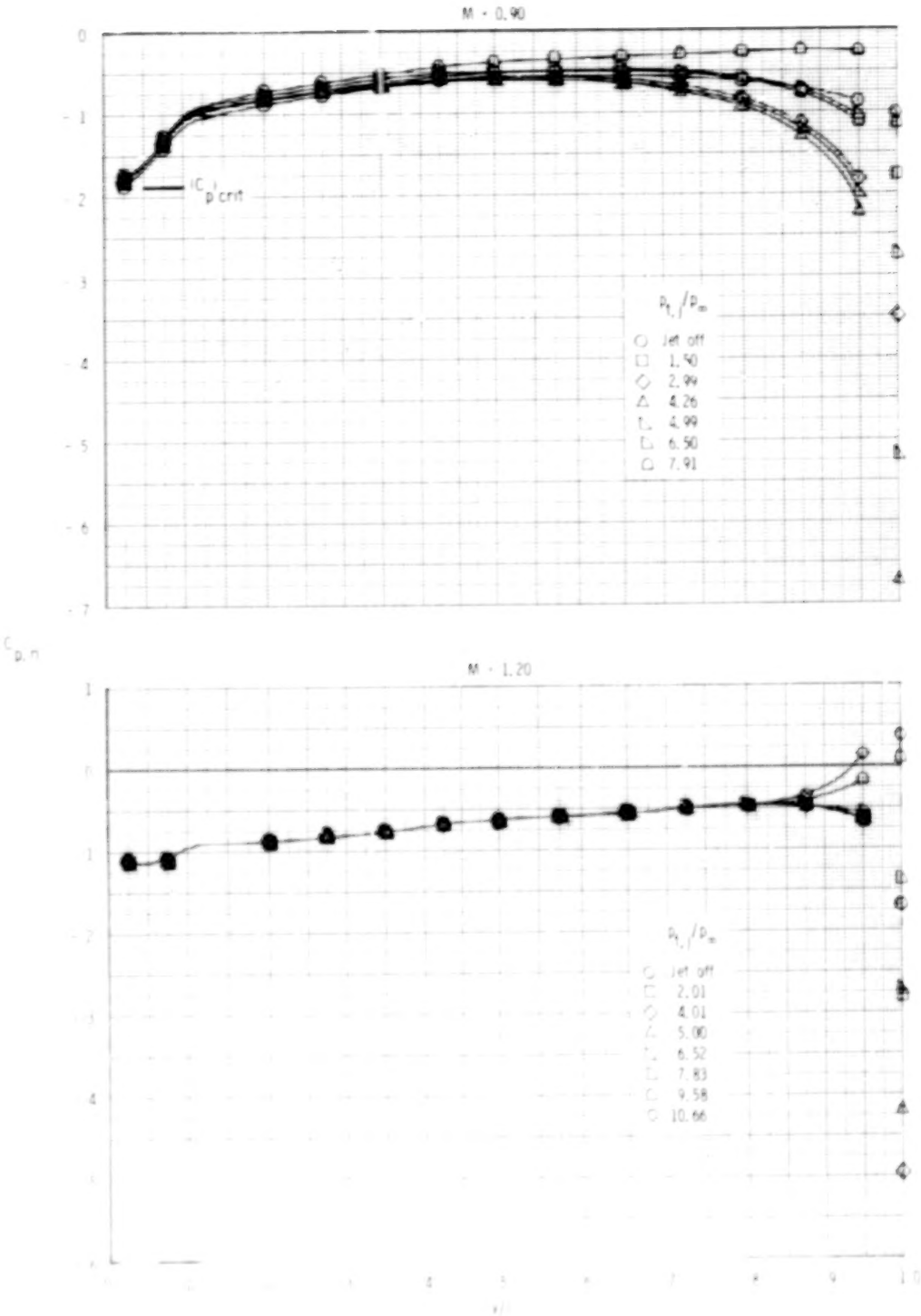

(b) M = 0.90 and 1.20.

Figure 41.- Concluded.

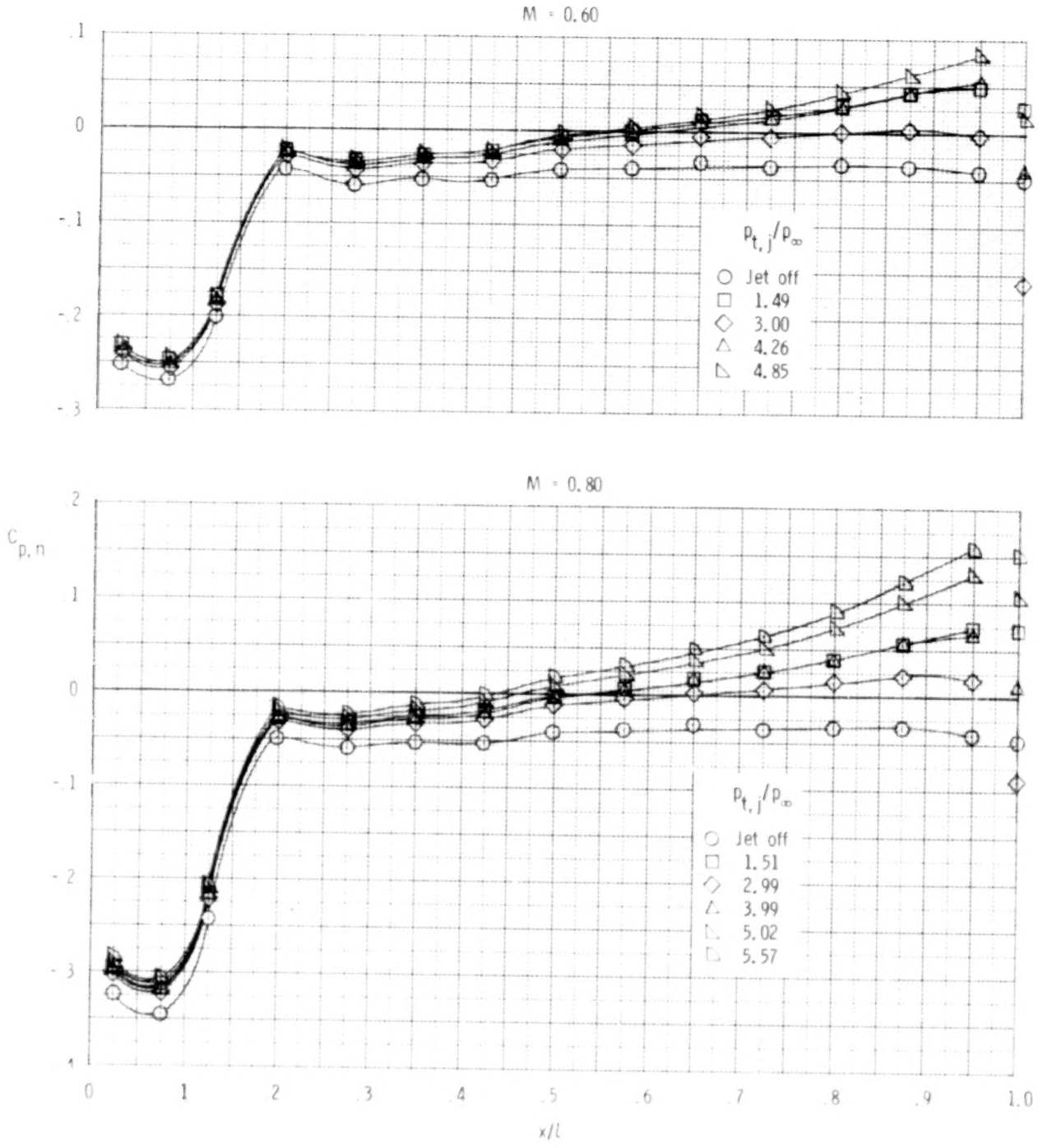

(a) M = 0.60 and 0.80.

Figure 42.- Nozzle pressure-coefficient distributions for configuration A-1.25-L(Cusp). Dashed line indicates theoretical values.

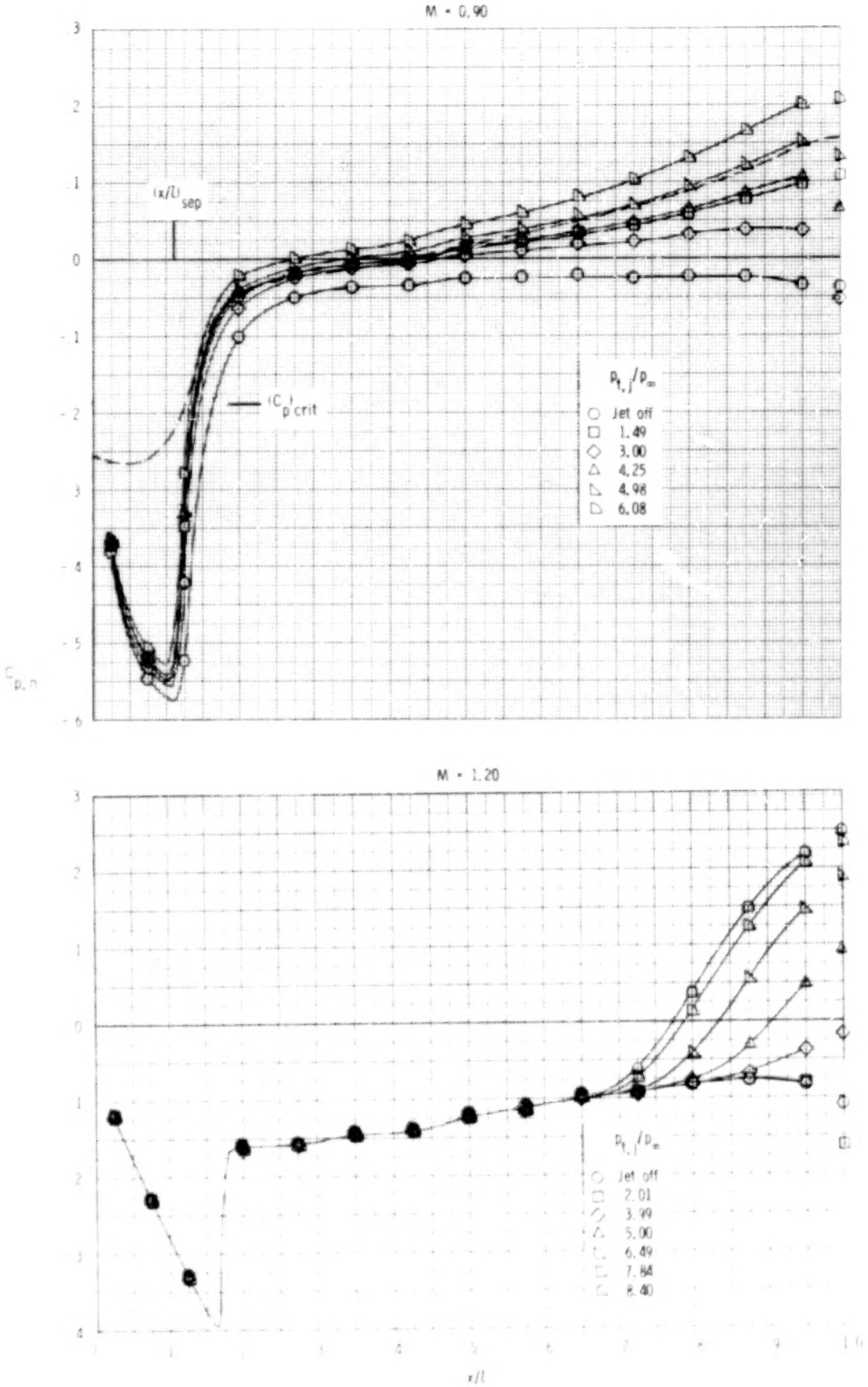

(b) M = 0.90 and 1.20.

Figure 42.- Continued.

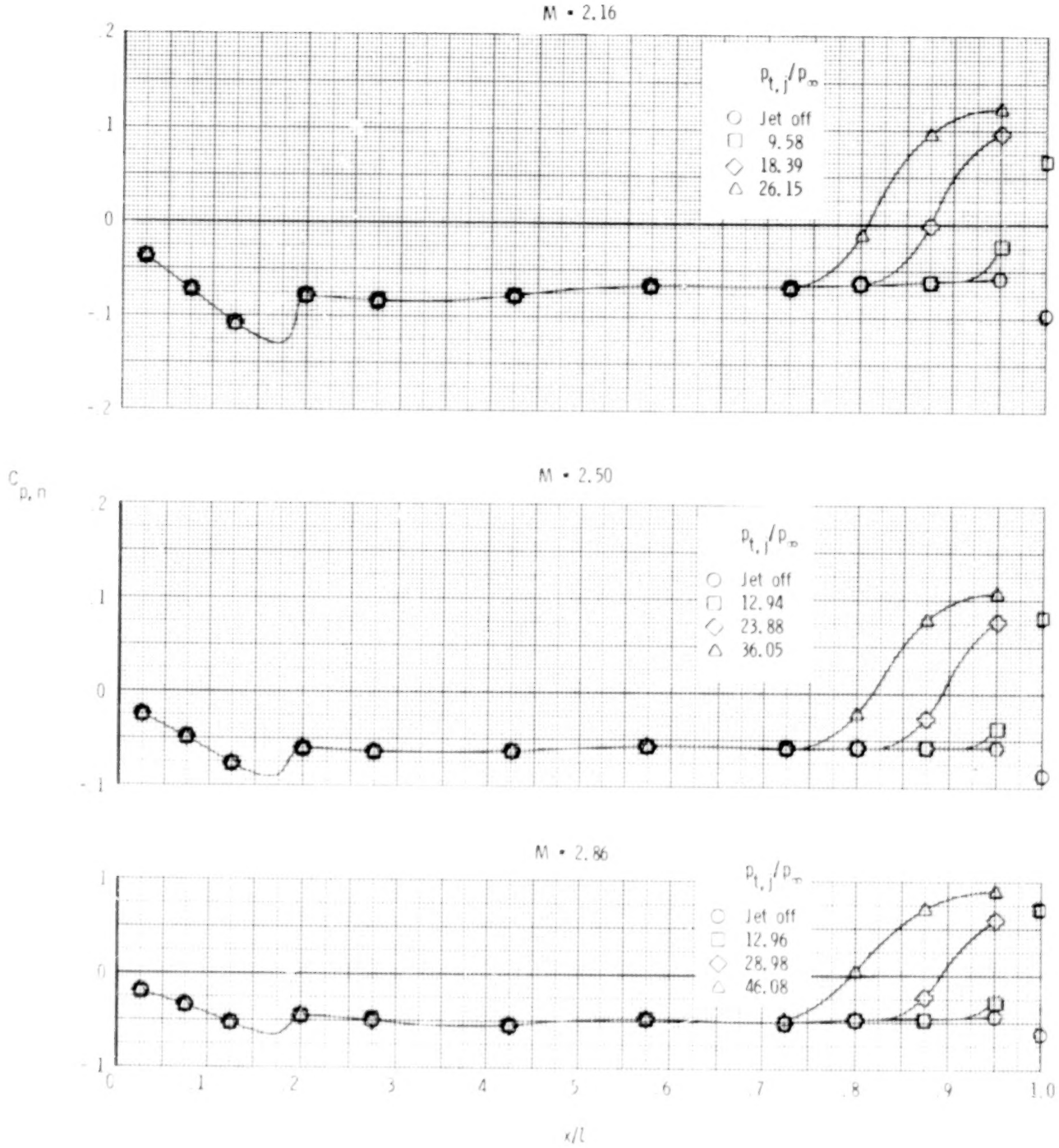

(c) M = 2.16 to 2.86.

Figure 42.- Concluded.

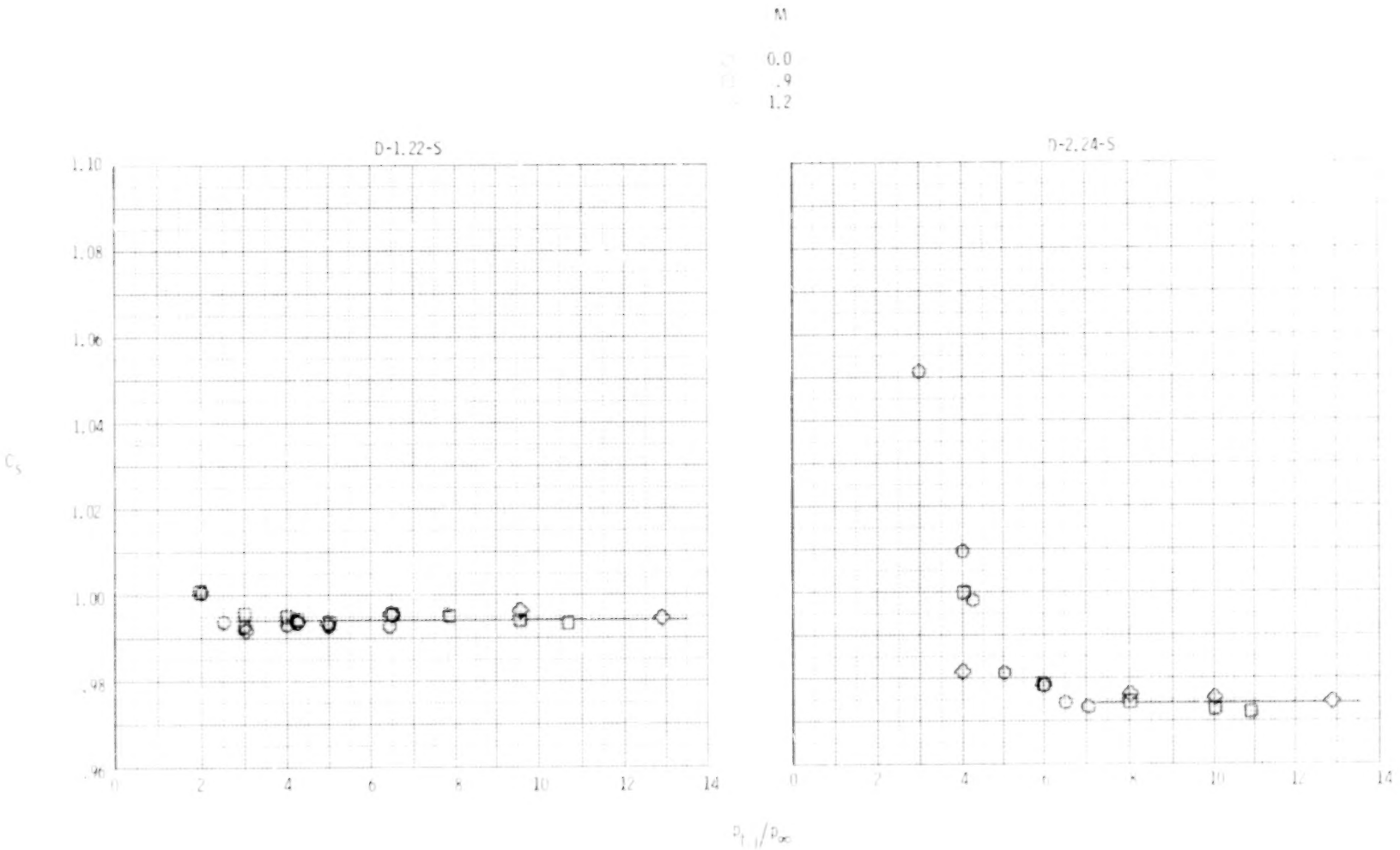

(a) Dry power, short length nozzles.

Figure 43.- Variation of stream thrust-correction factor with nozzle pressure ratio.

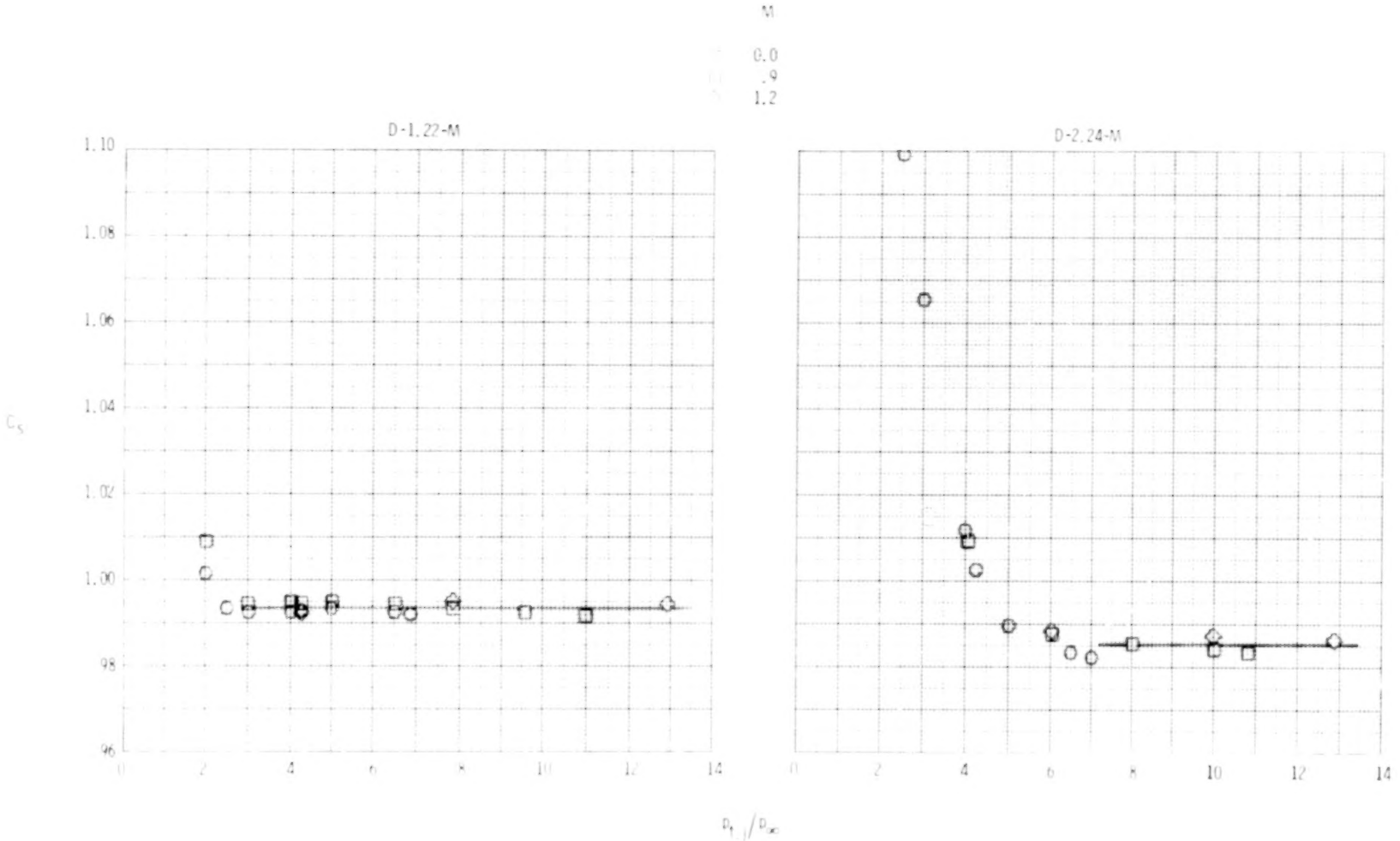

(b) Dry power, medium length nozzles.

Figure 43.- Continued.

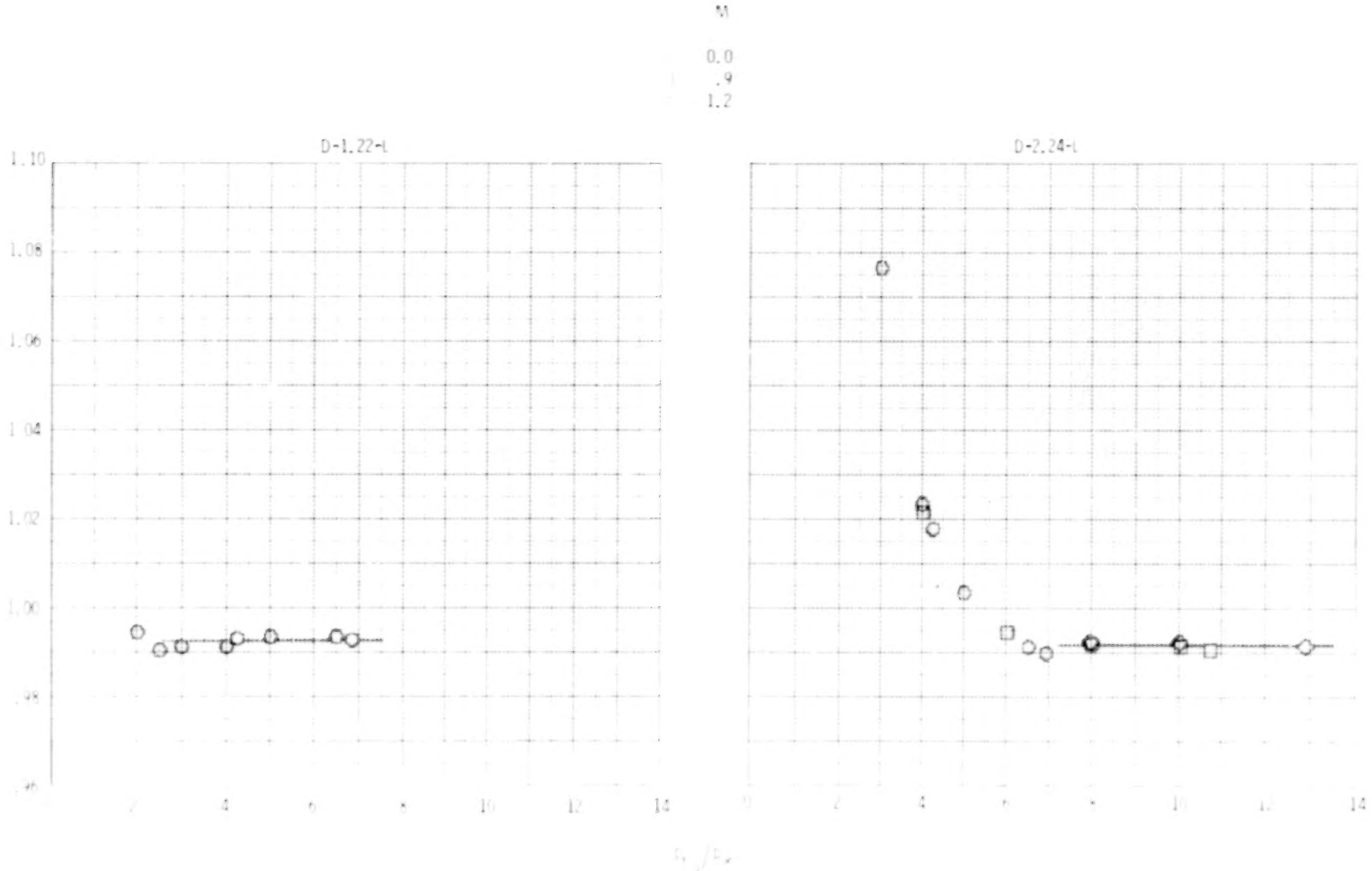

(c) Dry power, long length nozzles.

Figure 43.- Continued.

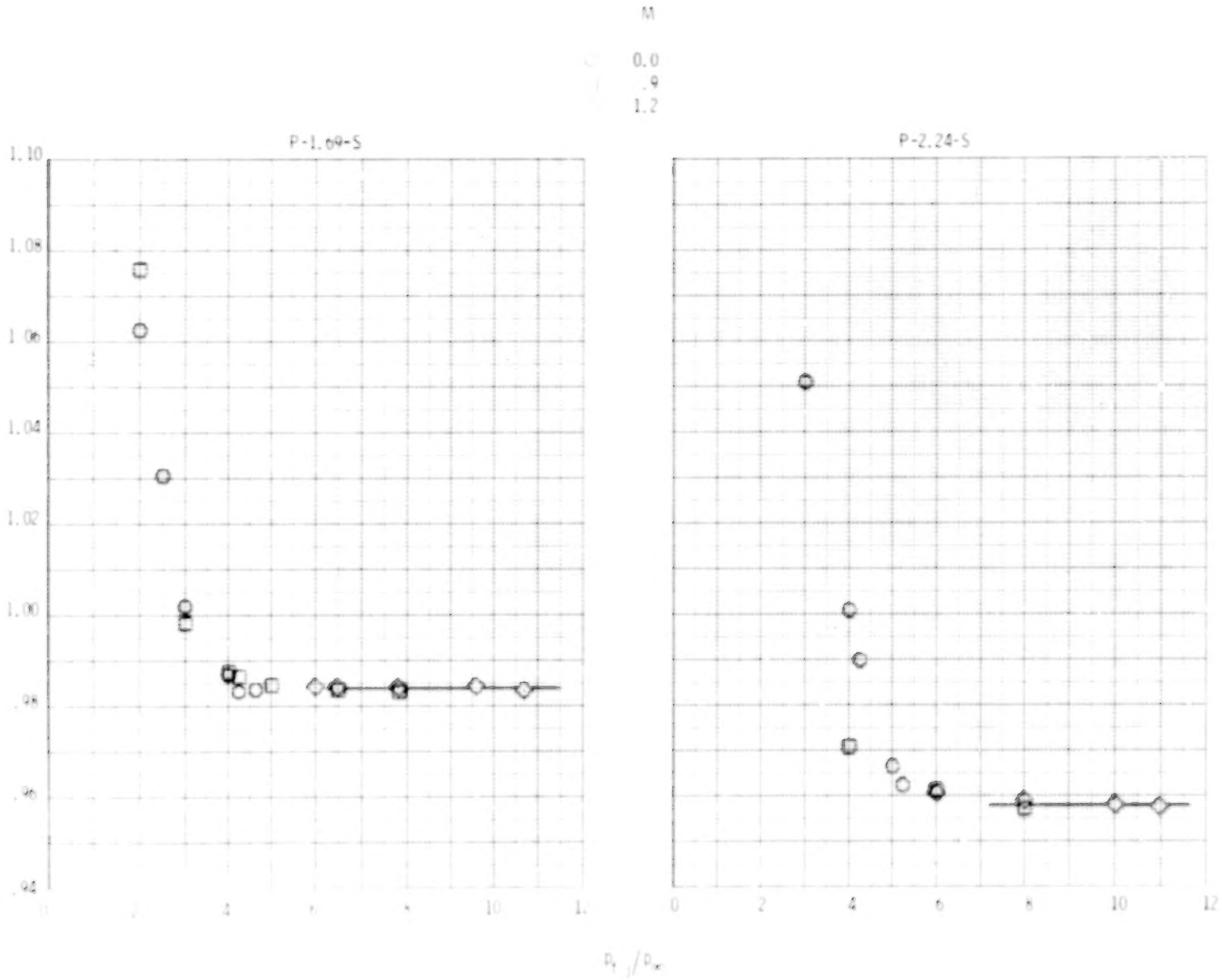

(d) Partial A/B, short length nozzles.

Figure 43.- Continued.

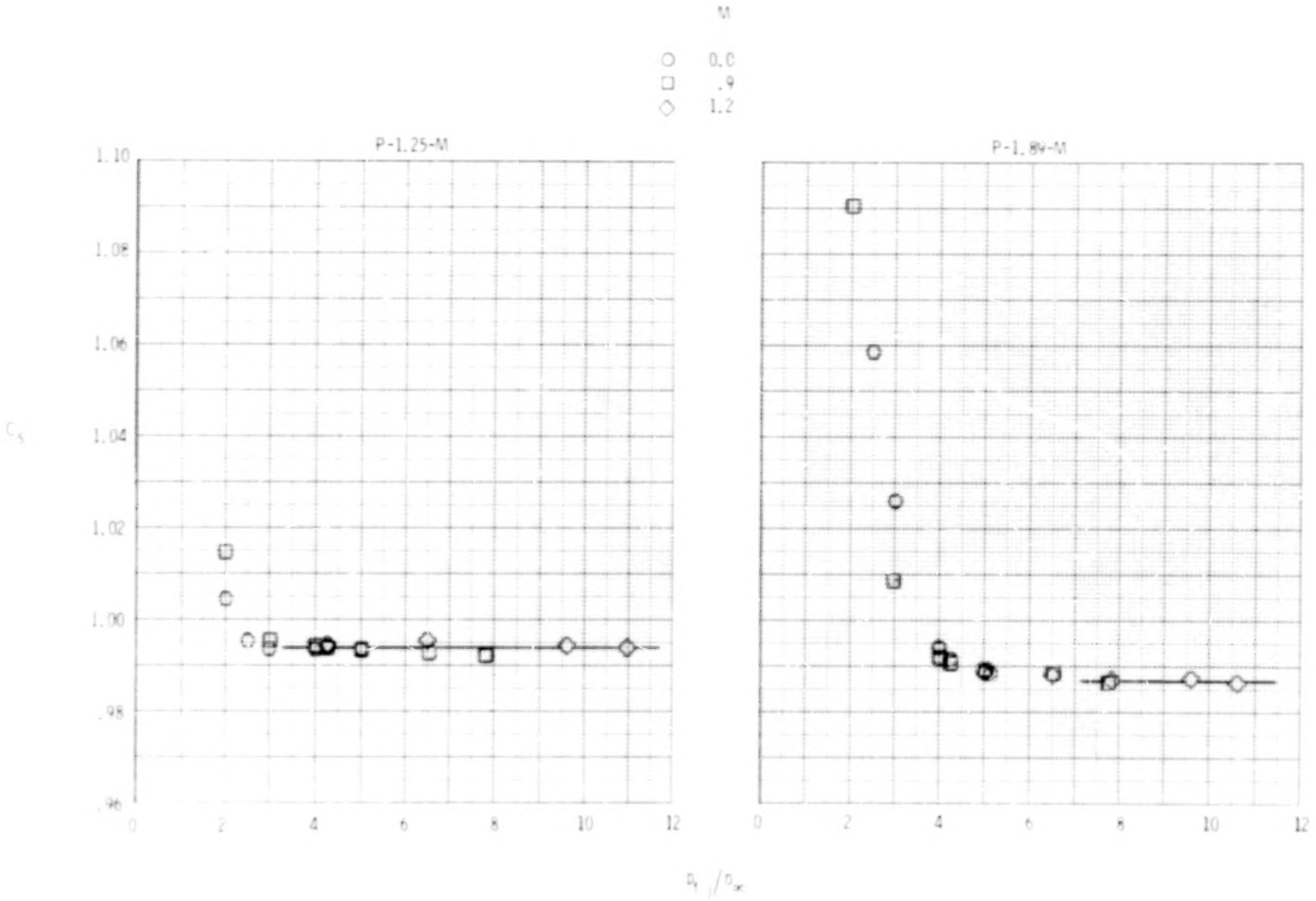

(e) Partial A/B, medium length nozzles.

Figure 43.- Continued.

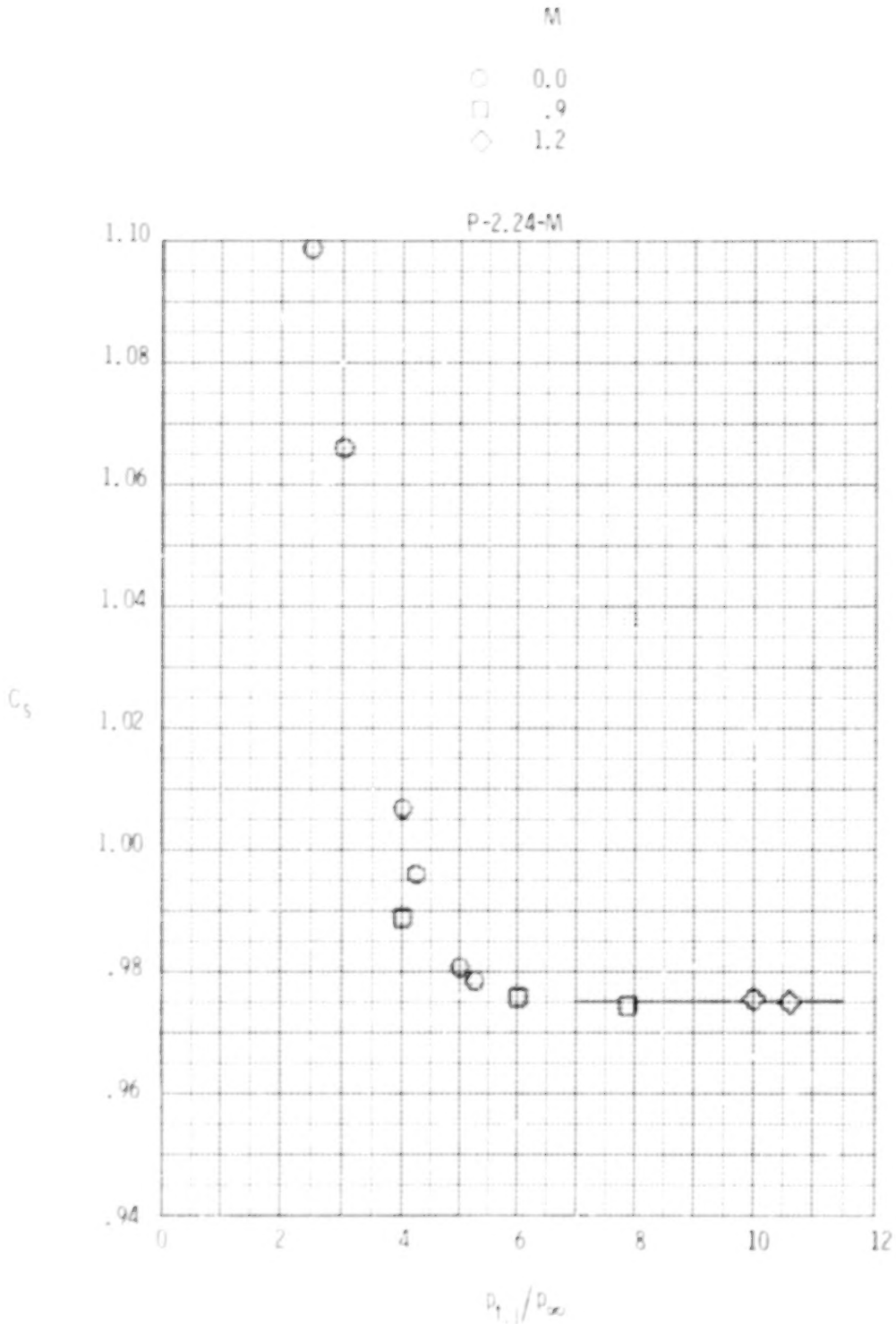

(e) Concluded.

Figure 43.- Continued.

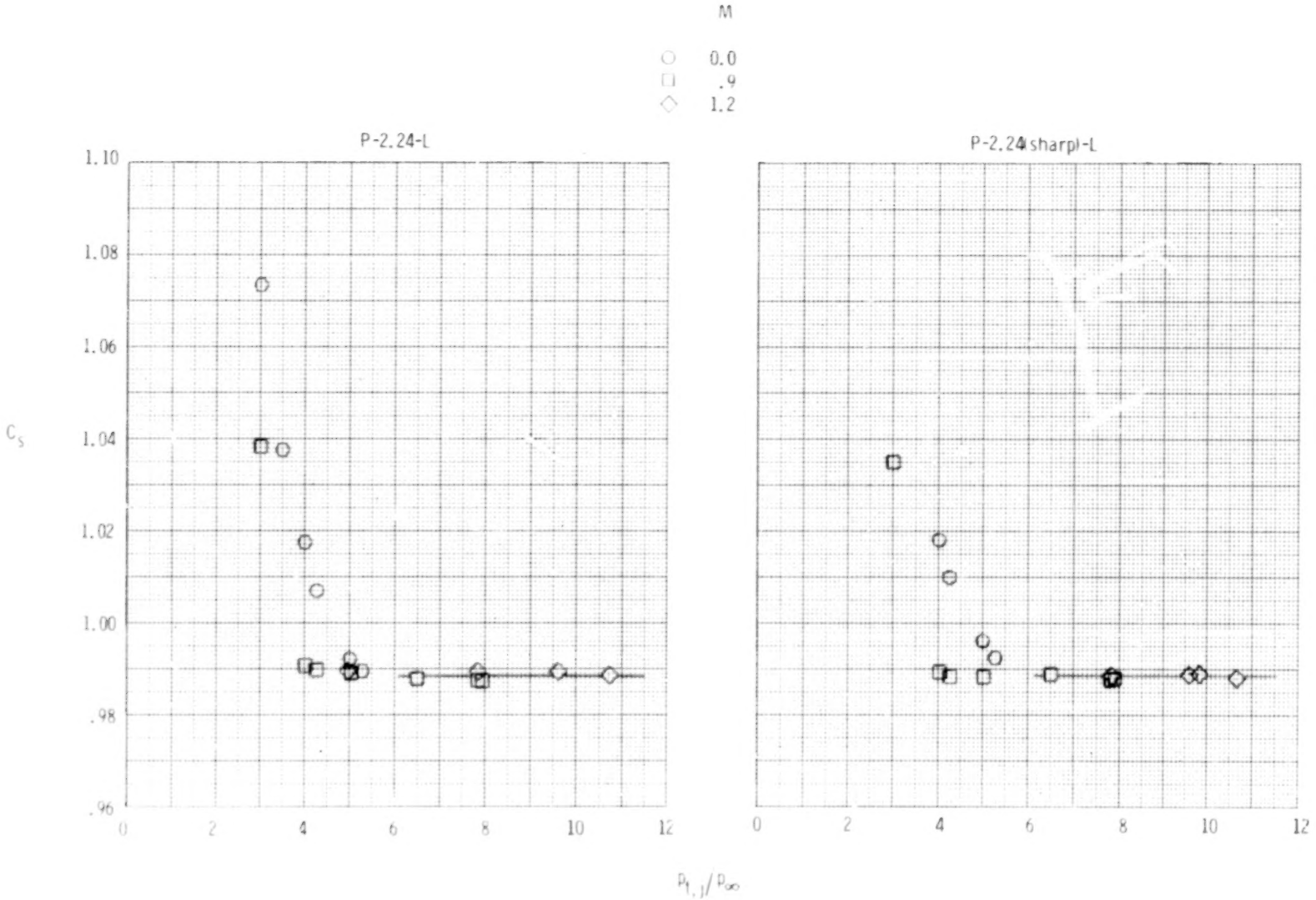

(f) Partial A/B, long length nozzles.

Figure 43.- Continued.

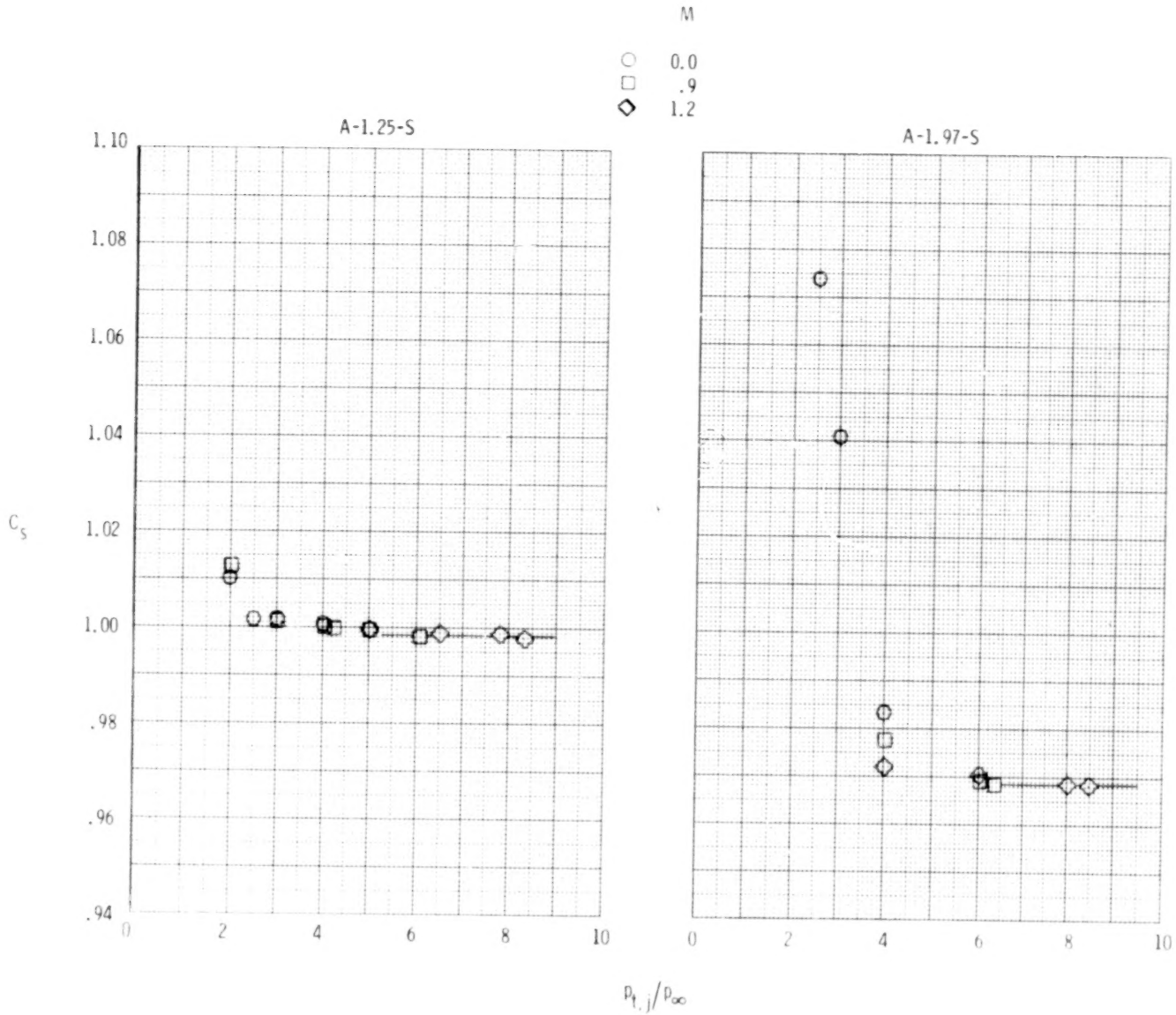

(g) Max A/B, short length nozzles.

Figure 43.- Continued.

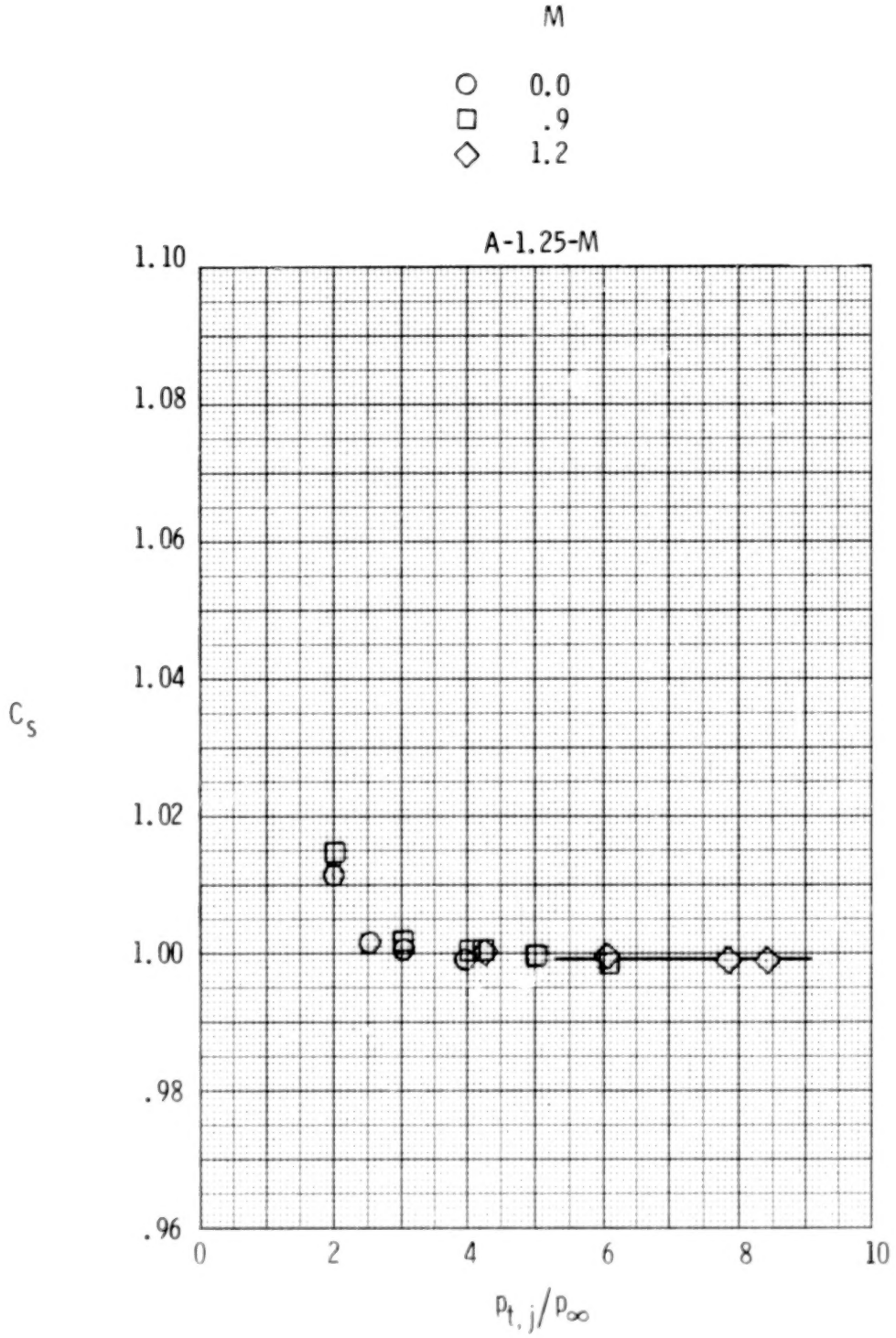

(h) Max A/B, medium length nozzles.

Figure 43.- Continued.

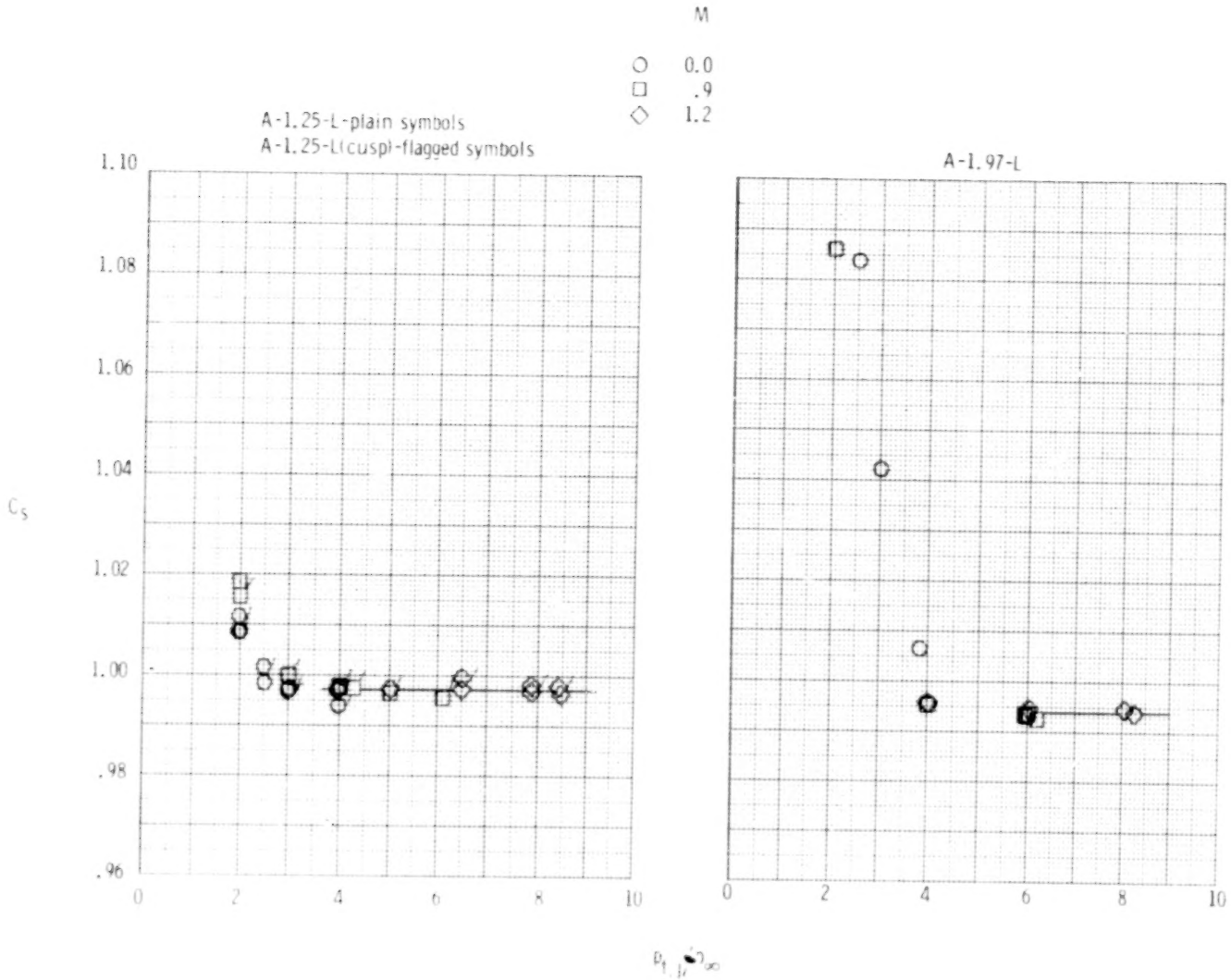

(i) Max A/B, long length nozzles.

Figure 43.- Concluded.

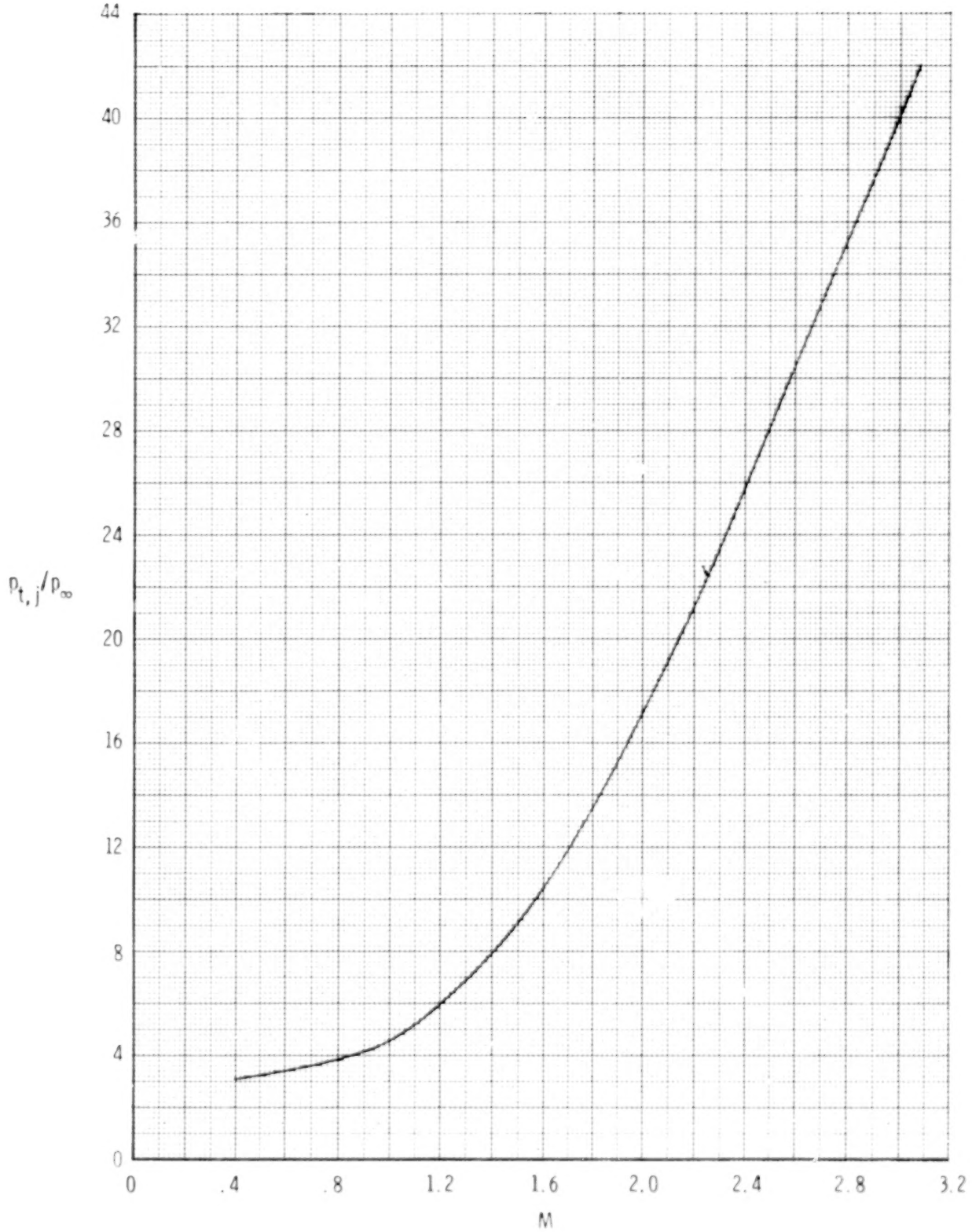

Figure 44.- Typical nozzle pressure-ratio schedule with Mach number.

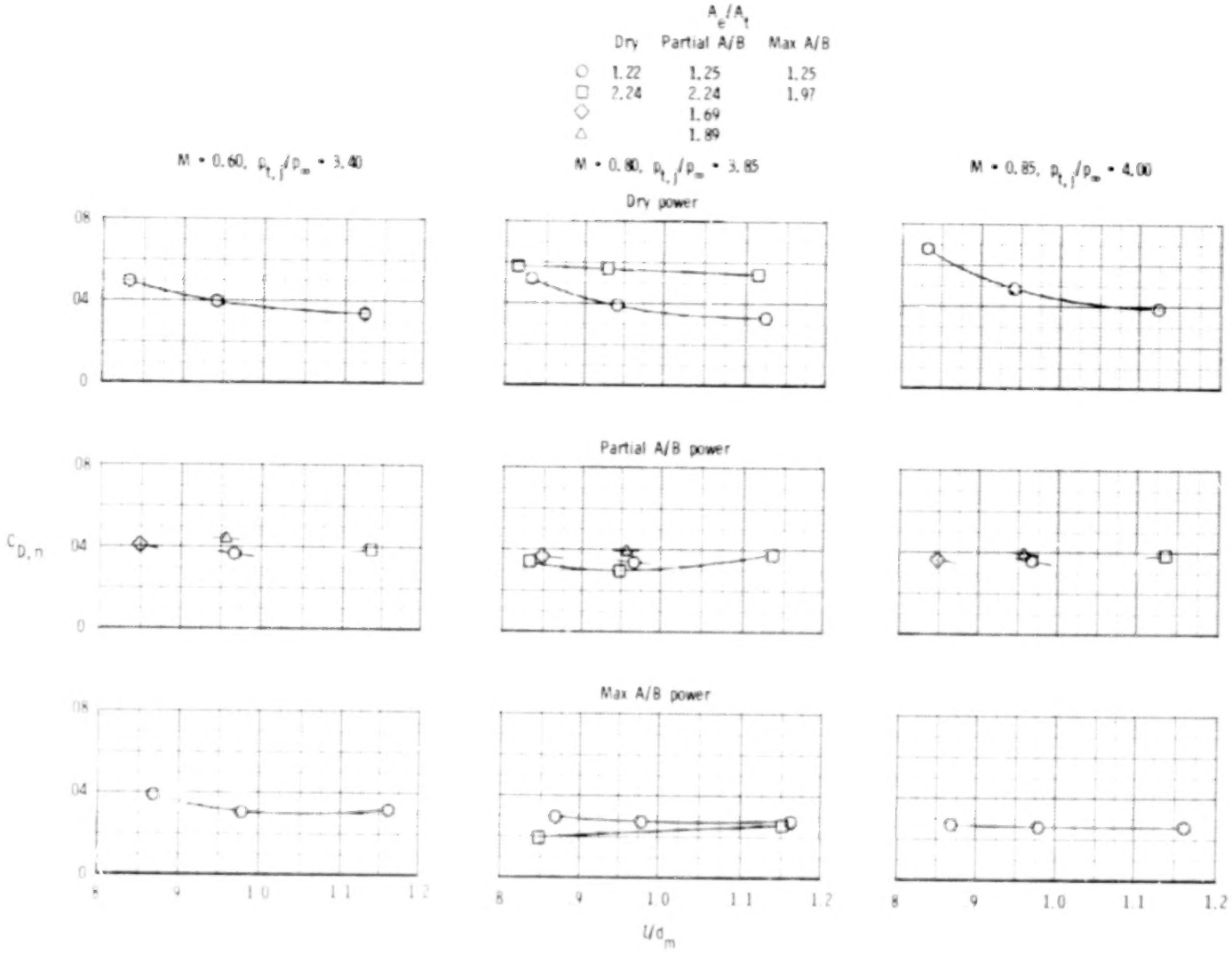

(a) M = 0.60 to 0.85.

Figure 45.- Effect of nozzle length (boattail angle) on nozzle drag coefficient at several Mach numbers and scheduled nozzle pressure ratios.

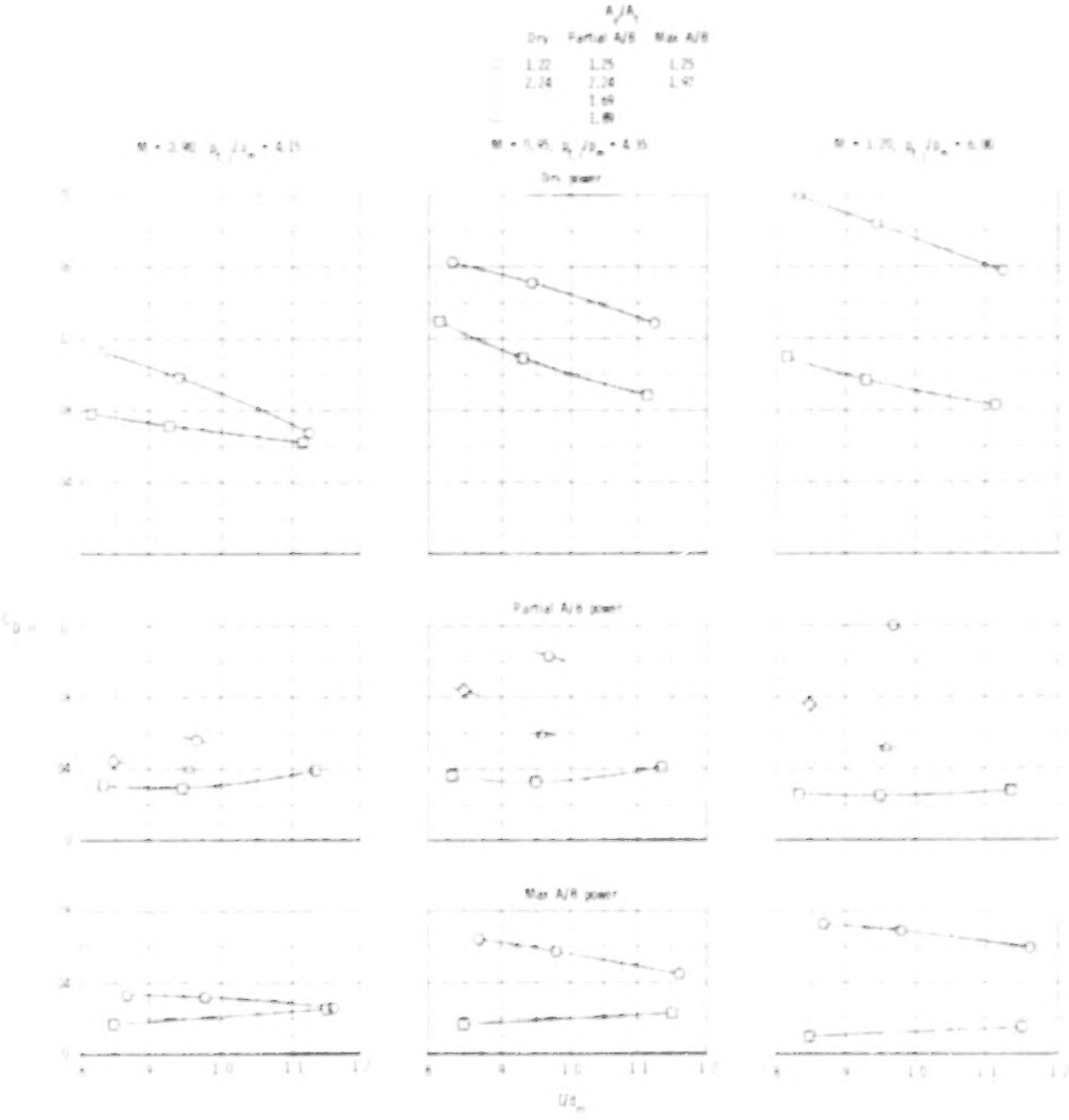

(b) M = 0.90 to 1.20.

Figure 45.- Continued.

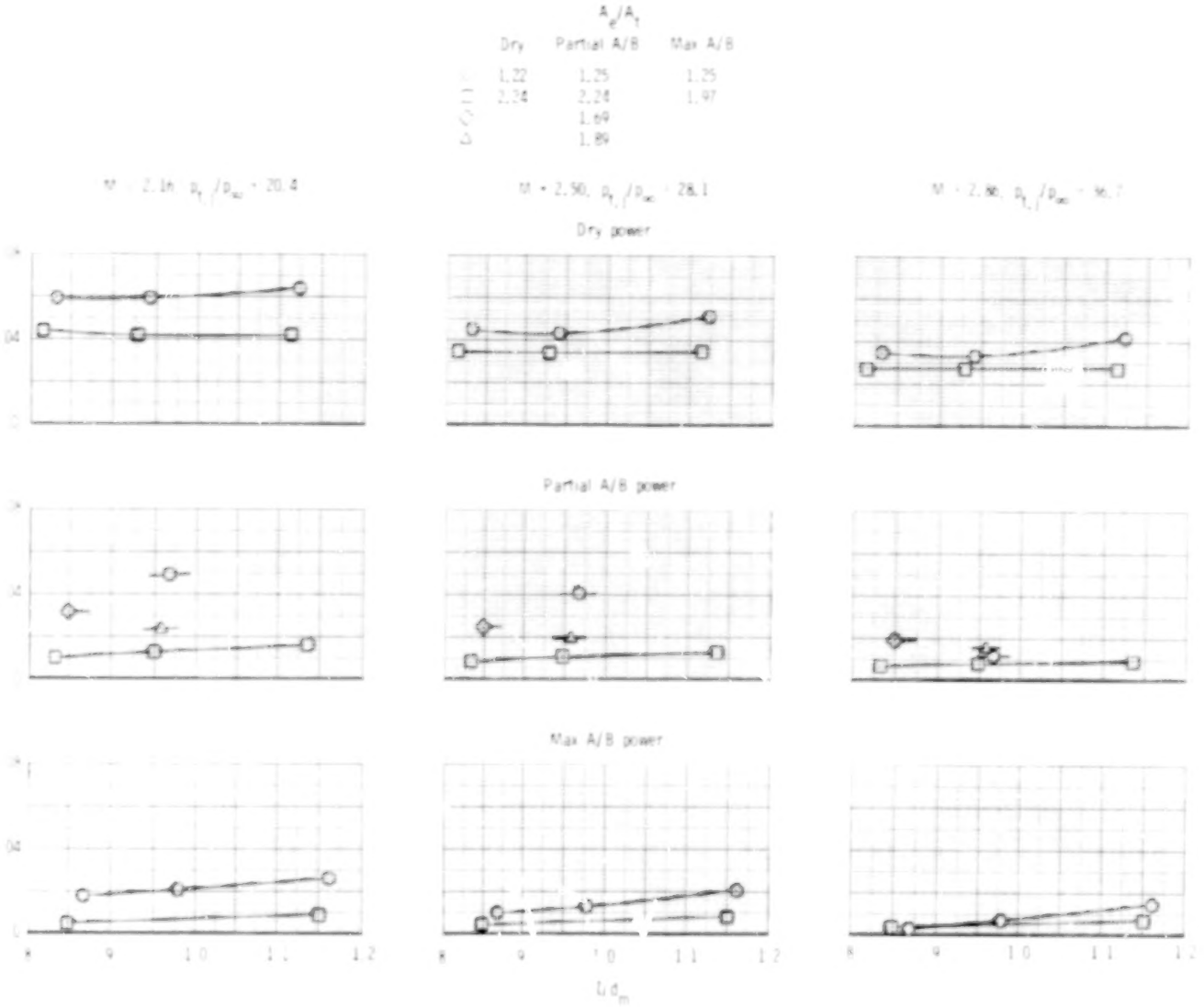

(c) M = 2.16 to 2.86.

Figure 45.- Concluded.

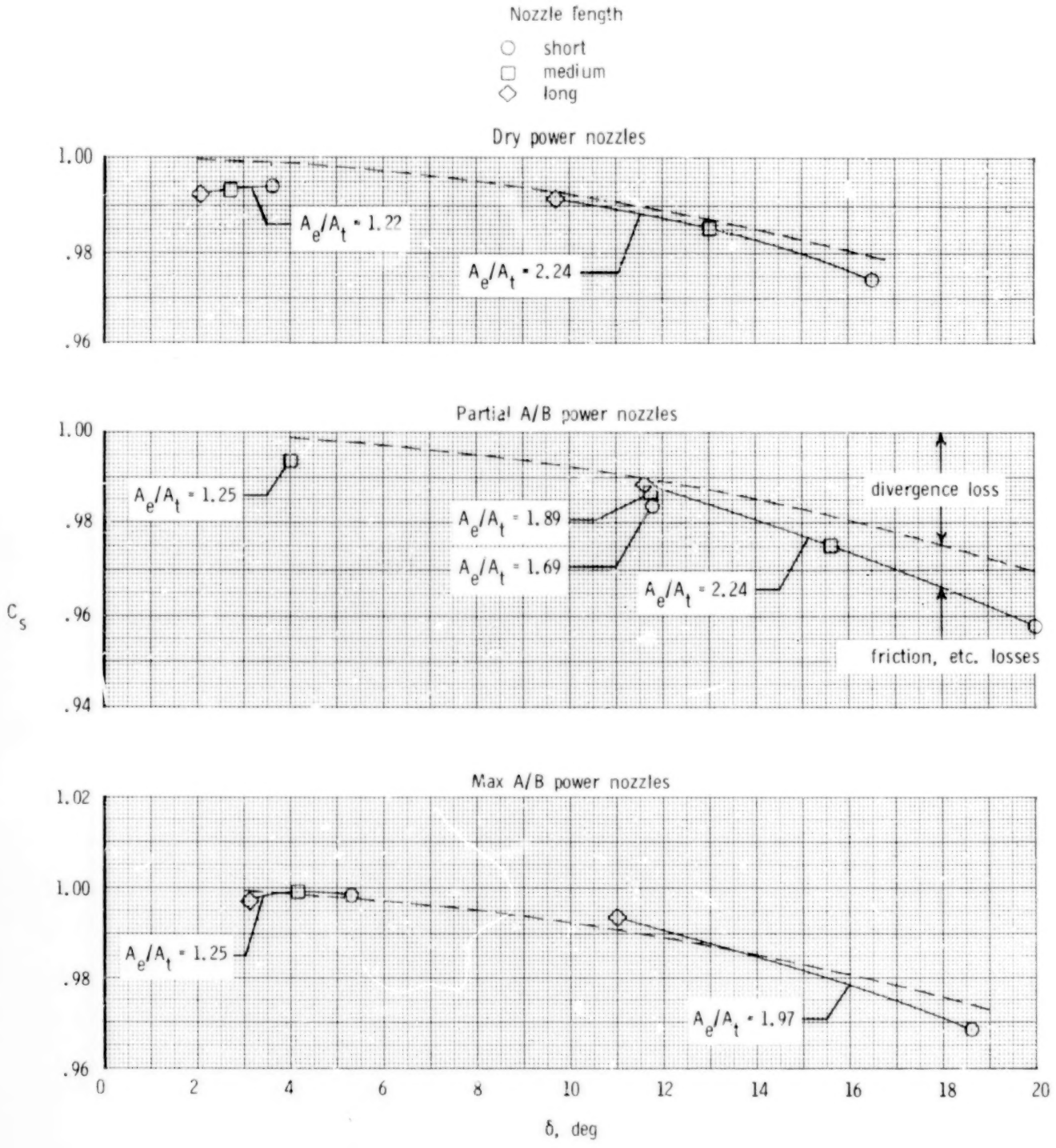

Figure 46.- Variation of stream thrust-correction factor with nozzle divergence angle. Dashed line indicates divergence loss from reference 12;

$$\text{Divergent loss} = 1.0 - \frac{(1 + \cos \delta)}{2}.$$

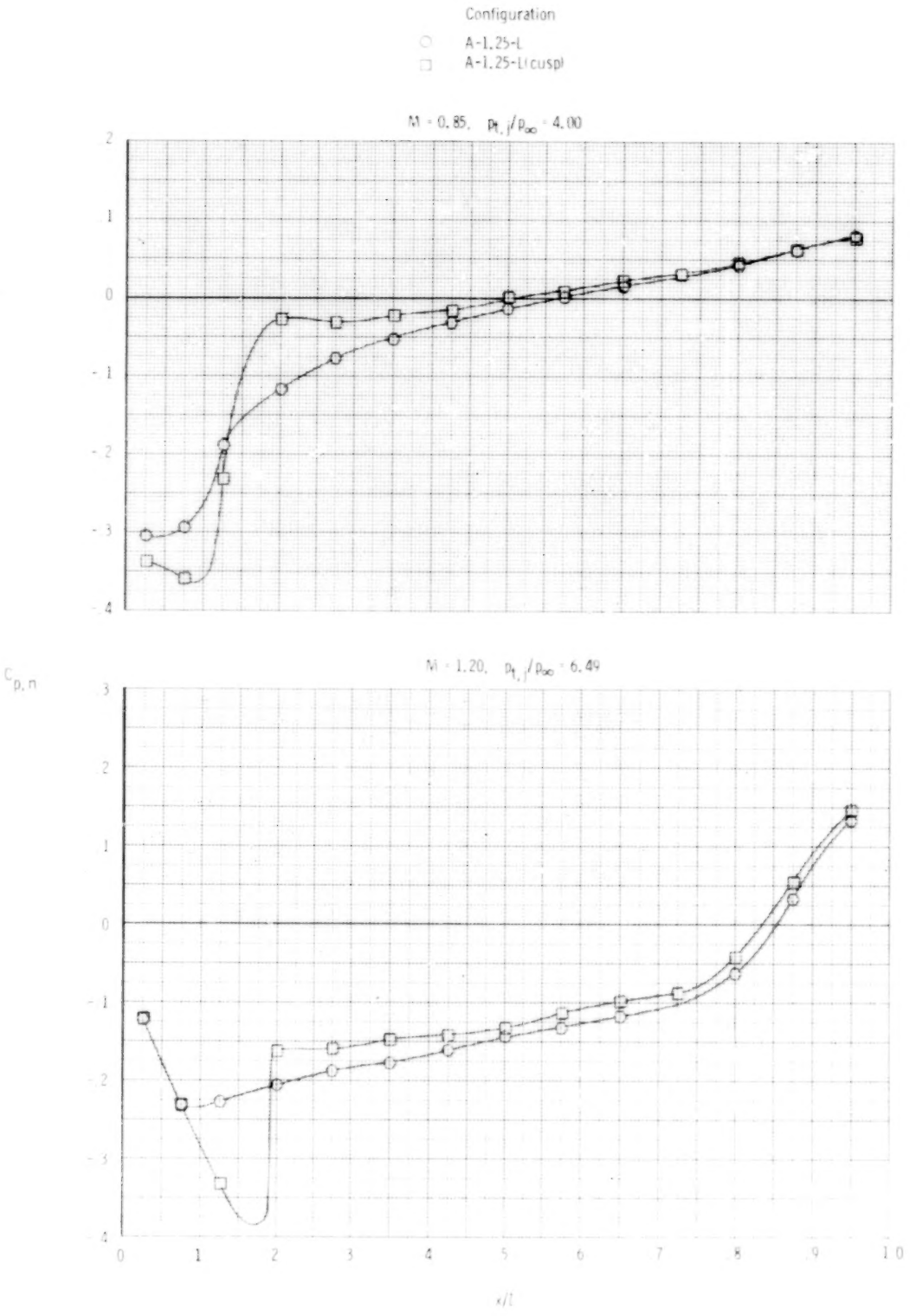

(a) M = 0.85 and 1.20.

Figure 47.- Effect of an external geometric cusp on nozzle boattail pressure distributions. $\phi = 0^{o}$.

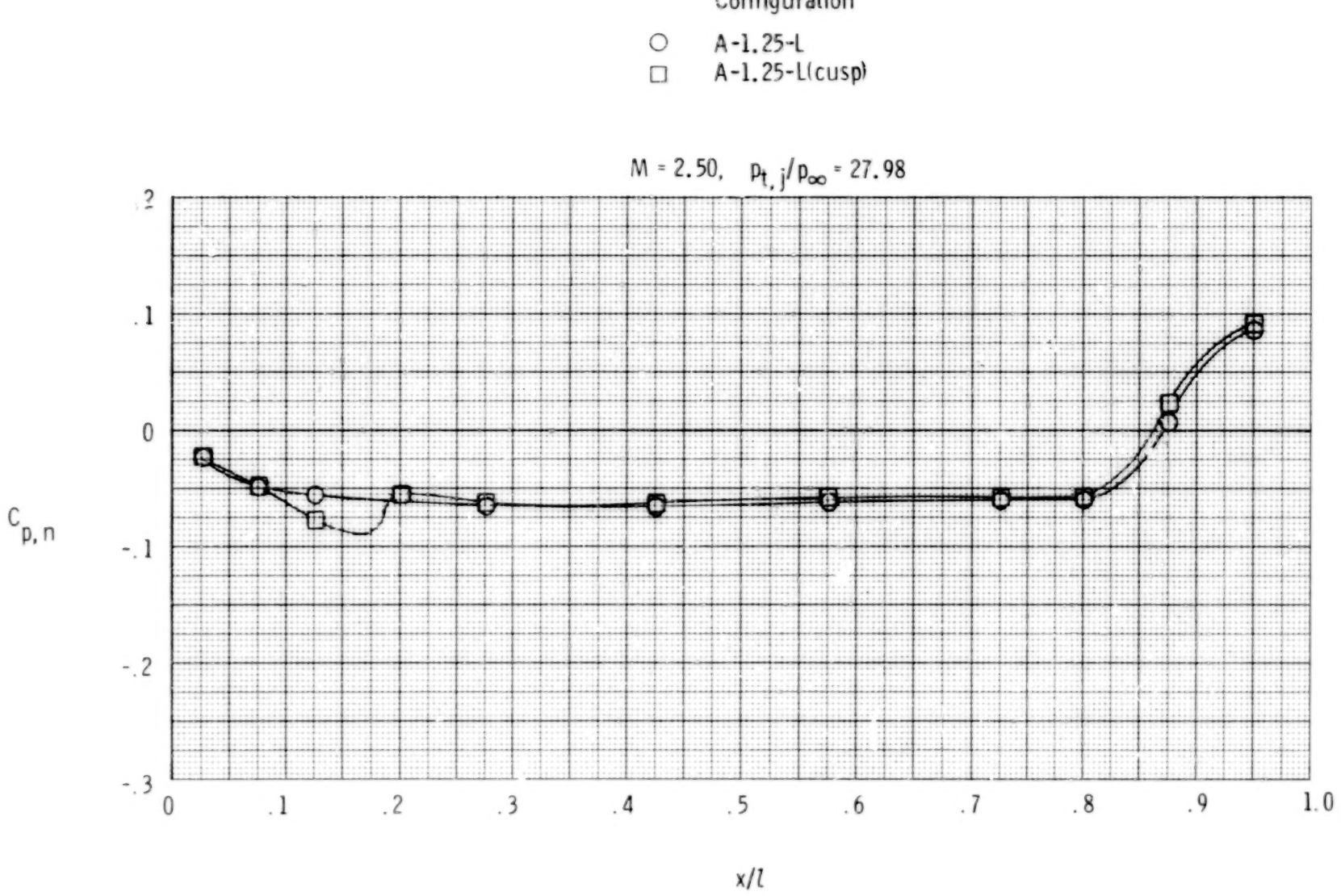

(b) M = 2.50.

Figure 47.- Concluded.

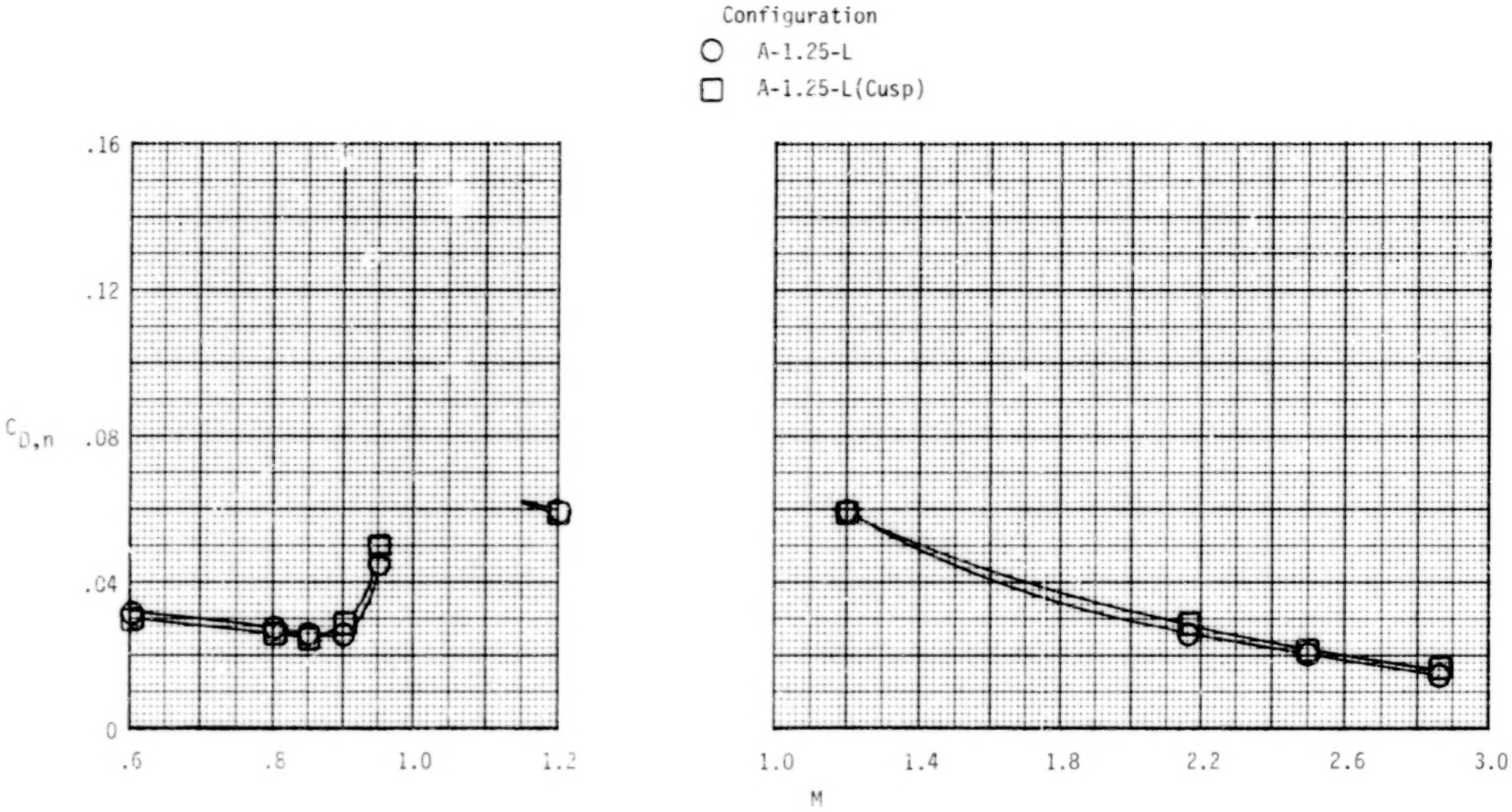

Figure 48.- Effect of an external geometric cusp on nozzle boattail drag at scheduled nozzle pressure ratios. Note Mach number scale change.

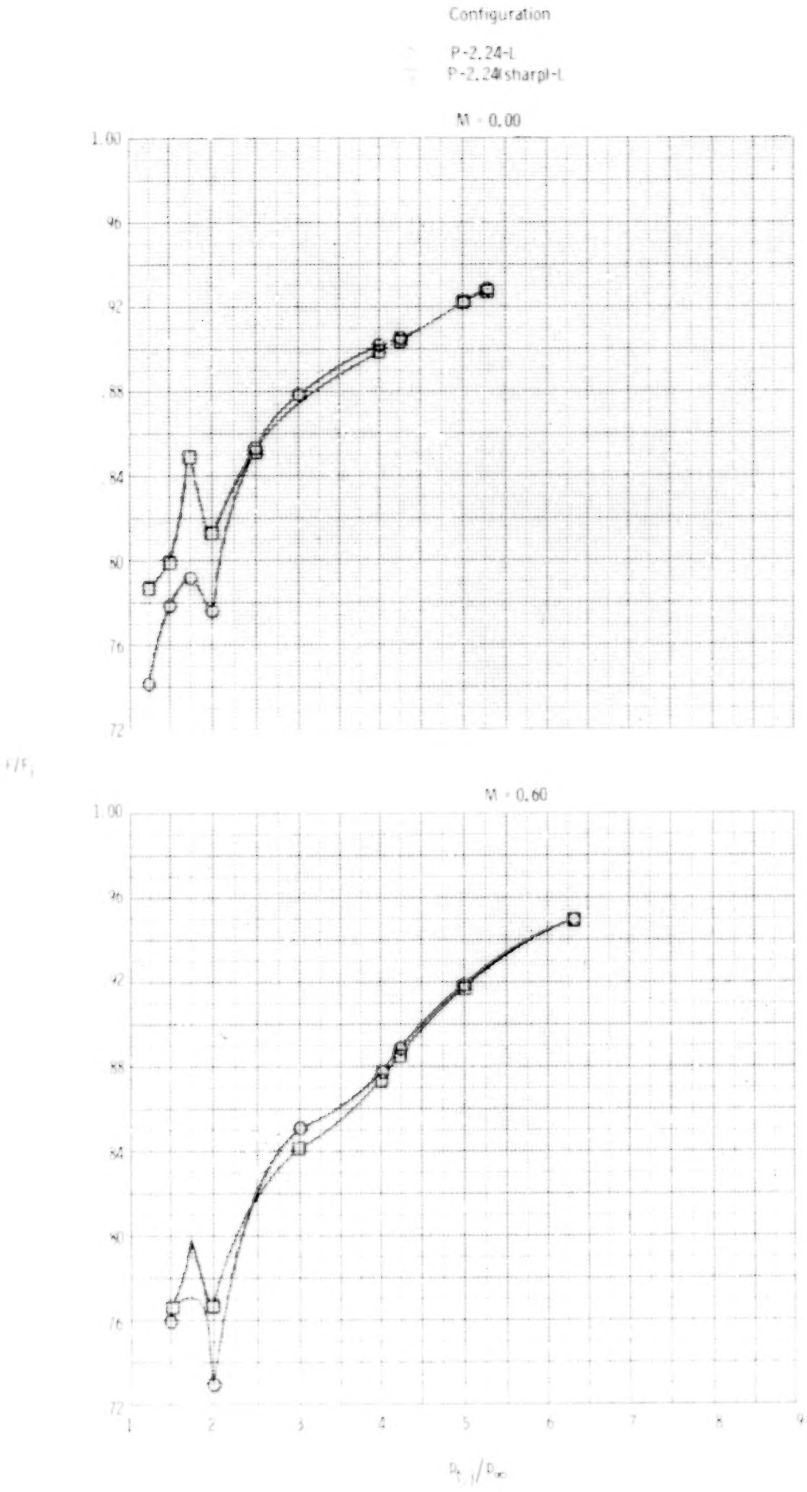

(a) M = 0.00 and 0.60.

Figure 49.- Effect of sharp geometric throat on nozzle thrust ratio.

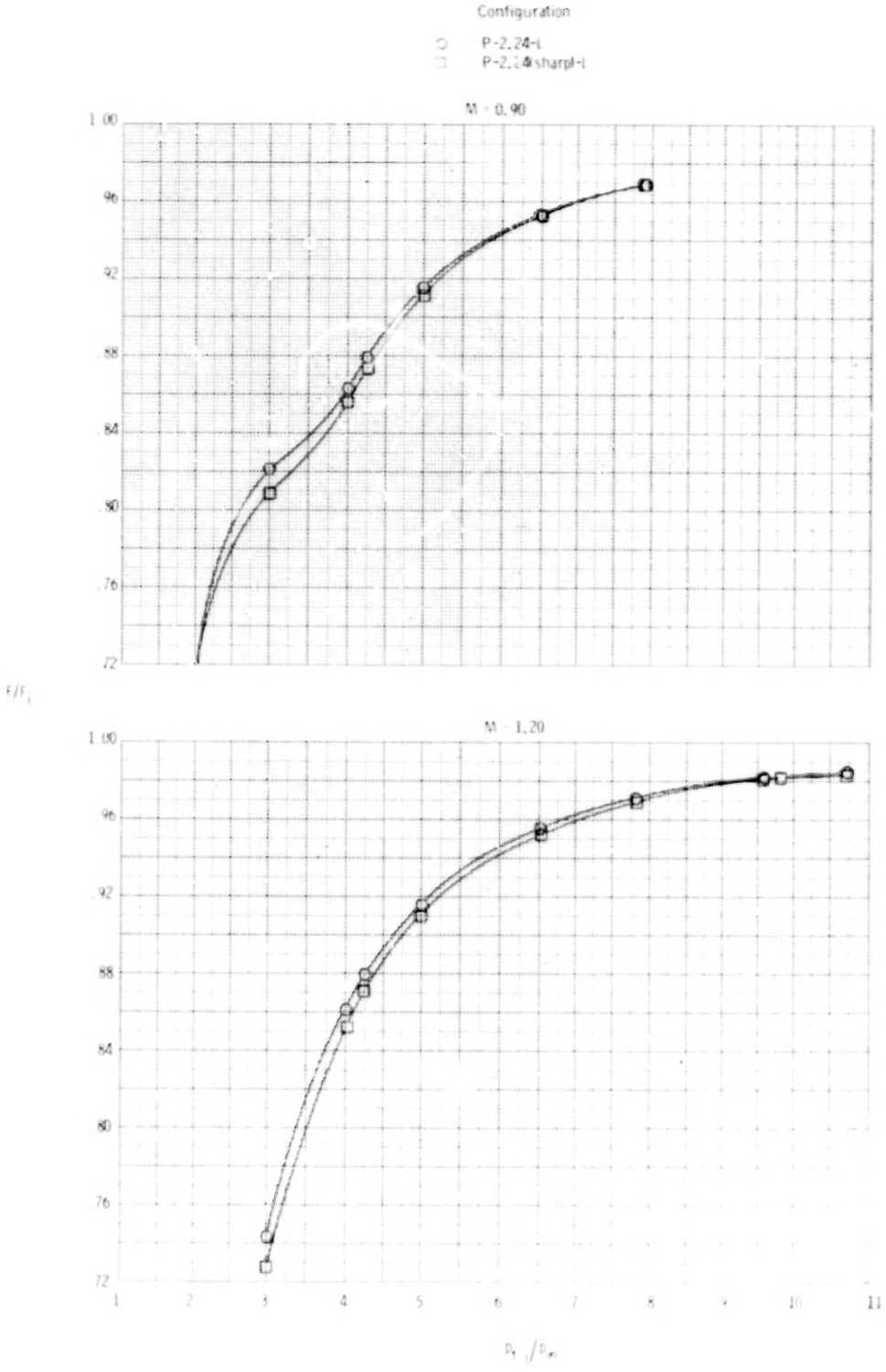

(b) M = 0.90 and 1.20.

Figure 49.- Concluded.

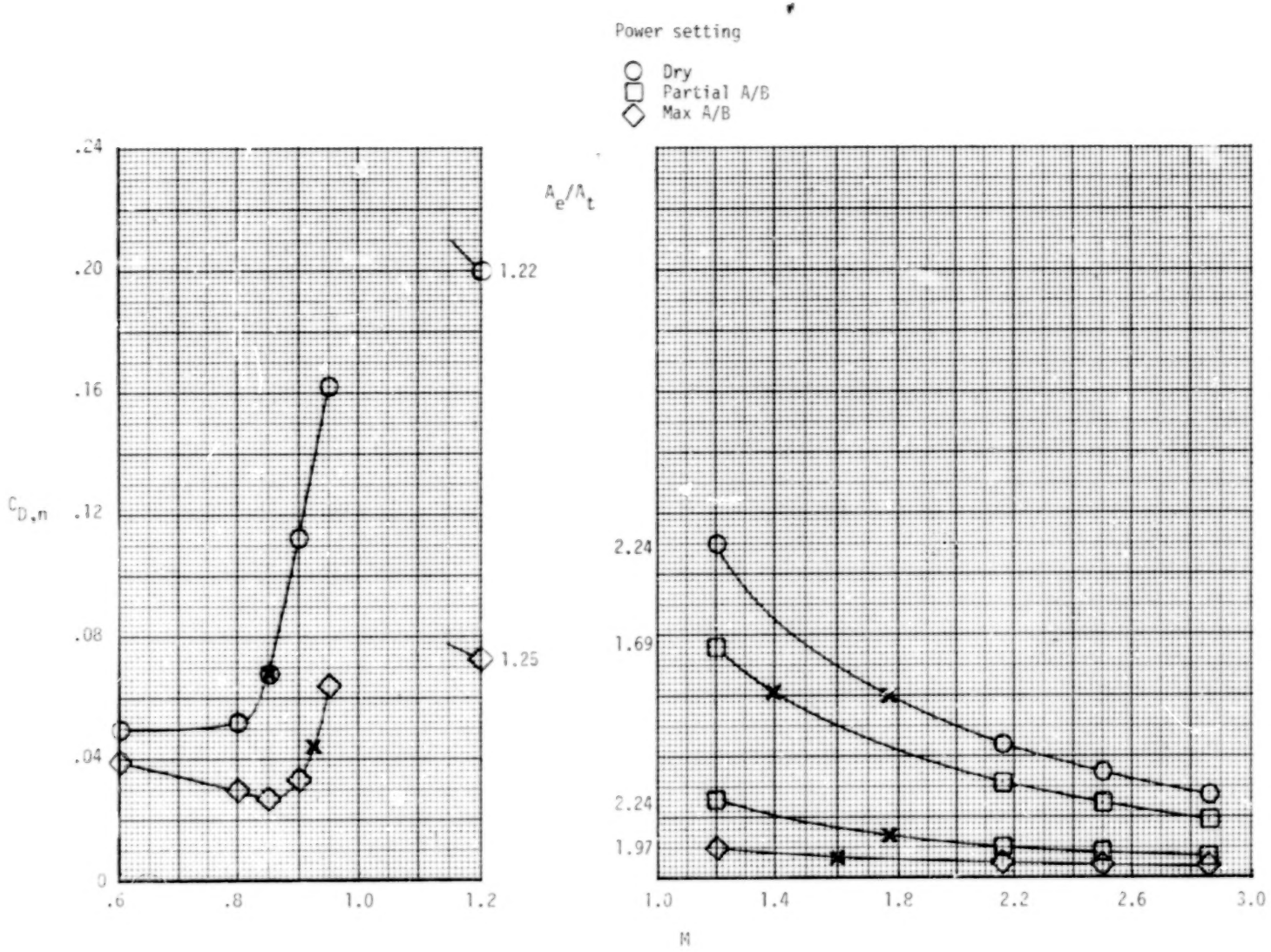

(a) Short length nozzles.

Figure 50.- Variation of nozzle drag coefficient with Mach number at scheduled nozzle pressure ratios. Cross marks indicate on-design operating condition. Note Mach number scale change.

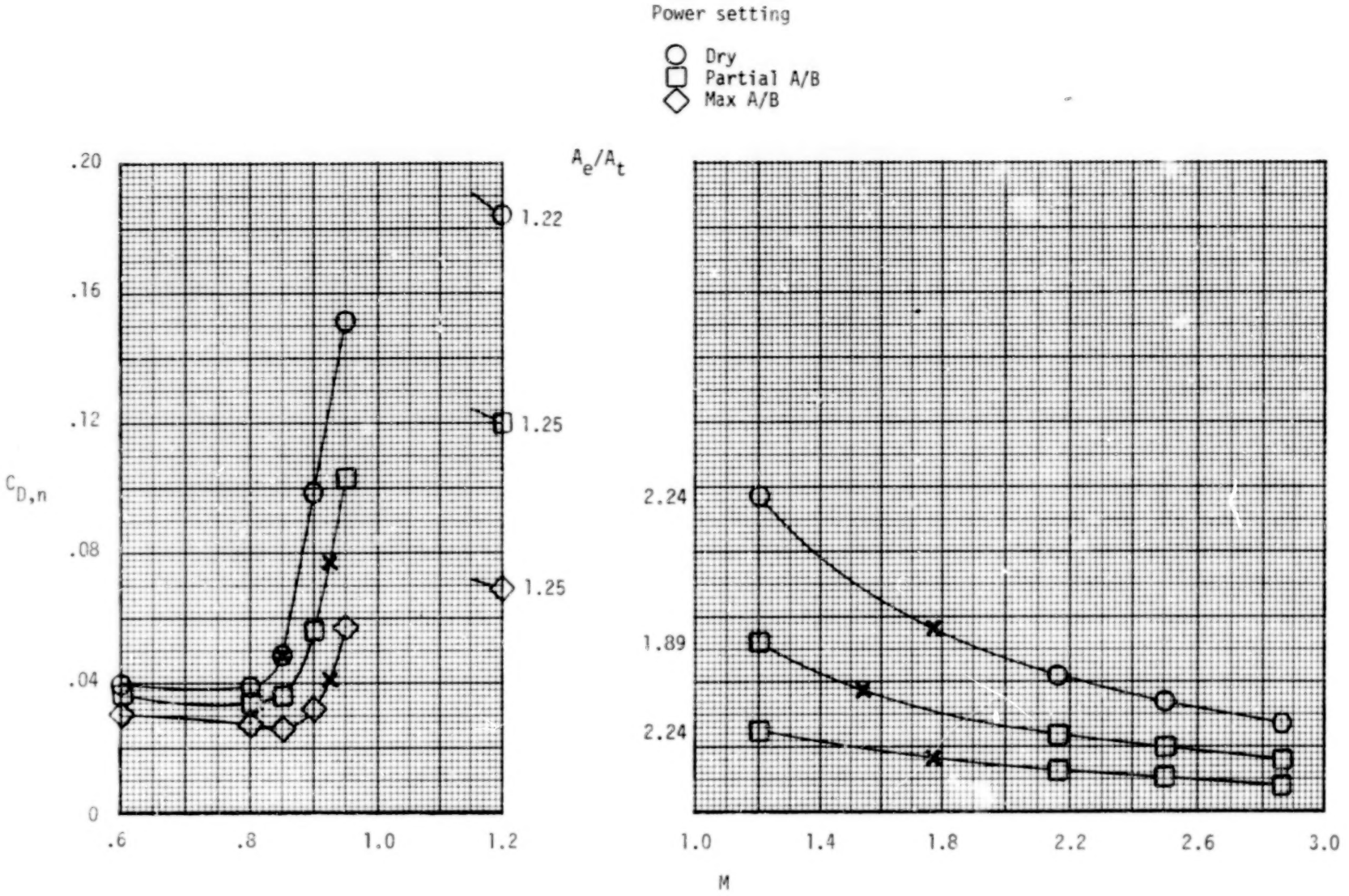

(b) Medium length nozzles.

Figure 50.- Continued.

BLANK PAGE

BLANK PAGE

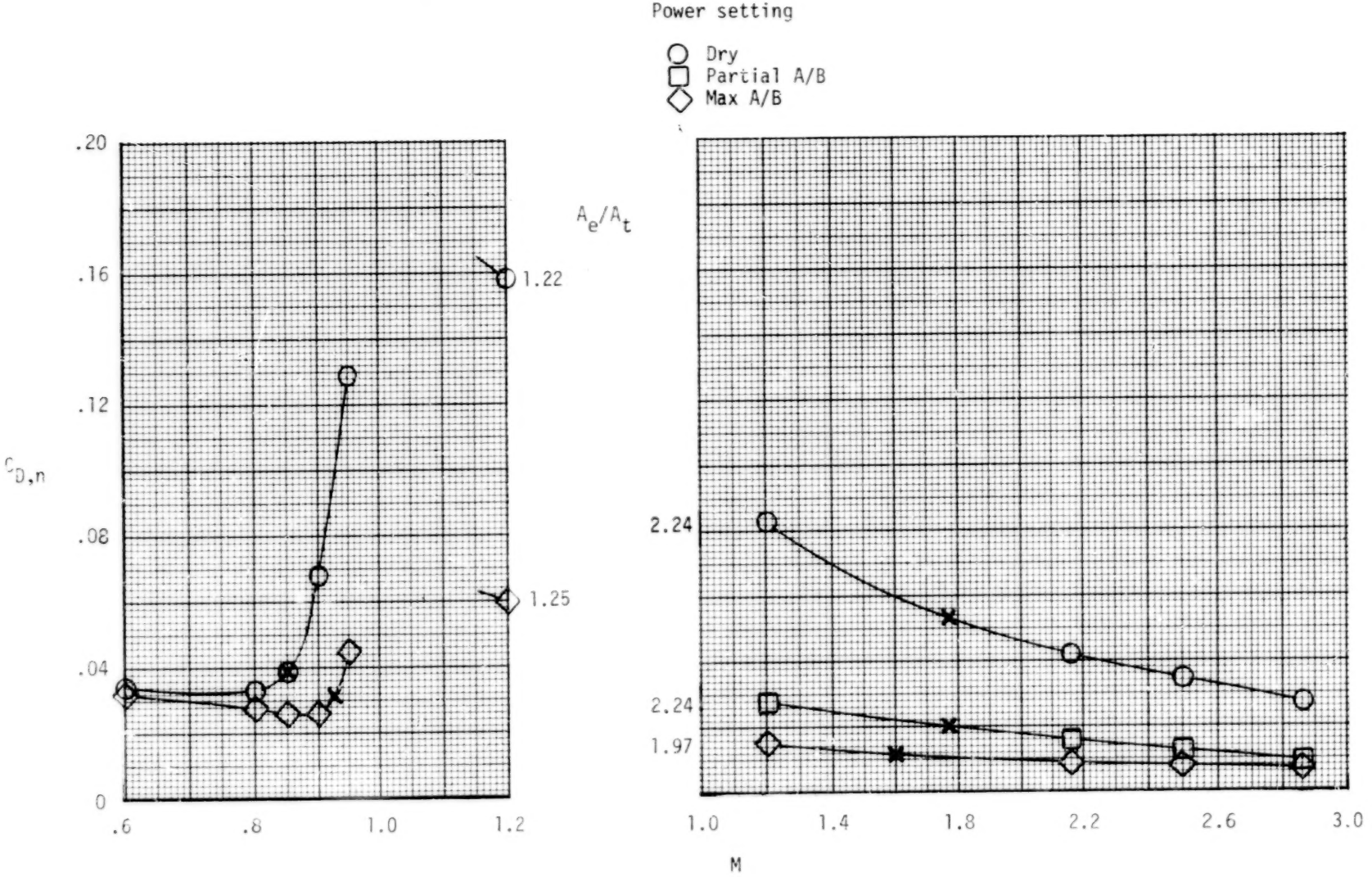

(c) Long length nozzles.

Figure 50.- Concluded.

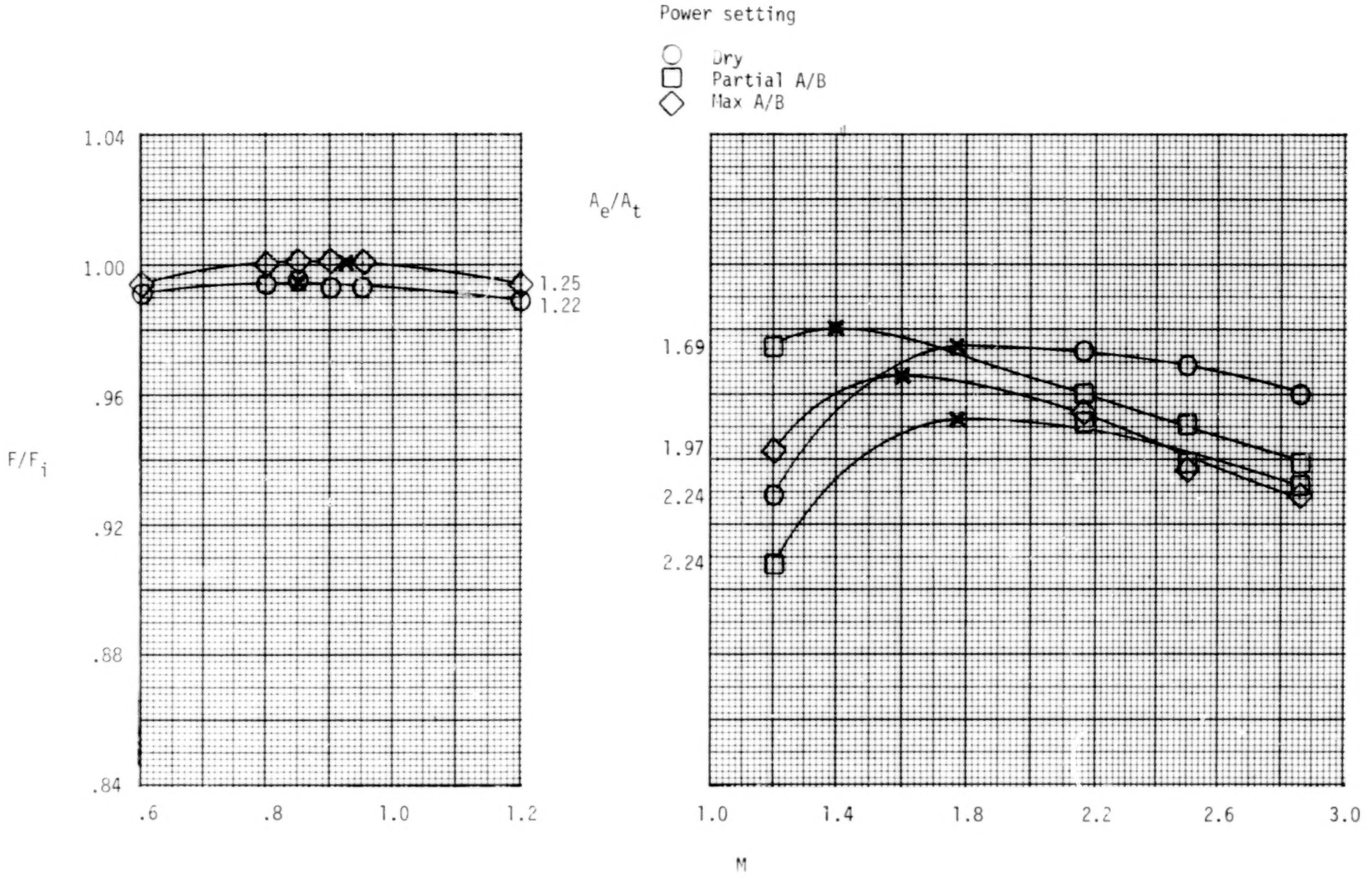

(a) Short length nozzles.

Figure 51.- Variation of nozzle thrust ratio with Mach number at scheduled nozzle pressure ratios. Cross marks indicate on-design operating condition. Note Mach number scale change.

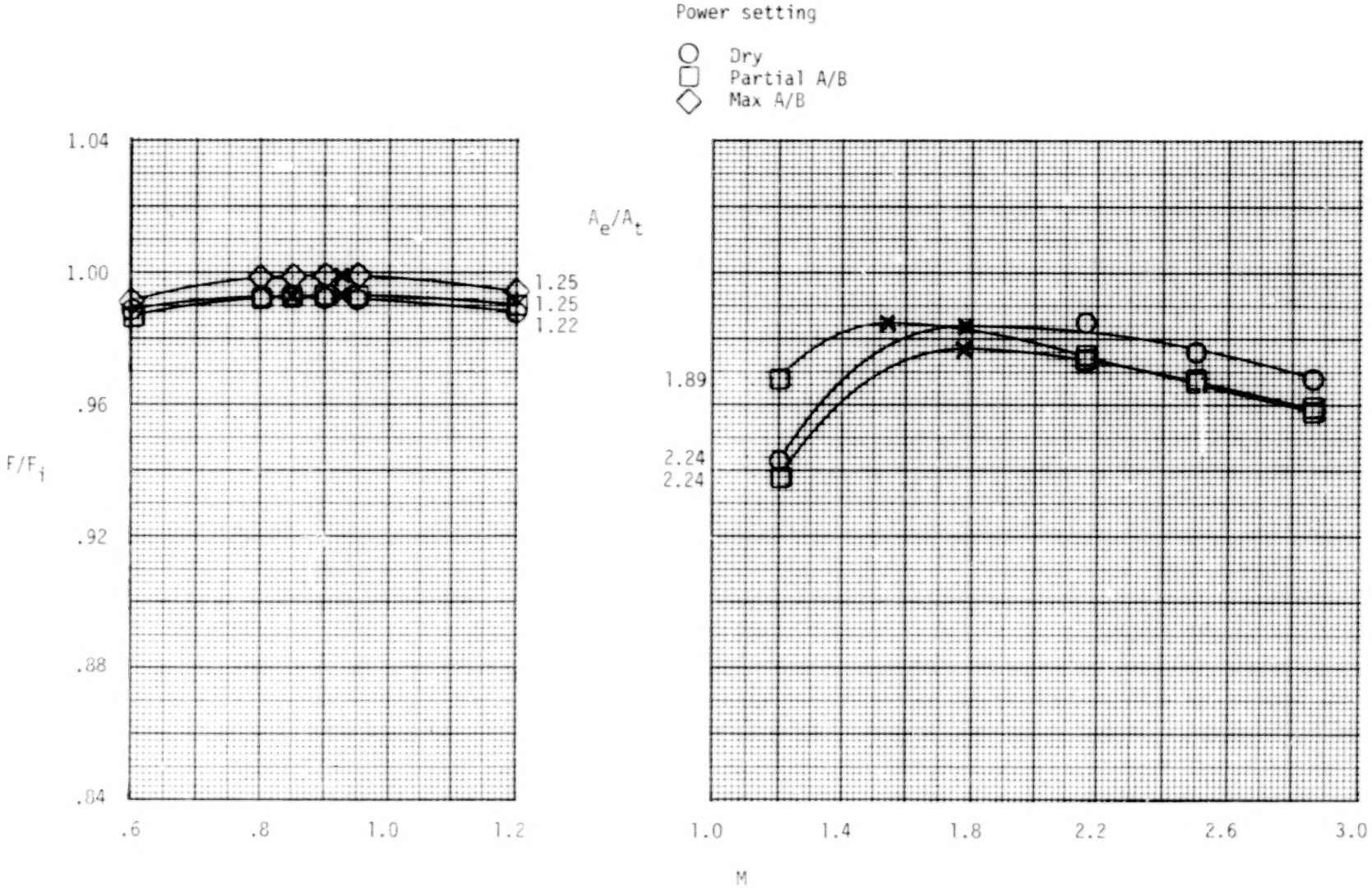

(b) Medium length nozzles.

Figure 51.- Continued.

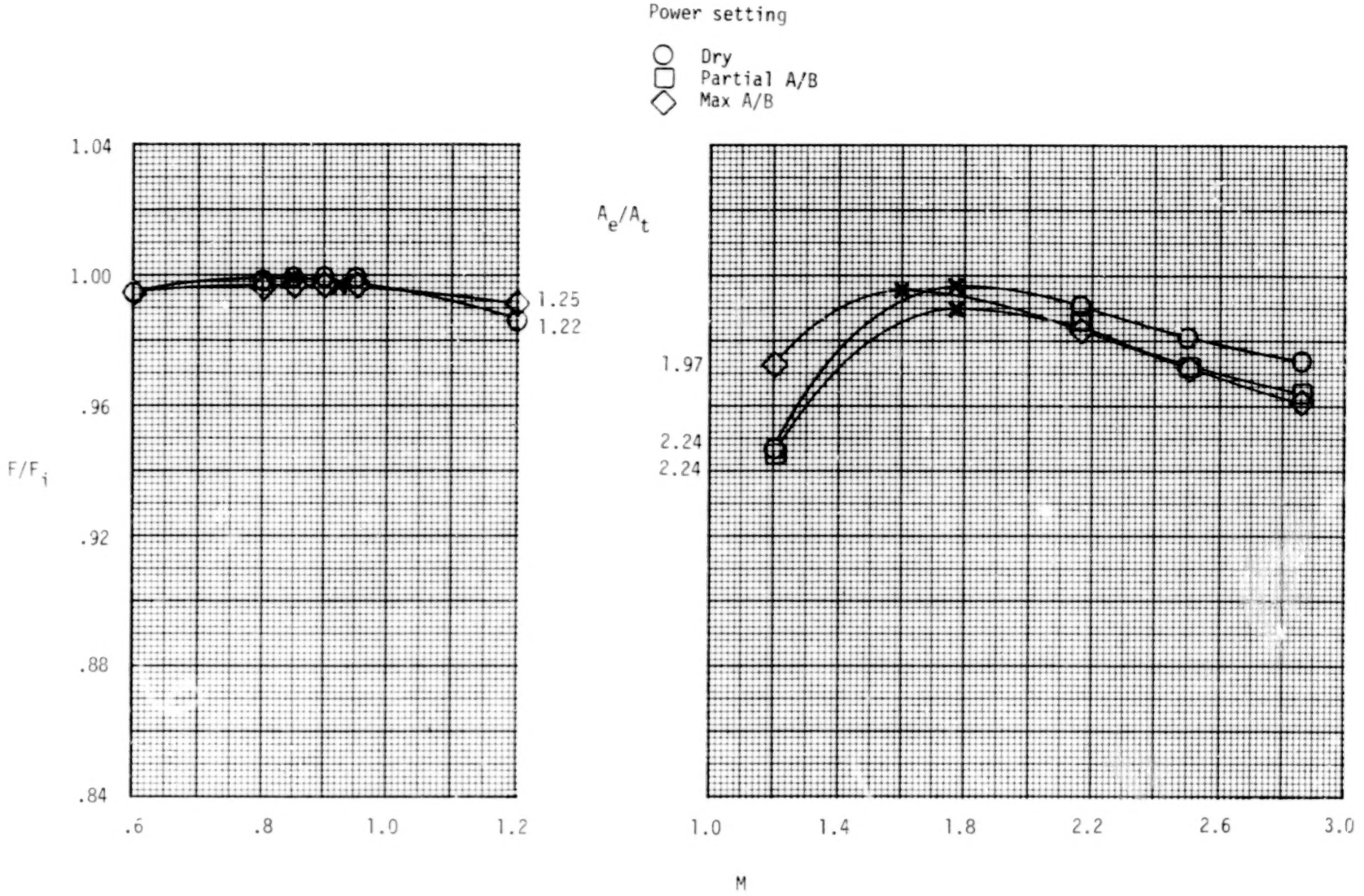

(c) Long length nozzles.

Figure 51.- Concluded.

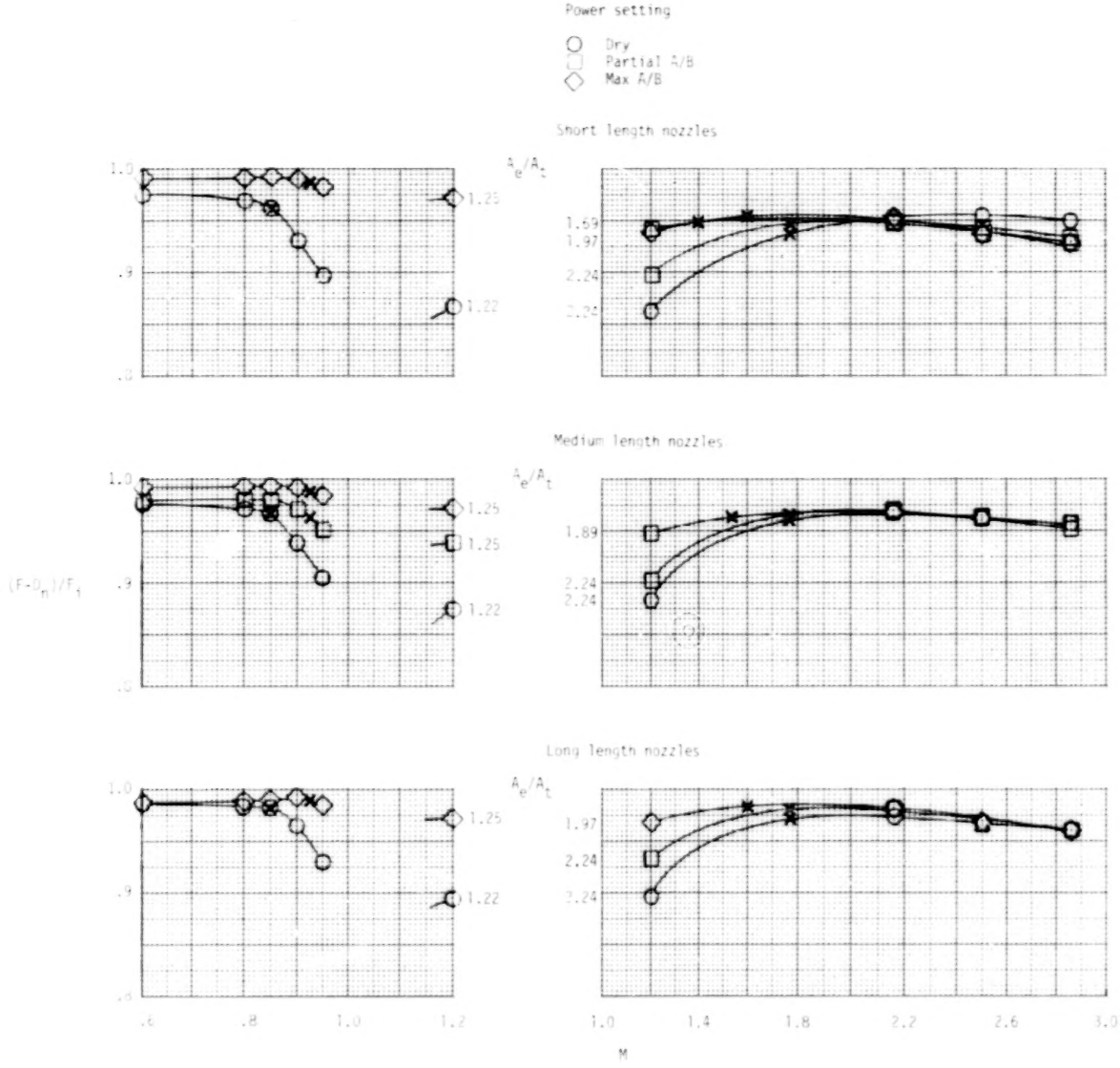

Figure 52.- Variation of nozzle thrust-minus-drag ratio with Mach number at scheduled nozzle pressure ratios. Cross marks indicate on-design operating condition. Note Mach number scale change.

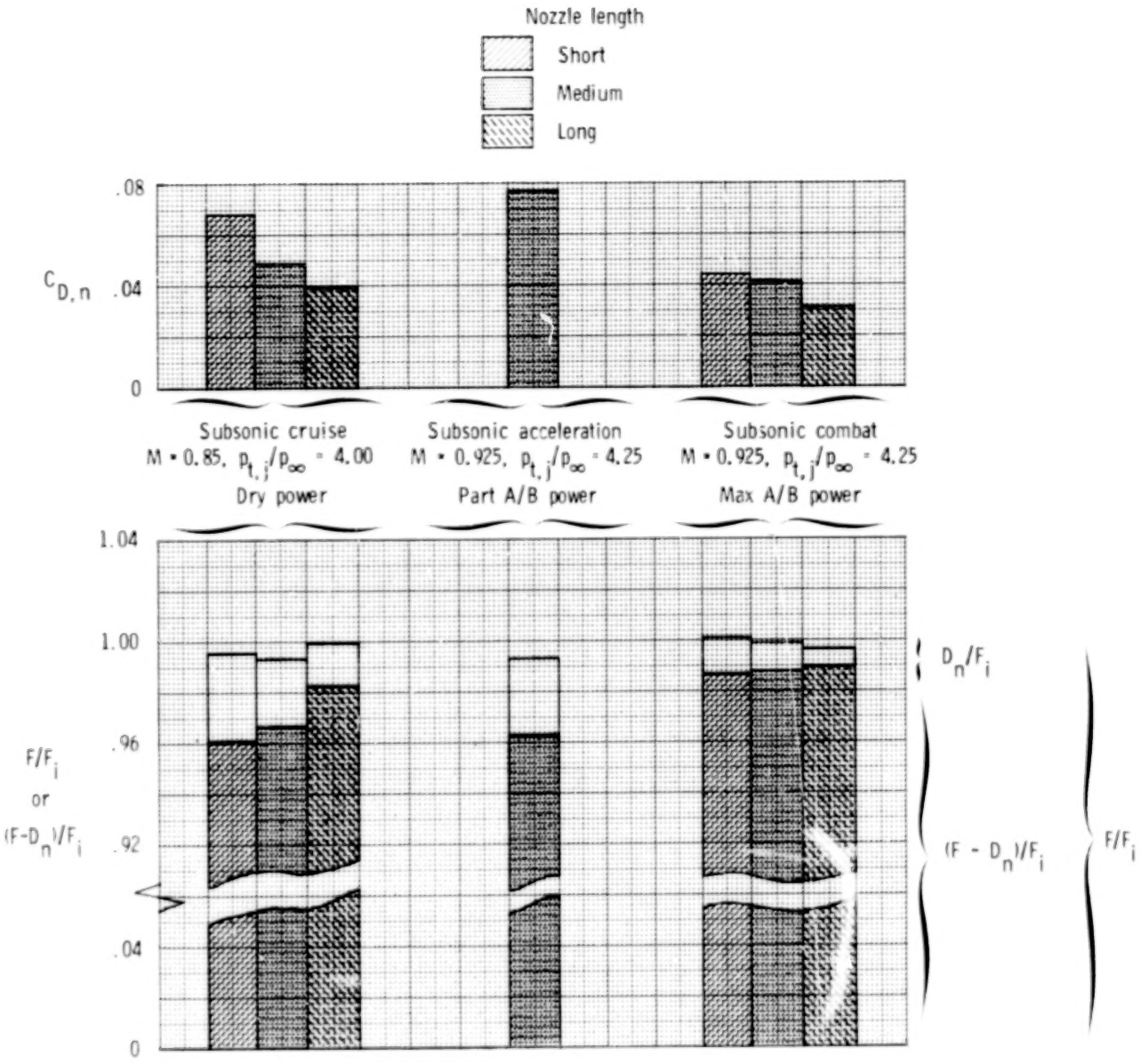

(a) Subsonic mission segments ($1.22 \leq A_e/A_t \leq 1.25$).

Figure 53.- Comparison of nozzle performance parameters at on-design operating conditions for various mission segments.

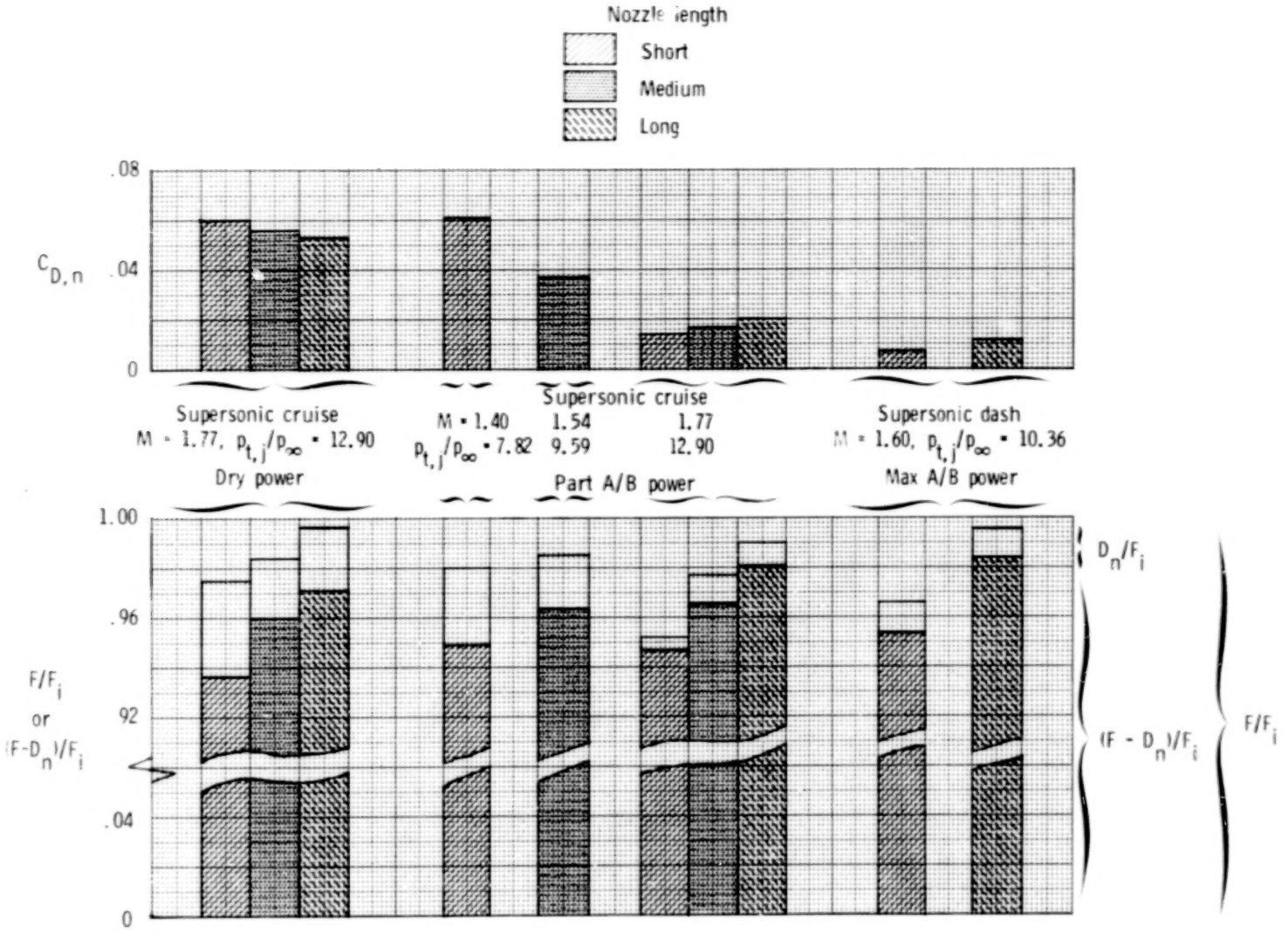

(b) Supersonic mission segments ($1.69 \leq A_e/A_t \leq 2.24$).

Figure 53.- Concluded.

1. Report No.	2. Government Accession No.	3. Recipient's Catalog No.
NASA TP-1766		

4. Title and Subtitle	5. Report Date
INVESTIGATION OF CONVERGENT-DIVERGENT NOZZLES APPLICABLE TO REDUCED-POWER SUPERSONIC CRUISE AIRCRAFT	December 1980
	6. Performing Organization Code 505-32-13-01
7. Author(s) Bobby L. Berrier and Richard J. Re	8. Performing Organization Report No. L-13974
	10. Work Unit No.
9. Performing Organization Name and Address NASA Langley Research Center Hampton, VA 23665	11. Contract or Grant No.
	13. Type of Report and Period Covered Technical Paper
12. Sponsoring Agency Name and Address National Aeronautics and Space Administration Washington, DC 20546	14. Sponsoring Agency Code

15. Supplementary Notes

16. Abstract

An investigation has been conducted of isolated convergent-divergent nozzles to determine the effect of several design parameters on nozzle performance. Tests were conducted using high-pressure air for propulsion simulation at Mach numbers from 0.60 to 2.86 at an angle of attack of 0° and at nozzle pressure ratios from jet off to 46.0. Three power settings (dry, partial afterburning, and maximum afterburning), three nozzle lengths, and nozzle expansion ratios from 1.22 to 2.24 were investigated. In addition, the effects of nozzle throat radius and a cusp in the external boattail geometry were studied.

The results of this study indicate that, for nozzles operating near design conditions, increasing nozzle length increases nozzle thrust-minus-drag performance. Nozzle throat radius and an external boattail cusp had negligible effects on nozzle drag or internal performance.

17. Key Words (Suggested by Author(s))

Nozzle
Supersonic cruise
Convergent-divergent
Internal performance

18. Distribution Statement

Unclassified - Unlimited

Subject Category 02

19. Security Classif. (of this report)	20. Security Classif. (of this page)	21. No. of Pages	22. Price
Unclassified	Unclassified	215	A10

For sale by the National Technical Information Service, Springfield, Virginia 22161

NASA-Langley, 1980

END

March 4, 1981